2026 Design, Build, Fly Competition Summary

The 2025-26 AIAA/Textron Aviation/RTX Design, Build, Fly Competition Flyoff was held at the Textron Aviation Employees Flying Club in Wichita, KS on the weekend of April 16-19, 2026. This was the 30th year of the competition. Of the 175 proposals submitted and judged, 102 teams were invited to submit a design report for the next phase of the competition. 98 teams submitted design reports and 89 teams attended the flyoff (17 international teams). Over 1200 students, faculty, and guests were present. Of the 89 teams in attendance, 83 successfully completed tech inspection. The weather did not cooperate on Friday afternoon but conditions were great on Saturday and Sunday. Of the 197 official flight attempts, 143 resulted in a successful score with 73 teams achieving at least one successful flight score and 17 teams successfully completing all missions (one ground and three flight missions). The quality of the teams, their readiness to compete, and the execution of the flights was exceptional.

The contest theme this year was a Banner Towing Bush Plane. The first mission was a Test Flight requiring the aircraft to complete three laps within five minutes. The second mission was a Charter Flight with the score based on the number of passengers (rubber ducks) and cargo (hockey pucks) carried plus the number of laps flown and battery capacity. The final mission was a Banner Towing flight with the score dependent upon banner length, the number of laps flown and RAC (wingspan). Teams were also required to complete a ground mission demonstrating the efficiency of loading and unloading passengers and then converting the airplane into a banner towing configuration. The team's final score is the product of the sum of the flight and ground mission scores and total report score plus participation score. More details on the mission requirements and scoring breakdown may be found at the competition website: http://www.aiaa.org/dbf.

First Place went to the **University of Ljubljana**, Second Place went to **the University of Washington-Seattle**, and Third Place went to the **University of California, Los Angeles**. A full listing of the results is included below. The Best Paper Award, sponsored by the Design Engineering TC for the highest design report score, went to the **University of Southern California** with a score of 91.98.

For the fifth year, the Stan Powell Memorial Award recognized a team that exhibited the Most Meaningful Lessons Learned during the competition. This year, it was awarded to **Washington University in St. Louis**. After crashing in their first two flight attempts with significant damage, the team maintained a very positive attitude, did not give up, put in many hours of work to rebuild their airplane and completed a successful flight with pride and excitement.

We owe our thanks for the success of the DBF competition to the efforts of many volunteers from Textron Aviation, RTX, and the AIAA sponsoring technical committees: Applied Aerodynamics, Aircraft Design, Flight Test, and Design Engineering. These volunteers collectively set the rules, judge the proposals and reports, and execute the flyoff. Thanks also to the Premier Sponsors: Textron Aviation and RTX, and to the AIAA Foundation for their financial support as well as to our Gold sponsors this year – General Atomics, Mathworks, Anduril and Reliable Robotics. Special thanks go to Textron Aviation for hosting the flyoff this year.

Finally, this event would not be nearly as successful without the hard work and enthusiasm from all the students and advisors. If it weren't for you, we wouldn't keep doing it!!

DBF Organizing Committee

The University of Southern California AeroDesign Team Presents

Trojan HorSCe

For the 2025-2026 AIAA
Design Build Fly Competition

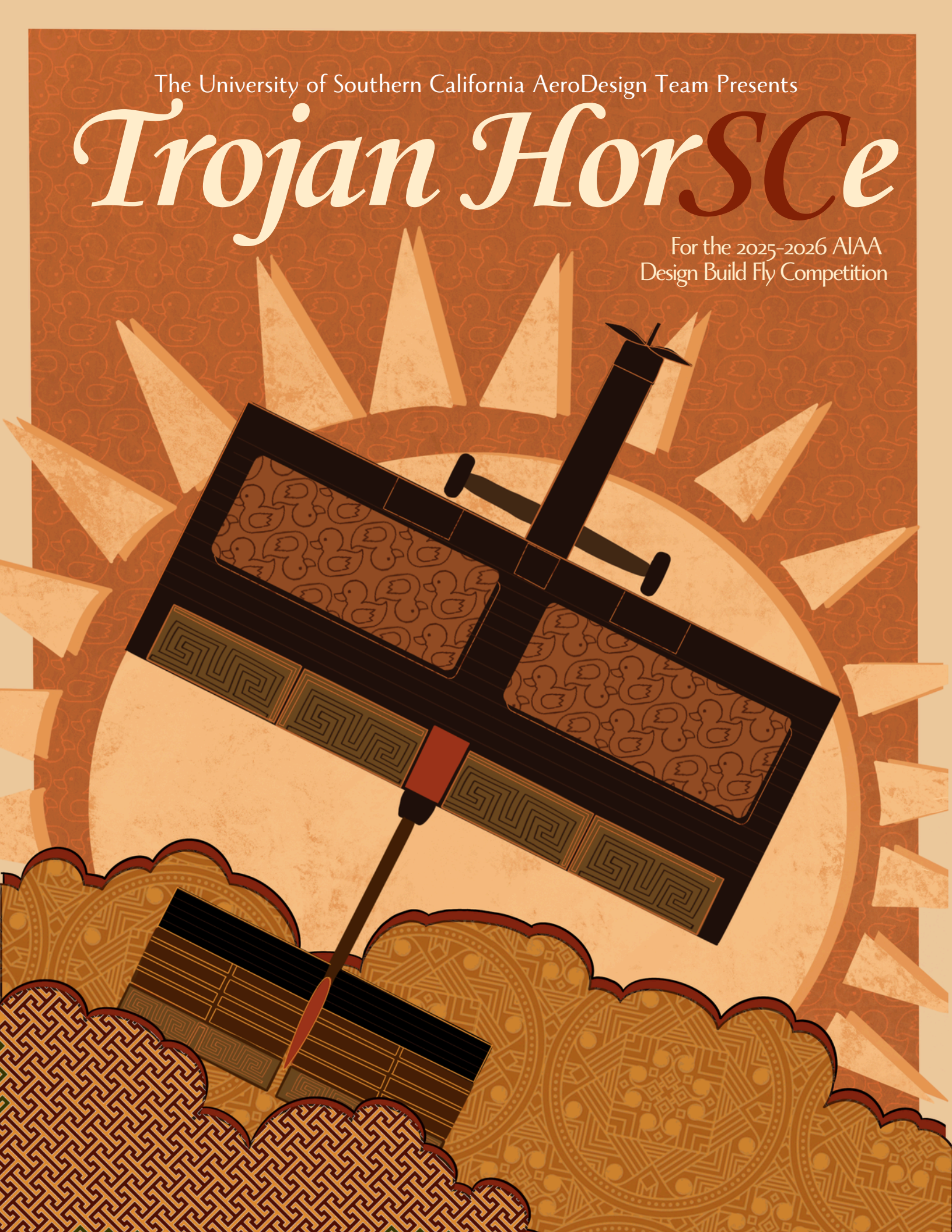

Acronyms, Abbreviations, and Symbols

α	Angle of Attack	C_h	Horizontal Stabilizer Volume Coefficient	h_{spar}	Spar Height	PT	Plane tools
δ	Control Surface Deflection Angle	C_H	Hinge Moment Coefficient	HT	Horizontal Tail	PVA	Polyvinyl Alcohol
ζ	Damping Ratio	C_L	3D Lift Coefficient	I	Current	q	Dynamic Pressure
η	Propulsion System Efficiency	c_l	2D Lift Coefficient	IF	Interference Factor	Q	First Moment of Area
λ	Taper Ratio	$C_{l,\beta}$	Roll Moment Stability Derivative W.R.T. Sideslip	i_h	Horizontal Stabilizer Incidence Angle	RAC	Rated Aircraft Cost
μ	Ground Friction Coefficient	GJ	Torsional Rigidity	IML	Inner Mold Line	RANS	Reynolds Averaged Navier Stokes
ρ	Air Density	c_m	Coefficient of Pitching Moment	I_{xx}	Second Moment of Area about the X-Axis	RC	Remote Controlled
σ	Crab Angle	C_n	Yaw Moment Stability Derivative	I_{yy}	Second Moment of Area about the Y-Axis	Re	Reynolds Number
σ_{bend}	Bending Stress	COTS	Commercial off-the-Shelf	I_{zz}	Second Moment of Area about the Z-Axis	Re_b	Banner Reynolds Number
σ_c	Compressive Bending Stress	C_P	Coefficient of Power	J	Advance Ratio	RoC	Rate of Climb
σ_{cr}	Critical Local Bending Stress	C_T	Coefficient of Thrust	k_{excr}	Excrescence Drag Factor	S	Planform Area
θ	Angle	C_V	Vertical Stabilizer Volume Coefficient	k_{ss}	Shear Buckling Coefficient	SF	Shear Force
τ	Shear Stress	C_y	Lateral Stability Derivative	L/D	Lift-to-Drag Ratio	S_g	Takeoff Ground Roll Distance
ω_n	Undamped Natural Frequency	D	Drag	l_{banner}	Banner Length	SM	Static Margin
ν	Poisson's Ratio	d	Lever Arm	LE	Leading Edge	T	Thrust
ADT	AeroDesign Team	DA	Flat Plate Equivalent Drag Area	l	Moment Arm	t/c	Thickness to Chord
AIAA	American Institute of Aeronautics & Astronautics	DBF	Design, Build, Fly	LiPo	Lithium Polymer	T/W	Thrust to Weight Ratio
AR	Aspect Ratio	DIF	Passengers in Fuselage	m	Mass	TM	Torsional Moment
a_{turn}	Turn Acceleration	DIW	Passengers in Wing	M#	Mission #	$t_{M\#}$	Time to Complete Mission (I.E. GM, M2)
AV	Avionics	d_{prop}	Propellor Diameter	MAC	Mean Aerodynamic Chord	TO	Takeoff
AVL	Athena Vortex Lattice	e	Oswald Efficiency Factor			TOFL	Takeoff Field Length
b	Span	E	Elastic Modulus	MLG	Main Landing Gear	T_{req}	Thrust Required
BEC	Battery Eliminator Circuit	$E_{battery}$	Battery Energy	MoC	Means of Compliance	t	Thickness
BM	Bending Moment	EF	Efficiency Factor			USC	University of Southern California
c	Chord	ESC	Electronic Speed Controller	MTOW	Maximum Takeoff Weight	V	Velocity
CA	Cyanoacrylate	FC	Flight Controller	n	Load Factor	V#	Version # of Team Aircraft
CAD	Computer-Aided Design	FEA	Finite Element Analysis	n_{cargo}	Number of Cargo Stored	V_{eff}	Effective Voltage
c_d	2D Drag Coefficient	FF	Form Factor	n_{laps}	Number of Laps Flown	VT	Vertical Tail
C_D $C_{D,0}$	3D Drag Coefficient	F	Force	n_{pax}	Number of Passengers	W	Weight
$C_{d,y}$	Side-Drag Coefficient	FoM	Figures of Merit	n_{rev}	Propellor Revolutions per Second	W/S	Wing Loading
C_f	Coefficient of Friction	FoS	Factor of Safety	n_{series}	Number of Cells in Series	XPS	Extruded Polystyrene
CF	Carbon Fiber	FPV	First-Person Viewer	OML	Outer Mold Line		
CFD	Computational Fluid Dynamics	GM	Ground Mission	P	Power		
CG	Center of Gravity	H	Hinge Moment	PLA	Polylactic Acid		

1.0 Executive Summary

This design report presents the design, manufacturing, and testing of *Trojan HorSCe*, the University of Southern California's aircraft entry for the 2025-26 American Institute of Aeronautics and Astronautics (AIAA) Design/Build/Fly (DBF) competition. This radio-controlled aircraft was designed to be a bush plane capable of charter flights and banner towing operations. Mission 1 (M1) is a validation flight. Mission 2 (M2) is a charter flight that aims to increase net income earned through maximizing the number passengers and cargo transported, represented by rubber ducks and hockey pucks respectively. Mission 3 (M3) is a banner-towing flight intended to maximize the number of laps completed while towing the longest banner within the allotted flight window, demonstrating in-flight deployment, towing, and release capability. The Ground Mission (GM) is a timed demonstration of transition between the M2 and M3 configurations.

Trojan HorSCe is the result of three design iterations across conceptual, preliminary, and detail design phases. Each iteration was designed, built, and tested by 77 students. During conceptual design, system requirements were derived. Sensitivity and constraint analyses guided configuration decisions. Preliminary design sized initial propulsion and aerodynamic parameters using performance trade studies and subsystem testing. Detail design refined structural sizing, payload design, integration, and build methods to minimize aircraft weight, guided by an sensitivity studies. The resulting design, shown in Fig. 1, is a 5-ft (1.52-m) span, high-wing monoplane with a wing aspect-ratio of 2.4 in a taildragger configuration. It features a conventional tail, single-tractor propulsion system with a 160-RPM/V motor with an 8S with 20X15E (M1/M2) and a 13S LiPo battery with 22X12E propellor (M3). To maximize M2 net income, a ducks-in-wing (DIW) passenger configuration was adopted, allowing *Trojan HorSCe* to carry 144 passengers constrained by Dacron. One cargo will be carried in the fuselage. To maximize M3 score, an externally mounted banner deployment and release mechanism was developed to carry a 196 × 39 in (5 × 1 m) Tissue Lamé banner in winds less than 16.8 mph (7.5 m/s) or a 79 ×15.75 in (2 × 0.4 m) otherwise. *Trojan HorSCe* is manufactured using a combination of vacuum-bagged wet composite layups, built-up structures, and 3D-printed mechanisms. The fuselage uses a semi-monocoque carbon-fiber (CF) construction with plywood and balsa internal structure. The wing and tail use a built-up plywood and balsa rib-spar-stringer structure with a semi-monocoque CF D-box. The landing gear is manufactured from unidirectional S-glass.

A testing campaign validated individual components prior to integration into the full aircraft. Each complete aircraft underwent structural, ground, and flight testing to verify payload operation, validate performance predictions (Table 1), and provide model corrections to improve simulations.

Figure 1. USC 2025-26 DBF aircraft, *Trojan HorSCe*.

Table 1. Predicted Performance of *Trojan HorSCe* with 14.5 mph (6.5 m/s) Headwind

Data	M1	M2	M3	GM
Gross Takeoff Weight [lbm]	14.3	21.5	14.2	-
Cruise Airspeed [ft/s]	76.1	65.6	46.6	-
Number of Laps [-]	3	5	2	-
Scored Payload	-	144 pax, 1 cargo	196x39 in (5x1 m) banner	-
Mission Time [s]	130	290	174	426
Net Income [-]	-	2005	-	-

2.0 Management Summary

The 2025-26 AeroDesign Team (ADT) at the University of Southern California (USC) is a student-led extracurricular organization comprised of 76 undergraduate and one postgraduate student.

2.1 Team Organization and Structure

The team structure, seen in Fig. 2 emulates a traditional aerospace company. The team management, consisting of the Program Manager and Chief Engineer, collaborate to drive the design process. The Program Manager oversees the team schedule, DBF documentation, and chairs the Logistics subteam. The Chief Engineer guides the sizing, design, build, and testing performed by the Hardware Design and Analysis subteams. Team leads complete assigned tasks and meet weekly for engineering discussions. The Chief Pilot, Faculty Advisor, and Industry Advisors meet with the team weekly to provide feedback. Each subteam composes of leads who are responsible for overseeing the tasks outlined in Table 2:

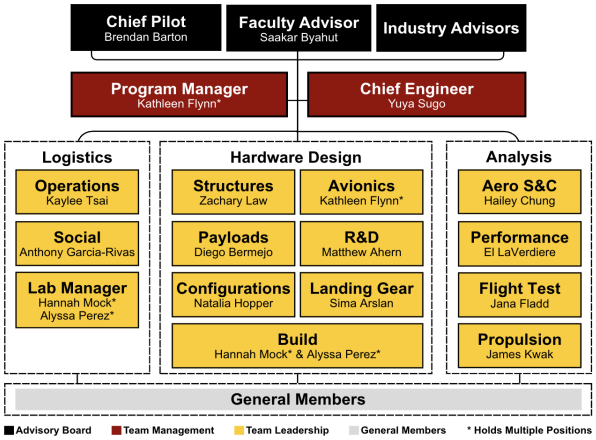

Figure 2. Diagram of team structure

Table 2. Overview of Team Leads, Positions, and Skills

Subteam	Position	Responsibilities	Skill Set Required
Logistics	Operations	Oversee budget and maintain sponsorship relationships.	Understanding of all available and potential funding streams.
	Social	Uphold the team's online presence.	Communication and marketing skills.
	Lab Manager	Maintain a safe and clean lab space.	Awareness of USC safety regulations.
Analysis	Aero Stability & Control (Aero S&C)	Analyze stability and control for airfoil, tail, and control surfaces.	Understanding of aircraft stability, control theory, and XFLR5.
	Performance	Perform trade studies to size the wing and payload.	Knowledge of aerodynamic performance, simulation, and sizing.
	Flight Test	Create flight test matrices and ground testing plans.	Flight test data processing and analysis.
	Propulsion	Trade, test, and select propulsion system components.	Understand RC propulsion systems and testing methods.
Hardware Design	Structures	Design and validate aircraft structure to meet predicted flight loads.	Knowledge of aircraft loading and structural analysis methods.
	Avionics	Select and integrate servos, sensors, and data-acquisition electronics.	Understanding of electronics selection and integration.
	Payloads	Design and optimize mission-specific aircraft components.	Ability to design, prototype, and test sub-components within aircraft and competition constraints.
	Research & Development (R&D)	Manage new research and development projects.	Ability to oversee and implement new technologies.
	Configurations	Oversee component mass tracking and aircraft layout modeling.	Understanding of aircraft configuration selection and computer-aided design (CAD) software.
	Landing Gear	Design, manufacture, and test the aircraft landing gear.	Ability to size and manufacture a gear given predicted landing loads.
	Build	Supervise aircraft build and create manufacturing documentation.	Experience using composite and built-up techniques for aircraft construction.

2.2 Schedule and Major Milestones

The Gantt Chart in Fig. 3 outlines the team's major milestones, aligned with overarching DBF deadlines. Following the release of competition rules, the team planned the development of three versions of the aircraft, V1, V2, and V3, with adequate time for design and testing in between. V1 served as a configuration validator. V2 aimed to further mature payloads concepts and serve as the critical design aircraft for aerodynamic, structural, and propulsion sizing. V3 is the competition aircraft.

Each aircraft progresses through a complete design cycle. This process consists of trade studies and component sizing, and payload component development. Manufacturing includes building the aircraft and payloads systems. Testing involves both ground structural testing and in-flight testing. Design reviews are conducted at the conclusion of each prototype design cycle. The Conceptual Design phase established the payloads configuration, and selected the initial wing, tail, propulsion, and landing gear configurations. The Preliminary Design phase selected a propulsion package and refined fuselage, wing, and tail sizing through trade studies and initial subsystem testing. The Detail Design phase focuses on subsystem development, including the banner deployment and release mechanism and improvement to manufacturing methods. Flight testing was conducted throughout the year for handling qualities, error-propulsive performance, and for mission testing.

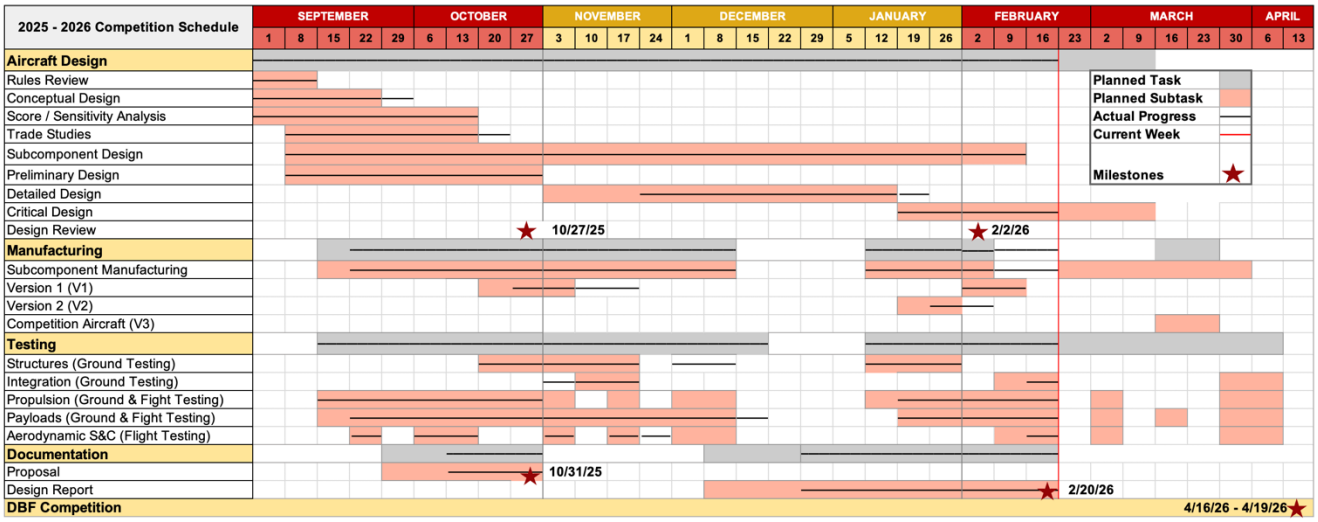

Figure 3. Team schedule with major milestones.

3.0 Conceptual Design

During the Conceptual Design phase, the team reviews rules and scoring to identify key design objectives. The predicted highest-scoring aircraft configuration is derived using relevant Figures of Merit (FoM).

3.1 Mission Requirements

The 2025-26 American Institute of Aeronautics and Astronautics (AIAA) Design, Build, Fly (DBF) competition challenges teams to design a banner-towing bush plane capable of carrying passengers and cargo. The competition consists of three flight missions and one ground mission: a test flight (M1), a charter flight (M2), a banner flight (M3), and a configuration-change demonstration (GM).

3.1.1 Mission and Scoring Summary

The total report score is expressed as a function of the proposal and design report scores, each out of 100 points.

$$\text{Total Report Score} = (0.15 \times \text{Proposal Score}) + (0.85 \times \text{Design Report Score}) \quad \text{Eq. 1}$$

Total Mission Score is expressed as the sum of the earned M1, M2, M3, and GM scores during the flyoff.

$$\text{Total Mission Score} = \text{M1} + \text{M2} + \text{M3} + \text{GM} \quad \text{Eq. 2}$$

Competition Score is the sum of Total Mission Score, Total Report Score, and Participation Score. Three points are awarded for participation: (1) attending the flyoff, (2) completing tech inspection, (3) attempting a flight mission.

$$\text{Competition Score} = \text{Total Report Score} \times \text{Total Mission Score} + \text{Participation Score} \quad \text{Eq. 3}$$

3.1.2 Staging and General Mission Requirements

After passing Technical Inspection, the aircraft will undergo staging before each flight mission. During the 5-min staging window, a crew member will install the propulsion battery, mission-specific payloads, and ensure the aircraft is in a flight-ready configuration with functional controls. Once positioned on the runway, the 5-min flight window begins upon throttle advancement. Next, the aircraft will fly the specified number of competition laps or as many laps permitted within the flight window. A competition lap, depicted in Fig. 4, consists of 180° upwind and downwind turns, two 1000-ft (304.8-m) straightaways, and a 360° turn. A lap is completed when the aircraft crosses the finish line in the air. A successful landing must be completed following the flight window and the aircraft must not incur significant damage.

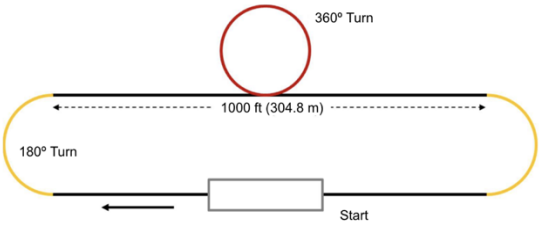

Figure 4. DBF competition flight path.

3.1.3 Mission 1 - Validation Flight

During M1, the aircraft must fly three laps within five minutes, without payload, to confirm its flight capability. One point will be awarded for completion.

$$\text{M1} = 1.0 \quad \text{Eq. 4}$$

3.1.4 Mission 2 - Charter Flight

During M2, the aircraft will conduct a charter flight, transporting passengers and cargo while flying as many laps as possible within a 5-min window. Passengers are rubber ducks measuring 2.0-2.3 in (5-5.8 cm) wide, 2.0-2.5 in (5-6.4 cm) long, and up to 2.5 in (6.4 cm) tall, weighing 0.6-0.7 oz (17-20 g). They must be individually loaded and fully restrained in an upright, vertical orientation within a dedicated passenger compartment. Cargo is represented by hockey pucks with a 3-in (7.6-cm) diameter and thickness of 1 in (2.5 cm). A minimum of one cargo item must be carried. Cargo must be housed in a restrained, isolated bay in front of, below, or behind the passengers.

The M2 score is the team's net income normalized by the highest net income, with a maximum possible score of two. Net income is a function of income and cost. Both depend on the number of passengers n_{pax}, cargo n_{cargo}, and laps flown n_{laps}. Additionally, income depends on several constants: the fixed income per passenger (6), income per passenger lap (2), fixed income per cargo item (10), and income per cargo item per lap (8). Cost depends on the base operating cost per lap (10), passenger operating cost per lap (0.5), cargo operating cost per lap (2), and total propulsion battery energy E_{prop}. The M2 score, income, and cost are defined in Eqs 5 - 8.

$$\text{M2} = 1 + \frac{\text{Net Income}}{\text{Max Net Income}} \quad \text{Eq. 5}$$

$$\text{Net Income} = \text{Income - Cost} \quad \text{Eq. 6}$$

$$\text{Income} = n_{\text{pax}} \ (6 + 2\, n_{\text{laps}}) + n_{\text{cargo}}(10 + 8 n_{\text{laps}}) \quad \text{Eq. 7}$$

$$\text{Cost} = n_{\text{laps}} \left((10 + 0.5\, n_{\text{pax}}) + (2\, n_{\text{cargo}}) \right) \frac{E_{\text{prop}}}{100} \quad \text{Eq. 8}$$

3.1.5 Mission 3 - Banner Flight

In M3, the aircraft will deploy, tow, and release a banner. The banner will have a minimum length of 10 in (25.4 cm), a maximum length-to-height ratio of 5, and will display the team's university logo on both sides. The stowage, deployment, towing, and release mechanisms may be internal or external to the aircraft, provided they do not interfere with flight or control functions. After the first 180° upwind turn, the banner will be remotely deployed and will remain unfurled in a vertical orientation for the remainder of the 5-min flight window. Upon crossing the finish line after the final lap, the banner will be remotely released and must not sustain any damage after landing. The M3 score (Eq. 9) has a maximum of three points and is a function of n_{laps}, banner length l_{banner}, the Rated Aircraft Cost (RAC), and is normalized by the highest scoring team.

$$\text{M3} = 2 + \frac{(n_{\text{laps}}\, l_{\text{banner}} / \text{RAC})_{\text{USC}}}{(n_{\text{laps}}\, l_{\text{banner}} / \text{RAC})_{\text{Max}}} \quad \text{Eq. 9}$$

RAC depends on wingspan *b* (Eq. 10). The minimum RAC of 0.90 corresponds to a 3-ft (0.914 m) wingspan.

$$\text{RAC} = 0.05 \times (b_{[\text{in}]}/12) + 0.75 \quad \text{Eq. 10}$$

3.1.6 Ground Mission

GM is a timed transition between M2 and M3 payload configurations. The aircraft will begin upright on its landing gear within the 10 × 10 ft (3.05 × 3.05 m) mission area without the propulsion batteries or payloads installed. On the start command, the timer begins, and a crew member will load the maximum passengers and cargo declared at Technical Inspection and return to the start line, after which the timer is paused. The pilot will then ensure flight controls are operational. Following a second start command, the time resumes, and the crew member will remove all M2 payloads and install the banner in its stowed configuration before returning to the start line, after which the timer is paused again. Flight controls are verified. The crew member then holds the aircraft vertically with the nose up while the pilot demonstrates banner deployment and release. Scoring is a function of the total mission time $t_{\text{GM,USC}}$, normalized by the fastest team's mission time $t_{\text{GM,min}}$, for a maximum possible score of one.

$$\text{GM} = \frac{t_{\text{GM,USC}}}{t_{\text{GM,min}}} \quad \text{Eq. 11}$$

3.2 Aircraft Design Constraints

Aircraft and payload design requirements derived from the 2025-26 rules and Q&As are summarized in Table 3 [1][2][3]. These requirements ensure that *Trojan HorSCe* complies with all regulations and performance requirements for the competition. Means of verifying compliance (MoC) for each requirement are represented as testing (T), inspection (I), and analysis (A).

Table 3. Aircraft Design Requirements and Means of Compliance

Category	ID	Requirement	MoC
Configuration	CO.01	The aircraft wingspan is between 3 ft (0.91 m) and 5 ft (1.52 m).	I
	CO.02	The total aircraft weight is less than or equal to 55 lbm (24.9 kg).	T
	CO.03	The aircraft is flown in the same configuration for all missions, unless specifically cited.	I
	CO.04	The aircraft is any configuration except rotary wing or lighter-than-air configuration.	I
	CO.05	The aircraft is capable of carrying at least 3 passengers.	T
	CO.06	The aircraft is capable of carrying at least 1 piece of cargo.	T
	CO.07	The aircraft is capable of carrying at least 3 passengers for each piece of cargo.	T
	CO.08	The airplane shall have an externally accessible switch to turn on the radio control system.	I
	CO.09	The aircraft is radio controlled and manually flown by a pilot.	I
Propulsion	PR.01	The propulsion batteries are NiCAD, NiMH or lithium-based chemistries.	I
	PR.02	Total propulsion energy is ≤ 100 Wh stored in unaltered, Commercial Off-The-Shelf batteries.	I
	PR.03	The blade-style arming fuse is rated for continuous currents not exceeding 100A.	I
	PR.04	The arming fuse is integrated into the electrical circuit on the positive (+ Red) wire between the battery and the electronic speed controller (ESC).	I
	PR.05	The arming fuse is mounted on the top or upper surface of the aircraft and at least 6 inches (15.2 cm) away from the plane of the propeller.	I
	PR.06	The aircraft is propeller driven and electric powered with a commercial, unmodified motor.	I
Structures	ST.01	All components can withstand expected flight loads, flutter, and aero-elastic effects.	T
	ST.02	Aircraft door(s) or hatch(es) shall remain rigidly attached at all times.	T
	ST.03	All structures, components, and payloads are mechanically fastened and do not rely on friction to be the primary retention method.	I
Operation	OP.01	All aircraft staging procedures shall be completed within 5 minutes.	T
	OP.02	All flight missions shall be completed within 5 minutes.	T
	OP.03	Two banners shall be declared at Technical Inspection.	I
	OP.04	The aircraft shall deploy and release the banner during GM while held vertically.	T
M2 Payloads (Passenger and Cargo)	PA.01	The passenger compartment is on a single plane parallel to the horizontal plane while in flight.	I
	PA.02	The passenger compartment is accessible from at least one door/hatch for (un)loading.	T
	PA.03	Passenger/cargo compartment door(s)/hatch(es) do not provide access to other aircraft sections.	I
	PA.04	The passengers are upright, vertical, and restrained to prevent movement during flight.	T
	PA.05	The passenger restraint system is in the aircraft at the start of each mission staging.	I
	PA.06	The cargo bay is in front, behind, or below the passengers.	I
	PA.07	The cargo bay is separated from the passenger compartment by a solid bulkhead or floor.	I
	PA.08	Each cargo compartment must only have one door/hatch for loading and unloading cargo.	I
	PA.09	The cargo is restrained to prevent movement of cargo during all phases of flight.	T
	PA.10	Should a cargo holding fixture be implemented, it shall be in the aircraft at the start of GM or when entering the staging box.	I
M3 Payloads (Banner)	PA.11	The banner is longer than 10 in (25.4 cm).	I
	PA.12	The banner has a maximum aspect ratio (length-to-height ratio) of 5.	I
	PA.13	The banner has the team's university name or logo on both sides.	I
	PA.14	The banner is stowed externally to the aircraft for take-off.	I
	PA.15	The banner, when stowed, shall not touch the ground during the take-off roll.	T
	PA.16	The banner is remotely deployed during flight.	T
	PA.17	The banner shall maintain a vertical orientation during flight.	T
	PA.18	The banner shall not sustain damage (fray, rip, tear), including upon ground impact after release.	T
***Trojan HorSCe* complies with all regulations and performance requirements listed in this table.**			

3.2.1 Subsystem Design Requirements and Objectives

Table 4 shows subsystem design requirements and objectives translated from the aircraft design requirements listed in Table 3. Satisfying all design requirements and derived subsystem requirements ensure compliance with technical limitations, completion of all missions, and aircraft design selections for maximizing scoring parameters.

Table 4. Derived Internal Design Requirements and Means of Compliance

Category	ID	Requirement	MoC
Performance	DE.01	The maximum takeoff field length is under 200 ft (60.9 m) (Sec. 3.2.2).	T
	DE.02	The aircraft is capable of flying an equivalent of 2.2 laps worth of distance (Sec. 4.2.4).	T
	DE.03	Propulsion battery use shall not exceed 80% for all missions (Sec. 4.2.1).	T
	DE.04	The aircraft is sized for expected wind conditions, but is capable of completing all flight attempts up to 95-percentile wind speeds expected in Wichita, KS (Sec 4.2.4).	A
	DE.05	Cruise stall speed is less than 49 ft/s (15 m/s).	A
	DE.06	The aircraft produces thrust equal to at least 1.1 times the predicted drag during cruise.	A
Stability	DE.07	The aircraft is statically and dynamically stability for all expected conditions (Sec 4.4.2-4.4.3).	A
Structures	DE.08	All components shall withstand maximum expected inertial, aerodynamic, and point loads.	T
	DE.09	A factor of safety (FoS) of 1.5 is applied to all limit loads.	A
***Trojan HorSCe* complies with all requirements listed in this table.**			

3.2.2 Constraint Analysis

To derive requirements for wing area and thrust, constraint analysis investigated the relationship between thrust-to-weight ratio *T/W*, and wing loading *W/S*. Equations 12-15 show the required *T/W* as a function of *W/S* for several segments: takeoff with ground roll distance S_g, cruise at speed V_{cruise} and dynamic pressure q_{cruise}, turns at speed V_{turn} and dynamic pressure q_{turn}, and stall at speed V_{stall} respectively.

$$\frac{T}{W} = \frac{1.21}{g\,\rho\,C_{L,\max}\,S_g}\frac{W}{S} + \frac{0.605}{C_{L,\max}}\left(C_{D,\mathrm{TO}} - \mu\,C_{L,\mathrm{TO}}\right) + \mu \qquad \text{Eq. 12}$$

$$\frac{T}{W} = q_{\mathrm{turn}}\left[\left(\frac{C_{D,\min}}{W/S}\right) + k\left(\frac{n}{q_{\mathrm{turn}}}\right)^2\left(\frac{W}{S}\right)\right] \qquad \text{Eq. 13}$$

$$\frac{T}{W} = q_{\mathrm{cruise}}\,C_{D,\min}\left(\frac{1}{W/S}\right) + k\left(\frac{n}{q_{\mathrm{cruise}}}\right)^2\left(\frac{W}{S}\right) \qquad \text{Eq. 14}$$

$$\frac{W}{S} = \frac{1}{2}\,\rho\,{V_{\mathrm{stall}}}^2\,C_{L,\max} \qquad \text{Eq. 15}$$

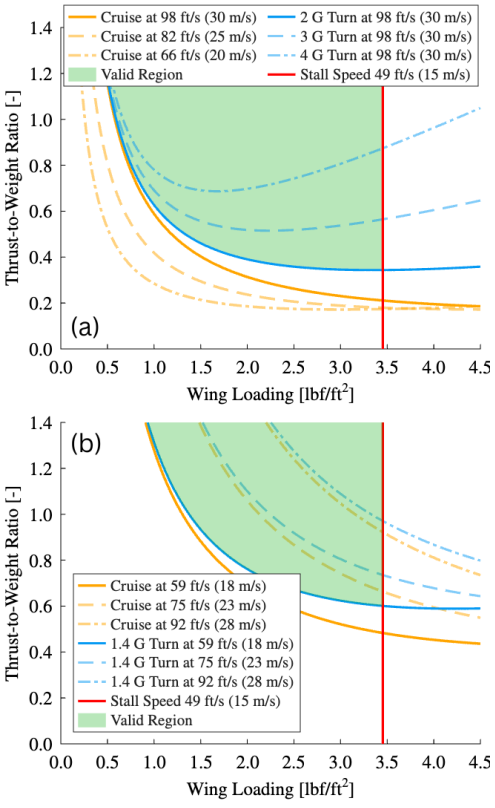

Figure 5. Constraint diagram for (a) M2 and (b) M3.

Target performance assumptions were based on the team's historical flight test data and aircraft sizing principles. V_{cruise}, V_{turn}, ground friction coefficient μ, load factor *n*, and turn deceleration a_{turn}, used measured values. A preliminary investigation of candidate airfoils and aspect ratio (AR) allowed for the assumption of a takeoff (TO) flap $C_{L,max}$ of 1.45. A TO drag coefficient of $C_{D,TO}$ of 0.04 was assumed from previous aircraft and literature [4]. As stated in Table 4, 200 ft (61.0 m) was used for S_g with a FoS of 1.2. The resulting constrain diagram is shown in Fig. 5. All aircraft in the region bound by the constraints, shaded green, met requirements. Figure 5 shows that constant-velocity turns at different load factors drive the required *T/W* for

M2, while cruise and turn-entry speeds drive *T/W* for M3 due to increased parasite drag from the towed banner. The required *T/W* is sensitive to turn load-factor for M2 and turn and cruise speeds for M3 for similar reasons. The takeoff field length (TOFL) is not a driving constraint for allowable *W/S* to meet the stall-speed requirement.

3.2.3 Score Sensitivity

Score sensitivity analysis determined the broader aircraft design focus. Parameters in the scoring equation were varied to observe their characteristics. Due to the binary nature of M1 and the difficulty in predicting GM time, only M2 and M3 were analyzed, resulting in Fig. 6. Notably, mission scoring is more sensitive to the number of laps for M3 than M2. However, this score analysis does not capture the additional effects that design parameters will have on the number of laps flown for each mission. To account for this effect, the range of the aircraft was investigated by varying the design parameters.

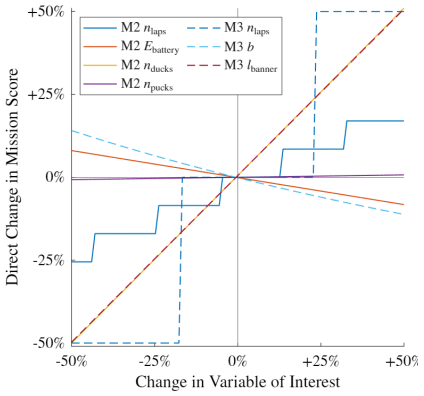

Figure 6. Sensitivity using purely scoring equations.

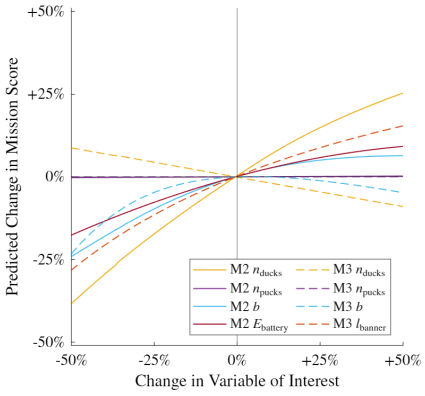

Figure 7. Predicted sensitivity combining score and range sensitivity.

$$\text{Range} = E_{\text{battery}}\,\eta_{\text{total}}\,\frac{1}{g}\frac{L}{D}\frac{1}{m_{\text{aircraft}}} \qquad \text{Eq. 16}$$

η_{total} represents the total efficiency across the propulsion chain. The score and range sensitivities were then combined by recalculating the scores, shown in Fig. 7. This captures the percent change in predicted score and helps the team prioritize specific parameters. Thus, n_{pax}, E_{battery} for M2, and l_{banner} were selected to be maximized. To guide design decisions, a sensitivity analysis for the aircraft was conducted to determine what specifications have the largest impact on performance. Using *Trojan HorSCe* as a baseline, variables were varied individually and the resulting aircrafts were simulated. The change in score is plotted against the change in variable (Fig. 8). The aircraft is most sensitive to W_{empty}, followed by e, and least sensitive to aircraft $C_{D,0}$. As a result, minimizing W_{empty} is a priority for the detail design of the aircraft.

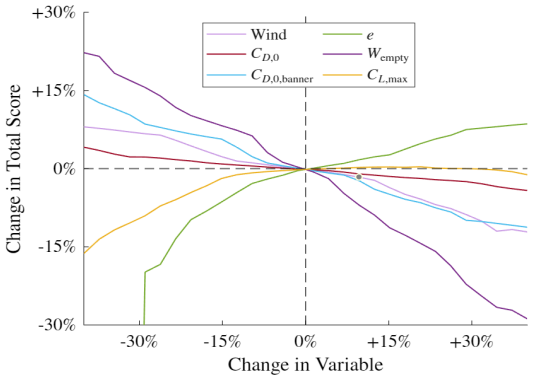

Figure 8. Sensitivity to modelling parameters.

3.3 Aircraft Configuration

Configurations for *Trojan HorSCe* and its subcomponents were determined using the down select process outlined in Table 5. The figures of merit (FoM) used to make configuration selections are listed in Table 6, along with their relevance to competition performance.

Table 5. Configuration Downselect Process

Step 1	Identify aircraft subsystems that require a configuration downselect.
Step 2	Select relevant FoM for each subsystem; assign a weight between 0 and 1 for importance.
Step 3	Grade configuration options in Table 7, guided by aircraft parameter sensitivity (Sec. 4.6.2), with a -1, 0, or 1 compared to the baseline.
Step 4	Calculate total score for each option by multiplying FoM weights with grades and summing.

Table 6. Configuration FoM

Subsystem	Reasoning
Banner Release Interference	Risk of the banner and tow-line interfering with the horizontal stabilizer during deployment and cruise is not permitted per competition rules [1].
$C_{L,max}$	Higher $C_{L,max}$ reduces V_{stall} which increases cruise L/D since $V_{L/D,max} < V_{stall}$ for M3.
Drag	Low aircraft parasite drag area increases score by increasing range for M2 and M3.
Ground Roll Stability	Predictable handling during takeoff under crosswind conditions.
Loading Time	Simplified payload access and loading increases scoring by decreasing t_{GM}.
Manufacturability	Manufacturability of components allows for reduced W_{empty}.
Maximum Thrust	High maximum thrust increases scoring for M3 by increasing the largest permissible banner.
Propulsion Efficiency	High total propulsion efficiency increases scoring for M2 and M3.
Propulsion Complexity	A less complex propulsion system allows for improved reliability, reduced potential failure points.
Stability & Control	Good stability and control characteristics improve pilot comfort with the aircraft, allowing for more repeatable, efficient laps and improving turn performance during competition laps.
Weight	Low W_{empty} raises score by increasing payload capacity (M2) and decreasing induced drag (M3).

3.3.1 Aircraft Configuration

Table 7. Aircraft Configuration Downselect

			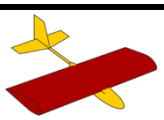	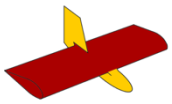
FoM	**Weight**	**Conventional (DIF)**	**Conventional (DIW)**	**Flying-Wing**
Weight	**0.5**	0	1	1
Drag	**0.3**	0	1	1
$C_{L,max}$	**0.1**	0	0	-1
Stability & Control	**0.1**	0	0	-1
		0	**0.8**	**0.6**

Table 7 shows the general aircraft downselect. Initial trade studies and conceptual analyses (Sec. 4.2.3) showed benefits to carrying a large number of passengers (100+) due to their light weight. Given their low density and requirement to be in a single horizontal plane, a ducks-in-wing (DIW) configuration was considered. This configuration reduced drag and mass by using the wing volume and minimizing fuselage size. While this does require a larger, heavier wing, initial simulations showed an increase in score of 41% when using a DIW configuration over placing ducks in the fuselage (DIF) (Sec. 4.2.3).

Next, conventional tube-and-wing and flying-wing configurations were compared. The banner-towing mission and expected high wind conditions at the competition location placed importance on stability and control. As a result, the flying-wing configuration was not selected due to reduced control authority, increased center-of-gravity sensitivity, and lower static stability relative to the conventional configuration.

Table 8. Wing Configuration Downselect

			
FoM	**Weight**	**High-Wing**	**Mid-Wing**
Structural Complexity	**0.7**	0	-1
Weight	**0.2**	0	-1
Manufacturability	**0.1**	0	-1
		0	**-1**

3.3.2 Wing

High- and mid-wing configurations were evaluated, as summarized in Table 8. A low-wing was infeasible for the DIW concept, as the passenger compartment must be on the same or higher plane than the cargo bay(s). A mid-wing would make the wing the primary load path for the aircraft, limiting the integration

area for the fuselage, nose, and boom. To minimize structural and manufacturing complexity, a high-wing configuration was chosen.

3.3.3 Propulsion

Four motor configurations were compared, as summarized in Table 9. The pusher was disregarded due to banner towing interference, and push-pull due to efficiency. As TOFL was not a driving constraint, the propulsion package was optimized for cruise efficiency. The dual-motor configuration reduces the overall propulsion efficiency due to the additional weight of ESCs, motors, and wiring, and increases W_{empty}. Therefore, the single-motor configuration was selected for its higher efficiency and reduced complexity.

Table 9. Motor Configuration Downselect

		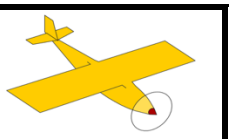	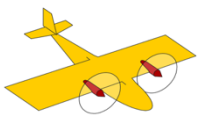	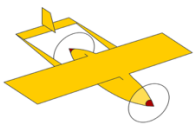	
FoM	**Weight**	**Single**	**Dual**	**Push-Pull**	**Pusher**
Weight	**0.3**	0	-1	-1	0
Efficiency	**0.3**	0	-1	-1	0
Maximum Thrust	**0.2**	0	1	1	0
Complexity	**0.2**	0	-1	-1	-1
		0	**-0.6**	**-0.6**	**-0.2**

3.3.4 Tail

Four tail configurations were analyzed, as shown in Table 10. Stability and control authority were prioritized to counteract banner-induced disturbances in M3 and maintain aircraft performance in windy conditions. Despite improved banner clearance, the V-tail and T-tail were eliminated due to reduced control authority and increased stall susceptibility, respectively. Although the H-tail provides two rudders, the selection of a single motor does not allow both rudders to be in the propeller wash. Therefore, the conventional-tail configuration was chosen.

Table 10. Tail Configuration Downselect

				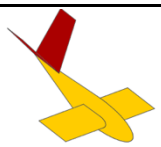	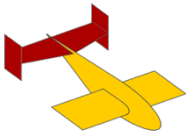
FoM	**Weight**	**Conventional**	**T-Tail**	**V-Tail**	**H-Tail**
Stability & Control	**0.5**	0	-1	-1	-1
Weight	**0.4**	0	-1	0	-1
Banner Release Interference	**0.1**	0	1	1	0
		0	**-0.8**	**-0.4**	**-0.9**

3.3.5 Payloads

3.3.5.1 Sizing Approach

To determine which payload should be prioritized during M2, the impacts of passengers and cargo on the mass and drag of the aircraft, and hence, mission performance, were investigated. Using V1 as a baseline aircraft, n_{pax} and n_{cargo} were varied and aircraft mass and drag were built up for each. The change in score, assuming 5 laps, was plotted against m_{TO} in Fig. 9(a) and flat-plate equivalent drag area (DA) in Fig. 9(b). To achieve the same increase in score with n_{cargo} the mass 3.9× more than with n_{pax}. Although increasing n_{cargo} yields a drag increase 2.4× less than increasing n_{pax}, the associated mass penalty outweighs this benefit. *Trojan HorSCe* was more

sensitive to mass than drag area ($D_i \sim m_{TO}^2$ vs $D_p \sim$ DA), and for M3, banner drag dominates, further reducing the significance of aircraft DA. Therefore, the mass penalty dominates, making an increase in n_{pax} preferable. As a result, n_{cargo} was initially set to 1, later confirmed by trade studies (Sec. 4.2.4).

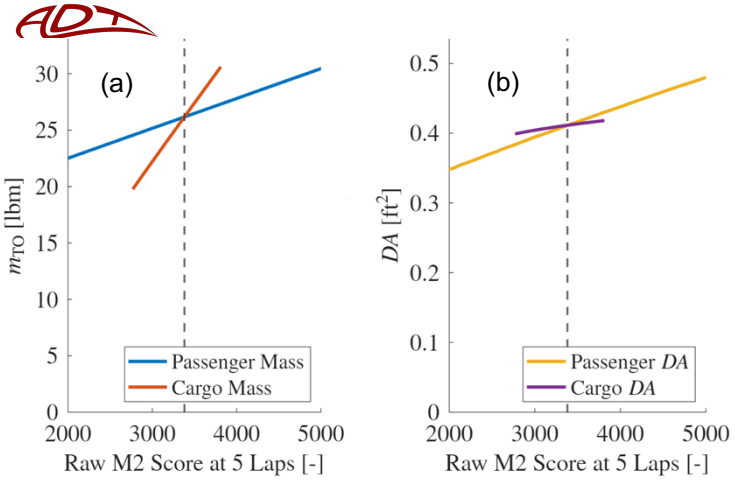

Figure 9. The impact of changing number of passengers or cargo on score, (a) m_{TO} and (b) DA

3.3.5.2 Passengers

Per Sec. 3.3.1, passengers will be loaded and secured in the wing. Three concepts were evaluated: a side hatch on the wingtip, a top hatch on the wing skin, and an aft hatch by hinging control surfaces. Passenger loading and restraints maximized packing efficiency while minimizing weight and loading time. The side hatch allows for a continuous top wing-skin construction, simplifying the wing structure. However, each passenger must be pushed from the side hatch to the opposite wingtip. A restraint for this must allow for spanwise motion during loading while also securing passengers upon entry, making the concept mechanically complex. The top hatch exposes the entire passenger compartment, allowing for top-down loading and simpler restraints, as the passengers are fully accessible during loading. However, the wing structure must be reinforced. The aft hatch, hinged at the control-surface, provides full-span access and reduces the distance each passenger must travel. However, this approach introduces risk by relying on control surfaces for payload access and adds complexity, given its proximity to servos and aircraft harnessing. The top hatch was selected for ease of loading and simple restraint system (Table 11). The top wing-skin could serve as vertical restraints for passengers. The top hatch was selected for its ease of loading and simple restraint system. The top wing-skin could serve as vertical restraints for passengers. The top hatch balances packing efficiency and ease of loading, despite resulting in increased wing structure.

Table 11. Passenger Loading Downselect

		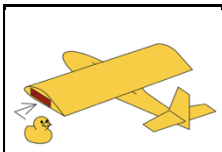	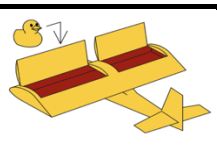	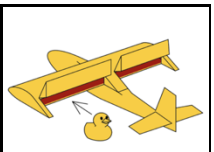
FoM	**Weight**	**Side Hatch**	**Top Hatch**	**Aft Hatch**
Packing Efficiency	**0.4**	0	1	0
Weight	**0.4**	0	-1	-1
Loading Time	**0.2**	0	1	0
		0	**0.2**	**-0.4**

3.3.5.3 Cargo

Table 12 shows multiple concepts for loading one cargo piece, per Sec. 3.3.5.1, focusing on weight, structural complexity, and loading time. Both wing and fuselage cargo bays were considered, with access provided through top, side, and empennage hatches. A wing-loaded cargo configuration would place a small hatch forward of the passenger compartment, consolidating cargo within the wing while complying with PA.06 (Table 3). However, this complicates the wing structure. Fuselage placement evaluated three potential hatch locations: a top hatch in the nose cone forward of the wing leading edge, a side hatch beneath the wing hardpoint, and an aft-facing hatch in

the empennage. A cargo hatch in the nose cone interfered with access to propulsion, landing gear, and avionics, increasing structural complexity. The empennage hatch required enlarging the fuselage cross-section, increasing W_{empty}. Furthermore, placing cargo aft of the center-of-gravity (CG) would make aircraft balancing difficult. Thus, cargo will be loaded via a side hatch below the wing into a restraint within the fuselage.

Table 12. Cargo Loading Downselect

		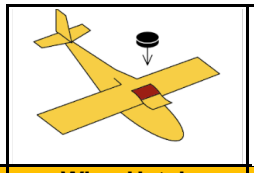	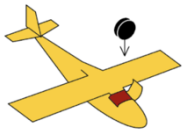		
FoM	**Weight**	**Wing Hatch**	**Front Top Hatch**	**Side Hatch**	**Empennage Hatch**
Weight	**0.5**	0	-1	0	-1
Structural Complexity	**0.3**	0	0	1	0
Loading Time	**0.2**	0	0	0	0
		0	**-0.5**	**0.3**	**-0.5**

3.3.5.4 Banner

Conceptual design focused on material selection, tow location, stowage, and to minimize payload weight, drag, and impact to flight handling characteristics. Banner material selection was driven by drag and in-air handling. Five candidate materials were selected for further evaluation based on the key characteristics summarized in Table 13.

Table 13. Physical Properties of the Materials Considered [5]

	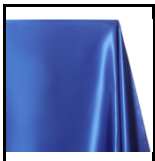				
Material	**Polyester Charmeuse Satin**	**Sheer Voile**	**Silk Chiffon**	**Tissue Lamé**	**Ripstop Nylon**
Area density [oz/yd^2]	2.80	1.33	0.88 (30)	0.88	0.68
Key Characteristics	Rigid; low surface roughness	Semi-flexible; low thread density	Soft, highly flexible; low thread density	Flexible; smooth film-like surface	Rigid; light weight

Towing the banner from either the empennage or the aircraft CG was evaluated. Aircraft handling and maneuverability were prioritized. A tail-mounted towline would eliminate the risk of horizontal stabilizer strikes. However, flight testing showed improved handling with a CG-mounted towline, as empennage towing increased the moment arm about the CG. Therefore, the CG-mounted tow line was selected.

Banner stowage did not depend significantly on tow location. Both wing-parallel and fuselage-aligned configurations were evaluated. While a stowed banner parallel to and below the wing would prevent ground strikes on take-off, span limitations complicated the design of the banner leading edge if it exceed the 5-ft (1.52 m) span limit, per CO.01 (Table 3). Flight testing with the banner stowed along the fuselage verified no ground interference, and allowed for a simpler, lighter design. Thus, a stowed position along the fuselage was selected.

3.3.6 Landing Gear

Tricycle and taildragger gear configurations were investigated. The tricycle gear would improve stability but the nosewheel integration would require additional space in the nosecone and would increase W_{empty}. In contrast, the taildragger configuration reduced weight and drag from the lack of a nose strut. Thus, the

taildragger configuration was chosen for its lighter weight, simpler design, and reduced drag (Table 14).

Table 14. Landing Gear Configuration Downselect

FoM	Weight	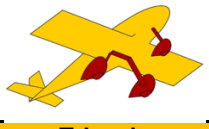 Tricycle	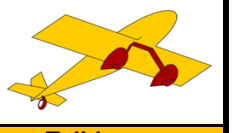 Taildragger
Weight	0.4	0	1
Ground Mission	0.2	0	-1
Drag	0.2	0	1
Manufacturability	0.1	0	1
Ground Roll Stability	0.1	0	-1
		0	0.4

3.3.7 Final Conceptual Design

The final conceptual aircraft is illustrated in Fig. 10. The aircraft is a high-wing monoplane with a conventional tail, single-tractor motor, taildragger landing gear, DIW and cargo-in-fuselage configuration, with an externally mounted banner deployment and release mechanism.

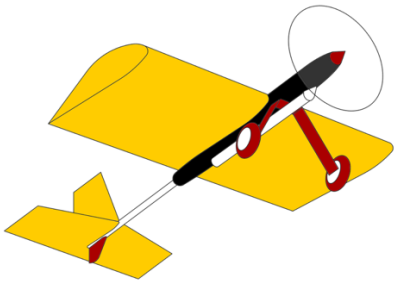

Figure 10. Conceptual aircraft design.

4.0 Preliminary Design

The goal of preliminary design was to converge on an aircraft optimized for the aircraft's weight and mission score. Each major component was sized after trade studies conducted across disciplines using a variety of simulations. Methods and results are outlined below.

4.1 Methodology

The design methodology, shown in Fig. 11, was based on previous team experience and industry practices. First, an aircraft configuration was selected by deriving mission requirements from the rules and conducting score analysis. From the sensitivity analyses in Sec. 3.2.3 and preliminary trade studies, it was determined that a high M2 scoring design should be used, while still considering the other missions for total competition score.

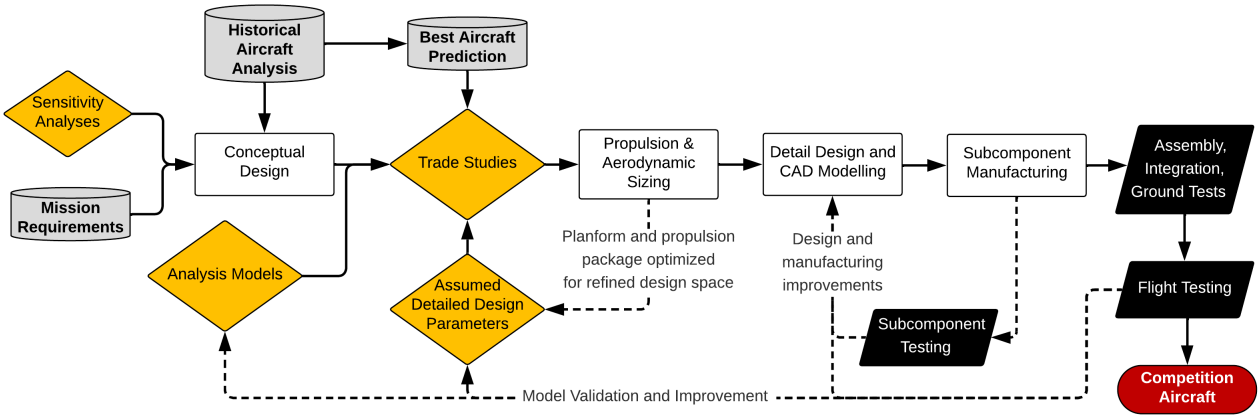

Figure 11. Design and testing methodology flow chart.

Once the conceptual design was selected, key aircraft parameters such as payload quantity, wing dimensions, and propulsion package were determined through trade studies. These trade studies were run using a team-developed mission model in MATLAB to predict performance and score for each possible aircraft. The model incorporates preliminary propulsion and aerodynamic sizing to capture their holistic effects on performance. Aircraft were failed if mission requirements were not met, in accordance with Sec. 3.2. Aerodynamic parameters including airfoil selection, tail sizing, and control-surface sizing were further refined using XFLR5 and Athena

Vortex Lattice (AVL) [5][6]. Propulsion sizing was refined using an in-house solver that uses APC Propeller Simulation data and commercial, off-the-shelf (COTS) motors to find RPM, current, thrust, and power [11].

Once the performance, propulsion, and aerodynamic designs converge, the aircraft enters the detail design and Computer-Aided-Design modeling phase where the team ensures all mission requirements and derived subsystem requirements are satisfied, according to Sec. 3.2 and weighing decisions from the sensitivity analysis in Sec. 3.2.6. Subcomponents are manufactured, tested, and improved until requirements and targets are satisfied. Once validated, subcomponents are assembled to create a full aircraft that is ground tested to ensure flight readiness. Then, the aircraft is flight tested and the collected data is used to validate and improve analysis models used for the next aircraft iteration. These corrected models and mission attempts conducted at flight tests are used to optimize competition strategies and inform aircraft limits based on actual performance. The team is scheduled to complete three design cycles for the 2026 DBF competition to maximize refinement from iterations and flight tests.

4.2 Trade Studies

To predict the performance of the preliminary aircraft design and explore areas for optimization, the team developed PlaneTools (PT), a multidisciplinary design optimization tool in MATLAB [7]. PT includes time-based mission simulations and physical models and equations governing aircraft dynamics, allowing the team to conduct trade studies by exploring the relationship between aircraft parameters and mission score.

4.2.1 Mission Model

PlaneTools' methodology and assumptions for each model are outlined below:

Aerodynamics – Airfoil lift coefficients are determined from airfoil geometry studies within XFLR5 [5]. Low aspect ratio (AR) wings have a reduced $C_{L,max}$ due to the strengthening of wingtip vortices, which interfere with lift. To account for this, 3D $C_{L,max}$ is calculated using a local linear correction as a function of AR.

Drag – Aircraft geometry is used for a component-based parasite drag buildup with corrections from flight test data, which considers Reynolds number (*Re)*, Oswald efficiency (*e*)*,* flow transitions, and increased airflow behind the propeller [4]. Propeller wash, calculated using a simplified momentum theory, creates additional drag from higher dynamic pressure and increased *Re*. The banner drag coefficient was estimated using the team's historical, Reynolds number-dependent testing data [8]. Compressibility effects and trim drag are ignored.

Propulsion - A static and dynamic propeller thrust model was integrated using data from APC propellers [11]. Battery voltage decay is modeled as a function of temperature, current, and state-of-charge (SoC) based on a curve-fit model of lithium-based batteries [9]. Propeller, battery, motor outputs, and efficiencies were verified through flight testing. The efficiency of both the motor and the propeller are considered.

Mass - Mass buildups are conducted using individually manufactured components, aircraft sizing, and build methods used by the team. Masses for COTS electronic components are input based on specification sheets.

Environment - Based on historical weather patterns during mid-April in Wichita, KS, trade studies were predominantly run using an average headwind of 14.5 mph (6.5 m/s) [21]. As shown in Fig. 12, historical wind speed and direction at a nearby airport showed that having the wind aligned to the runway was most common and, therefore, was assumed in analysis. However, due to the high impact of wind on performance, trade studies

were run at a variety of wind speeds ranging from 0 to 30 mph (0 to 13 m/s). The elevation was set to 1300 ft (396 m) for calculating air density at standard temperature.

Flight Path - Physics models were used to simulate four segments of the competition course: takeoff (TO), climb, cruise, and turns. Figure 13 displays the competition course as modeled. The assumptions for each flight segment are detailed below.

1. Takeoff – Assumes throttle is linearly increased to 100% over 1.7 seconds during TO roll to avoid propeller stall and torque impulse. The model accounted for a lab-measured rolling resistance coefficient of 0.03 and dynamic thrust based on APC dynamic thrust data [11]. To incorporate a margin of safety, the rotation speed was set to 120% of the TO configuration stall speed.

2. Climb – The aircraft is assumed to climb at full throttle until it reaches a cruise altitude of 200 ft (61 m) above ground level. The rate of climb (*RoC*) was calculated with excess power.

$$RoC = \frac{V\,(T - D)}{W} \qquad \text{Eq. 17}$$

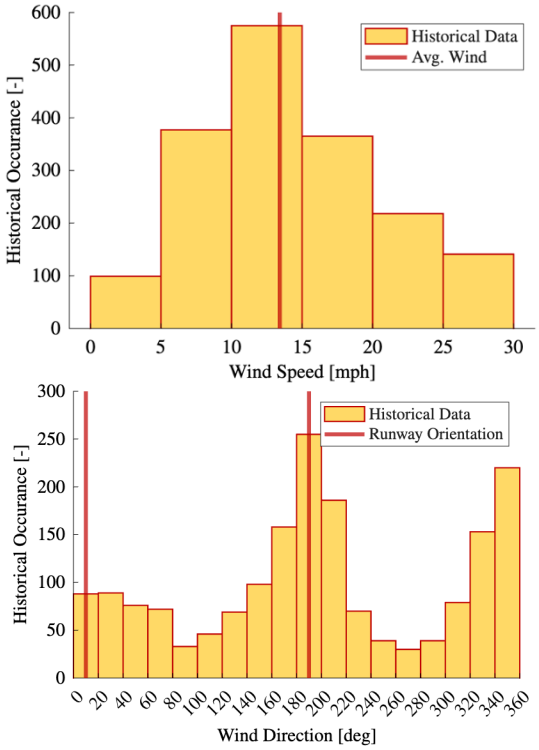

Figure 12. Historical wind speed and direction at a nearby airport.

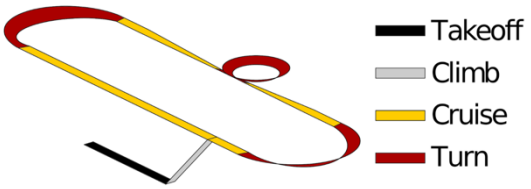

Figure 13. Flight segments of competition course.

3. Cruise – The aircraft is assumed to fly level during straightaways. The mission throttle is traded to find the throttle that will result in the highest n_{laps} within the 5-minute flight window for each aircraft. Due to the constant throttle throughout the mission but changing drag between straightaways and turns, the plane is allowed to accelerate and decelerate. M3 is modelled with a 10% increase in $C_{L,max}$ to represent lowered flaps for cruise, which increases M3 score by 2.5% due to the low speed of $V_{L/D,max}$. The mission ends once the plane reaches one of three conditions: stall, the 5-minute time limit, or the battery SoC dropping below 20%. The SoC limit was implemented to account for landing in high winds and a potential go-around.

4. Turn – The aircraft is assumed to perform coordinated, near-maximum lift, level turns for both the 180º and 360º turns with a maximum permissible load factor of 6. $C_{L,turn}$ is given by Eq. 18 with a FoS of 20% to better reflect real flight conditions.

$$C_{L,turn} = 0.9 \times C_{L,max} - 0.1 \qquad \text{Eq. 18}$$

PT was developed to make trade studies and evaluate the effects of every dimension, allowing for large design spaces to be both studied and optimized. A simplified schematic of how PT simulates aircraft is shown in Fig. 14. The logic can be summarized as follows: for every plane traded, simulate takeoff. If the aircraft meets a 200 ft (61 m) TOFL limit, fly the mission until a failing condition is met. The number of laps the plane is able to fly before failure is used for n_{laps}. This is done for both M2 and M3, and the cycle is repeated until all planes in the study are simulated. M1 can be simulated, but does not drive sizing. PT was validated with flight testing as seen in Sec. 8.2.

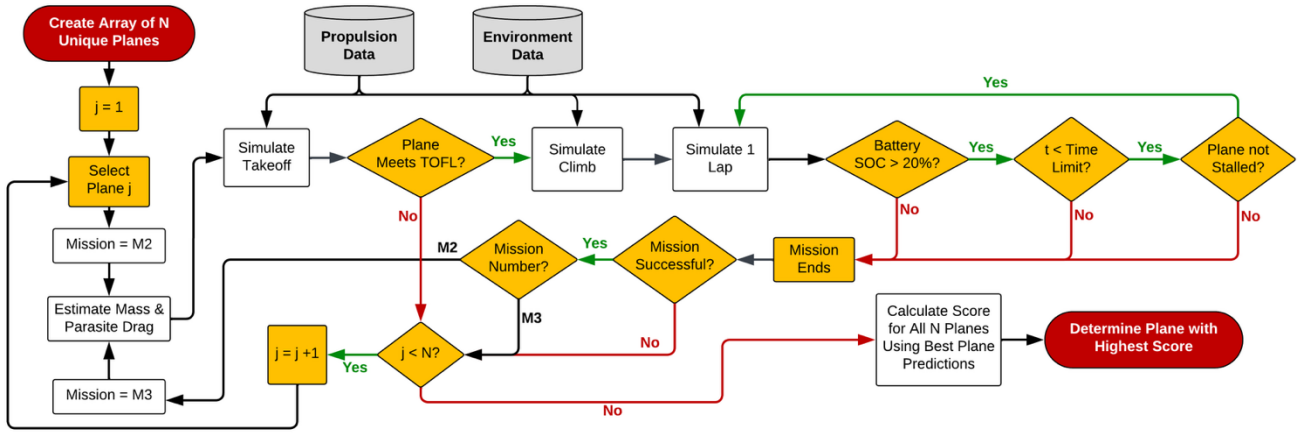

Figure 14. PlaneTools flowchart for evaluating aircraft.

4.2.2 Best Plane Predictions

PT was used to conduct trade studies of key parameters for competition to determine the optimal wing size, M2 and M3 payload size, and preliminary propulsion sizing to maximize score. To perform these trade studies and optimize score, a best team score was required for each mission, which necessitated predicting the performance of the best scoring team for M2 and M3. These predictions were made by running sparse trade studies to optimize a plane for M2 and M3 individually. Each plane was assumed to use a conventional configuration with the passengers stored in the fuselage, while assuming the top competitor would achieve a lower $C_{D,0}$ than *Trojan HorSCe*. The predicted scores are shown in Table 15. Due to the uncertainty in predicting the performance of the best aircraft, a sensitivity analysis was conducted to determine the impact that inaccurate best plane assumptions would have on the design of the optimal USC aircraft. This was done by first conducting a trade study investigating propeller choice and n_{pax}. The score of each plane was then recalculated with a perturbation to the best plane prediction for one mission, and the new optimal USC aircraft was determined. AR, which is dependent on n_{pax} because of DIW, was chosen to represent the variation in optimal USC aircraft. AR was plotted against percent change for each mission's best plane assumption (Fig. 15). The optimal aircraft is least sensitive to M3 best plane predictions. AR stays within 10% of its optimal value if any prediction is between 43% and 163% of the originally predicted value. Additionally, non-integer laps were allowed in the scoring equation for the simulations. This prevented sizing the aircraft for a

Table 15. Best Plane Predictions

Mission	Score	Value
GM	30 seconds	30
M2 Income	$115\ \text{pax}\ (6 + 2 \times 5\ \text{laps}) + 20\ \text{cargo}\ (10 + 8 \times 5\ \text{laps})$	2840
M2 Cost	$5\ \text{laps}\ \frac{100}{100}(10 + (0.5 \times 115\ \text{pax}) + (2 \times 20\ \text{cargo}))$	537
M2 Score	Income - Cost	2303
M3 Score	$4\ \text{laps} \times \frac{211\ \text{in}}{0.05 \times (5\ \text{ft}) + 0.75}$	846

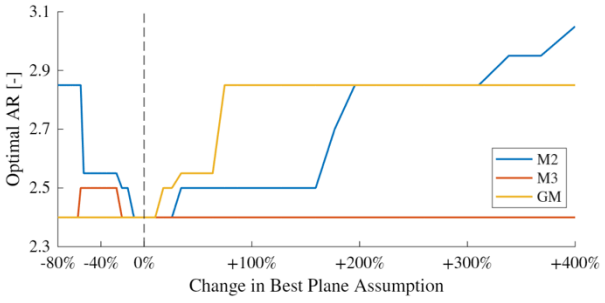

Figure 15. Design sensitivity to best plane predictions.

specific n_{laps}, and instead encouraged sizing for the overall best plane, accounting for the variabilities in performance from possible winds gusts and model uncertainty.

4.2.3 Initial Payload Sizing

The Ducks-in-Wing (DIW) configuration was compared with the Ducks-in-Fuselage (DIF) configuration. For both, the fuselage was modelled with a minimum size required to fit electronics, the volume of cargo, and in the case of DIF, the volume of passengers. For DIW, the number of passengers that can fit in the wing is linearly approximated, reserving space for a D-box and control surfaces. For each case, an aircraft was optimized to compare the best DIF aircraft and the best DIW aircraft. The DIW plane was able to fly farther and carry more payloads with lower DA and W_{empty}, resulting in a 41% higher total score.

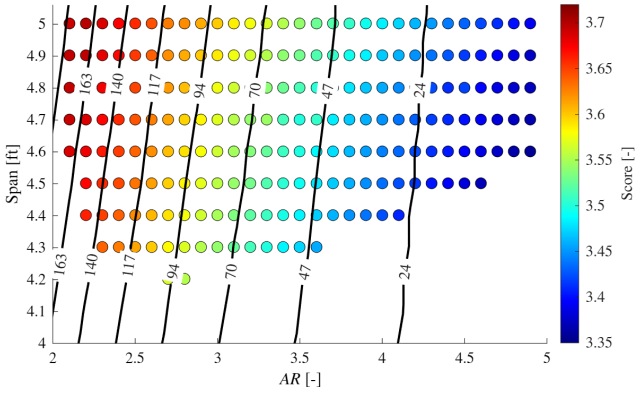

Figure 16. Summary of wing sizing with isolines for n_{pax}.

The initial wing sizing considered both AR and span (*b)*. Because of the DIW configuration, wing size is directly coupled with payload capacity. A larger wing increases W_{empty} and flat-plate equivalent drag area, DA, but may improve overall performance of the aircraft by enabling higher n_{pax}. Conceptually, M2 and M3 n_{laps} would favor a higher span, as reducing span loading decreases induced drag and thus improves performance. However, lower-span aircraft are more structurally efficient by decreasing aircraft mass, and span has a direct penalty on M3 score through Rated Aircraft Cost (RAC).

However, increasing *b* and selecting a low AR (Fig. 16) provide a net benefit. Larger *b* was consistently favored for all AR within the span limit per CO.01 and continued to perform well at higher AR. Larger *b* also performed better while holding n_{pax} constant. Lower-AR wings generally performed better as this allowed for a larger n_{pax}. Consequently, the maximum allowable *b* was selected, with the knowledge that the wing would have a low AR.

4.2.4 Payload Refinement

Because high n_{pax} was preferred, a penalty was applied to the score for high loading times to ensure the aircraft could be staged for M2 within the 5-minute window. A Gaussian model was constructed to estimate the likelihood of success of a given loading time using data from several M2 staging practices on a prototype aircraft. The mean was shifted according to the number of payloads. For each aircraft, the probability of passing staging was determined by integrating the Gaussian model, with the final probability presented in Fig. 17. This was then multiplied by the M2 score to represent a statistical score and provide a soft cutoff for the quantity of payloads. Results from the M2 payloads trades with this penalty are presented in Fig. 18. Results were obtained using an average wind speed of 14.5 mph (6.5 m/s),

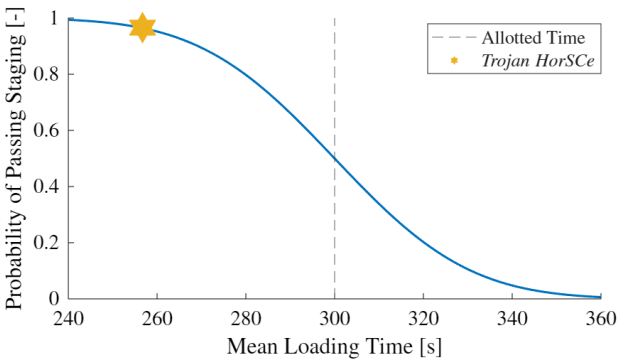

Figure 17. Penalty for high staging times, resulting in the black triangle of Fig. 18.

with an ideal *AR* of 2.4 remaining consistent from 0 to 26.8 mph (0 to 12 m/s) winds. Although score generally increased with payloads, for high n_{pax} + n_{cargo}, the plane was unable to fly 2.2 laps as required by DE.02 (green triangle). With a low chord and high n_{cargo}, insufficient passengers fit into the wing to achieve the required 3:1 ratio as required by CO.07 (blue triangle). For large quantities of payloads, a score drop-off occurs where the staging penalty begins to take effect (black triangle). The highest score is achievable at 1 cargo, confirming the conceptual analysis in Sec. 3.3.5.1. Therefore, an *AR* of 2.4 was selected with 1 cargo and 144 passengers.

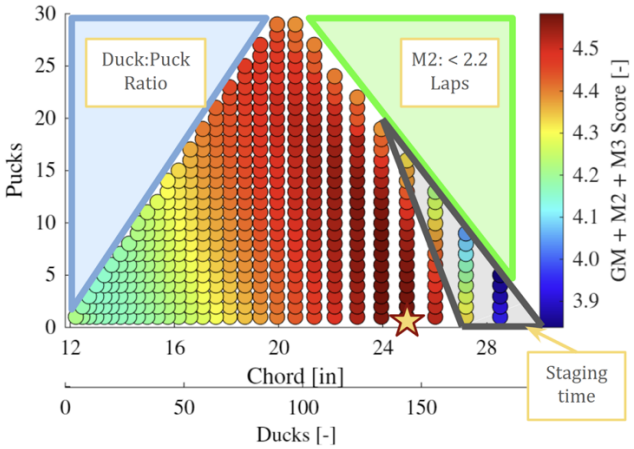

Figure 18. Summary of M2 payload sizing.

Due to the significant impact of wind on range, banner sizing was conducted by considering the likelihood and impact of wind speeds. For every 3.3 ft/s (1 m/s) increment of wind speed, several banner sizes were traded for the aircraft. Propellers were also traded to account for wind-induced changes in the optimal airspeed; each data point in Fig. 19(a) represents performance using the best selected propeller. As shown in Fig. 19 (a), for a given wind speed, larger banners resulted in a higher score, but were not successfully flown in higher head winds. Constrained by OP.03, two banner lengths were selected. Two optimal banner lengths were determined to maximize score given wind speed during competition is currently unknown. Therefore, the probability of each wind speed was multiplied by the score for each banner, seen in Fig. 19 (b). Two banners were selected to maximize the area under the resulting curves, resulting in a high-wind banner 79 in (2 m) long to be used in winds from 16.8 to 29.1 mph (7.5 to 13 m/s), and a low-wind banner 196 in (5 m) long in winds below 16.8 mph (7.5 m/s).

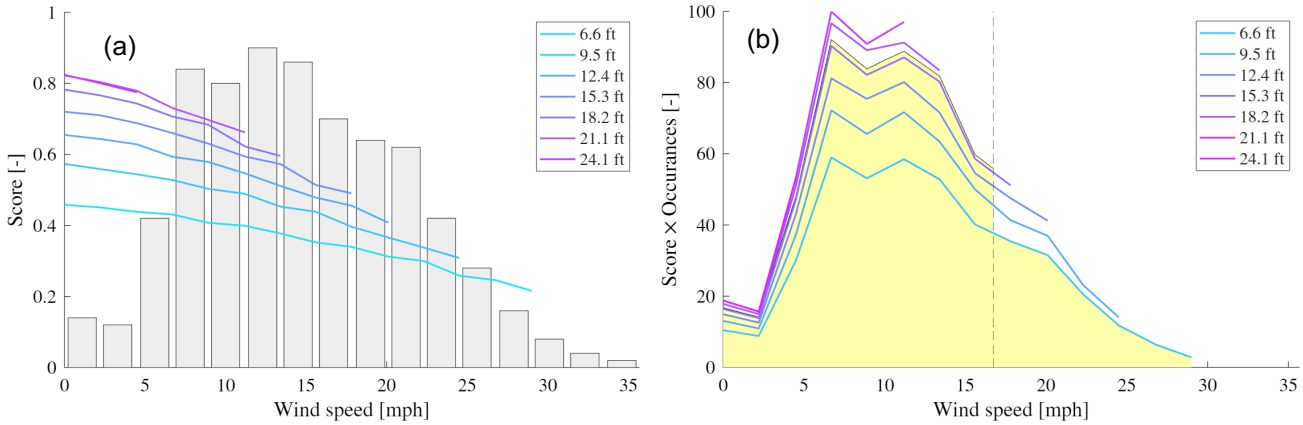

Figure 19. (a) Performance of various banner sizes in a range of wind conditions with wind distribution overlaid. (b) Predicted score multiplied by wind distribution for various banner sizes.

4.2.5 Initial Propulsion Sizing

The two main considerations for battery selection are total energy and voltage. While increasing total energy E_{prop} is beneficial for performance, and thus should be maximized for M3, it is directly penalized in the rules for M2 by increasing the efficiency factor (EF) and therefore cost. This relationship was investigated by determining the

theoretical, optimal battery capacity for M2. Assuming the aircraft is constrained by range rather than time, n_{laps} is proportional to E_{prop} due to the behavior of the Breguet range equation (Eq. 16). E_{prop}, with a proportionality constant p, can then be substituted for n_{laps}, resulting in

$$\text{Income} = n_{\text{pax}}(6 + 2\,p\,E_{\text{prop}}) + n_{\text{cargo}}(10 + 8\,p\,E_{\text{prop}}) \quad \text{Eq. 19}$$

$$\text{Cost} = p\,E_{\text{prop}} \times \frac{E_{\text{prop}}}{100}(10 + 0.5\,n_{\text{pax}} + 2\,n_{\text{cargo}}) \quad \text{Eq. 20}$$

To determine the theoretical maximum capacity, the maximum of this function is found by differentiating the expression and setting it equal to zero. E_{prop} was then solved as seen in Eq. 21. The optimal battery energy for a variety of n_{pax} and n_{cargo} are given in Fig. 20.

$$E_{\text{prop}} = \frac{2\,n_{\text{pax}} + 8\,n_{\text{cargo}}}{10 + 0.5\,n_{\text{pax}} + 2\,n_{\text{cargo}}} \quad \text{Eq. 21}$$

At n_{pax} = 144 and n_{cargo} = 1, the optimal E_{prop} is 352 Wh, above the limit of 100 Wh set by PR.02 (Table 3). Therefore, a maximum battery capacity is preferred for M2 and M3. Of the COTS batteries available, only 8S and 13S batteries had an energy between 98 and 100 Wh. Additionally, in trade studies, 8S and 13S batteries with higher E_{prop} consistently outperformed the 10S and 12S batteries. Therefore, battery selection was narrowed to these two options.

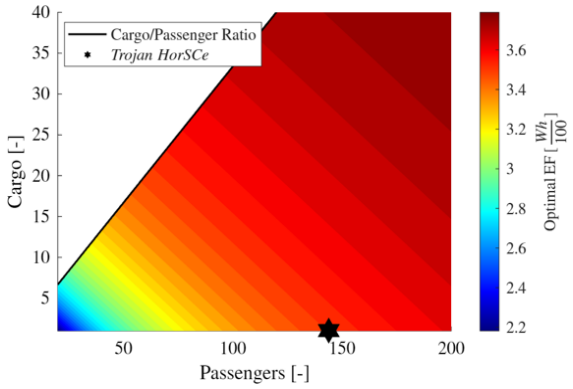

Figure 20. Optimal efficiency factor (EF) for a given combination of n_{cargo} and n_{pax}.

Across these battery voltages, both missions, and a variety of wind speeds, a lower-K_V motor with a larger propeller consistently showed higher efficiency. While a lower-K_V motor would be heavier and a larger propeller would require larger landing gear, these drawbacks were offset by the efficiency gains. Lower-K_V motors consistently outperformed higher-K_V motors, varying from 1% to 25% improvement in score.

While the 8S and 13S batteries had comparable efficiencies and scores, they have different continuous power ratings. The 13S battery has a maximum continuous current of 54 A, which is lower than the 8S battery. However, the 8S battery would not reach its current limit at 100% throttle with diameters less than 23 in (58.4 cm) with optimal pitch, meaning the 8S has a lower risk of being damaged, but the mission must be flown at a high throttle setting. As a result, an 8S battery was selected for M2, and due to the higher average power required, a 13S battery was selected for M3. The propeller selection is determined in Sec. 4.5.2 and confirmed through PT trade studies.

4.3 Aerodynamics

Aerodynamic performance was evaluated using XFOIL and XFLR5 to analyze a custom-designed airfoil. AVL was used for empennage sizing and static and dynamic stability assessment [12][5][6]. Python-based automation tools were developed to streamline XFOIL and AVL simulations, allowing large-scale parametric studies and design optimization [12][6]. A winglet and wingtip fence trade study was conducted using ANSYS Fluent for RANS CFD analysis [13].

4.3.1 Airfoil Selection

4.3.1.1 Preliminary Airfoil Selection

To meet the design requirement of storing passengers within the wing, a thick airfoil with a minimum thickness-to-chord ratio, *t/c,* of 15% was required. Several catalog airfoil candidates satisfying this constraint were evaluated during the preliminary selection process due to their demonstrated success in DBF-type aircraft and similar performance characteristics. These include the Clark YM-15 (*t/c* = 15%), SM 701 (16%), NACA 2421 (21%), and the symmetric NACA 0021 (21%) to assess potential drag benefits. Based on a comparative analysis of airfoil polars in XFLR5, the SM 701 was selected as the preliminary airfoil due to its gentle stall characteristics and highest $C_{L,max}$, allowing a lower stall speed and a larger banner for improved M3 scoring [5]. Additionally, the SM 701 exhibited the highest lift-to-drag ratio at the designed M2 and M3 C_L, making it the most competitive choice for overall mission performance. However, as shown in Fig. 21, the airfoil exhibits a large pitching moment coefficient. This effect is further amplified by the large wing chord, as shown in Eq. 22, requiring a larger horizontal tail (HT) and moment arm.

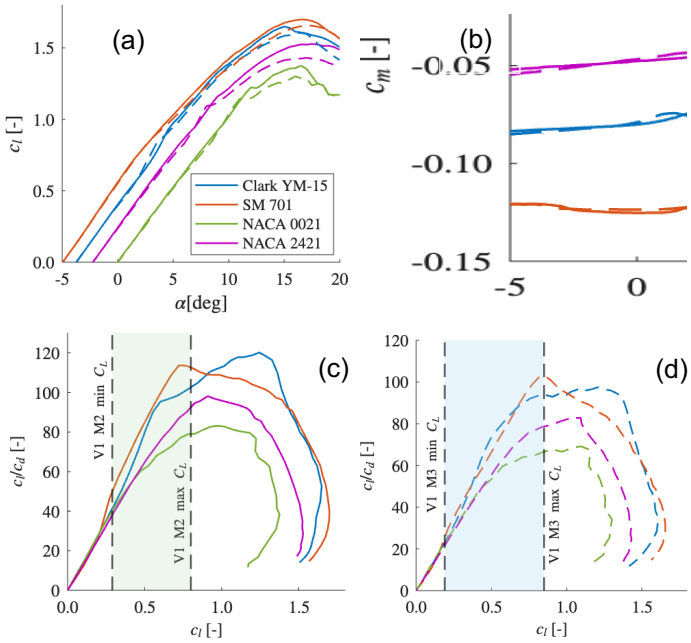

Figure 21. Dashed line represents M2 cruise *Re* = 1×10^6, solid line represents M3 cruise *Re* = 5×10^5 (a) Lift curves, (b) coefficient of moment across α, and (c)(d) airfoil 2D lift-to-drag ratio at M2 and M3 respectively.

$$C_h = \frac{S_h\, l_h}{S_w\, c} \qquad \text{Eq. 22}$$

To reduce tail size, two alternative configurations were investigated: a reflexed wing airfoil and a cambered horizontal stabilizer. The effects of these configurations on tail sizing were evaluated and compared against the baseline configuration of a SM 701 wing paired with a symmetric HT airfoil.

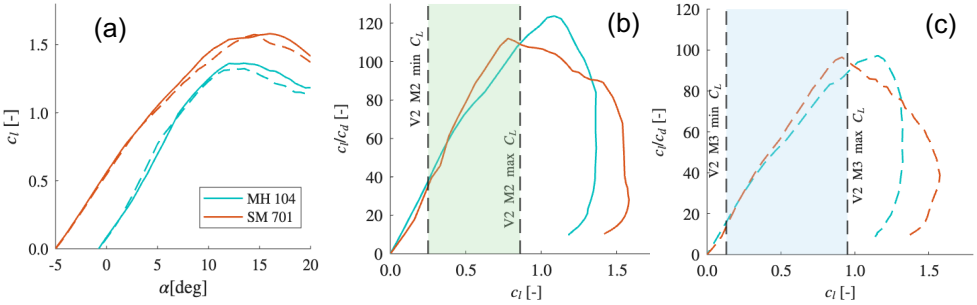

Figure 22. Dashed line represents M2 cruise *Re* = 1×10^6, solid line represents M3 cruise *Re* = 5×10^5. (a) Lift curves, (b) airfoil 2D lift-to-drag ratio at M2 cruise condition (c) airfoil 2D lift-to-drag ratio at M3 cruise condition.

The heat maps (Fig. 23) illustrate the relationship between the HT incidence angle i_h in the x-axis and the horizontal tail volume coefficient C_h in the y-axis. The color bar represents the required elevator deflection to counteract the wing pitching moment and achieve trimmed, stable flight at the maximum M3 cruise C_L, obtained from AVL simulations [6]. Negative δ_e indicates upwards elevator deflection and positive indicates downwards

deflection. The black dashed line marks the boundary at an upward elevator deflection of 10°, separating cases where the required deflection exceeds this limit. The 10° constraint ensures adequate margin relative to the maximum elevator deflection of ± 25°. This boundary is used to identify the minimum C_h that satisfies the trim requirement while preserving sufficient control authority.

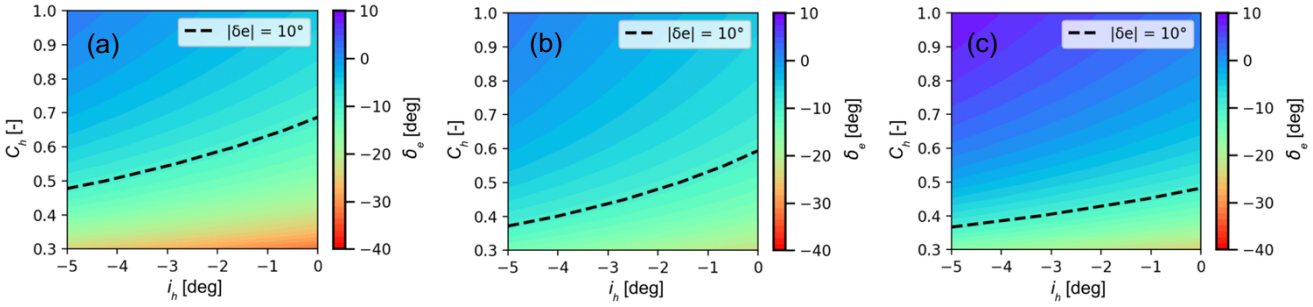

Figure 23. (a) SM 701 wing airfoil with a symmetric NACA 0010 horizontal tail airfoil (b) MH 104 reflexed wing airfoil (t/c = 15%) with a symmetric NACA 0010 horizontal tail airfoil (c) SM 701 wing airfoil with a cambered NACA 2408 horizontal tail.

The results indicate that both a reflexed wing airfoil and a cambered HT reduce the minimum required C_h. Although a cambered HT allows for a smaller C_h, the reflexed airfoil is more efficient as it reduces the wing's pitching moment and the tail downforce required for trim. Meanwhile, a cambered HT compensates for this moment at the expense of decreased total aircraft lift.

Although the MH 104 reflexed airfoil allows for a ~25% reduction in required C_h and a similar lift-to-drag ratio as SM 701 at the target M2 and M3 cruise C_L (Fig. 22(b) and(c)), it has a lower $c_{l,max}$ compared to SM 701 (Fig. 22(a)). To maintain M3 competitiveness, custom airfoils were investigated to reduce the pitching moment of SM 701 while maintaining comparable $C_{L,max}$.

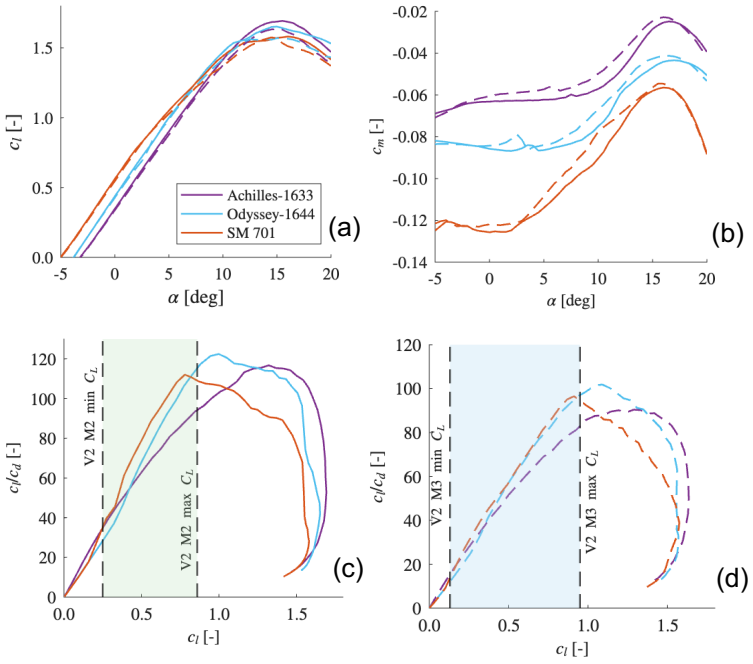

Figure 24. Dashed line represents M2 cruise Re = 1×10^6, solid line represents M3 cruise Re = 5×10^5 (a) Lift curves, (b) coefficient of moment across angle of attacks, and (c) airfoil 2D lift-to-drag ratio at M2 cruise condition (d) airfoil 2D lift-to-drag ratio at M3 cruise condition.

4.3.1.2 Custom Airfoil Design

The SM 701 serves as the baseline and is merged with a selected set of catalog airfoils, including reflexed and a blend of thick and thin airfoil with low pitching moments c_m. A thick airfoils typically offers high-lift, while a thin airfoil is better suited for low-drag. The benefits of both were captured to achieve a balanced design and reduce c_m. To evaluate a large number of candidates efficiently, the team developed a Python tool to automate XFOIL simulations across different blending percentages. Each resulting airfoil was

required to meet two criteria: c_m lower than that of the SM 701 across all angles of attack and a $c_{l,max}$ of at least 1.5. Airfoils that passed these criteria were then ranked based on their lift-to-drag ratio at the designed M2 and M3 C_L. Finally, Odyssey-1644, shown in Fig. 26, was selected, as it achieves a comparable $C_{L,\max}$ and lift-to-drag ratio at the designed M2 and M3 C_L relative to SM 701 while exhibiting a lower pitching moment, as shown in Fig. 24(a), (c) and (d). Achilles-1633 was also evaluated due to its low pitching moment shown in Fig. 24 (b). However, its lift-to-drag performance at the M2 and M3 cruise conditions, as shown in Fig .24(c) and (d), is not optimized for the mission requirements, making it a less favorable option.

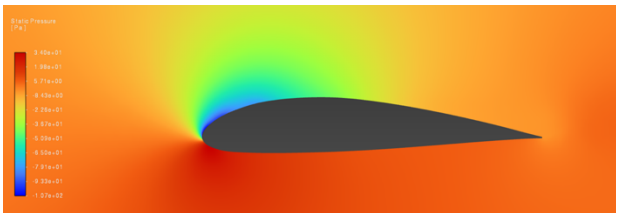

Figure 25. Static pressure distribution from RANS CFD analysis for Odyssey-1644 at Re = 5×10^5 and α of 12°.

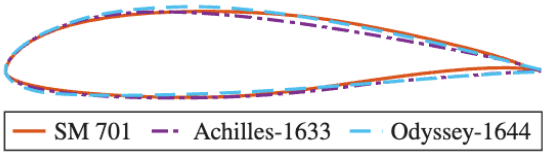

Figure 26. Comparison of airfoil profiles for SM701, Achilles-1633, and Odyssey-1644.

To validate Odyssey-1644, 2D RANS CFD analysis was conducted using ANSYS Fluent. XFLR5 and Fluent show strong agreement in the linear portion of the lift curve as shown in Fig. 27(a) but begin to diverge as the airfoil approaches stall, which is expected due to differences in how each model captures separated flow. Additionally, the c_m from XFLR5 and Fluent do not agree closely, however, c_m from both models consistently fall within a range of -0.09 to -0.04, which is noticeably smaller in magnitude than SM 701. Overall, the RANS CFD results support that Odyssey-1644 preserves the high $C_{L,max}$ performance of SM 701, maintaining M3 competitiveness, while achieving a reduced pitching moment.

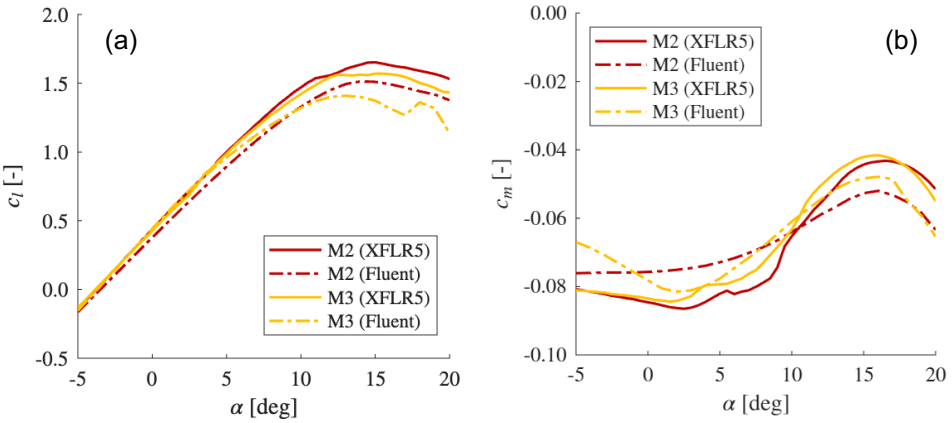

Figure 27. (a) Lift curves and (b) pitching moment coefficient as function of angle of attack for Odyssey-1644, comparing results from XFLR5 and RANS CFD simulations using ANSYS Fluent

4.3.2 Drag Analysis

Energy losses due to drag on the aircraft can be attributed to two components: parasite drag D_0, and induced drag D_i. A component drag buildup was used to determine $C_{D,0}$ of the aircraft using methods from Gudmundsson and Hoerner [4][14] as

$$C_{D,0} = \frac{1}{S_{\text{ref}}} \left(\sum_{i=1}^{N} C_{f,i} \times S_{\text{wet},i} \times FF_i \times IF_i \right) k_{\text{excr}}, \qquad \text{Eq. 23}$$

where N is the number of components; C_f is the skin friction coefficient; S_{wet} is the wetted area; FF is the form factor, which estimates the pressure drag; and IF is the interference factor, which accounts for the additional drag

caused by the boundary layer interaction of attached components. k_{excr} is the excrescence drag factor to account for any sources of drag that were not explicitly modeled such as access hatches and control horns, and is derived from flight test data. Figure 28 shows the $C_{D,0}$ contributions from different components at the design cruise speeds, where "Misc" includes antennas and an increase in drag due to propeller wash.

To initially determine the drag of the banner for trade studies, empirical data from the team's 2020 DBF report was used [8]. While the materials tested were not permitted, this data was collected at the correct banner Reynolds number (Re_b), banner aspect ratio, and similar material density, resulting in an acceptable representation. Of the materials tested, low-density polyethylene (LDPE) had the lowest drag coefficient. Banner c_f was fit to Re_b for LDPE using Eq. 24 for initial performance simulations.

$$c_f = \frac{93{,}000}{Re_b} \qquad \text{Eq. 24}$$

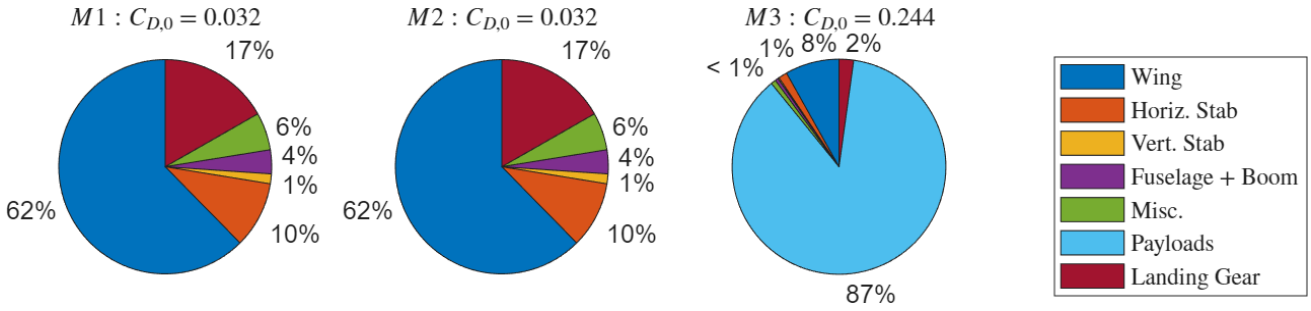

Figure 28. Drag buildup of aircraft components

The other primary source of drag, D_i, is calculated using

$$C_{D,i} = k\,{C_L}^2 = \frac{1}{\pi\, e\, \mathrm{AR}}{C_L}^2. \qquad \text{Eq. 25}$$

C_L is calculated from flight conditions, including turn load factor, n. Oswald efficiency factor, e, is calculated as a function of taper ratio, λ, and AR:

$$e = \frac{0.73}{1 + f\,\mathrm{AR}} \qquad \text{Eq. 26}$$

where

$$f = 0.0524\lambda^4 - 0.15\lambda^3 + 0.1659\lambda^2 - 0.0706\lambda + 0.0119. \qquad \text{Eq. 27}$$

These coefficients of drag were used to calculate drag force in PlaneTools (PT), and the drag energy was calculated using Eq. 28.

$$\text{Drag Energy} = \int_{t_{\text{segment end}}}^{t_{\text{segment start}}} \left(\left(C_{D,i} + C_{D,0}\right) q\, S_{\text{ref}}\right) V\, dt \qquad \text{Eq. 28}$$

Turns contribute significantly to total energy consumption (Fig. 29) because $D_i \sim C_L^2 \sim n^2$, the aircraft cannot be sized considering straightaways alone. Consequently, the drag curve provided in Fig. 30**.** includes both straightaway C_L and prescribed turn C_L. M2 average V_{cruise} is 65.3 ft/s (19.9 m/s), and M3 average V_{cruise} is 46.6 ft/s (14.2 m/s). While M2 turn C_L does not occur at maximum

L/D, a higher turn C_L results in a shorter turn segment. While M2 is flown around L/D_{max}, M3 must be flown at lower C_L due to the proximity of V_{stall} to $V_{L/D,\ max}$.

4.3.3 Wingtip Device Analysis

Given the low AR and untapered planform resulting from the DIW configuration, wingtip devices were investigated using RANS CFD in ANSYS Fluent to mitigate induced drag [13]. Both the winglet and endplate configurations feature identical geometries with a winglet height-to-span ratio of 15% and a taper ratio of 0.3. The winglet incorporates a symmetric NACA 0010 airfoil and a 2° toe-in angle. As shown in Fig. 30, the RANS CFD results indicate that the winglet and endplate yield comparable aerodynamic performance improvements. However, these results do not account for the additional weight of the wingtip devices, which increases the lift required, leading to potentially higher D_i. The endplate configuration was selected for further investigation using PT due to its manufacturing simplicity, relative to the baseline clean wing. The Oswald efficiency factor and $C_{D,0}$, obtained from RANS CFD analysis, and the mass build-up of each wingtip device were presented in Table 16. D_{tot} was calculated using Eq. 29.

$$D_{tot} = C_{D,0}\, q\, S + \left(\frac{W}{b}\right)^2 \frac{1}{\pi\, e\, q} \qquad \text{Eq. 29}$$

Compared to the baseline wingtip configuration, endplates resulted in a 12% increase in total predicted score. This is broken into a 12% increase for M2 and an 11% for M3. While endplates do increase W_{empty} and $C_{D,0}$, this change is outweighed by the increase in e, resulting in a net benefit. Therefore, the end plate configuration was chosen as the final design.

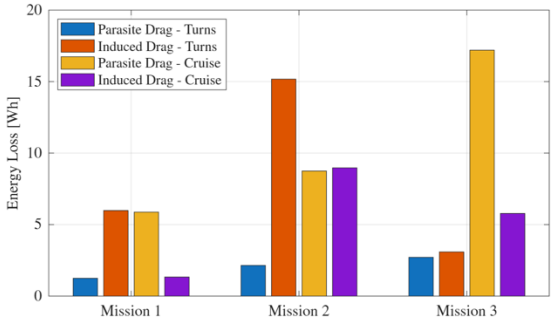

Figure 29. Power consumption by flight phase.

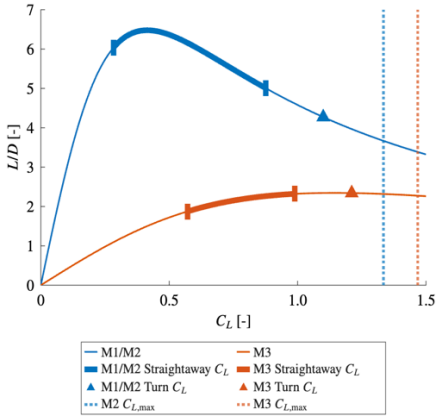

Figure 30. L/D vs C_L for M1, M2, and M3 (flapped cruise) with straightaway and turn C_L indicated.

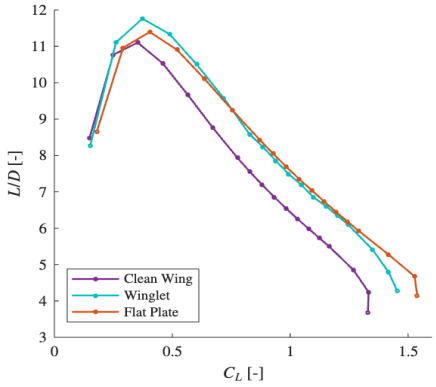

Figure 31. Lift-to-drag ratio of different wingtip devices configuration at Re = 1×10^6.

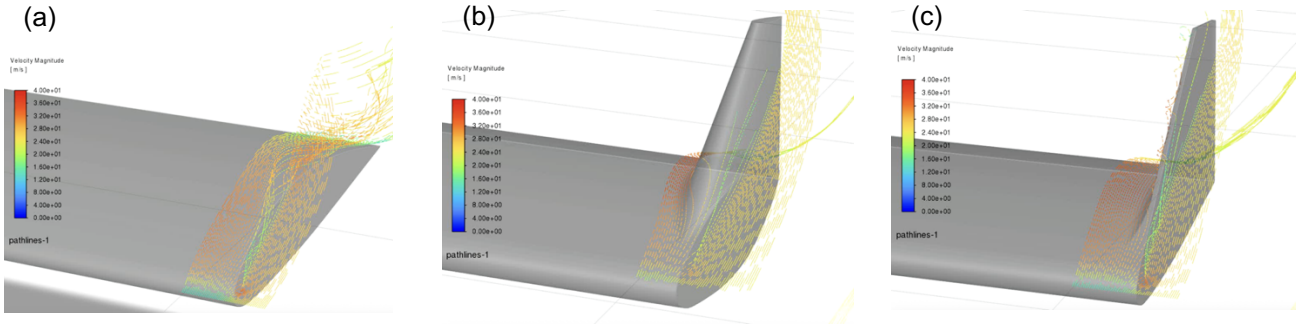

Figure 32. Pathlines of the (a) clean wing, (b) winglet, and (c) endplate configuration at the wing tip from RANS CFD analysis at Re = 1×10^6 and α of 12° degree.

Table 16. Wing Drag Estimation of Different Wingtip Devices Configuration for M2 and M3 Cruise Conditions

Configuration	Additional mass [lbm]	e [-]	$C_{D,0\ wing}$ [-]	D_{tot} (M2 / M3) [lbf]	ΔD_{tot} (M2 / M3) [%]
Clean wing	-	0.866	0.017	1.85 / 1.42	-
Winglet	0.146	1.03	0.018	1.81 / 1.32	-1.94 / -6.83%
Endplate	0.051	1.05	0.020	1.76 / 1.26	-4.69 / -11.3%

4.3.4 Trim Condition Analysis

Trim conditions for M1, M2, and M3 were analyzed using AVL to determine the trimmed α, the elevator trim deflection, δ_e, and e [6]. The outputs for each mission and Trefftz plot for 3.4 G M2 turns are presented in Table 17 and Fig. 33, respectively.

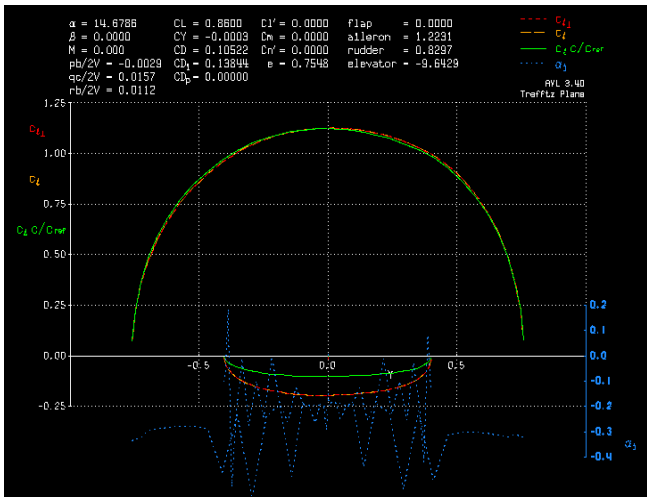

Figure 33. Trefftz plane analysis of the aircraft for M2 tight turning condition.

4.4 Stability and Control

4.4.1 Tail Sizing

The HT sizing is selected with a C_h of 0.425 and an i_h of −4°, such that the required δ_e to trim the aircraft at the maximum design cruise C_L remains below 10° to ensure an adequate safety margin while maintaining controllability.

Due to the windy conditions of Wichita, KS in April, with crosswind reaching up to 30 mph (13.4 m/s) [15], the vertical tail (VT) and rudder are designed to ensure directional control under the worst-case scenario when the aircraft is operating at stall speed with the presence of maximum crosswind. Under this condition, the rudder must generate adequate yaw moment to balance the side force induced by the crosswind, and the aircraft must maintain ground track with a maximum rudder deflection of 25° and a rudder chord fraction of 40%. The corresponding rudder deflection (δ_r) and crab angle (σ) are determined using Eq. 30 and Eq. 31 [16].

Table 17. Trim δ_e with Lift and Drag Coefficients for each Mission During Straightaway Cruise

Data	M1	M2	M3
α [°]	-1.57	0.01	15.3
δ_e [°]	5.67	4.53	-6.33
e [-]	0.71	0.71	0.71
C_L [-]	0.17	0.25	0.95
$C_{D,0}$ [-]	0.032	0.032	0.244

$$\frac{1}{2}\rho\, V_t^2\, S\, b\, (C_{n,o} + C_{n,\beta}(\beta - \sigma) + C_{n,\delta r} + \delta_r) + F_w\, d_c\, \cos\sigma = 0 \qquad \text{Eq. 30}$$

$$\frac{1}{2}\rho\, V_w^2\, S_s\, C_{d,y} - q\, S\, (C_{y,o} + C_{y,\beta}(\beta - \sigma) + C_{y,\delta r}\ \delta_r) = 0 \qquad \text{Eq. 31}$$

β is the sideslip angle (Eq. 32), V_t is the total speed (Eq. 33) where V_w is the crosswind speed and V_∞ is the flight speed.

$$\beta = tan^{-1}\left(\frac{V_w}{V_f}\right) \qquad \text{Eq. 32}$$

$$V_t = \sqrt{V_w^2 + V_\infty^2} \quad \text{Eq. 33}$$

The coefficients $C_{n,0}$, $C_{n,\beta}$, and $C_{n,\delta r}$ are the directional stability derivatives, representing the yaw moment due to zero sideslip, sideslip angle, and rudder deflection, respectively. Similarly, $C_{y,0}$, $C_{y,\beta}$, and $C_{y,\delta r}$ are the lateral stability derivatives, corresponding to the side-force due to zero sideslip, sideslip angle, and rudder deflection. These derivatives are obtained from AVL simulations [6].

The distance between the centroid of the aircraft projected side area and the CG is d_c. The crosswind-induced side force, F_W, is given by Eq. 34, where S_s is the aircraft projected side area, $C_{d,y}$ is the side-drag coefficient which is determined empirically [16]. In this analysis, a conservative value of 0.8 was used to account for the effects of the fixed landing gear and externally stowed banner on takeoff.

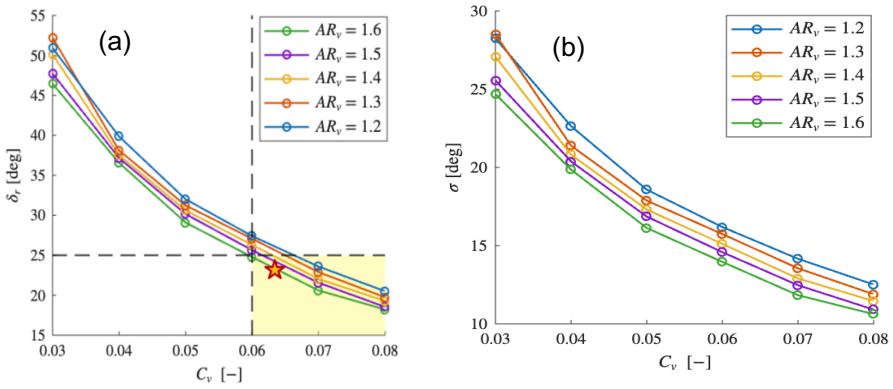

Figure 34. Required rudder deflection (δ_r) to trim the aircraft at stall speed in the presence of a 25 mph (11.2 m/s) crosswind, shown in (a) as a function of vertical tail volume coefficient (C_v) and vertical stabilizer AR, for a rudder chord fraction of 40%, with the corresponding crab angle (σ) shown in (b).

$$F_w = \frac{1}{2}\rho\, V_w^2\, S_s\, C_{d,y} \quad \text{Eq. 34}$$

The study evaluates the rudder deflection required to trim the aircraft across a range of vertical tail volume coefficients C_v and vertical stabilizer ARs under this condition. The shaded region in Fig. 34(a) indicates the vertical stabilizer geometries that satisfy the requirement of rudder deflection less than 25°. The final VT is selected with a C_v of 0.625 and an AR of 1.6 with an added margin of safety.

4.4.2 Static Stability

A static margin (SM) of 18% was determined based on pilot comfort and feedback during flight tests. Analysis in AVL showed tail downloads with sufficient margin to prevent tail stalls during both cruise and turn conditions [6]. The static stability derivatives as calculated in AVL are shown in Table 18, which includes the pitching moment derivative with respect to angle of attack, $C_{m,\alpha}$, roll moment derivative with respect to sideslip, $C_{l,\beta}$, and yaw moment derivative with respect to sideslip, $C_{n,\beta}$. Based on these AVL results, the aircraft is statically stable in all flight missions.

Table 18. Static Stability Derivatives for M1, M2, and M3

Derivatives	$C_{m,\alpha}$ [rad^{-1}] (Longitudinal)	$C_{l,\beta}$ [rad^{-1}] (Lateral)	$C_{n,\beta}$ [rad^{-1}] (Directional)
Requirement	Negative	Negative	Positive
Mission 1	-0.531	-0.0727	0.125
Mission 2	-0.532	-0.0503	0.123
Mission 3	-0.520	-0.267	0.204

4.4.3 Dynamic Stability

The dynamic stability of the aircraft was analyzed using AVL for all missions. A root locus plot, shown in Fig. 35, was used to analyze the longitudinal and lateral-directional modes of the aircraft. Five dynamic modes: roll, spiral, phugoid, Dutch roll, and short period were analyzed for takeoff and cruise conditions for M1, M2, and M3. A mode is stable if the real component is negative. As shown Fig. 35 and Table 19, all modes exhibit negative real components across each mission and flight condition, confirming dynamic stability of the aircraft.

Table 19. Dynamic Stability Results for M3: Values are Listed as Cruise Value with the Banner Stowed / Deployed

Mode		ζ [-]	ω_n [rad/s]	Decay rate [rad/s]	Time to Half Amplitude [s]
1	**Roll**	-	-	3.65 / 3.10	0.190 / 0.224
2	**Spiral**	-	-	0.009 / 0.169	74.0 / 4.10
3	**Phugoid**	0.017 / 0.121	0.498 / 1.00	0.009 / 0.121	81.6 / 5.73
4	**Dutch Roll**	0.229 / 0.010	8.66 / 5.29	1.98 / 0.054	0.350 / 12.9
5	**Short Period**	0.656 / 0.663	15.9 / 5.34	10.4 / 3.54	0.067 / 0.196

4.5 Propulsion

4.5.1 Battery Selection

Lithium-Polymer (LiPo) batteries were selected for the propulsion package due to their higher specific energy and superior discharge rate compared to the other allowed battery types: nickel-metal hydride and nickel-cadmium [18]. LiPo batteries are sized by their number of cells (n_{series}) with each cell having a nominal voltage of 3.7 V. Additionally, the energy (Wh) of the battery is calculated using Eq. 35,

$$\text{Energy (Wh)} = \text{Voltage (V)} \times \text{Capacity (Ah)} \quad \text{Eq. 35}$$

where voltage is the total nominal voltage calculated as $n_{series} \times 3.7$ V and capacity (Ah) is the total amount of charge that the battery can store. Due to the banner's high parasite drag, M3 has a higher power required. Batteries with higher cell counts were considered for the trade study for the increased power required. The trade study of 8S, 10S, 12S, and 13S batteries in Sec. 4.5.2 showed that the 8S and 13S batteries were favored for M2 and M3, respectively. Therefore, the Thunder Power RC Rampage Series 8S 3300 mAh battery was selected for M2, and the MaxAmps 13S 2000mAh battery was selected for M3.

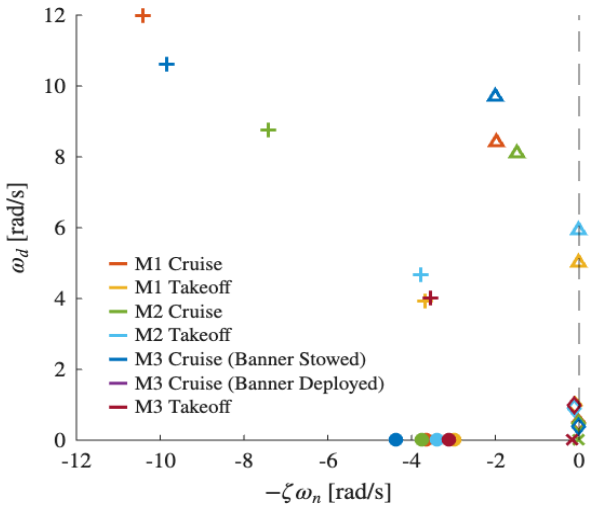

Figure 35. Root locus plot of the dynamic stability of the aircraft in roll (●), spiral (✕), phugoid (◊), Dutch roll (▵), and short period (✚)

4.5.2 Propeller and Motor Selection

First, a range of APC electric propellers and motors were traded along with other aircraft parameters through PT. The propellers varied diameter and pitch, while the motors varied in motor K_V, which represents the ratio between unloaded motor revolutions per minute (RPM) and input voltage. Then, PT determines airspeed, thrust, and power required during flight. The propulsion package was optimized for cruise with an emphasis on efficiency. The package was tailored for M3, as it demands significantly more propulsive power over other missions.

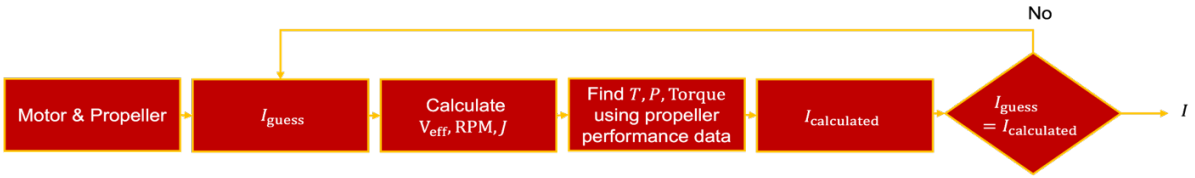

Figure 36. Flow chart of the RPM Matcher.

An in-house trade study code (RPM Matcher) sized and optimized the propulsion package based on metrics provided by PT such as average cruise velocity (V_{cruise}) and thrust required (T_{req}) for both M2 and M3. RPM Matcher seeds a guessed current (I_{guess}) and calculates the RPM, thrust, power, and torque. Then, using these values, the code iterates the current until the difference between I_{guess} and $I_{calculated}$ equals 0, shown in Fig. 36.

Using simulation data from APC Propellers [11], a list of COTS motors and their parameters were added to a database. Using this information, trade studies of motor K_V, internal resistance, and back electromotive force were conducted to find the most efficient propulsion package.

A sample propeller of APC Thin Electric 20x10E propeller was analyzed and compared with the wind tunnel test data from the UIUC Propeller Database [17] to verify the accuracy of the APC simulation. This propeller was simulated across advance ratios (J) to estimate the coefficient of power (C_P), coefficient of thrust (C_T), and efficiency (η_{prop}) at 4000RPM. The equations for the calculated values are shown in Eq. 36 to Eq. 39,

$$C_T = \frac{T}{\rho {n_{rev}}^4 {d_{prop}}^4} \quad \text{Eq. 36}$$

$$\eta_{prop} = \frac{T\,V}{P} = \frac{P_{propeller}}{P_{shaft}} \quad \text{Eq. 37}$$

$$C_P = \frac{P}{\rho {n_{rev}}^3 {d_{prop}}^5} \quad \text{Eq. 38}$$

$$J = \frac{V}{n_{rev}\, d_{prop}} \quad \text{Eq. 39}$$

where T represents thrust, P represents propulsion power, n_{rev} represents propeller revolutions per second, and d_{prop} represents propeller diameter. The difference between the data arises from the UIUC Propeller Database being from experimental testing and the APC data being simulated results. Despite this discrepancy, the trend between the curves indicates that the simulation results capture the experimentally observed propeller performance, supporting their use as a reliable input for this study. Thus, the APC propeller and UIUC propeller data brought the trade study pool to 104 propellers.

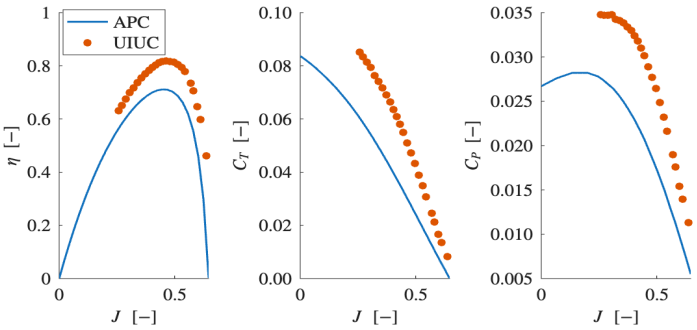

Figure 37. Comparison of APC simulation data vs UIUC wind tunnel data of APC 20x10E propeller at 4000 RPM.

Given the V_{cruise} and T_{req}, the range of propellers and motors were traded using batteries at different throttle values. Combinations that could not provide the 1.1 × T_{req}, which accounts for additional drag from manufacturing error and externally mounted components, were eliminated. Additionally, 8S and 10S batteries with current exceeding 100A; for 12S and 13S batteries with current exceeding 54 A, were eliminated as set by PR.03 (Sec 3.2) or the battery specifications, respectively [18].

The motor-propeller combinations that can produce the T_{req} at V_{cruise} were then ranked by η_{prop}. Due to the high power required for M3, using an 8S battery required a higher diameter propeller. This leads to an increase in W_{empty} from greater landing gear height and fuselage reinforcement required for propeller clearance and increased

torque, respectively. Therefore, an 8S battery was chosen for M2 and a 13S battery was chosen for M3 with a T-motor AT8030 160KV. The propellers were then ranked with efficiency, shown in Table 20.

Table 20. Successful Propulsion Package Based on the Motor Selected

Mission	Battery [S]	Throttle [%]	Propeller	Current [A]	RPM	J [-]	η_{prop} [-]
M2	8	85	APC 20x15E	22.4	4300	0.62	0.79
	12	60	APC 20x13E	29.1	4500	0.57	0.78
	8	85	APC 20.5x14E	20.7	4300	0.57	0.78
	8	80	APC 26x15E	49.0	3800	0.56	0.77
	10	75	APC 19x12E	21.3	4800	0.56	0.77
M3	13	60	APC 22x12E	42.7	4700	0.34	0.67
	13	60	APC 21x13E	41.1	4800	0.36	0.66
	13	55	APC 26x13E	47.9	4254	0.32	0.66
	13	60	APC 20.5x14E	42.4	4800	0.37	0.66
	13	70	APC 20x10E	35.1	5700	0.32	0.65

Based on the highest η_{prop} for each mission, the following propulsion package was selected.

Table 21. Selected Propulsion Package for M2 and M3

Motor	Mission	Propeller	Battery [S]	Throttle [%]	Current [A]	RPM	Thrust [lbf]	Prop Power [W]	Torque [lb-ft]	J [-]	η_{prop} [-]
AT 8030 160 KV	M2	APC 20x15E	8	85	22.4	4300	4.27	480	0.78	0.62	0.79
	M3	APC 22x12E	13	60	42.7	4700	10.68	1130	1.68	0.34	0.67

4.5.3 Electronic Speed Controller (ESC) Selection

The KDE Direct ESC's KDE-UAS85UVC was selected for its CAN-BUS data logging and the ability to support a 13S battery. Since results in Table 22 shows that the maximum continuous current is 42.7 A and with factor of safety 2, an ESC with a 85 A continuous current rating was selected.

4.6 Predicted Aircraft Performance

Utilizing PT (Section 4.2), the performance of the preliminary design was simulated. Table 22 presents relevant aircraft performance values for all flight missions at 14.5 mph (6.5 m/s) of constant wind.

Table 22. Simulated Results in 14.5 mph (6.5 m/s) Winds

Metric	M1	M2	M3	GM
Payload	-	144 pax, 1 cargo	196 ×39 in (5 × 1 m)	-
Net Income [-]	-	1,934	-	-
Throttle [%]	90	90	60	-
Battery Usage [%]	24	73	69	-
Number of Laps	3	5	2	-
Mission Time [s]	130	290	174	426
Score	1.00	1.84	2.47	0.07

4.6.1 Capabilities and Uncertainties

While the team continuously updates its models, uncertainties remain due to modeling errors and real-world variability. To account for the latter, an additional 10% is added to lap lengths to account for a human pilot. Additionally, the aircraft was sized using non-integer laps to account for the uncertainty in conditions. An 80% battery cutoff was applied as a factor of safety. To account for possible modelling errors, mass and drag results from flight tests were compared to predictions, and correction factors were applied. As a potential source of

limitations, while the aircraft was sized for Wichita, KS winds, it was flown predominately in Los Angeles, CA with calm winds. Additionally, gusts were not considered for performance.

5 Detail Design

During detail design, aircraft components including wing, tail, fuselage, landing gear, and payload systems are analyzed, tested, and optimized. Additionally, individual propulsion and avionic components are chosen.

5.1 Dimensional Parameters Table

The characteristics of *Trojan HorSCe* are listed in Table 23 and are further discussed in subsequent sections.

Table 23. Subsystem Characteristics and Dimensional Parameters

Wing		**Horizontal Tail**	**Vertical Tail**
Airfoil	Odyssey-1644	NACA 0010	NACA 0010
Span (*b*)	5 ft (1.52 m)	2.64 ft (0.805 m)	1.26 ft (0.383 m)
Mean Aerodynamic Chord (MAC)	2.08 ft (0.63 m)	1.06 ft (0.322 m)	0.784 ft (0.239 m)
Planform Area (*S*)	10.4 ft^2 (0.96 m^2)	2.79 ft^2 (0.259 m^2)	0.99 ft^2 (0.092 m^2)
Aspect Ratio (*AR*)	2.40	2.5	1.6
Incidence Angle	2°	-4°	0°
Taper Ratio (*λ*)	1.0	1.0	1.0
Twist	0°	0°	0°
Winglet Height	8.98 in (22.8 cm)	N/A	N/A
Aileron / Flap	25% chord fraction 43% semi-span fraction	**Propulsion**	
		Motor K_V	160
Fuselage		**M1 Battery**	8S 3300 mAh
Total Length	6.07 ft (1.85 m)	**M2 Battery**	8S 3300 mAh
Maximum Width	3.94 in (10 cm)	**M3 Battery**	13S 2000 mAh
Maximum Height	3.94 in (10 cm)	**Propeller**	
Landing Gear		**Mission 1 (M1)**	APC 20x15E
Track	18.4 in (0.47 m)	**Mission 2 (M2)**	APC 20x15E
Height	15.0 in (0.38 m)	**Mission 3 (M3)**	APC 22x12E

5.2 Structural Characteristics and Capabilities

The aircraft structure was designed to withstand aerodynamic and inertial loads sustained during takeoff, climb, level cruise, coordinated turns, gusts, and landing. Loads and dynamics were obtained from aerodynamic analysis, performance simulations, and flight test data. The *V-n* diagram in Fig. 38**.** synthesizes this information to inform sizing for all structural components. A limit load factor of 3.4, derived from a coordinated 73° banked turn at maximum takeoff weight (MTOW), and dive speed (V_D) of 144 ft/s (44.1 m/s), defined by 1.4V_C (where V_C is the maximum cruise speed), bound the operating region, shaded green, in Fig. 38.

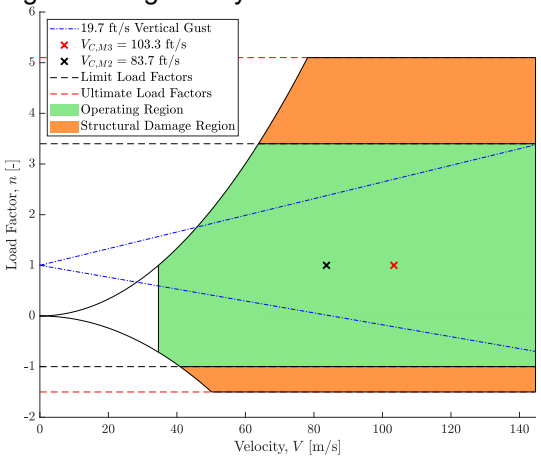

Figure 38. V-n diagram with M2 and M3 V_C.

5.3 Subsystem Integration

Aircraft systems and sub-systems were designed to satisfy all mission requirements shown in Sec. 3.2, while minimizing W_{empty} and banner drag, as guided by the sensitivity study shown in Sec. 3.2.3.

5.3.1 Fuselage

The semi-monocoque fuselage was designed to transfer loads from the wing, boom, motor, and main landing gear (MLG) through plywood hardpoints and formers into the carbon-fiber (CF) skin, shown in Fig. 39. Cross-section

width and height of the fuselage outer mold line (OML) were constrained to 3.94 in (10 cm) by the motor diameter but otherwise minimized to the volume needed to carry the avionics and cargo. This reduced cross-section, resulting in reduced area moments of inertia I_{yy} and I_{zz}, drove requirements for the CF skin ply schedule and thickness t_{fuse}. The fuselage was analyzed as a thin-walled beam, where bending stresses σ_{bend} and shear stresses τ calculated using Eq. 40-41, along the x-axis were developed based on the shear force (SF) and bending moment (BM) envelope seen in Fig. 40. This diagram encompasses a coordinated 3.4-G turn (represented by the top-left corner of the operating region in Fig. 38) and a 4-G landing to avoid failure if MLG bolts shear.

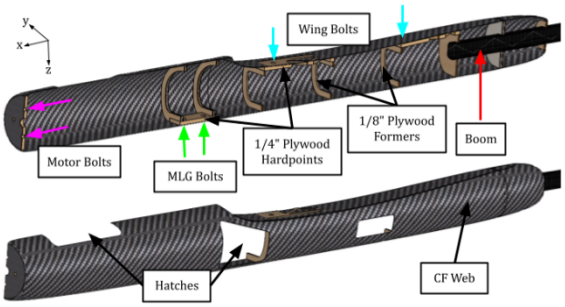

Figure 39. Fuselage structural design.

$$\tau = \frac{(SF)\,Q}{I_{yy}\,t_{\text{fuse}}} \qquad \text{Eq. 40}$$

$$\sigma_{bend} = \frac{(BM)\,z_{\max}}{I_{yy}} \qquad \text{Eq. 41}$$

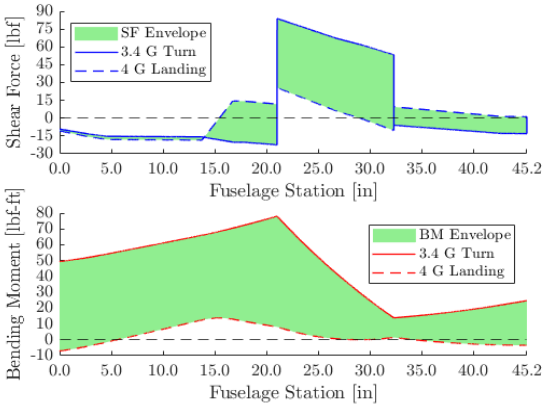

Figure 40. Fuselage SF and BM diagram along x-axis.

The ply schedule chosen was 5.7-oz/yd^2 (193-g/m^2) 3k 2x2 twill-weave CF fabric in a [±45/0-90]° orientation, with an additional ply of 2-oz/yd^2 (67.8-g/m^2) fiberglass (FG) in a [±45]° orientation in the nose cone for electrical insulation from the propulsion system. With this laminate, the fuselage can withstand the maximum expected 14.6-psi (101-kPa) bending and 0.953-psi (6.57-kPa) shear stress.

To aid the initial analysis, a representative test-bed fuselage was constructed to observe load transfer into the skin at the boom-fuselage and MLG-fuselage interfaces. The testbed was dropped from a height of 3.63-in (9.22-cm) at a weight of 22.9-lbf (102-N) to simulate the 4-G landing load case, as seen in Fig. 41. The loads transferred into both interfaces did not damage the testbed, validating the integrity of the laminate structure against overload and buckling.

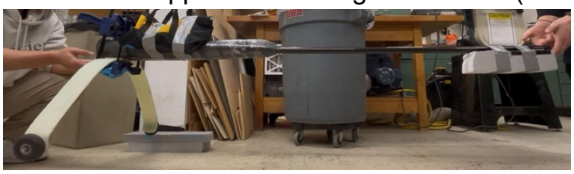

Figure 41. Fuselage testbed drop test setup.

5.3.1.1 Boom

A square cross-section boom was chosen as an alternative to tapering the fuselage to the tail, motivated by manufacturing simplicity and weight reduction, given a tail moment arm of 3.26-ft (1-m). The boom was analyzed as a thin-walled cantilevered beam and sized under the same load cases as the fuselage, resulting in a maximum SF of 13.1-lbf (58.1-N) and BM of 24.7-lbf.ft (33.5-N.m), which must be reacted into the three aftmost fuselage formers that the boom is adhered to. A minimum inner width of 1-in (2.5-cm) was chosen to provide enough surface area for tail integration and enough volume to route avionics wiring. Commercial FG and CF tubes of various thicknesses t_{boom} were then traded to obtain the lightest boom that met strength and buckling requirements.

To ensure buckling would not occur, the critical local buckling stress σ_{cr} of the boom wall, calculated using Eq. 42, was enforced to be greater than the shear strength of the boom material.

$$\sigma_{cr} = 0.43\frac{\pi^2 E}{12(1-\nu^2)}\left(\frac{t_{\text{boom}}}{1\text{ in}}\right)^2 \quad \text{Eq. 42}$$

A 0.065-in (1.65-mm) thick, 3k 2x2 twill-weave square CF tube was the lightest available option that satisfied all structural requirements. The resulting boom-fuselage structure is 10.4% lighter compared to a completely semi-monocoque fuselage.

5.3.2 Wing

Based on the duck-in-wing (DIW) configuration chosen in Sec 3.3.1, the team explored designs that incorporated 144 passengers into a compartment in the wing structure. The structure illustrated in Fig. 42 uses the compartment walls as shear webs (front and rear spars), the compartment floor to transfer inertial passenger loads to the spars, and two compartment hatches (each 24.4 × 10 in, 62 × 25.4 cm) over the top wing skin.

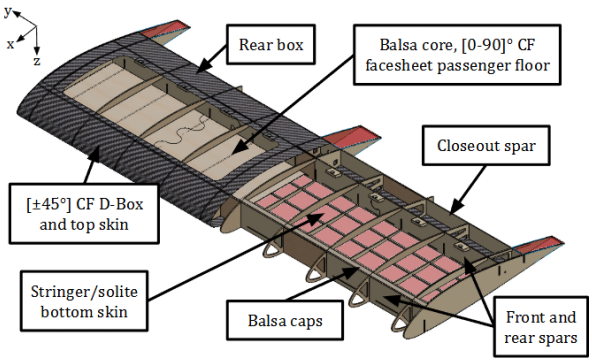

Figure 42. *Trojan HorSCe* wing structure.

The wing was sized against aerodynamic loads induced by maximum flap deflection and inertial loads in a coordinated 3.4-G turn at MTOW, from which SF, BM, and torsional moment (TM) distributions were calculated. This is plotted in Fig. 43. Since *Trojan HorSCe*'s airfoil has a maximum thickness of 4.05 in (10.3 cm), the spars and caps have a large second moment of area, I_{xx}. Thus, shear web thickness was sized for shear failure and web shear buckling.

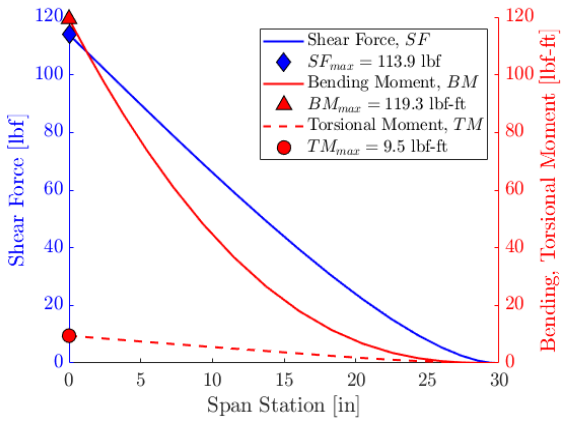

Figure 43. Wing SF, BM, and TM diagram.

The balsa spars were sized to a thickness t_{spar} of 1/8-in (0.318 cm), with fibers oriented along the *y*-axis. The spars must handle a maximum SF of 114 lbf (509 N) and shear stress τ of 607 psi (4.18 MPa), calculated with Eq. 43, where Q is the first moment of area. Web shear buckling modeled the spars as quasi-isotropic clamped plates, which ruled out a t_{spar} of 1/16 in (0.159 cm). The critical local buckling stress σ_{cr} was calculated and enforced to be less than τ using Eq. 44, where k_{ss} is the shear buckling coefficient, E is the elastic modulus of balsa cross-grain, ν is the in-plane Poisson's ratio of balsa, and h_{spar} is the spar height.

$$\tau = \frac{(SF)\,Q}{I_{xx}t_{\text{spar}}} \quad \text{Eq. 43}$$

$$\sigma_{cr} = k_{ss}\frac{\pi^2 E}{12(1-\nu^2)}\left(\frac{t_{\text{spar}}}{h_{\text{spar}}}\right)^2 \quad \text{Eq. 44}$$

Spar caps of 1/16-in balsa construction were chosen to bear a maximum BM of 120 lbf-ft (163 N-m) and compressive bending stress σ_c of 671 psi (4.63 MPa), calculated with Eq. 45, where z_{max} is the maximum distance of the top wing skin from the neutral axis. These caps also bond to the D-box for greater bending stiffness.

$$\sigma_c = \frac{(BM)\, z_{\max}}{I_{xx}} \quad \text{Eq. 45}$$

The passenger hatches in the top skin reduces the wing structure's torsional rigidity, since the skins no longer form a closed cell with the webs. As a result, the D-box and rear box were sized to limit torsional deflection. Both were modeled as composite thin-walled closed cells and sized using Eq. 46, where t_{wall} is the wall thickness, and A_e is the enclosed cell area. A 5.7-oz/yd^2 (193-g/m^2) CF D-box and rear box was chosen to handle the maximum TM of 9.48-lbf.ft (12.9-N.m) and maximum τ of 786-psi (5.42-MPa), and to limit the torsional deflection θ to 1.5°. A final deflection of 1.48° at the wingtip was calculated using Eq. 47, where b is the wing span and GJ is the torsional rigidity of the box cross sections.

$$\tau = \frac{TM}{2A_e t_{\text{wall}}} \quad \text{Eq. 46}$$

$$\theta = \frac{(TM)\,(b/2)}{GJ} \quad \text{Eq. 47}$$

1/4-in plywood wing- and fuselage-side hardpoints provide an interface for four 1/4"-20 nylon bolts to clamp the wing to the fuselage. The wing-side hardpoints were bonded to the spars and central ribs to react wing loads into the fuselage structure. The fuselage-side hardpoints were bonded to the fuselage formers and skin to distribute this reaction into the fuselage web. Finite Element Analysis (FEA) through Altair OptiStruct [19] verified that no wing-components would fail under the limit load, as seen in Fig. 44. The wing semispan was analyzed, with distributed forces applied at each rib station and translational degrees of freedom fixed at center span. The various CF, balsa, and plywood components were modeled as orthotropic laminates, yielding composite failure indices based on Tsai-Wu failure criteria, where a value greater than 1 indicates failure.

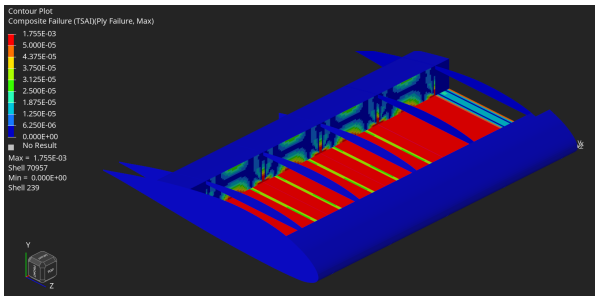

Figure 44. Composite failure index plot of the wing structure under aerodynamic loads during the 3.4 G turn. The floor experiences the greatest stress, but no components fail.

5.3.3 Empennage

The horizontal tail (HT) and vertical tail (VT) were sized against the aerodynamic loads induced by maximum elevator and rudder deflection in a corner turn. Both use a front and rear 1/8-in balsa spar to resolve internal SF and BM reactions. The HT spars were sized using Eq. 45 to the minimum thickness required to handle a maximum 4.65-lbf.ft (6.31-N.m) BM, yielding a tip deflection of 0.00917-in (0.233-mm). The VT spars were sized similarly for a maximum 3.25-lbf.ft (4.40-N.m) BM, yielding a tip deflection of 0.0107-in (0.271-mm). Tip deflections were not significant enough to affect aerodynamic load distributions and were deemed acceptable.

The HT and VT also use a 5.7-oz/yd^2 (193-g/m^2) CF D-box to resolve the TM due to each tail's pitching moments. The D-box must handle shear stress τ due to a maximum equipollent TM (about the shear center) of 2.52-lbf.ft (3.42-N.m) for the VT and 1.11-lbf.ft (1.50-N.m) on the VT. The D-box was analyzed as a thin-walled closed cell using Eq. 46. Carbon fiber was determined to be the lightest material available that was torsionally rigid yet moldable enough to meet the curvature of the LE. 3/16-in balsa stringers transfer load from the remaining Solite skin towards the ribs and into the spars.

Both tail control surfaces must withstand the normal aerodynamic force F_N related to the maximum hinge moment H (Eq. 48-49). C_H is the hinge moment coefficient, S_{ref} and c_{ref} are the wing area and mean aerodynamic chord. Assuming a triangular pressure distribution along the chord, the lever arm d for F_N is one-third of the CS chord. Flight test showed 1/8-in balsa spars and ribs with a 1/16-in balsa skin construction handled the resultant 4.68-lbf (20.8-N) force on the elevators, and 2.23-lbf (9.91-N) force on the rudder.

$$H = C_h \, q \, S_{\text{ref}} \, c_{\text{ref}} \quad \text{Eq. 48}$$

$$F_N = \frac{H}{d} \quad \text{Eq. 49}$$

The integration method for the tails to the tail boom is shown in Fig. 45. The HT is attached in two halves and clamped to the sides of the boom by one M4 bolt in double shear, sized by hole bearing due to the maximum SF. Both halves slot onto a 0.0394-in (9.31-mm) CF rod to react the BM into a continuous member. The VT is clamped to the top of the boom by two M3 bolts with threaded inserts in shear, driven by hole bearing. These bolts are placed next to the spars to transfer loads into the boom without inducing additional TM and shear stresses on the innermost 1/8-in plywood ribs, which serve as the tail hardpoints.

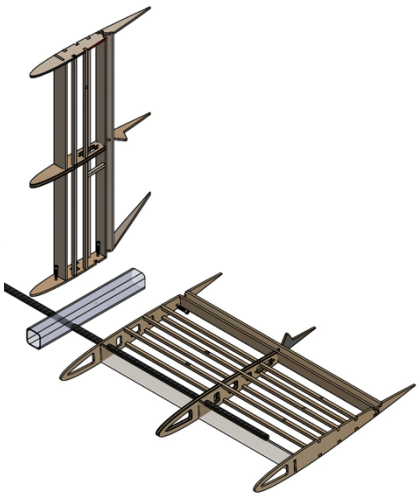

Figure 45. Integration structure of the HT and VT.

5.3.4 Landing Gear

The main landing gear (MLG) was designed using GearSizer, a spreadsheet created by team advisor Blaine Rawdon [20]. The gear was designed for an MTOW of 20.4 lbm (9.25 kg) and a maximum 2-G load to the fuselage to allow for sufficient flex during landings below MTOW. The design sink rate was 3.12 ft/s (0.95 m/s), determined as a worst-case value based on prototype flight testing. At MTOW, the gear compresses vertically by 1.5 in (3.8 cm) and maintains 2.5 in (6.4 cm) of propeller clearance. The MLG has a height of 15 in (38.1 cm) to maintain sufficient propeller clearance and a 19 in (48.3 cm) track width to produce a strut angle which efficiently transfers vertical loads into outward bending. The gear is made from 4.2-oz/yd^2 (142-g/m^2) unidirectional S-glass to allow larger elastic deflection than stiffer materials like CF, given its lower modulus. At maximum loading, GearSizer outputs interlaminar stresses less than the 500 psi (3.45 MPa) recommended limit for the material, and a maximum shear stress of 90 psi (620 kPa), confirming an adequate stress distribution.

The gear mounts to a hardpoint with steel tee-nut inserts by four 1/4"-20 bolts. Four nylon bolts were selected as controlled failure points to reduce excessive shear loads, to prevent damage to the hardpoint and fuselage during hard landings. The root integration region is 2 × 3 in (5.1 × 7.6 cm), which places the bolt pilot holes away from the central load-bearing fibers. The bow tapers toward the wheel, with maximum width near the top of 2.0 in (5.1 cm). The main gear was placed to produce an angle of 20° between the vertical main wheel on the gear and CG. An acceptable range is 16-25° for lateral stability during take-off and landing [21]. 1.75-in (4.45-cm) wheels were selected for the competition runway to reduce drag and weight.

The aircraft's tail gear is a skid designed in-house and 3D printed using 40% filament and 5 layer walled Thermoplastic Polyurethane (TPU) with a 90% filament Polylactic Acid (PLA) core. The skid is secured with two nylon bolts to prevent rotation and slipping. The height is 4 in (10 cm) for a sitting angle at 13.4°, within the acceptable range of 10-15°.

5.3.5 Payloads

5.3.5.1 Passengers & cargo

The passenger compartment spans from 13% to 58.3% chord. It is bounded by a floor constructed of a 11.5 × 60 in (0.292 × 1.52 m) 1/16-in balsa sheet with a bottom face sheet of [±45]° 5.7-oz/yd^2 (193-g/m^2) CF twill, the front and aft spars and solid wing tip ribs. Each hatch weighed 0.26 lbm (120 g), are hinged by four 5/8 × 1.125 in (16 × 28 mm) nylon hinges, each weighing 0.02 oz (0.5 g), seen in Fig. 46 (a). The top skin of each hatch and the fixed wing skin share the same construction, with a 3-in (7.62-cm) thick section of 6.9-oz/yd^2 (234-g/m^2) Dacron foam, adhered with CA to the underside of the wing hatches. An additional 0.5-in (1.27-cm) layer of Styrofoam stiffens the hatch and lowers the Dacron ceiling. To maximize packing efficiency, passengers are arranged hexagonally, which resembles 6 rows by 24 columns. When the hatches are closed, the Dacron foam conforms around each passenger, preventing vertical and lateral movement, fully restraining each passenger, seen in Fig 46.(b). The hatches are locked in the closed position by four picture-frame tabs, constructed of 1-in (2.5-cm) plastic servo arms, and bolted to the 0.5-in (1.27-cm) section of wing skin protruding from the aft spar. To prevent the tabs from bowing the skin when closed, a 1 × 1 in (2.5 × 2.5 cm) 1/16-in plywood plate is adhered beneath each tab to both the wing skin and the aft spar.

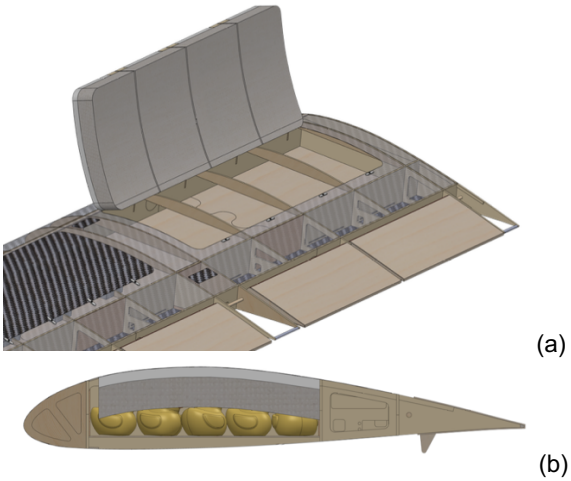

Figure 46. (a) Passenger compartment and (b) restrained.

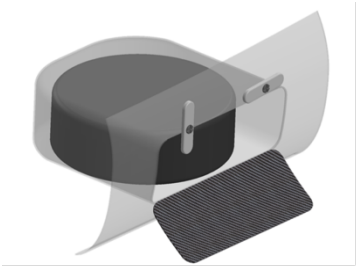

Figure 47. Internal cargo restraint with hatch and latches.

Cargo is restrained by a custom 0.04 lbm (20 g) PLA housing located 10.5 in (26.7 cm) aft of the wing leading edge inside the fuselage. The housing has a 3.1 × 1.1 in (7.9 × 2.8 cm) opening on the starboard side of the fuselage to accept one cargo item, and is 3.1 in (7.9 cm) deep, seen in Fig. 47**.** It adheres to the fuselage inner-mold-line (IML), sealing off the cargo bay from the rest of the aircraft. A nylon hinged CF hatch is held in place by a pair of picture-frame latches.

5.3.5.2 Banner deployment and release

The banner stowage system retains the banner until after the first 180° turn, when it is then released for towing. Low weight and drag were prioritized. The banner is restrained along the fuselage centerline by two mechanisms:

a retention cup at the front and a servo-actuated elastic band at the back. The retention cup, with a maximum cross section of 2 in (5.08 cm), depicted in Fig. 48(a), keeps the rolled-up banner fixed in the forward direction and parallel to the fuselage. The opening faces aft to receive the banner and tapers towards the front of the aircraft to an outer diameter of 0.2 in (0.508 cm). Openings at both ends serve to reduce pressure drag. The retention cup is constructed of PLA and is 3D printed for rapid prototyping and adheres to the fuselage 0.4 in (1.02 cm) forward of the wing leading edge using a single 2.5 × 3.5 in (6.35 × 8.89 cm) strip of velcro, weighing a total of 0.03 lbm (15 g). Since the retention cup sees minimal loading during flight, the attachment method is designed to be as light and removable for M1 and M2.

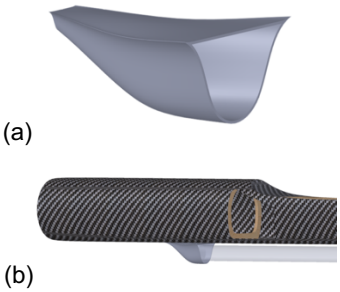

Figure 48. (a) Forward banner retention cup (b) and as attached to the aircraft with stowed banner.

Translation of the banner is prevented by a 1.5 × 6.5 × 0.02 in (3.8 × 16.5 × 0.05 cm) elastic band located 15.5 in (0.4 m) aft of the retention cup (Fig. 49). One end of the elastic band is fixed to a PLA housing that encloses a 0.04 lbm, 3.04 lbm-in (17 g, 3.5 kg-cm) servo motor. To restrain the banner, the elastic band is stretched over a 2-in outer diameter (5 cm) stowed banner. It is locked into place when a 1/32-in diameter annealed A2 steel rod, actuated linearly by a servo motor, pierces through a small 1/8-in plywood tab at the end of the elastic band that slots into the PLA housing. To ensure consistent servo connection, a 3-pin female connector interfaces with the servo motor upon attachment to the fuselage. The entire assembly weighs 0.14 lbm (65 g) and is attached to the fuselage by two 0.7-in (1.8-cm) quarter turn fasteners. Each fastener is secured through a 0.2-in (0.5-cm) opening in the PLA housing and latches into receptacles on the fuselage floor. Following the first 180° turn, the pilot commands the deployment servo, retracting the steel rod from the plywood tab, which releases band tension. Once released, the banner slides rearward out of the retention cup and unfurls into the towing configuration.

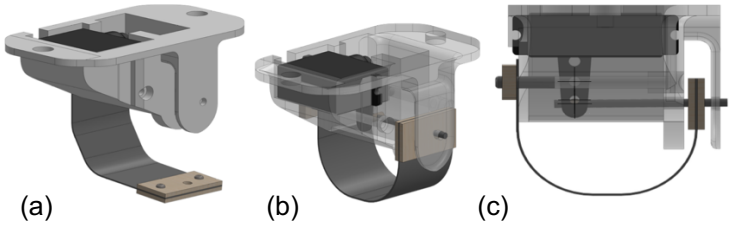

Figure 49. Banner deployment mechanism in the (a) open, (b) closed (center), and (c) front configurations.

Once the banner is deployed, its tow line is held in place at the aircraft CG by a 3.04-lbm-in (3.5-kg-cm) servo-actuated, 4-in (10.2-cm) long, 1/16-in steel rod**.** The banner release mechanism is adhered to the fuselage floor, with a 0.2-in (0.5-cm) diameter cutout for the towline to enter prior to flight. Once inserted, the servo is actuated and the steel rod pierces through a loop at the end of the towline. Most of the towline is braided fishing line with the last 6 in (15 cm) being a steel fishing leader. The lower coefficient of friction of the steel fishing leader on the metal rod ensures easier release. Furthermore, the steel rod is supported by a 1/2-in (1.27-cm) balsa strip along its length to prevent bowing under the banner drag force acting through the towline, as shown in Fig. 50.

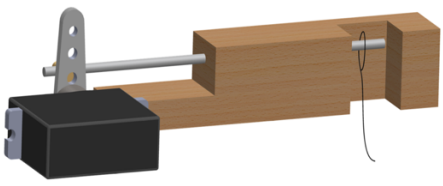

Figure 50. Release mechanism with towline.

5.3.5.3 Banner

Banner scoring is a function of length, directly proportional to the banner aspect ratio. For a fixed length, reducing aspect ratio increases wetted surface area and drag without improving score. Therefore, the maximum banner aspect ratio of 5 was selected. Tissue Lamé was selected as the final banner material, as truck testing, presented in Sec. 8.1.3.5, showed it produced the lowest drag within the design banner Reynolds number range. Wooden dowels were used in early iterations but were replaced by hollow aluminum airfoil-shaped leading-edge rods to reduce drag (Fig. 51).

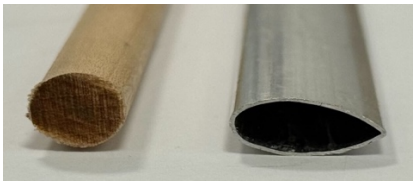

Figure 51. Banner leading edge rods.

To ensure the banner remains vertical, a towline, made from 80-lbf (356-N) braided fishing line, extends from two split-rings attached to the top and bottom corners of the banner leading edge to create a right angle at the top of the banner. To complement the upright and vertical banner orientation encouraged by the right angle, 0.13 lbm (60 g) of ballast was attached to the bottom of the banner leading edge rod. A three-way swivel was tied to each tow line, allowing for a single tow line to emerge, which was attached to a 6-in (15.2 cm) steel fishing leader via barrel swivel, shown in Fig. 52. The steel fishing leader contains a fixed loop at the end, which interfaces with the banner release mechanism. The USC logo will be hand drawn using permanent marker, after it was determined that spray paint would smear off the banner surface. Conventional paint and stitching were deemed overly heavy and may cause interference with the banner unfurling during deployment.

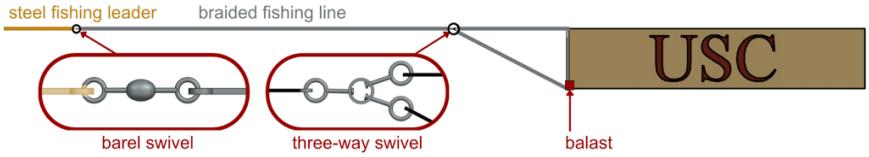

Figure 52. Banner towline configuration.

5.3.6 Propulsion

Each component has been tested to optimize propulsion system efficiency (η_{total}) for each mission. Flight testing and simulations confirmed that power and current requirements are met for each mission. The mission breakdown is shown in Table 24.

Table 24. Propulsion System Breakdown by Mission

	M1 & M2	M3
Propeller	APC 20x15E	APC 22x12E
Motor	T-motor AT8030 160KV	
ESC	KDE-UAS85UVC 85A+UHV	
Battery	Thunder Power RC Rampage 8S, 3300 mAh Lithium Polymer (LiPo)	MaxAmps 13S 2000mAh LiPo

5.3.7 Wiring

Propulsion is powered using an 8S battery for M1 and M2 and 13S battery for M3. Using the maximum continuous current from Table 21, the 8-gauge wires are used to extend the battery to the ESC given the fuse and its holder must remain more than 6 in (15.2 cm) from the propeller plane [1]. A 60 A fuse is used with the 13S battery given the battery specifications, and a 100 A fuse is used for 8S batteries as constrained by requirement PR.03 (Table 3). The detailed wiring diagram of the propulsion unit is shown in Fig. 53.

The avionics (AV) system is powered by a 3S battery to satisfy the minimum 12 V requirement of the Walksnail first-person viewer (FPV) system. A 5 V battery eliminator circuit (BEC), supplied regulated 5 V to the flight

controller (FC), which in turn provided 3.3 V to telemetry components and sensors, including the 3DR SiK Telemetry Air Radio, MATEKSYS ASPD-4525 digital airspeed sensor, Holybro M10 GPS module, and TMP102 temperature sensor. The ESC was connected to the FC to record ESC data. Two Radiomaster ER8 receivers (Rx1 and Rx2) were connected to the FC. Rx1 provided pulse width modulated (PWM) signals to the ESC, payload servos, and flap servos. Aileron, rudder, and elevator PWM signals were routed through the HobbyWing A3 Pro 6-axis gyro, which stabilized the aircraft by applying attitude corrections to the control surfaces. Rx2 was used to adjust the gains of the gyro and flight modes. These components were installed to record data and inform future aircraft designs. The DAQ setup is used for test flight data collection only and will not be used during the fly-off to comply with DBF competition rules [1]. In addition to powering the FC, the AV battery was split via y-cable to power the FPV camera and a 7.4-V BEC, which provided power to the receiver's PWM outputs which actuates the control surface's servos. Servo hinge moments were calculated from AVL hinge-moment coefficients using Eq. 48 at the higher of the M2 and M3 airspeeds, with a factor of safety of 1.25 [6]. Table 25 displays the required servo torque for a given control surface and corresponding chosen servo.

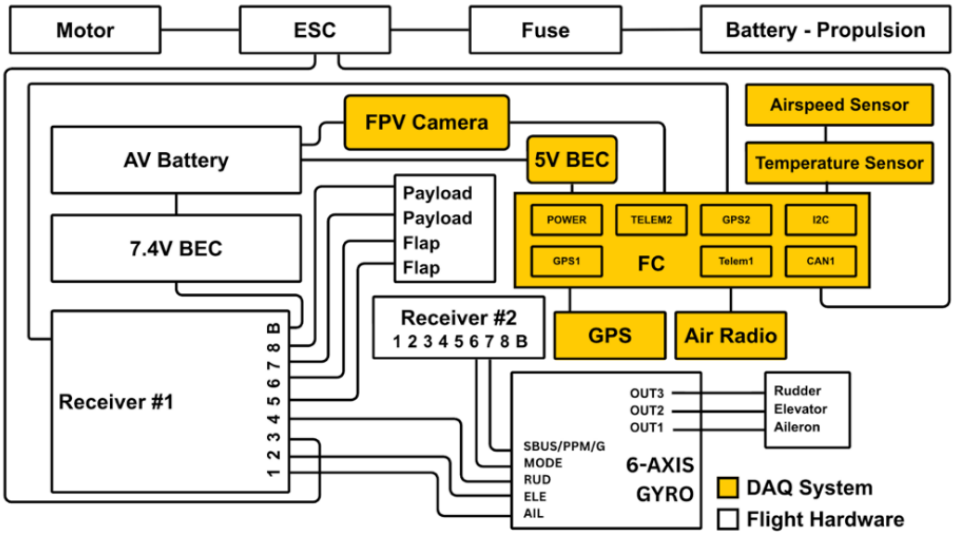

Figure 53. Wiring diagram

Table 25. Required Servo Torque Loads and Chosen Servos

Control Surface	Required Servo Torque [lbf-in]	Servo Chosen	Servo Torque [lbf-in]
Ailerons	9.13	FrSky Coreless Xact 5300 Series HV 8.4V MD5301H	19.94
Flaps	16.3		
Elevators	3.58	KST X10-710 V8.0 HV Mini	5.90
Rudder	2.01		

5.4 Weight & Balance

W_{empty} for *Trojan HorSCe* is 11.8 lbm (5.33 kg), with the included battery's location adjusted to allow for the CG to be within the SM range of 18% to 20%. Table 27 shows the CG and SM for each mission. The mass balance for the aircraft was analyzed using previously measured component masses, component CGs, and empirical material properties. Table 26 tabulates the mass and displacement of each component relative to the coordinate system shown in Fig. 54 components distributed throughout the aircraft such as the ESC, fuse, and other electronic components were resolved into an equivalent mass and displacement. The cargo and passenger restraint weights were included in the fuselage and wing weights, respectively. The M3 banner deploy and release mechanisms were permanently attached to the aircraft and denoted as fixed banner mechanisms. Given the banner stow mechanism is detachable, it is only included in the M3 weight subsection.

5.4.1 Mission Mass Breakdown

Table 26. Mass and Corresponding Displacement of Aircraft Components

	Aircraft Component	Mass		X Displacement		Z Displacement	
		[lbm]	[g]	[in]	[cm]	[in]	[cm]
General	Fuselage (Includes Wiring & Motor)	4.04	1830	-7.8	-19.9	-2.1	-5.32
	Wing	5.18	2350	10.4	26.4	0.7	1.90
	Tail	1.32	599	47.6	121	0.7	1.65
	Main Landing Gear	0.650	295	-3.11	-7.90	-8.7	-22.0
	Tail Landing Gear	0.200	90.7	49.9	127	-5.9	-15.0
	Fixed Avionics	0.963	437	-10.3	-26.1	-3.1	-8.00
	Fixed Banner Mechanisms	0.154	70.0	9.29	23.6	-4.4	-11.1
M1	Propeller	0.216	98.1	-22.0	-56.0	-2.0	-5.00
	Battery	1.61	731	-7.9	-20.0	-3.2	-8.05
	Total	14.3	6500	4.68	11.89	-1.4	-3.50
M2	Propeller	0.216	98.1	-22.0	-56.0	-1.97	-5.00
	Battery	1.61	731	-13.6	-34.5	-3.17	-8.05
	Cargo (Pucks)	0.551	250	15.3	38.8	-2.96	-7.51
	Passengers (Ducks)	6.59	2990	8.9	22.6	0.98	2.50
	Ballast	0.661	300	-17.7	-45.0	-3.94	-10.0
	Total	21.5	9740	5.27	13.4	-0.82	-2.07
M3	Propeller	0.300	136	-22.0	-56.0	-1.97	-5.00
	Battery	1.39	631	-11.8	-30.0	-2.56	-6.50
	Banner	0.397	180	9.45	24.0	-4.72	-12.0
	Banner Stow Mechanism	0.0441	20.0	-0.472	-1.20	-5.51	-14.0
	Total	*14.7	*6660	**4.47	**11.4	-1.41	-3.59

**Mass becomes 14.3 lbm (6480 g) after banner is released*

***Total X displacement becomes 4.34 in (11 cm) after banner is deployed and then 3.98 in (10.1 cm) after it is released*

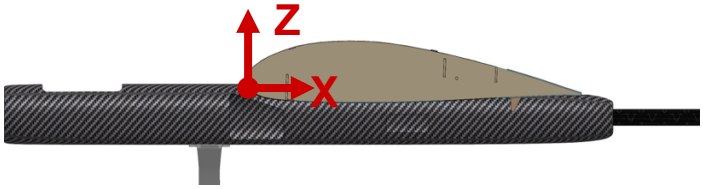

Figure 54. Aircraft coordinate system with origin at wing root LE.

Table 27. CG Location and SM per Mission

	M1	M2	*M3
CG Location	4.37 in	5.09 in	4.47 in
SM	19.8%	17.9%	19.2%

*CG is 4.37 in, SM is 19.7% after deploy and 4.37 in, SM is 19.8% after release

5.5 Flight Performance Parameters for Final Design

Table 28 summarizes mission performance and expected mission score with M2 net income is 2354 - 420 = 1934.

Table 28. Simulated Mission Performance in Average Wichita Wind (14.5 mph, 6.5 m/s)

Metric	M1	M2	M3	M3 (29.1 mph, 13 m/s)	GM
Payload	-	144 passengers 1 cargo	196 × 39 in (5 × 1 m)	79 × 16 in (2 × 0.4 m)	-
m_{TO}	13.9 lbm (6.29 kg)	20.6 lbm (9.33 kg)	16.0 lbm (7.24 kg)	15.8 lbm (7.16 kg)	-
Cruise Throttle	90%	90%	60%	80%	-
V_{cruise}	76.1 ft/s (23.2 m/s)	65.6 ft/s (20.0 m/s)	46.6 ft/s (14.2 m/s)	63.6 ft/s (19.4 m/s)	-
V_{stall}	31.0 ft/s (9.45 m/s)	37.6 ft/s (11.5 m/s)	33.1 ft/s (10.1 m/s)	33.1 ft/s (10.1 m/s)	-
Battery Usage	24%	73%	69%	71%	-
n_{laps} & Time	3 laps in 130 s	5 in 290 s	2 laps in 174 s	2 laps in 176 s	426 s
Score	1.00	1.84	2.47	2.19	0.07

5.6 Drawing Package

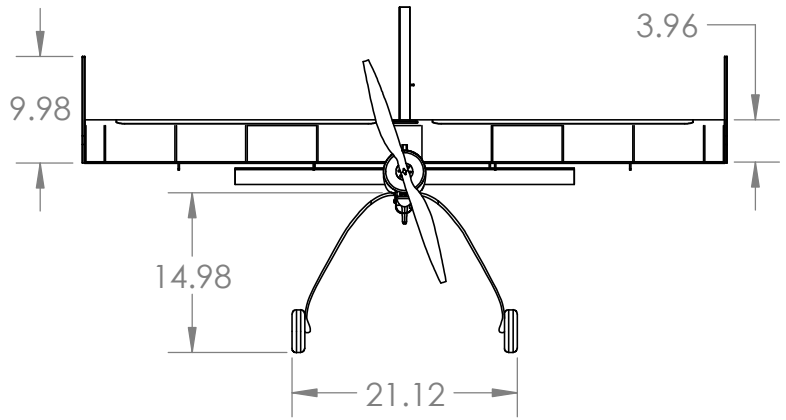

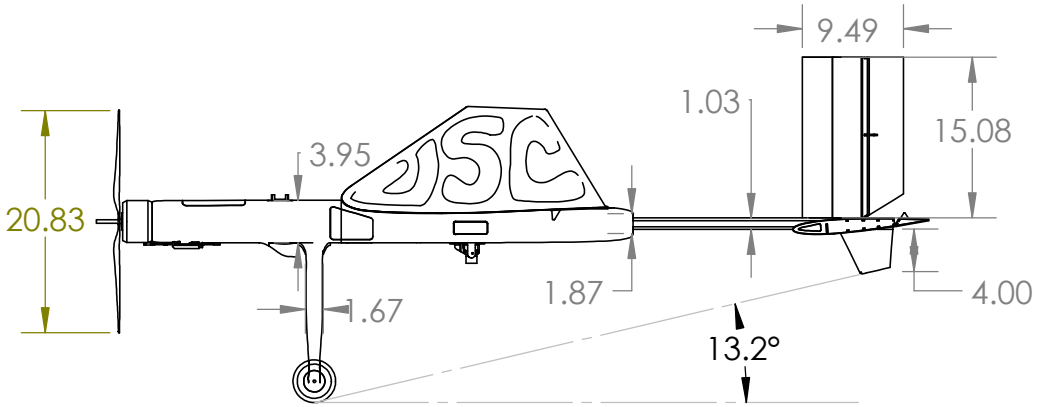

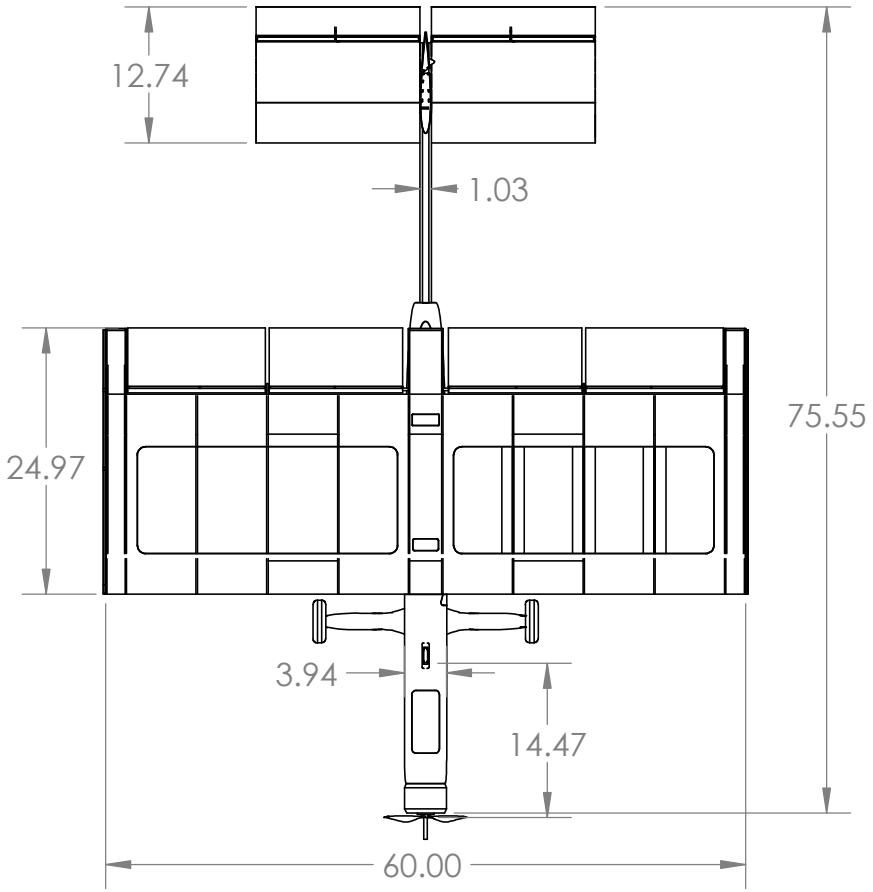

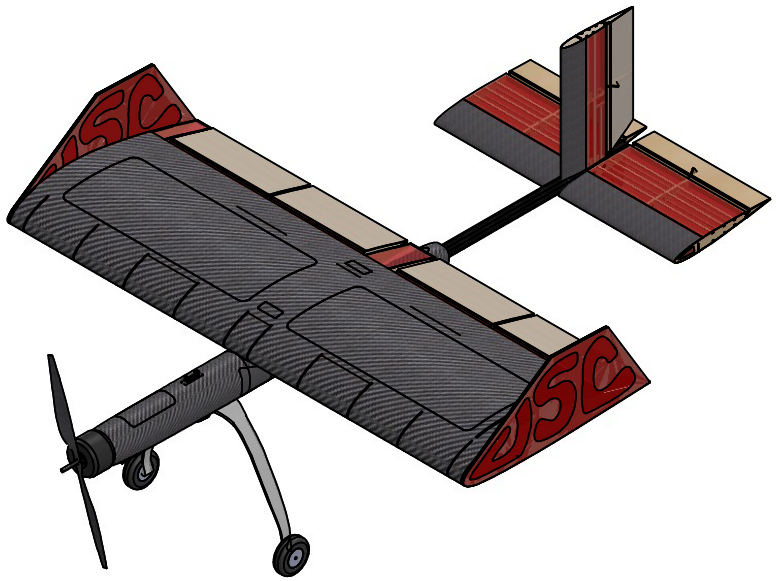

UNIVERSITY OF SOUTHERN CALIFORNIA AERODESIGN TEAM		
UNLESS OTHERWISE SPECIFIED: DIMENSIONS IN INCHES		
SIZE A	DWG. NO. Aircraft 3 - View	REV 1
SCALE: 1:18	DRAWING PACKAGE	SHEET 1 OF 4

NO.	PART NAME	DESCRIPTION	QTY
1	Wing Spars	1/8" Balsa, 1/16" Ply	3
2	Wing Ribs	1/8" Balsa	12
3	Wing Bottom Skin	Solite, 3/16" Balsa Stringers	1
4	Passenger Hatch	±45° CF, XPS Foam	2
5	Wing LE & Top Skin	±45° CF	1
6	Flap & Aileron Skin	1/16" Balsa, Solite	4
7	Flap & Aileron Ribs	1/8" Balsa, 1/8" Plywood	12
8	Hinging Dowel	1/4" Plywood	1
9	Wing Endplate	1/8" Balsa, Solite	2
10	Passenger Floor	1/16" Balsa	1
11	Passenger Floor Reinforcement	±45° CF	1
12	Boom	CF	1
17	Tail LE Skin	±45° CF	3
14	V-Stab Ribs	1/8" Balsa, 1/16" Plywood	3
15	Tailskid	TPU, PLA	1
16	Tail Integration Bolts	M4 Nylon	4
17	Tail Skin	Solite, 3/16" Balsa Stringers	1
18	Tail Integration Rod	CF	1
19	H-Stab Ribs	1/8" Balsa, 1/16" Plywood	6
20	Motor Mount	1/8" Plywood	1
21	Fuselage Formers	1/8" Balsa, 1/16" Plywood	8
22	MLG Hardpoint	1/4" Plywood	1
23	Wing Hardpoint	1/4" Plywood	2
24	Wing Integration Bolts	1/4" - 20 Nylon	4
25	Boom Integration	1/8" Balsa, 1/16" Plywood	3

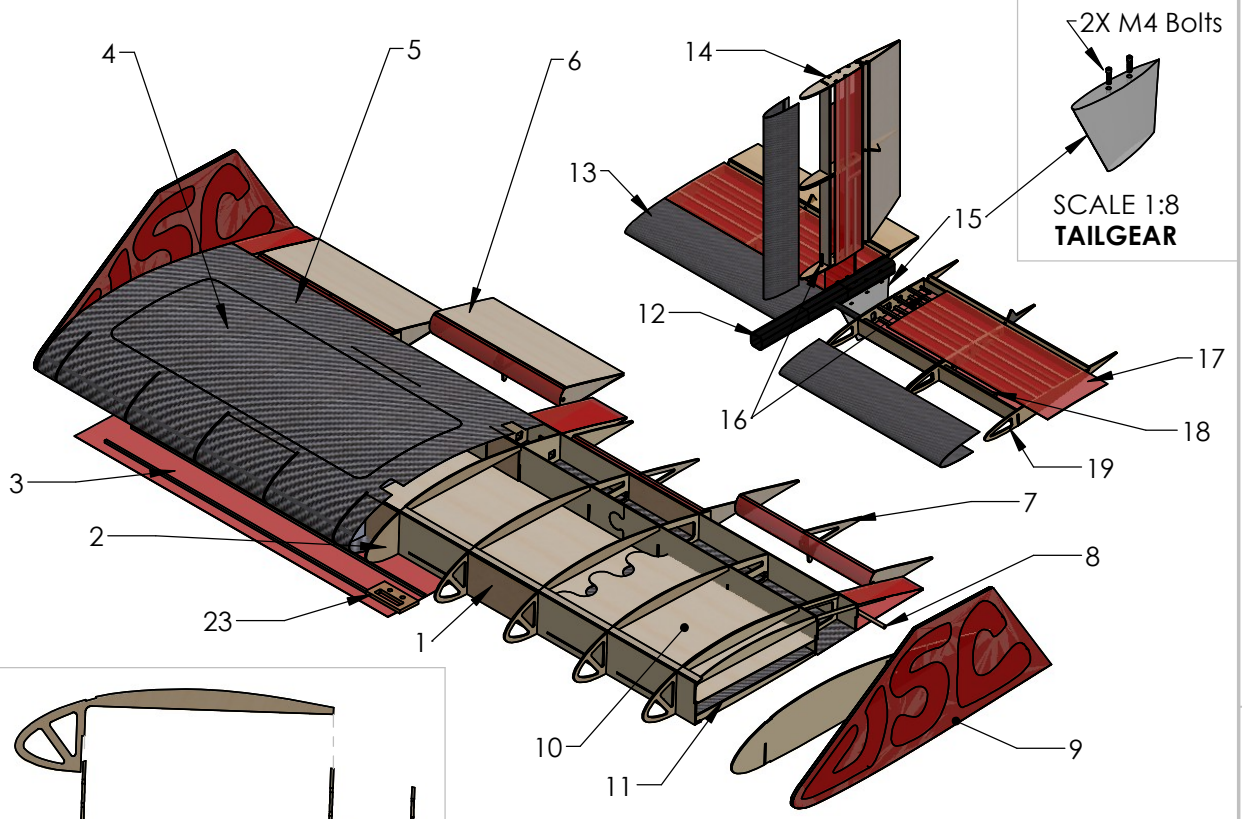

SCALE 1:8
TAILGEAR

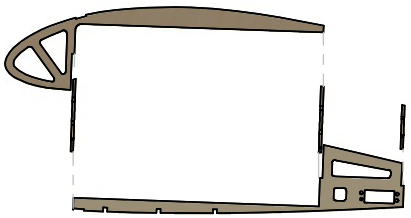

WING RIB TO SPAR INTEGRATION
SCALE 1:9

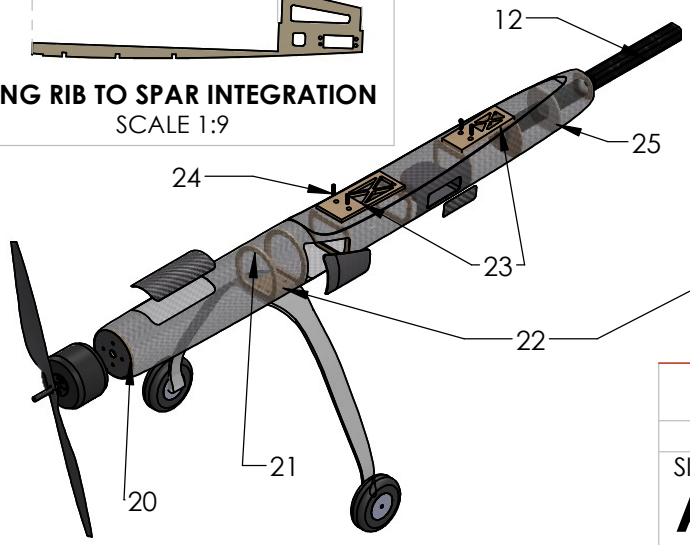

SCALE 1:10

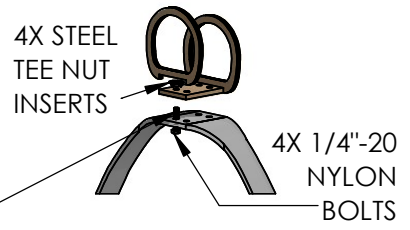

LANDING GEAR INTEGRATION

UNIVERSITY OF SOUTHERN CALIFORNIA
AERODESIGN TEAM

UNLESS OTHERWISE SPECIFIED: DIMENSIONS IN INCHES

SIZE	DWG. NO.	REV
A	Structural Layout	1

SCALE: 1:13	DRAWING PACKAGE	SHEET 2 OF 4

Propulsion Electronics			
NO.	ITEM (QTY.)	M1/M2 DESCRIPTION	M3 DESCRIPTION
1	Propeller (1)	APC 20x15E	APC 22x12E
2	Motor (1)	T-Motor AT8030 160KV	
3	Battery (1)	Thunder Power 8S 3300mAh	MaxAmps 13S 2000mAh
4	ESC (1)	KDE-UAS85UVC 85A+UHV	
5	Fuse (1)	100A	60A

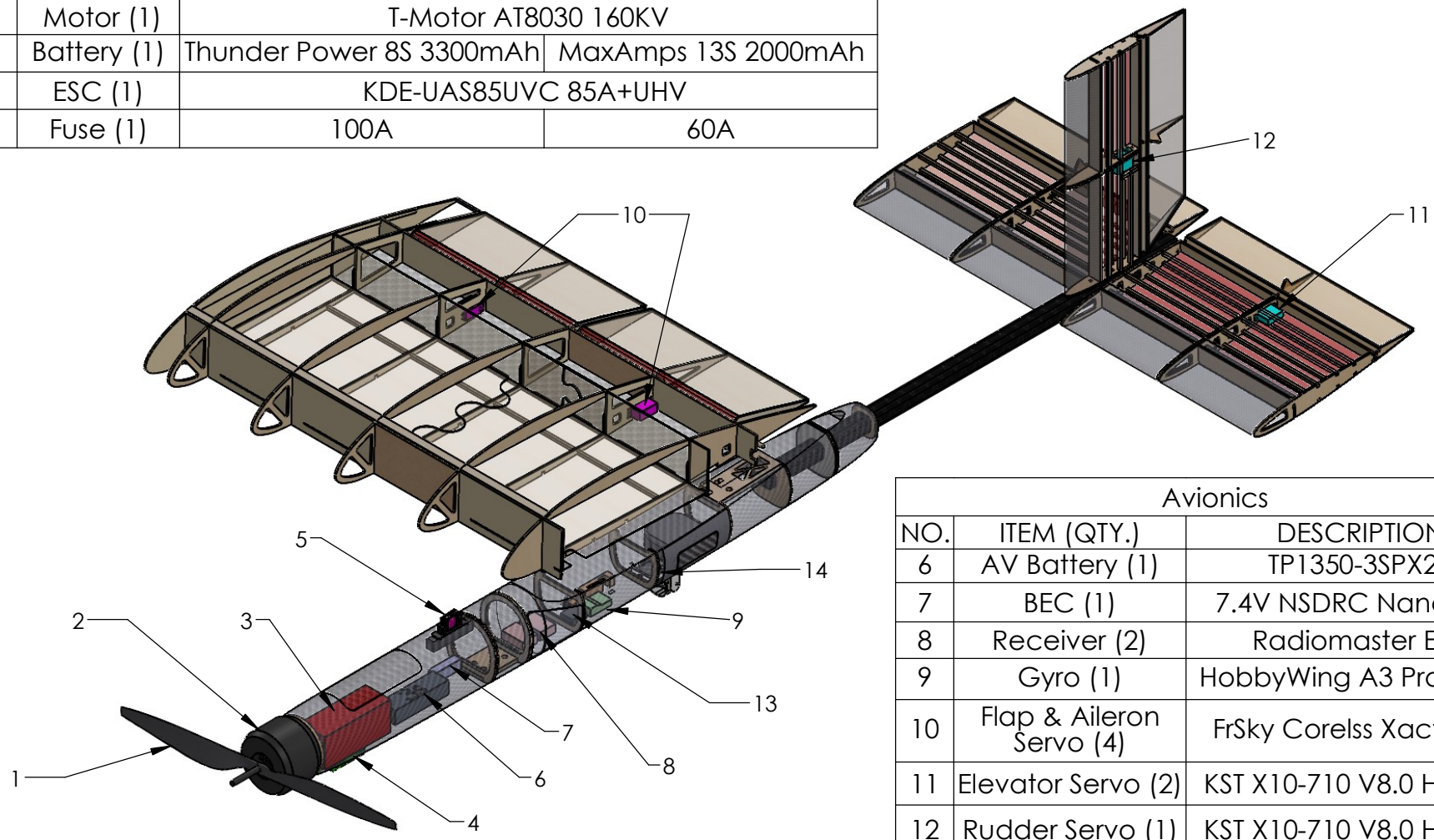

Avionics		
NO.	ITEM (QTY.)	DESCRIPTION
6	AV Battery (1)	TP1350-3SPX25
7	BEC (1)	7.4V NSDRC Nano Bec
8	Receiver (2)	Radiomaster ER8
9	Gyro (1)	HobbyWing A3 Pro 6-Axis
10	Flap & Aileron Servo (4)	FrSky Corelss Xact 5300
11	Elevator Servo (2)	KST X10-710 V8.0 HV Mini
12	Rudder Servo (1)	KST X10-710 V8.0 HV Mini

Payload Electronics		
NO.	ITEM (QTY.)	DESCRIPTION
13	Banner Release Servo (1)	JX PS-1171MG
14	Banner Deploy Servo (1)	JX PS-1171MG

UNIVERSITY OF SOUTHERN CALIFORNIA
AERODESIGN TEAM

UNLESS OTHERWISE SPECIFIED: DIMENSIONS IN INCHES

SIZE	DWG. NO.	REV
A	Systems Overview	1

SCALE: 1:9 | DRAWING PACKAGE | SHEET 3 OF 4

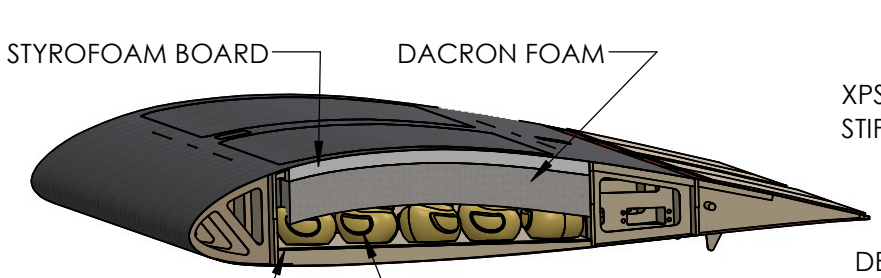

PASSENGER COMPARTMENT

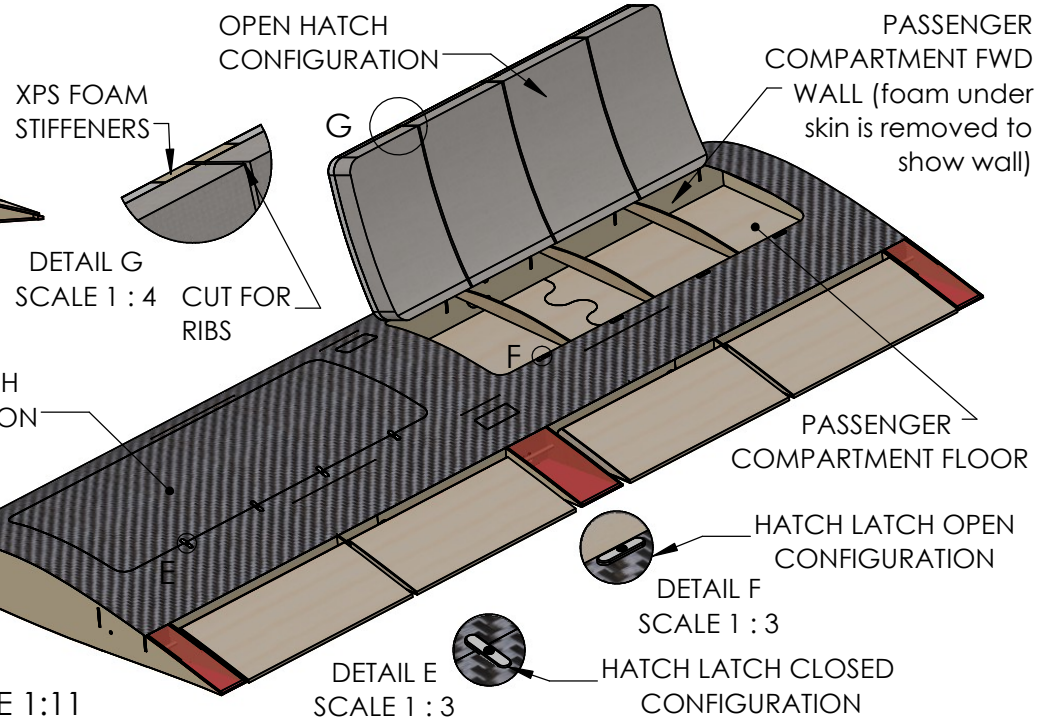

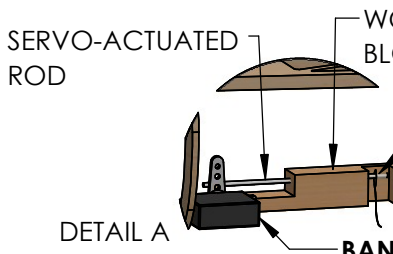

BANNER RELEASE MECHANISM

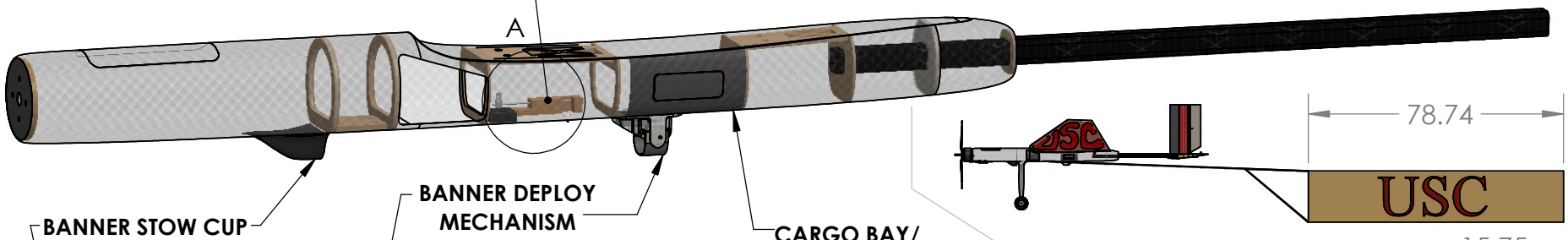

BANNER IN FLIGHT
SCALE 1:50

SCALE 1:4

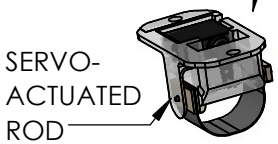

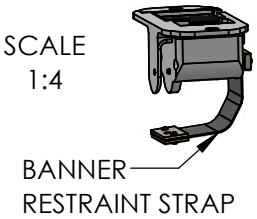

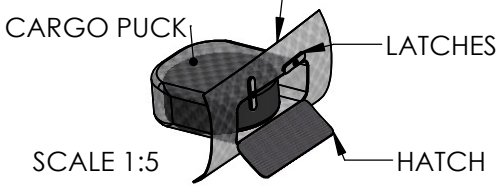

UNIVERSITY OF SOUTHERN CALIFORNIA AERODESIGN TEAM		
UNLESS OTHERWISE SPECIFIED: DIMENSIONS IN INCHES		
SIZE A	DWG. NO. Payload Systems	REV 1
SCALE: 1:7	DRAWING PACKAGE	SHEET 4 OF 4

6.0 Manufacturing Plan

6.1 Manufacturing Processes Investigated

Several manufacturing processes were evaluated for aircraft components and mission-specific payload elements.

6.1.1 Hotwire CNC: A 2-axis CNC hotwire operated with a GRBL Hotwire Controller, an open-source G-code firmware, and Arduino CNC Foam Cutters, produce complex foam geometries, otherwise difficult to cut by hand. However, the lack of a third axis limits it to 2D profiles, such as airfoils, to create molds for composite layups.

6.1.2 3D Printing: 3D printing offers a simple method of producing complex shapes with replicability. However, these components have low strength-to-weight ratios and do not allow load-path optimization. Thus, 3D printing was preferred for smaller elements. A 3D printing access allows rapid production of molds versus CNC machining.

6.1.3 Molded Composites: Composites have high stiffness, strength-to-weight ratios, and part reproducibility when using molds but at a high material cost, mold preparation complexity, and long manufacturing time. Therefore, composites are reserved for lightweight components that require precise curvature and strength.

6.1.4 Balsa-Plywood Build Up: Structures built using balsa and plywood components with cyanoacrylate (CA) adhesive are often lighter than equivalent monocoque composite and foam-core components. Strategically placed plywood parts reinforce structures in areas requiring strength, optimizing weight through specific load paths. With access to CAD and laser cutting manufacturing time is greatly reduced, and precision increased.

6.1.5 Steam Bending: A lightweight solution to manufacture components with unique geometry. Combined with built-up structures or composites, it allows for reinforcement but weakens wood and produces residual stresses.

6.1.6 Foam Core: Extruded polystyrene (XPS) foam is affordable. It can be precisely cut with a CNC hotwire, allowing rapid fabrication of curved components. Fiberglass layups over the foam create smooth surfaces and strengthen components, but with a lower strength-to-weight ratio versus molded composites and built-up methods.

6.2 Manufacturing Processes Selected

Table 29. Material Downselect

		Material		
Criteria	**Factor**	**Composite**	**Balsa & Plywood**	**Foam core**
Mass	0.5	0	1	-1
Surface Finish	0.3	1	-1	0
Durability	0.2	0	-1	1
	Total	0.3	0	-0.3

Table 30. Manufacturing Processes Downselect

		Method			
Criteria	**Factor**	**Steam Bending**	**Laser Cutting**	**CNC**	**3D Printing**
Experience	0.5	0	1	-1	1
Time & Availability	0.3	0	1	-1	1
Cost	0.2	0	1	0	-1
	Total	0	1	-0.8	0.6

Manufacturing materials and processes were selected using weighted criteria. Materials selection prioritized mass, the most sensitive parameter (Sec. 3.2.3). Other considerations included the ability to produce a low-drag surface finish and provide sufficient durability for repeated flight and ground handling. These criteria were weighted, as shown in Table 29 and applied to candidate material groups. Manufacturing process selection was weighted based on team experience, schedule availability, and cost (Table 30). Processes familiar to the team were favored to reduce manufacturing risk. This process led to the use of composite skins with balsa and plywood members for the fuselage, wing, and empennage providing a balance of low weight, surface quality, and durability. Laser cutting was selected for wooden structural components, given its availability. Foam molds were CNC hotwired to minimize manufacturing time. 3D printing was favored for payloads components given its availability. Foam-core components were used for rapid manufacturing of prototypes.

6.2.1 Fuselage

The fuselage is a semi-monocoque carbon-fiber (CF) composite skin with a COTS 1.00 × 1.08 × 66.0-in square intermediate modulus CF boom with a rigid shell molded to the outer mold line (OML). A female mold of each half was 3D printed from polylactic acid (PLA) filament and was assembled. Both molds were sanded and primed with two coats of SEM Primer. Next, 3-5 layers of Partall mold-release wax were applied and buffed. The molds were sprayed with 2-3 layers of Fibre Glast polyvinyl alcohol (PVA) release film. Once dry, a wet layup with 12-hr epoxy was performed using 5.7-oz/yd^2 (193-g/m^2) 3k twill-weave CF plies in [±45/0-90]° orientations and an insulating layer of 5.7-oz/yd^2 (193-g/m^2) 3k plain weave fiberglass placed in the nosecone. The layup was placed under full vacuum pressure at room temperature to cure, after which the laminates were removed. 1/8-in plywood formers and 1/4-in plywood hardpoints were bonded using 5-min epoxy to one half of the fuselage. The tail-boom was bonded into three formers at the aft end of the fuselage. The other half was bonded to the exposed formers using 15-min epoxy. The two halves were sealed with 1-in (2.5-cm) strips of [±45]° 5.7-oz/yd^2 (193-g/m^2) CF under vacuum pressure over the seam. The complete build is depicted in Fig. 55.

Figure 55. Fuselage build.

6.2.2 Wing

The wing structure was constructed using semi-monocoque and built-up methods. To layup the CF top skin, female wing molds were created from XPS foam and cut using a hotwire CNC. Molds were prepared by covering the sides with packing tape and laying a sheet of 0.010-in Mylar against the foam, taping one edge to prevent warping during the layup. The mold enclosed the top surface of the airfoil, D-box, and a portion of the bottom surface up to 13% of the chord. The top skin was manufactured using a wet layup of 5.7-oz/yd^2 (193-g/m^2) 3k twill-weave CF fabric in a [±45]° orientation and was bonded to the laser-cut rib-and-spar assembly. The ribs were cut from 1/8-in balsa and plywood, and were bonded to the spars using CA. The wing floor was constructed of 1/16-in balsa and laid up with one ply of [0/90]° 5.7-oz/yd^2 (193-g/m^2) 3k twill-weave CF. The bottom skin was constructed using 3/16-in square balsa stringers and covered with Solite. The ailerons and flaps were built-up with a laser-cut rib structure of 1/16-in plywood and 1/8-in balsa. They were hinged to the wing using a 1/4-in maple dowel. Each control surface was skinned with Solite.

Figure 56. Wing spar-rib structure.

6.2.3 Empennage

The horizontal and vertical stabilizers were of built-up construction with a CF D-box. Similar to the wing, the D-box female molds were made with 1.75 lb/ft^3 (29.03 kg/m^3) XPS foam and cut with a hotwire CNC covering the leading edge up to 30% chord. A wet layup of one ply of 5.7-oz/yd^2 (193-g/m^2) 3k twill-weave CF was laid up inside the molds. Once cured, the D-boxes were adhered with 15-min epoxy to the leading edge of the spar-rib structures. 3/16-in balsa stringers were adhered with CA to the spar-rib structures to support the Solite skin.

6.2.4 Landing Gear

The main landing gear bow is manufactured in-house by a wet layup process. Slow cure epoxy was used to wet 38 plies of unidirectional S-glass. The layup was cured under 12 psi (82.7 kPa) of pressure for 16 hours. Once cured, the bow was trimmed and sanded to size. Integration holes were drilled and the wheels were mounted. The tailskid was integrated to the end of the boom via two M4 bolts.

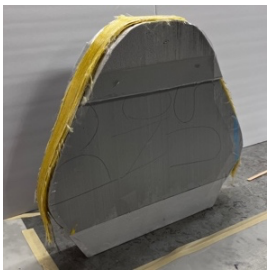

Figure 57. Landing gear layup.

6.2.5 Payload

6.2.5.1 Passengers & Cargo

The two passenger hatches are cut from the cured top wing skin following the wing layup in Sec. 6.2.2. A hand-hotwired 0.5-in thick sheet of 0.07-lbm/ft^2 (342-g/m^2) Styrofoam was bonded to the inner surface of the hatch using CA. A 2-in (5.08 cm) layer of Dacron foam was bonded to the Styrofoam to create the passenger restraint system. Both wing hatches were hinged using nylon hinges adhered to the inner surface and front spar caps. Each hatch was latched shut using four rotating servo arms. Each servo arm was bolted from the underside of the fixed wing skin and reinforced with a 1/16-in plywood backing plate epoxied to the wing skin and forward face of the aft spar. The cargo housing was 3D printed out of PLA with a wall thickness of 0.04 in (1 mm). It was bonded to the fuselage using 5-min epoxy resin.

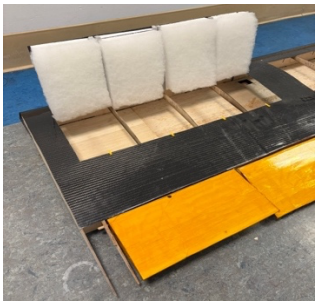

Figure 58. Passenger compartment and restraints.

Figure 59. 3D printed cargo housing.

6.2.5.2 Banner Deployment and Release

The retention cup and aft mechanism housing were 3D printed for easy interfacing with the elastic band, servo, and fasteners. The forward retention cup was printed with 0.04 in (1 mm) PLA wall. A 2.5 × 3 in (6.4 × 7.6 cm) strip of female Velcro was adhered to the top surface of the retention cup using 5-min epoxy.

The aft mechanism housing was 3D printed with variable wall thickness to restrain a 0.04 lbm, 3.04 lbm-in (17 g, 3.5 kg-cm) servo motor and transfer all loads to the fuselage via two quarter-turn fasteners. Cutouts were designed into the PLA housing for the servo motor, and two M3 bolts sandwich the elastic band between a 2.5 × 0.75 in (6.35 × 1.91 cm) piece of 1/8-in plywood. The banner release mechanism consists of a 0.04 lbm, 3.04 lbf-in (17 g, 3.5 kg-cm) servo motor, 1/32-in steel rod, and balsa support block. Two cutouts were drilled into the balsa block: a channel sized to the diameter of the steel rod and a slot to allow for banner towline attachment, shown in Fig. 61. The steel rod was installed through the balsa block and attached to the servo arm. The banner-release servo and the balsa support block were bonded to the fuselage floor using 5-min epoxy.

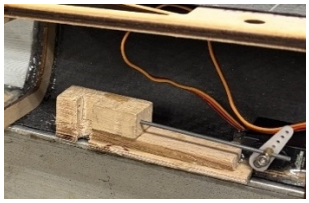

Figure 60. Deployment and release mechanisms.

Figure 61. Tissue Lamé banner with the airfoil leading edge rod and split ring attached.

6.2.5.3 Banner

The fabric edges are heat-sealed to prevent fraying. The leading edge of the banner was folded and sewn to form a pocket for the leading-edge rod. A hole was drilled approximately 0.5 in (1.27 cm) from each end of the aluminum

rod to allow for a 1-in-diameter split ring to pass through the rod and banner material, preventing the banner from slipping down the leading-edge rod. All towlines were tied using Palomar knots.

6.3 Manufacturing Milestones / Timeline

A manufacturing plan was created to guide the team schedule and allot enough time and resources to build each subcomponent. Roughly two weeks have been allocated to build each aircraft version. Figure 62 shows the planned schedule for Version 2 (V2), where the red vertical line indicates the current week of the design cycle. This timeline will remain the same for the final competition aircraft, with additional days allocated for unforeseen delays and spare-part manufacturing.

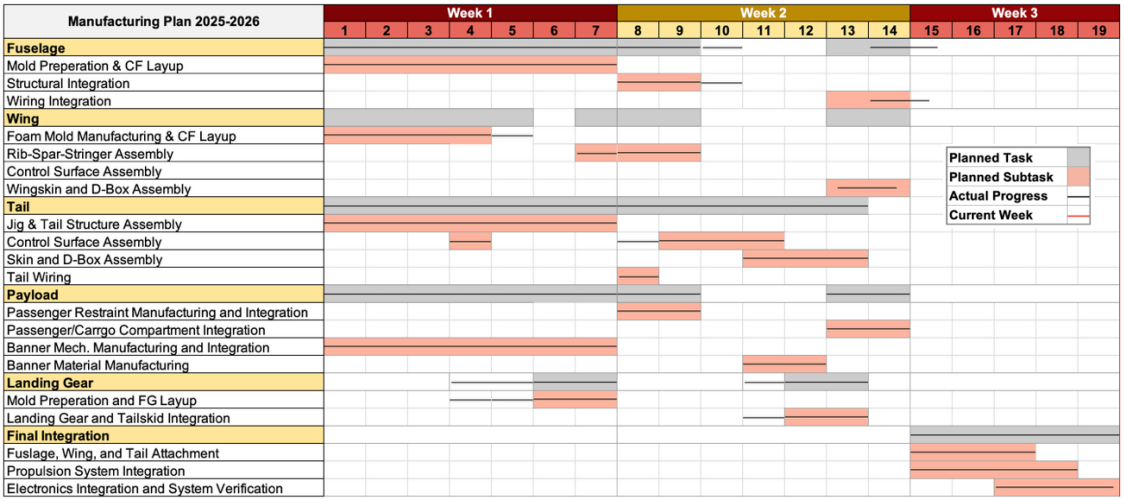

Figure 62. Manufacturing plan for Version 2.

7 Testing Plan

The following testing plan verified structures, payloads, propulsion, and flight decisions. Experimental data was collected by the team in laboratory and flight testing. Aerostructures, payloads, and landing gear testing simulated ground, flight, and landing loads to verify strength and reliability. Ground mission (GM) simulations, banner drag characterization, banner deploy and release mechanism, and banner handling qualities tests validated payloads decisions. Lastly, in-flight stall and cruise testing assessed aerodynamic and propulsion performance to aid in mission score prediction. Testing began during Preliminary Design and continued into subsequent phases.

7.1 Testing Schedule

The testing schedule is presented in Fig. 63 and is further detailed in Sec 7.4.

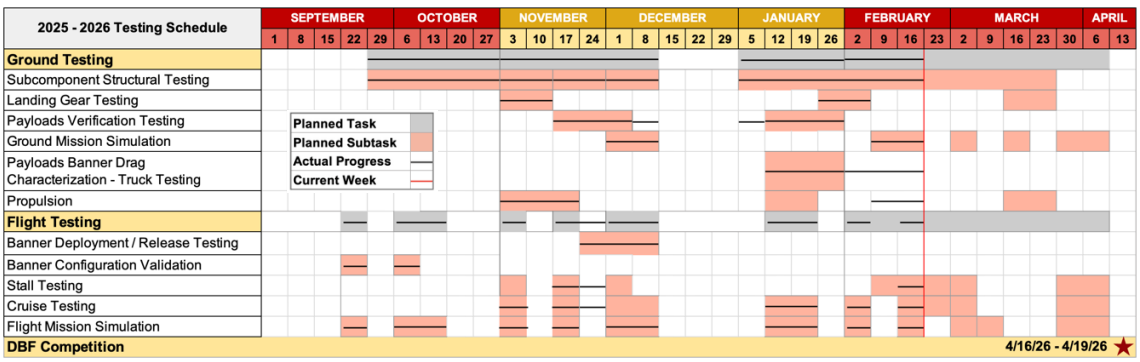

Figure 63. Subsystem and flight-testing schedule.

7.2 Subsystem Testing - Ground Testing

Subsystem testing was performed to verify compliance with all aircraft requirements in Sec. 3.2. Individual components were prototyped for standalone testing, then sub-assemblies for structural testing, and subsequently the integrated aircraft for aircraft-level structural and performance testing. Table 31 shows a general ground test checklist used to ensure safe and effective execution.

Table 31. Ground Testing Checklist

Pre-Test	
Test Objective	Defined
Test Procedure	Reviewed
Fixtures & Tools	Prepared
Test Component	Inspected
Fasteners & Latches	Secured
Sensors	Installed
DAQ	Logging
Safety Brief	Complete
Post-Test	
Damage Inspection	Completed
Data Logs	Saved
Pass/Fail	Evaluated
Results Notes	Documented

7.2.1 Wing Static Load Testing

An up-bend test was conducted on the wing structure to verify that it would survive limit aerodynamic and inertial loads from a 3.4-G coordinated turn. The wing was bolted to a Douglas fir wood 2 × 4 in (5 × 10 cm) at the hardpoints to simulate the clamped fuselage joint and suspended upside-down (Fig. 64). Masses were applied according to Table 32. These were the equivalent point forces required to match the maximum shear force and bending moment transferred through the hardpoint. Both leading and trailing edge deflections were measured. Success was defined as the lack of plastic deformation, fracture, or buckling.

Table 32. Wing up-bend test matrix.

Configuration	Mass Applied [lbm]	
	33% Semispan	67% Semispan
1	10.2	0
2	10.2	6.56

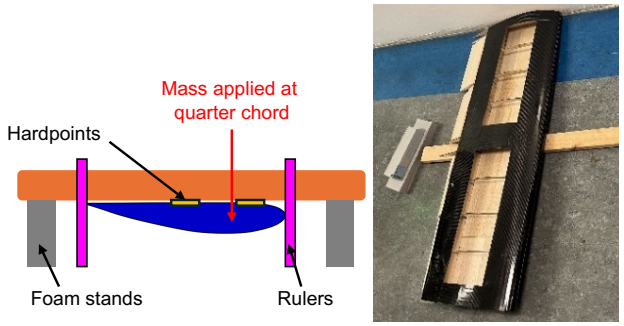

Figure 64. (Left) Side view of wing up-bend test setup. (Right) Top view of wing attached to 2x4 in.

7.2.2 Control Surface Load Testing

Aircraft control surfaces were load tested to verify the strength of the servo and control geometry under maximum load. For each, hinge moment at full deflection was calculated in AVL with an additional factor of safety (FoS) of 1.4 [6]. These loads were applied to each control surface with metal bars at a specified moment arm relative to the hinge axis generating equivalent hinge moments.

7.2.3 Landing Gear

The landing gear underwent static, dynamic, and ground roll testing to validate its performance. Static loading was done by placing weights on the gear. Using a skateboard under one strut and a support to keep the bow level on the other, weights were added in increments of 7 lbm (3.18 kg) until the expected maximum load of 42 lbf (190 N) was achieved. Then, the gear was integrated onto the aircraft at MTOW and dropped from 2 in (5.1 cm) to replicate a worst-case sink rate of 3.12 ft/s (1 m/s). Ground roll testing was then conducted by pushing the aircraft forward from rest in each mission configuration to verify tracking.

7.2.4 Payload - Subcomponents

7.2.4.1 Passenger Restraints

The passenger restraint system was tested on a wing testbed to assess the validity of the Dacron restraint (Fig. 65). Passengers were intentionally spaced in the compartment to visualize the effects of lateral and vertical

acceleration. Their initial positions were marked, and the wing hatch was closed. 8 Gs of lateral and vertical acceleration were applied by shaking the test bed, measured with accelerometers in a smartphone. The target acceleration was derived by finding the maximum acceleration of every flight test with a FoS of 1.5. After testing, the passengers' final locations were recorded, and the test was considered successful if no measurable passenger displacement occurred.

Figure 65. Passenger restraint testing.

7.2.4.2 Banner Deployment and Release

The banner deployment was tested on a fuselage testbed to verify reliability under static conditions (Fig. 66). The testbed was inclined incrementally from 0º to 90° with respect to the horizontal to simulate various pitch angles. A successful test was assessed on a binary scale, with any extra effort required to deploy the banner constitute a failure. The banner-release mechanism was tested to verify reliability under expected in-flight loads. The mechanism, detailed in Sec. 5.3.5.2, was clamped to a fixed surface, with the towline threaded onto the servo-actuated steel rod. Once in the closed position, a load of 12.4 lbf (55 N), a FoS of 2 above the expected banner drag, was applied at a simulated tow angle. The release servo was actuated when both angle and force conditions were met. The test was successful if the banner towline ejected.

Figure 66. Banner deployment testing

7.2.4.3 Ground Mission and Staging Simulation

Ground mission (GM) testing was completed on the full-scale aircraft to improve estimated GM score and staging time. Each GM segment was attempted 5 times and video recorded to pinpoint areas for improvement. To incorporate staging, an additional segment was completed, where the ground crew member installed the propulsion battery and 100-A fuse. Static margin and gyroscopic response were demonstrated. The sum of the corresponding GM segment and additional staging segment times was the final staging time. A staging run was deemed successful if completed within 5 minutes. Times for each segment were extracted from video recordings.

7.2.4.4 Banner - Material Truck Testing

Banner testing aimed to quantify the C_D of each banner material and leading-edge (LE) device to determine the best banner. Banner testing was conducted using a wooden rig secured to the hooks on a pickup truck with ratchet straps, shown in Fig. 67. A CF rod was attached to the rig to extend the height such that the rig was 11 ft (3.35 m) above the ground to ensure the banner was outside of the wake of the truck, as determined from RANS CFD, shown in Fig. 68 [22]. A uniaxial load cell, rated with sufficient capacity for the expected 2.5 lbf (11 N) of drag using data from the team's 2020 DBF report [7], was tied to a hole at the top of the CF rod using braided fishing line. As the loadcell was in-line with the

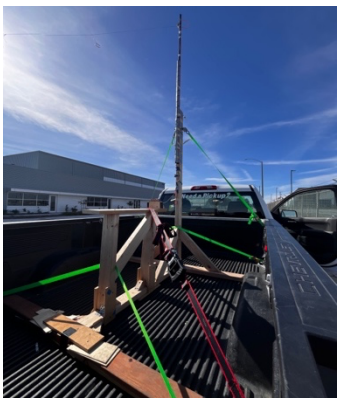

Figure 67. Testing rig secured to the truck bed.

towline, the banner drag was found with Eq. 49, where m_{banner} is the mass of the banner and the leading-edge rod and F_D is the banner drag.

$$F_D = \sqrt{F_{\text{measured}}{}^2 - (m_{\text{banner}}\, g)^2} \qquad \text{Eq. 49}$$

A pitot tube, mounted 3 ft (0.9 m) above the truck bed, allowed for force data to be paired with measured airspeed. Time stamps, calibrated force, and airspeed were logged throughout testing. To match the expected Reynolds number of the banner, Re_b, for the 16.4-ft (5-m) banner ($Re_b = 5\times10^6$), the vehicle accelerated from 0-35 mph (0-15.4 m/s), then held a speed of 35-45 mph (16-20 m/s). Testing was conducted on a straight road with a usable distance of 0.37 mi (600 m) next to Long Beach Airport. The checklist shown in Table 33 was used to ensure proper testing practices.

Table 33. Banner truck testing checklist

Pre-test	
Banner Test Rig	Secured
Banner Material	Recorded
Wind Conditions	Recorded
Banner Test	
Road Clear	Clear
DAQ	Start
Accelerate	To Target Speed
Abort	If Required
Decelerate	To Complete Stop
DAQ	End and Save
Banner	Check Damage

7.2.5 Propulsion

Propulsion testing consisted of endurance testing and measuring thrust and torque during a simulated takeoff. Using a Tyto Robotics 1780 thrust stand [23] equipped with a current sensor and load cell, the selected battery, ESC, motor, and propeller for each mission were mounted, as shown in Fig. 69. Using an open-source RCbenchmark software [24], thrust, torque, current, and voltage were recorded. The motor endurance was then tested by running it at 20 A for 6 min, longer than any mission success window. The expected structural load during takeoff is measured by increasing the throttle to 100% in less than 2 sec to measure the torque and static thrust under takeoff conditions.

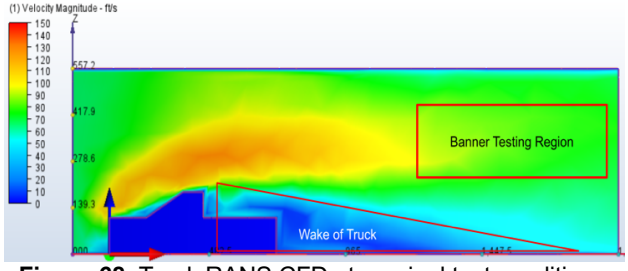

Figure 68. Truck RANS CFD at nominal test conditions, with banner test region indicated.

7.3 Flight Testing

Flight testing validated and improved the aircraft design. Quantitative and qualitative data was collected for each flight. All aircraft iterations undergo multiple flight tests following ground testing, with defined objectives and plans for each flight.

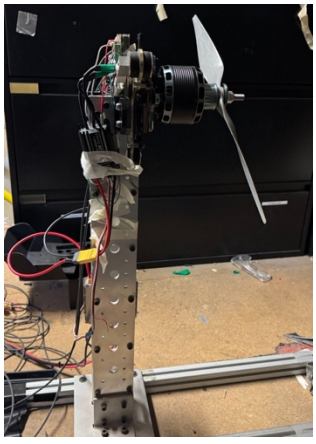

Figure 69. Propulsion unit mounted on a thrust stand.

7.3.1 Data Collection

Data from flight testing was gathered from numerous sources. Performance data was collected via the DAQ system in Sec. 5.3.7. In addition to the external sensors onboard, the CubePilot Orange flight controller (FC) includes three inertial measurement units (IMU), a barometer, and a magnetometer. Propulsion performance data such as RPM, voltage, current, and throttle are logged on the ESC and communicated to the FC via CAN protocol. The FC saves propulsion and sensor data such as throttle settings, servo outputs, airspeed, ground speed, altitude, acceleration, location, orientation, avionics battery voltage, and temperature. In addition to data logging, the telemetry radio installed on the aircraft transmits data to the ground station, Mission Planner. Finally, Walksnail

first-person-viewer (FPV) installed on the empennage, facing the nose of the aircraft transmits live video footage and metrics including ESC data, airspeed, groundspeed, throttle percentage, receiver signal strength indicator (RSSI), and climb and cruise efficiency to an additional ground station. The pilot provides qualitative feedback throughout on stability and handling characteristics.

7.3.2 Flight Checklist

To ensure safety and collection of data, the checklist in Table 34-35 and Fig. 70 was used before each flight test.

Table 34: Preflight Checklist

Aircraft Assembly
Trojan HorSCe …….. Airworthy
Propulsion ……..…… Secure
Avionics ……..…….. Secure
Final Exterior
Weight and Balance ……. Check
AV and Prop. Hatch ... Secure
Avionics
Batteries..... Charged
Controls ..…… Correct
Failsafe …….. Check
RSSI ……..…….. Check
Aircraft Payload
Banner ……..…….. Secure
Passengers..…..…. Secure
Cargo ……..…….. Secure
Banner Release..... Check
Passenger Hatch…. Secure

Table 35: Flight Line Checklist

Before Takeoff
Flight Plan……..…. Verify
Pilot Go/No-Go ……..…. GO
Transmitter ….. Verify Charge
Controls ….. Free and Correct
Flaps……..…….. Takeoff
Arming Fuse……..…….. Armed
Throttle Cut ……. ……... Armed
Runway …. …….. Clear
Before Landing
Runway ……..…….. Clear
Flaps ……..…….. Landing
After Landing
Throttle Cut ……..…… Cut
Arming Fuse …….. Disarmed
Arming Fuse……..…Disarmed
Post Flight
Debrief …….. Complete

7.3.3 Flight Testing Procedures

Multiple flight test procedures were developed to validate the aircraft in all mission configurations, quantify key characteristics, compare achieved performance to predictions, and practice lap strategy. Autopilot capabilities were used during selected tests to minimize the uncertainties caused by manual flying and wind disturbances.

7.3.3.1 Banner Configuration Validation Flights

Flight testing validated banner towline length, location, release, and deployment. For towline length testing, banners with 10.5-ft (3.20-m) and 30-ft (9.14-m) towlines were stowed and deployed in-flight after the first 180° turn. Full M3 flights were attempted. Towline location was validated at the aircraft CG and empennage. The banner was released following each test. Pilot feedback was recorded and assessed before, during, and post-flight.

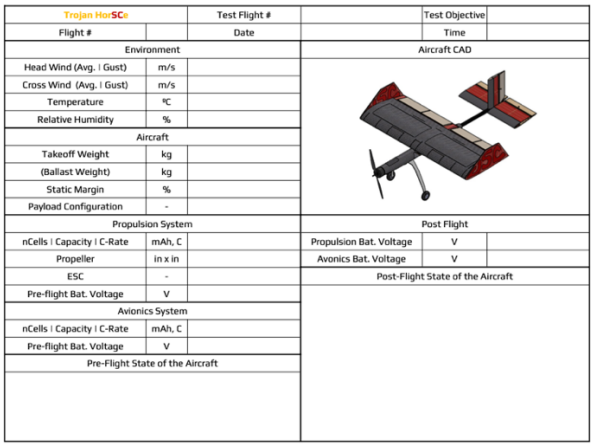

Figure 70. Checklist and DAQ chart of V2 aircraft.

7.3.3.2 Low Speed Handling and Stall Testing

Flight testing aimed to understand the aircraft's low-speed handling qualities (HQ) and experimentally find the trimmed 3D $C_{L,\max}$. This was determined through unpowered stall tests inspired by CFR Part 23 Section 23.2110 (Table 36) [25]. Stall was identified by an uncommanded pitch down of the aircraft or 5 sec of maximum elevator deflection. The time-trace of Eq. 50 was used to find the $C_{L,\max}$.

$$C_{L,\max} = \frac{n\,W}{0.5\;V_{\text{stall}}{}^{2}\;\rho\;S_{\text{ref}}}\,, \qquad \text{Eq. 50}$$

where n is the load factor derived from IMU measurements, W is the aircraft weight, ρ is the air density derived from the temperature and humidity, S_{ref} is the reference wing area, and V_{stall} is the stall speed.

Table 36. Stall Test Checklist

Preflight
Aircraft Mass …… Recorded
Static Margin …… Recorded
Stall Maneuver
Airspace …… Clear
Altitude …… Safe Alt.
Flaps …… Desired Config.
Level Flight …… Achieved
Throttle ……... Gradually Idle
Constant Alt. …… Adjust Pitch
Stall …… Identify
Recover ……... Recover

Short tufts (braided fishing line) attached to the top surface of the wing visualized the flow separation during a stall maneuver. To record this, a Run-Cam was mounted to the end of the VT, while ensuring the aircraft achieved the desired SM. HQ as the aircraft approached stall and during recovery was recorded to identify qualitative areas of improvement.

Table 37. Cruise Test Checklist

Preflight
Aircraft Mass ..... Recorded
Static Margin ..... Recorded
Propeller ..... Recorded
Cruise Maneuver
Airspace ..... Clear
Altitude ..... Safe Alt.
Flaps ..... Retracted
Flight Mode ..... FBW-A
Throttle ..... Desired Setting
Terminal Velocity ..... Achieved
Flight Mode ..... Manual
Return to Test Area ..... Return

7.3.3.3 Cruise Testing

Cruise tests characterized the aircraft propulsion system in-flight. Using the recorded RPM from the ESC and airspeed from the pitot-static tube, the time trace of advance ratio J was found using Eq. 39. This was used to look up the propeller's coefficient of power C_P and coefficient of thrust C_T based on APC Propeller's performance [11] data to find dimensional thrust and power (using Eq. 36 and 38) as well as propeller efficiency η_{prop}. The total propulsion system chain efficiency η_{total} was found as the ratio of the thrust-power generated by the propeller and the ESC power output (Eq. 51). Therefore, the lumped efficiency of the motor, wiring, and ESC can be derived using the Eq. 52.

$$\eta_{\text{total}} = \frac{T\,V}{V_{\text{ESC}}\,I_{\text{ESC}}} \qquad \text{Eq. 51}$$

$$\eta_{\text{motor+wire+ESC}} = \frac{\eta_{\text{total}}}{\eta_{\text{prop}}} \qquad \text{Eq. 52}$$

For each test point, Fly-by-Wire A (FBW-A) stabilization mode, which automatically keeps aircraft roll and pitch level, was used to minimize errors caused by manual flying and wind disturbances. Throttle was set to a desired setting and kept constant until reaching terminal velocity. Then the aircraft was returned to the manual, unaugmented control of the pilot to execute a turn and set up for another test point.

7.4 Flight Test Plan

Flights using previous team aircraft quantitatively assessed HQ impacts of banner towing. These tests de-risked banner flights on *Trojan HorSCe* iterations and provided pilot training. The first *Trojan HorSCe* iteration, V1, served as a proof-of-concept demonstrator for the ducks-in-wing (DIW) concept and practice for data acquisition, processing, and testing procedures. V1 flight testing aimed to evaluate HQ with the DIW concept for M2, low-speed handling qualities at M3 cruise speed, conduct unpowered stall tests, and determine propulsion system efficiencies. M2 and M3 performance metrics were also compared between flight testing and PlaneTools (PT, Sec.

Table 38. Flight Test Schedule and Objectives at Santa Fe Recreational Area, Irwindale, CA

Date	Aircraft	Objectives
09/21/25 - 11/09/25	Previous ADT Aircraft	Investigate banner's impact (tow-location, tow-line length). Pilot practice flying consistent laps with banner.
11/24/25 - 02/08/26	V1	DIW Proof-of-Concept Investigate DIW impact on HQ Validate predicted metrics with stall and cruise testing
02/22/26 - 03/28/26*	V2	Practice competition laps to optimize fight path and identify improvements for V3.
04/05/26 - 04/13/26*	V3	Practice competition laps to optimize fight path and overall competition strategies.

* Tests are tentatively scheduled for listed dates.

Table 39. 01/25/2026 Flight Test Matrix w/ *Trojan HorSCe* V1

Flight	Objective	Configuration	Flight Plan
1	Trim Flight & Landing Practice	8S 3300 mAh APC 16x10E No Payloads	Lap 1: Takeoff, trim Lap 2: Trim, 360º turns Lap 3: Low runway approaches Lap 4-5: Touch and Go's Lap 6: Landing
2	Cruise Testing	12S 2000 mAh APC 20.5x14EPNC No Payloads	Lap 1: Takeoff, test FBW-A Lap 2-5: Cruise (Sec. 7.3.3.3) Lap 6: Landing
3	Stall Testing	8S 3300 mAh APC 18x8E No Payloads	Lap 1: Takeoff Lap 2-5: Stall (Sec. 7.3.3.2) Lap 6: Landing
4	Banner Testing	12S 2000 mAh APC 18x8E LDPE Banner	Lap 1: Takeoff Lap 2-4: Turns with varying radii Lap 5: Landing

4.2). V2 aims to ensure all sub-components work as intended in-flight, simulate GM, M1, M2, and M3 at USC, and further refine the models used in simulations, which will be used in competition strategy planning. Table 38 outlines *Trojan HorSCe's* flight test schedule and objectives. For each iteration, multiple flight tests were conducted until all planned tests were complete. Each flight test contains multiple flights, each with its own set of objectives. A representative flight test plan is shown in Table 39.

8 Performance Results

This section describes the results from ground and flight tests outlined in Sec. 7.

8.1 Demonstrated Performance from Subsystem Testing

8.1.1 Wing Static Load Testing

Following the test matrix in Table 32 from Sec. 7.2.1, the bending deflection at quarter chord $\delta_{c/4}$ and torsional deflection θ due to the applied masses were calculated using Eq. 53-54, where δ_{LE} and δ_{TE} are the deflections at the leading and trailing edges and c_{ref} is the reference chord. These values, along with the equivalent shear force and bending moment, are compared to expected values in Table 40.

$$\delta_{c/4} = \delta_{\mathrm{LE}} + 0.25(\delta_{\mathrm{TE}} - \delta_{\mathrm{LE}}) \quad \text{Eq. 53}$$

$$\theta = \tan^{-1}\left(\frac{\delta_{\mathrm{TE}} - \delta_{\mathrm{LE}}}{c_{\mathrm{ref}}}\right) \quad \text{Eq. 54}$$

8.1.2 Control Surface Load Testing

Control surface testing was conducted, as detailed in Sec. 7.2.2. A 7.4-V battery eliminator circuit (BEC) was used to power the control surface servos. As shown in Table 41, all control surfaces were able to sustain maximum deflection and actuate back to the zero-deflection state, indicating success.

Table 40. Wing Up-bend Test Results for Configuration 2

	Shear Force [lbf]	Bending Moment [lbf-ft]	Bending Deflection [in]	Torsional Deflection [deg]	PASS?
Tested	37.3	58.6	0.788	1.95	PASS
Expected	38.4	52.4	*0.0633	1.48	

* This underprediction is likely caused by an overprediction of balsa and carbon fiber stiffnesses.

Table 41. Control Surface Load Testing

Control Surface	Required Servo Torque [lbf-in]	Max. Tested Torque [lbf-in]	PASS?
Ailerons	9.13	9.23	PASS
Flaps	16.3	18.47	PASS
Elevators	3.58	4.92	PASS
Rudder	2.01	2.27	PASS

8.1.3 Landing Gear

Static load testing (Fig. 71) showed 1.5 in (3.8 cm) of deflection, meeting maximum load conditions. Post drop-test measurements showed the gear recovered to its 1-G loading condition with no delamination. Roll testing verified the aircraft tracked straight for 6 ft (1.82 m) and did not nose-over.

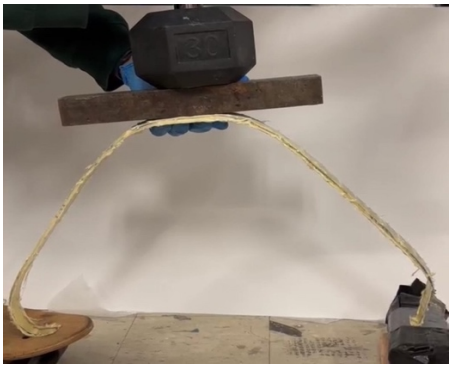

Figure 71. Gear loaded with 42 lbf.

8.1.4 Payload - Subcomponents

8.1.4.1 Passenger Restraints

Passenger restraint testing was conducted 10 times, as detailed in Sec. 7.2.4.3. Data showed a maximum of 8 Gs applied along all three axes. Visual inspection of the passenger compartment following each test showed no noticeable displacement.

8.1.4.2 Banner

Optimal banner towline length was determined through flight tests, discussed in Sec. 7.2.4.2. When flying competition laps, pilot feedback indicated that a short towline of 10.5 ft (3.2 m) was optimal for handling and maneuverability, especially during turns. The banner deployment and release mechanisms were primarily tested on the ground to validate design and build confidence through consistent execution. The deployment mechanism underwent 10 trials, with a 100% success rate across all pitch angles tested. The release mechanism was successful over 20 trials with at least 12.4 lbf (55 N) of force, performed according to Sec 7.2.4.2. Both the deploy and release mechanisms were flight tested twice on a trainer aircraft.

Figure 72. Banner deployment verification.

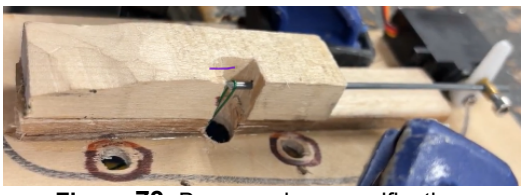

Figure 73. Banner release verification.

8.1.4.3 Ground Mission and Staging

Ground Mission was simulated five times, as detailed in Sec. 7.2.4.3. Individual segments were recorded for each trial, with averages displayed in Fig. 74. Across the trials, passenger packing strategy, the most time-consuming task, was improved. From Trial 1 to Trial 5, GM time decreased by 65 s, achieving a best total time of 426 s, giving a predicted score of 0.07. The average M2 staging time was 4 min and 9 s, providing a 51 s margin within the staging window. M3 staging was not a constraint.

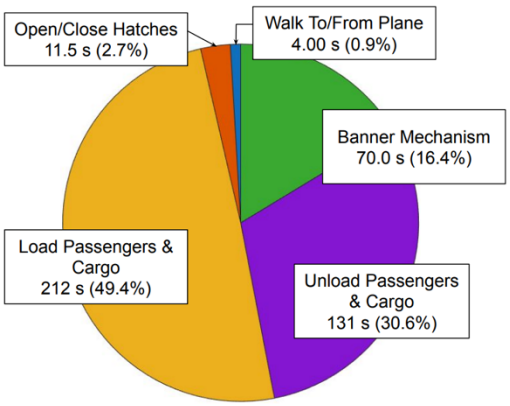

Figure 74. Recorded GM times.

8.1.4.4 Banner - Material Truck Testing

Truck testing was conducted as described in Sec. 7.2.4.4. During testing, an average wind speed of 8 mph (3.58 m/s) was reported at Long Beach Airport. For banner Reynolds numbers (Re_b) tested, the results indicate that while Ripstop Nylon exhibited a steep reduction in drag as Re_b increases, both Tissue Lamé and Polyester Charmeuse Satin consistently exhibited lower drag coefficients. During testing, both materials exhibited more stable behavior compared to the other materials, which is likely due to their greater rigidity and shape retention. In contrast, Sheer Voile and Silk Chiffon, characterized by low area density and high permeability, produced the highest drag across all Re_b. Both materials also exhibited significant flapping and trailing edge flutter. Tissue Lamé was selected for the banner material for its low drag coefficient within the design Re_b range of 4.3 - 6.0 $\times 10^6$.

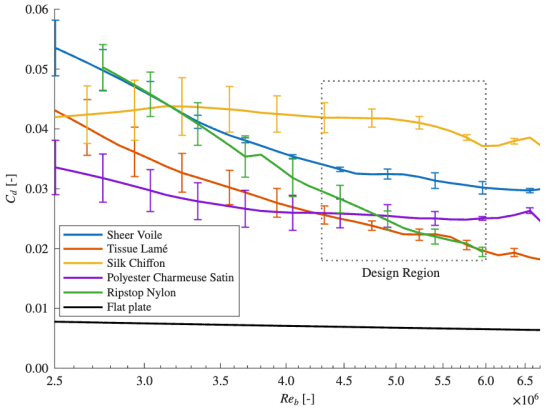

Figure 75. Comparing tested banner-material drag to the flat-plate assumption.

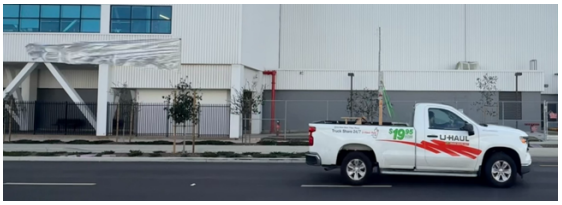

Figure 76. Snapshot of the Tissue Lame banner under tow.

8.1.5 Propulsion

Propulsion testing was conducted, as described in Sec. 7.2.5. To stay within the load-cell limit, the propulsion package, mounted on the thrust stand, was adjusted to use an 8S battery and an APC 20x15E propeller (Fig. 77). The motor, ESC, and battery were able to run for 6 min with a final voltage of 3.4 V/cell. Measured thrust and torque (Table 42) verified the aircraft could withstand the structural load as the measured values were below the predicted.

Table 42. Max Static Measurements

Variable	Thrust [lbf]	Torque [lbf ft]
Expected	13	9.2 ± 0.2
Measured	1.31	1.19 ± 0.04

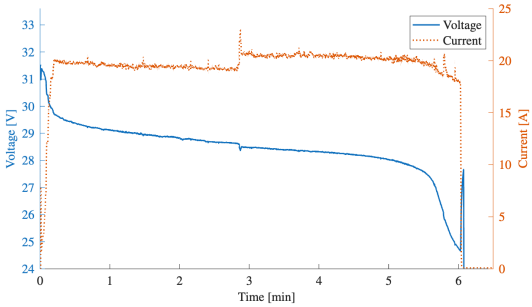

Figure 77. Voltage and current measurement of the endurance testing.

8.2 Demonstrated Aircraft Performance

8.2.1 Stall Testing

Stall testing was conducted, as described in Sec. 7.3.3.2 across two flights (11/30/25 and 01/25/26) with V1 for two flap configurations (retracted and M3 cruise). Measured air density was 0.07 lbm/ft^3 (1.2 kg/m^3) and no surface winds were recorded for both flights. Figure 78 shows the data during a single retracted-flap stall test, with a $C_{L,max}$ of 1.29. Table 43 shows the experimentally determined $C_{L,max}$ across multiple stall maneuvers compared to PT's prediction, derived in Sec. 4.2.1. Here, all stalls were identified by an uncommanded pitch down of the aircraft. Note that stall maneuvers with roll excursions of greater than 20° and sudden spikes in C_L caused by transient effects during post-stall recovery were excluded, as these do not represent steady cruise conditions. Figure 79 shows the tufts attached onto the right wing as the aircraft enters a stall maneuver. Flow separation (indicated by the tufts not flowing along the chord) grows outward from the center (~20% semi-span) and expands from there. This matched the predicted behavior for a rectangular, low-AR wing with no geometric twist. Throughout the entire maneuver, the flow around the ailerons were attached. Post-recovery, all tufts indicated attached flow.

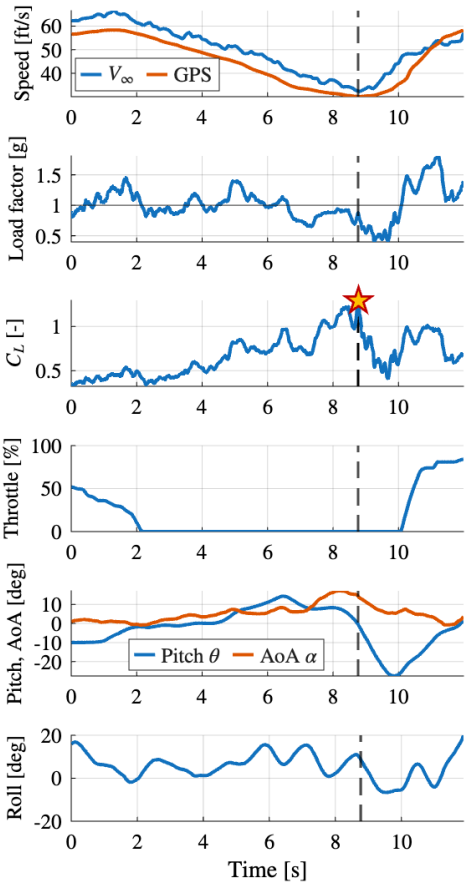

Figure 78. Stall test maneuver time-trace.

Figure 79. Flow visualization during stall using tufts on the right wing of V1.

Table 43. $C_{L,max}$ Testing Results

Flaps Configuration	PT Predicted	Measured	Number of Tests	Δ [%]
Retracted	1.33	1.3 ± 0.1	9	-2.3
M3 Cruise	1.47	1.5 ± 0.2	5	+2.0

8.2.2 Cruise Testing

Cruise testing, as described in Sec. 7.3.3.3, was conducted on 01/25/26 using V1 with a Hobbywing Platinum FW 5230 motor (K_V = 190 RPM/V), KDEDirect UAS125UVC ESC, ThunderPower 8S battery, and an APC 20.5x14 EPNC propeller. Measured air density was 0.07 lbm/ft^3 (1.2 kg/m^3) and the winds were calm for this test. Seven segments were identified to have steady-state conditions, where the aircraft reached terminal velocity. The results are shown in Table 44. For cruise throttle settings (70-100% throttle), no throttle or current effect on $\eta_{motor+wire+ESC}$ was observed, with the average $\eta_{motor+wire+ESC}$ measured as 0.55 ± 0.08. Comparing simulated $\eta_{motor+wire+ESC}$ of 0.63 for a nominal M2 and 0.62 for a nominal M3 mission in PT, it was found that the propulsion model was overpredicting the $\eta_{motor+wire+ESC}$. Therefore, PT applied a knockdown factor to $\eta_{motor+wire+ESC}$ to more accurately represent the aircraft for future iterations and competition strategy planning.

Table 44. Cruise Testing Results. Note that Green Colors Indicate Higher Efficiency

ID	Throttle [%]	Airspeed [ft/s]	J [-]	Current [A]	η_{prop} [-]	$\eta_{motor+wire+ESC}$ [-]	η_{total} [-]
1	45	58 ± 1	0.67 ± 0.01	11.90 ± 0.05	0.80 ± 0.01	0.40 ± 0.01	0.32 ± 0.01
2	54	71 ± 2	0.70 ± 0.02	15.7 ± 0.4	0.77 ± 0.02	0.42 ± 0.02	0.33 ± 0.02
3	70	80 ± 1	0.65 ± 0.01	28.6 ± 0.3	0.811 ± 0.003	0.51 ± 0.01	0.41 ± 0.01
4	74	69 ± 3	0.54 ± 0.02	31.4 ± 0.7	0.79 ± 0.01	0.67 ± 0.01	0.53 ± 0.01
5	90	97 ± 2	0.66 ± 0.01	46.6 ± 0.7	0.81 ± 0.01	0.52 ± 0.01	0.42 ± 0.01
6	100	113 ± 2	0.71 ± 0.01	55 ± 1	0.75 ± 0.02	0.47 ± 0.02	0.35 ± 0.02
7	100	103 ± 2	0.65 ± 0.01	56.4 ± 0.9	0.81 ± 0.01	0.56 ± 0.03	0.46 ± 0.02

8.2.3. Mission Performance: Mission 2

An M2 attempt was flown with V1 on 11/04/25 to gather performance metrics and to validate the DIW concept in-flight. Takeoff weight (W_0) was 26.9 lbm (12.2 kg) with 177 passengers in the wing and 1 cargo in the fuselage. The air density was 0.07 lbm/ft^3 (1.2 kg/m^3) and surface winds were 3 mph (1.34 m/s). This M2 attempt was simulated in PlaneTools (PT) matching W_0, propeller, starting battery voltage, cruise throttle setting, and headwind to compare against the test flight data, as seen in Fig. 80. The PT simulations match flight test data, and the data supports that the correct propeller was selected for this mission, as V1 cruised near max η_{prop}. Further, flight test data was used to populate the *V-n* diagram seen in Fig. 81. The datapoints that lie outside this envelope were during descent, whereas the envelope is for level cruise. Flying four competition laps, the M2 score for this attempt was 1.92. The pilot did not report any notable impact in roll responsiveness from having the passengers in the wing, which increased the roll inertia. The passengers stayed in their initial positions after landing.

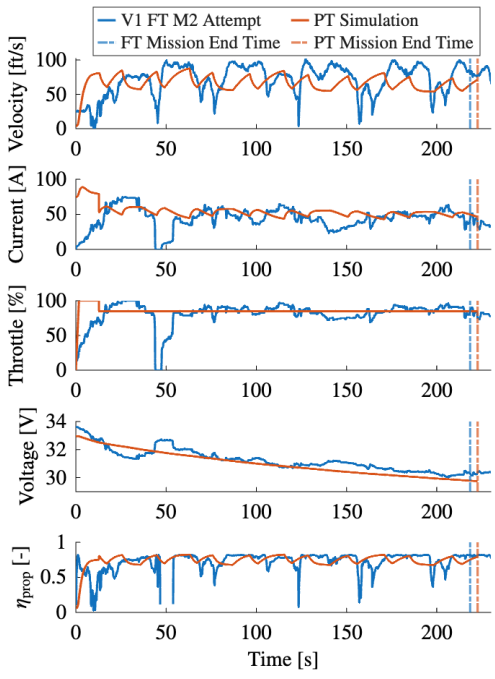

Figure 80. M2 comparison of PlaneTools (PT) simulation and flight test (FT) data

8.2.4 Mission Performance: Mission 3

An M3 attempt was flown with V1 on 01/25/26 to gather performance metrics in flight. W_0 was 19.8 lbm (9.0 kg) with a 360-in (9.14-m) long low-density polyethylene banner. The measured air density was 0.07 lbm/ft^3 (1.2 kg/m^3), and no surface winds were recorded. This attempt was simulated in PT matching W_0, propeller, starting propulsion battery voltage, banner dimensions, and headwind to compare against the test flight data (Fig. 82). In PT, the cruise throttle setting was raised to 85% from the flown 75% throttle as PT claimed the aircraft was stalling in cruise. This difference stems from how PT represents forces during cruise; at high-pitch attitudes, the vertical component of thrust relative to the horizon must be included along lift. Both PT and FT show an average η_{prop} of 0.5, indicating that the team should investigate higher-diameter, lower-pitch propellers. Figure 82 shows the flight path and altitude for this flight, demonstrating three consistent competition laps. The M3 score for this attempt was 3.00; however, this flight was flown with no surface winds.

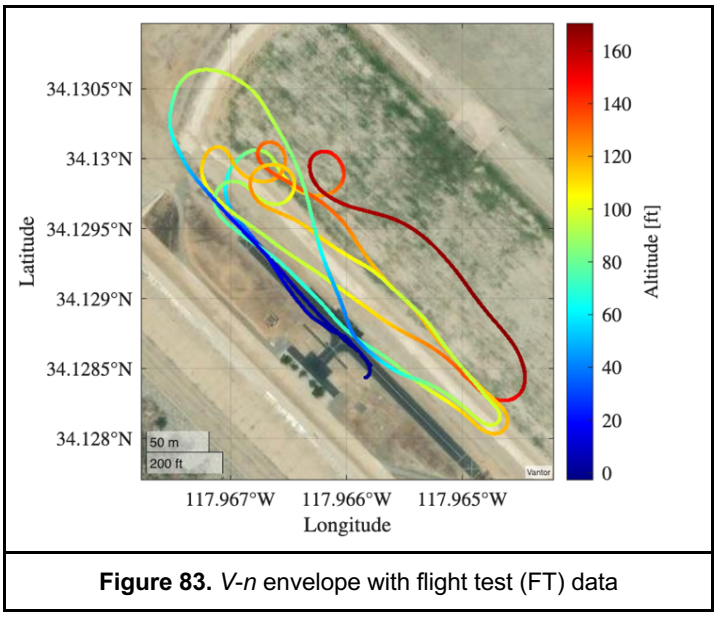

Figure 83. *V-n* envelope with flight test (FT) data

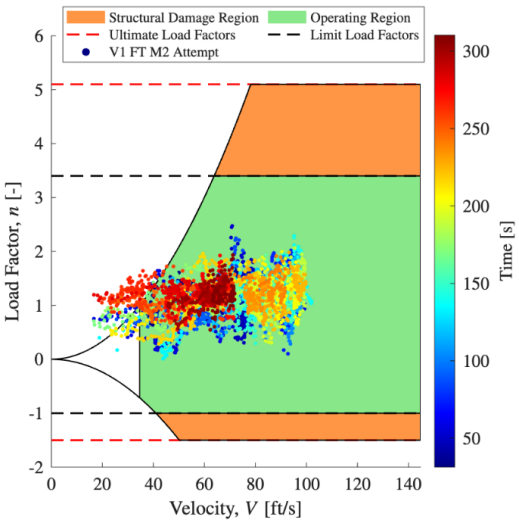

Figure 81. *V-n* Envelope with flight test (FT) data

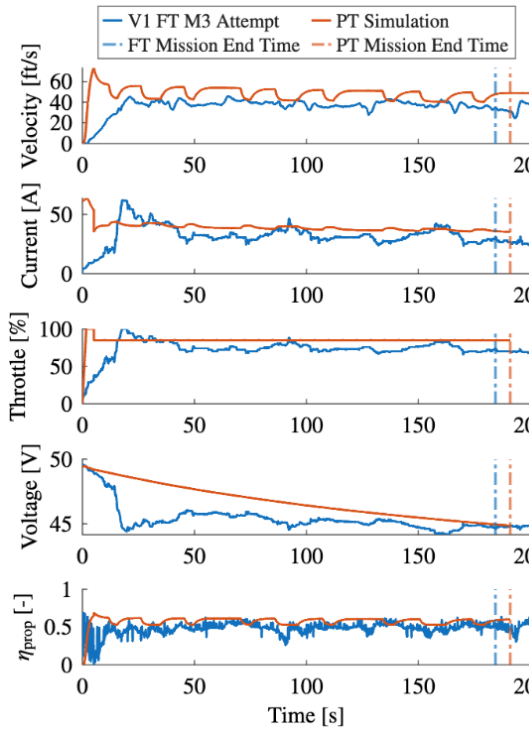

Figure 82. M3 Comparison of PT simulation and FT data

8.3 Future Flight Testing

Verification of design, qualitative insights, and model correction factors from V1 flight testing and V2 subcomponent testing will be incorporated into the V3 design cycle and competition strategy planning. V3 will undergo similar testing to ensure flight readiness and to experimentally determine aircraft performance metrics. In parallel, greater emphasis will be placed on achieving more efficient flight by optimizing lateral and vertical flight paths assisted by live telemetry, while refining competition strategies through data-driven flight testing.

9 Bibliography

[1] AIAA, "2025-2026 DBF Rules," Reston, VA, 2025.

[2] AIAA, "2025-2026 DBF Q&A #1," Reston, VA, 2025.

[3] AIAA, "2025-2026 DBF Q&A #2," Reston, VA, 2025.

[4] Gudmundsson, S., General Aviation Aircraft Design: Applied Methods and procedures, Oxford: Butterworth-Heinemann, 2022

[5] “Fabric Wholesale Direct” [Online]. Available here.

[6] “Matlab,” Mathworks. [Online]. Available here.

[7] "XFLR5," 2019. [Online]. Available here.

[8] Drela, Dr. M., and H. Youngren, "AVL," 2017. [Online]. Available here.

[9] “Performance Data,” APC Propellers. [Online]. Available here.

[10] USC AeroDesign Team, "Aircraft Design Report, 2020 AIAA DBF Competition," 2020.

[11] C. Zhang, J. Jiang, L. Zhang, S. Liu, L. Wang, P. C. Loh, “A Generalized SOC-OCV Model for Lithium-Ion Batteries and the SOC Estimation for LNMCO Battery,” Energies, 2016. Available here.

[12] “Meteostat Python,” 2026. [Online]. Available here.

[13] Drela, Dr. M., “XFOIL,” XFOIL Subsonic Airfoil Development System, Dec. 2013

[14] “Ansys Fluent,” Synopsys. [Online]. Available here.

[15] Hoerner, S.F, “Fluid-Dynamic Drag”, 1st ed., Hoerner Fluid Dynamics, 1965.

[16] “April Weather in Wichita,” Weather Spark, Cedar Lake Ventures, Inc. [Online]. Available here.

[17] O. Al-Shamma, A. Rashid, H. Hasan, “An Educational Rudder Sizing Algorithm for Utilization in Aircraft Design Software,” 2018.

[18] "What’s the difference between Nickel Cadmium (Nicad), Nickel-metal hydride (NiMH), and Lithium Ion (Li-Ion)," Battery Universe. [Online]. Available here.

[19] J. B. Brandt, R. W. Deters, G. K. Ananda, D. Dantsker, M. S. Selig, “UIUC Propeller Data Site,” University of Illinois at Urbana-Champaign, Dept. of Aerospace Engineering. [Online]. Available here.

[20] MaxAmps, “MaxAmps Lithium Ion Polymer (LiPo) Battery Model No: MA-2000-12s-Lipo-Pack Datasheet,” MaxAmps, Spokane Valley, WA, Tech. Data Sheet, n.d.

[21] Altair OptiStruct, "Altair OptiStruct," [Online]. Available here.

[22] B. Rawdon, Landing Gear Design, 2009.

[23] Raymer, Daniel P. Aircraft Design: A Conceptual Approach. 2nd ed. Washington, DC: American Institute of Aeronautics and Astronautics, 1992

[24] “Series 1780 Dynamometer Test Stand,” Tyto Robotics. [Online]. Available here.

[25] “RCbenchmark Software,” Tyto Robotics. [Online]. Available here.

[26] Code of Federal Regulations, “23.2110 Stall speed” [Online]. Available here.

BRVINC

AIAA Design/Build/Fly 2025/26

Edvard Rusjan Team, University of Ljubljana

Contents

Abbreviations, Acronyms, and Symbols

α, AoA	Angle of Attack
φ	Thrust Angle
θ	Bank Angle
τ	Time Constant
ω_{cmd}	Commanded Heading (Yaw) Rate
AIAA	American Institute of Aeronautics and Astronautics
APC	APC Propeller Company
AR	Aspect Ratio
ASA	Acrylonitrile Styrene Acrylate
C_D	Drag Coefficient
C_f	Skin Friction Coefficient
C_L	Lift Coefficient
C_m	Pitching Moment Coefficient
CAD	Computer-Aided Design
CAM	Computer-Aided Manufacturing
CF	Carbon Fiber
CFD	Computational Fluid Dynamics
CG	Center of Gravity
CNC	Computer Numerical Control
D	Drag Force
DAQ	Data Acquisition
DBF	Design Build Fly
DoF	Degrees of Freedom
ESC	Electronic Speed Controller
FC	Flight Controller
FEA	Finite Element Analysis
FDM	Fused Deposition Modeling
FF	Form Factor
FoM	Figure of Merit
G	Gravitational Force
g	Gravitational Acceleration
GF	Glass Fiber
GM	Ground Mission
GPS	Global Positioning System
IRF	Inverse Reserve Factor
kt	Knots
KV	Motor Speed Constant
L	Lift Force
LLT	Lifting-Line Theory
LiPo	Lithium Polymer
m	Airplane Mass
M#	Mission #
MAC	Mean Aerodynamic Chord
MDF	Medium Density Fiberboard
MTOW	Maximum Takeoff Weight
N_L	Number of Laps Flown
NiCd	Nickel Cadmium
NiMh	Nickel Metal Hydride
PSF	Primary Score Factor
PVA	Polyvinyl Alcohol
q	Dynamic Pressure
RC	Radio Controlled
RPM	Revolutions per Minute
Re	Reynolds Number
S	Side Force
SD card	Secure Digital card
SoC	State of Charge
S_{ref}	Reference Surface
S_{wet}	Wet Surface
T	Thrust Force
T_v	Vertical Thrust Force Component
T_h	Horizontal Thrust Force Component
TMS	Total Mission Score
TPU	Thermoplastic Polyurethane
UD	Unidirectional
VLM	Vortex Lattice Method
V	Airspeed
v_{cruise}	Cruise Speed
v_{stall}	Stall Speed

1 Executive Summary

This report details the design, manufacturing, and testing of the University of Ljubljana aircraft for entry into the 2026 American Institute of Aeronautics and Astronautics (AIAA) Design, Build, Fly (DBF) competition. Edvard Rusjan Team devised a radio-controlled (RC) banner-towing bush plane named *Brvinc*, deriving from a Slovenian dialect word for an ant.

Brvinc strives to successfully complete three flight missions and one ground mission, while adhering to AIAA's competition requirements. This year's tasks entail a demonstration flight, efficient passenger and cargo charter transport, banner towing, and a timed static demonstration of all payload-securing mechanisms.

The aircraft's low-wing configuration, conventional tail design and tricycle landing gear contribute to great flight characteristics and offer easy access to mission payloads. Brvinc's design provides sufficient space to accommodate three passengers and one piece of cargo, as well as a stowed 226.25" long banner to be deployed and released mid-flight. The aircraft is powered by a single Kontronik PYRO 700-45 brushless electric motor and an APC 15x10E propeller. The maximum takeoff weight (MTOW) of 8.05 lbs is carried in it's banner towing configuration.

Brvinc was devised, designed, manufactured, and tested by a team of 48 students from the University of Ljubljana. The team is divided into seven sub-teams: Simulations & Testing, Aerodynamics, CAD, CAM, Manufacturing, Electronics, and Finances & Public Relations. Weighted decision matrices were used to determine the aircraft's conceptual design and a comprehensive sensitivity analysis was carried out to better understand the parameters affecting mission scores. Based on the simulation's results, the team decided to adopt a Ground Mission oriented design approach by implementing quickly accessible mechanisms, and low passenger and cargo count to minimize the Ground Mission time.

To maximize total mission score, the base conceptual characteristics were refined during the preliminary design phase. The team addressed all shortcomings and implemented improvements through detailed design. Before finalizing the design, a technically refined prototype of the aircraft was developed and thoroughly tested. The manufacturing process included CNC milling, 3D printing, composite molding, laminating, and vacuum bagging. The main aircraft's skin is made from a carbon fiber structure combined with foam or honeycomb cores, creating a lightweight sandwich design that maximizes structural strength. Ground and flight tests were performed and have been essential for continuously improving the design.

Based on the mission model's predictions, the team seeks to achieve optimal flight performance and maximize the final score. For Mission 2, the aircraft is capable of carrying 3 passengers and 1 piece of cargo for 13 laps within the 5 minute window. With a propulsion battery capacity of 50 Wh and net income of 122.25, it is anticipated to earn a score of 1.02. For Mission 3, it is expected to tow a 226.25" long banner for 5 laps, still within the 5 minute mission window, securing an expected score of 3.00 given the rated airplane cost of 1.00. Ground Mission is expected to be completed in 26.3 seconds, reaching a score of 1.00. With all missions successfully completed the maximum Total Mission Score of 6.02 was calculated.

2 Management Summary

2.1 Team Organization

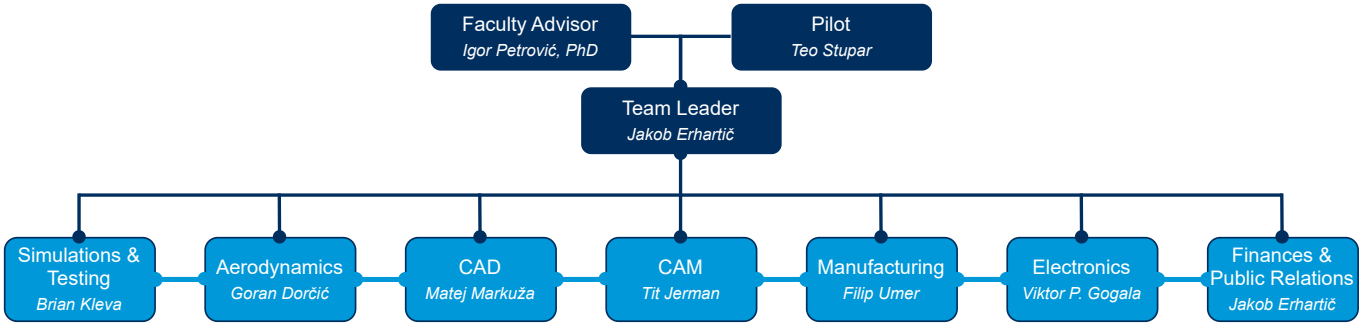

Figure 1: Team Structure

Edvard Rusjan Team consists of 48 students from the University of Ljubljana, 23 of whom are freshmen, sophomore or junior students, and a faculty advisor. Members are divided into 7 sub-teams, each covering their respective aspects of the project: Simulations & Testing, Aerodynamics, Electronics, CAD, CAM, Manufacturing, and Finances & Public Relations (Figure 1). Responsibilities and required skills for each sub-team are outlined in Table 1. Students are assigned to sub-teams based on their interests and skills, with each sub-team led by an experienced member who has been with the team for at least a year. Sub-team leaders manage tasks, plan work, and communicate with the team leader, also an experienced member, who oversees tasks, enforces deadlines and monitors progress. The pilot shares feedback after flight tests, while the faculty advisor offers expert guidance. Technical risks are identified and mitigated through early prototyping, sub-system testing and conservative safety margins. Schedule buffers are implemented before any major milestones, allowing ample time for possible delays and ensuring good workload distribution. Weekly meetings are held to track progress, address challenges, discuss risk concerns and plan next steps.

Table 1: Required Skills and Responsibilities by Sub-teams

Sub-Team	Responsibilities	Required Skills
Simulations & Testing	Simulating and testing various airplane configurations and subsystems, determining the best mission configurations	Computer programming, computational modeling, data analysis, basic understanding of electronics and experimental methods
Aerodynamics	Wing design, performance and stability analysis	Understanding of aerodynamics and numerical computations, OpenVSP and Ansys expertise
Electronics	Electronic component selection and testing, development of testing hardware	Understanding of RC plane electronics, sensors and data acquisition systems
CAD	Airplane design and documentation, mechanism design and testing, 3D mold models	CAD software proficiency, quick-prototyping skills, sense for component design
CAM	Production of molds for aircraft components, 3D-printed components	CAM software proficiency, CNC machines operation, 3D printing
Manufacturing	Post processing of molds, lamination of components, aircraft assembly, banner manufacturing	Knowledge of composite materials and manufacturing techniques, sewing
Finances & Public Relations	Sponsorship acquisition, budget planning, public outreach, event organization, competition logistics, social media	Resourcefulness, financial literacy, communication and organizational skills

2.2 Milestone Chart

To efficiently manage and track the project timeline, a Gantt chart with main tasks and milestones has been used (Table 2). The planned duration of the tasks was based on experience from previous DBF competitions.

Table 2: Milestone Chart

UL DBF 2025-26 Schedule	September				October					November				December				January					February				March				April		
	1	2	3	4	5	6	7	8	9	10	11	12	13	14	15	16	17	18	19	20	21	22	23	24	25	26	27	28	29	30	31	32	33
Analysis & Simulations																																	
Rules Review	//////////																													Planned Task			
Requirement Decomposition			//////////																										////	Progress			
Design Optimization			//////////																														
Sensitivity Analysis				//////////																													
Aircraft Design																																	
Conceptual Design					//////////																												
Preliminary Design						//////////																											
Subcomponent Design									//////////											//////////			////										
Detailed Design										//////////												////////	////										
Manufacturing																																	
Workshops				//////////																													
Testing Manufacturing Techniques	//////////																																
Prototype Aircraft														//////////							////												
Competition Aircraft																								////////									
Banner Manufacturing								////////											////////														
Testing																																	
Preliminary Testing						////////																											
Ground Testing										//////////																							
Flight Testing																					//////////												
Milestones																																	
Proposal						10/31/2025																											
Preliminary Design Review													12/17/2025																				
Final Report																						02/20/2026											
Competition Fly-off																												04/16–04/19/2026					

3 Conceptual Design

The team examined the competition criteria and flight simulations to identify a suitable configuration with the highest potential for maximizing the overall score, all within the design constraints. Furthermore, a sensitivity scoring analysis was conducted to pinpoint the crucial factors that exert the greatest influence on the total score. The proposed design is presented in Section 3.5.

3.1 Mission Requirements and Scoring

The objective for this year is to design, build and test a banner towing bush airplane that is capable of executing a simulated charter flight and a banner towing mission, including midair deployment and release of the banner. The competition entails four missions – three flight and one ground mission. Flight missions call for: proof of flight (Mission 1), a charter flight (Mission 2), and a banner flight (Mission 3). The Ground Mission is a timed configuration demonstration. The total competition score is calculated as:

$$SCORE = WRS \cdot TMS + P \tag{1}$$

where WRS is Written Report Score, TMS is Total Mission Score, and P is Participation Score. The WRS is attained through the proposal (15% of the WRS) and the design report (85% of the WRS). The TMS is calculated as the sum of the scores obtained in Ground Mission (GM), Mission 1 (M1), Mission 2 (M2), and Mission 3 (M3), using the following equation:

$$TMS = GM + M1 + M2 + M3. \tag{2}$$

Lastly, Participation Score (P) can be earned as follows: one point for attending the Fly-off, two points for completing the tech inspection, and three points for attempting a flight mission.

3.1.1 Mission Flight Rules

Each flight mission requires completing a specified number of laps within the designated time window on the flight course, which is shown in Figure 2. The procedure for each mission commences with the following steps: the aircraft must enter the staging box with the propulsion battery packs removed. For M1, the aircraft enters without payload. The ground crew has to configure the airplane, install the batteries and any mission-specific payload. A successful flight mission requires the aircraft to perform a successful takeoff and landing at the end. There is no limit on the takeoff distance this year.

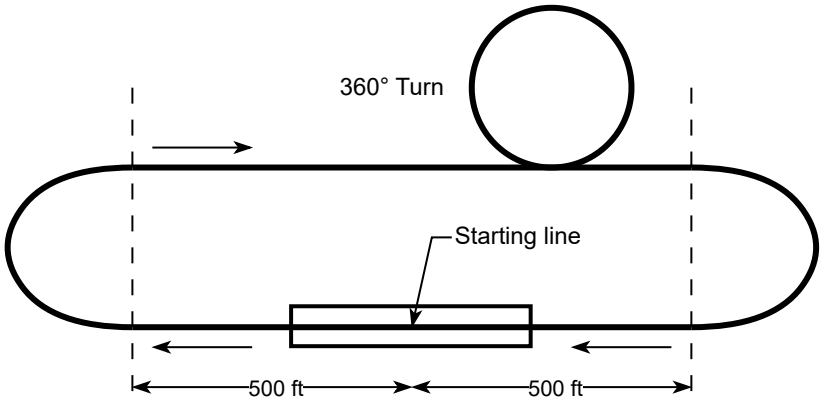

Figure 2: Official Flight Course

3.1.2 Mission 1: Test Flight

M1 is considered completed if the aircraft carries out three laps within the 5-minute flight window while adhering to the specified flight mission rules outlined in Section 3.1.1. The team will receive one point for successfully completing the mission; otherwise, no points will be awarded:

$$M1 = 1.0. \tag{3}$$

3.1.3 Mission 2: Charter Flight

M2 is completed when the aircraft successfully carries a predeclared number of passengers and units of cargo while flying as many laps as possible within the 5-minute time limit, adhering to the mission flight rules. The mission score is based on the net income Net generated during the flight, which is normalized relative to the best-performing team, shown as Equation 4.

$$M2 = 1 + \frac{Net}{\max[Net]}. \tag{4}$$

Net income is calculated as the difference between total income $Income$ and total operating cost $Cost$ as in Eq. 5. Income is determined from the number of passengers N_p and cargo units N_c carried, and the number of laps completed N_l, with fixed and per-lap income coefficients from Table 3 applied to each payload type using Eq. 6. The operating

cost is calculated per lap with Eq. 7 and includes a base cost Ce as well as additional costs proportional to the number of passengers Cp and cargo Cc carried (shown in Table 4), all multiplied by an efficiency factor EF. The efficiency factor is defined as the total propulsion battery energy E_{Bat} measured in Wh and divided by 100, thereby penalizing higher energy capacity systems.

$$Net = Income - Cost \quad (5)$$

$$Income = (N_P \cdot (I_P1 + I_P2 \cdot N_L)) + (N_C \cdot (I_C1 + I_C2 \cdot N_L)) \quad (6)$$

$$Cost = N_L \cdot (Ce + (N_P \cdot Cp) + (N_C \cdot Cc)) \cdot EF \quad (7)$$

$$EF = E_{Bat}/100 \quad (8)$$

Table 3: Income Coefficients

Description	Symbol	Value
Fixed income per passenger	Ip1	6
Income per passenger per lap	Ip2	2
Fixed income per cargo	Ic1	10
Income per cargo per lap	Ic2	8

Table 4: Cost Coefficients

Description	Symbol	Value
Base operating cost per lap	Ce	10
Passenger operating cost per lap	Cp	0.5
Cargo operating cost per lap	Cc	2

3.1.4 Mission 3: Banner Flight

Mission 3 evaluates banner-towing performance within a fixed 5-minute flight window. The banner is deployed by a remote command on the downwind leg following the first upwind turn, and then released by a remote command soon after the aircraft crosses the finish line on the final lap. The mission score is based on the number of completed laps N_L, the banner length L_{Banner}, and the RAC value, which depends on the airplane's wingspan WS as shown in Eq. 9. L_{Banner} and WS are both measured in inches. A successful landing is required for a valid score. The mission score is normalized based on the result of the best-performing team, as shown in Eq. 10.

$$RAC = 0.05 \cdot (WS/12) + 0.75 \quad (9)$$

$$M3 = 2 + \frac{N_L \cdot L_{Banner}/RAC}{\max[N_L \cdot L_{Banner}/RAC]} \quad (10)$$

3.1.5 Ground Mission: Demonstration

Ground Mission involves measuring the time required to complete tasks detailed in 2025-26 AIAA DBF Rules [1]. All assembly and payload-handling tasks must be performed with the aircraft upright and supported by its landing gear. Additionally, only the designated assembly crew member may physically interact with the aircraft. Mission timing starts upon the official command "GO" and includes sequential loading and securing of passengers and cargo, removal of the payload, and installation of the banner in the stowed configuration, with required demonstrations of flight control functionality by the pilot at each stage. The mission concludes with a successful banner deployment and release. The Ground Mission score is determined solely by the elapsed time for the entire attempt t_{GM}, normalized by the time of the best-performing team, as given by Eq. 11.

$$GM = \frac{\min[t_{GM}]}{t_{GM}}. \quad (11)$$

3.2 General, Mission, and Subsystem Requirements

Based on the mission requirements stated in Section 3.1 together with the 2025-26 AIAA DBF Rules [1], a set of fundamental requirements, with which the aircraft and its subsystems must comply, was derived. General aircraft requirements, such as limitations regarding dimensions, weight or electrical characteristics, are outlined in Table 5. Requirements addressing specific mission aspects are detailed in Table 6.

Table 5: General Aircraft Design Requirements

Subcategory	General Aircraft Design Requirement
Configuration	The aircraft wingspan must be between 3 ft and 5 ft in length.
	The aircraft can be of any design, except for rotary wing or lighter-than-air.
	The aircraft take-off gross weight with payload must be less than 55 lb.
	All structures/components must remain attached in-flight, except for the banner during M3.
	All aircraft configurations shall be configured and checked for flight within 5 minutes.
Structure	The aircraft must pass a wingtip load test with the maximum designed takeoff weight.
	All critical fasteners must be secured with an additional secondary retention method (eg. threadlocker).
Propulsion	The aircraft must be propeller driven and electrically powered.
	The battery, electric motor and propeller must be commercially available off-the-shelf parts.
	Propulsion batteries must be NiCd, NiMH, or lithium-based.
	Total stored propulsion energy must not exceed 100 Wh.
	The arming fuse must be a "blade" style fuse with a maximum continuous current rating of 100 A.
Operation	All flight missions must be completed within 5 min.
	The aircraft must remain airworthy after each flight (including landing), with no structural damage and no loss of required function.
	The airplane must have an externally accessible switch to turn on the radio control system.
	The aircraft must have a separate avionics battery for the receiver/servos.

Table 6: Mission Subsystem Design Requirements

Subcategory	Mission Subsystem Design Requirement
Internal Payloads	The airplane must be capable of carrying at least 3 passengers for each piece of cargo declared in Tech Inspection and a minimum of 3 passengers and 1 cargo piece overall.
	The passengers must be carried in a single passenger compartment on a single plane parallel to the horizontal plane while in flight.
	Passenger and cargo compartments must be separate and respectively be individually accessed by at least one rigidly attached door or hatch.
	All passengers and cargo pieces must be fully mechanically restrained, preventing movement in all stages of flight.
	The passenger loading system must allow passengers to be installed and removed individually.
Banner	The banner must have a minimum length of 10” and a maximum AR of 5.
	The banner must have the team’s university name or logo on both sides.
	The banner must be compactly stowed externally to the airplane for take-off without interfering with any flight or control functions.
	The banner must remain in the vertical orientation during flight.
	The banner must not sustain any wear or damage during tow or at ground impact after release.

To complement the mandatory rule-derived requirements, the team introduced self-imposed conditions, presented in Table 7, which are based on the team’s past competition experience to address safety margins and reduce operational risk while pursuing competitive performance.

Table 7: Self-Imposed Design Requirements

Subcategory	Self-Imposed Design Requirements
Configuration	The aircraft should be modular and simple to assemble, along with all main subsystems.
Structure	The aircraft’s structure must withstand an ultimate load equal to 1.5 times the limit load without failure.
Operation	The aircraft must fly reliably and achieve stable flight under varying conditions, especially windy weather.
	The aircraft must maintain sufficient stability, control and speed when towing the banner.
Internal Payloads	The passenger restraint mechanism must accommodate passengers of slightly varying shapes and sizes.
	The passengers and cargo pieces must be easy to restrain and release reliably and quickly to minimize loading and unloading times.
Banner	The banner must be easy to stow and install fast.
	The banner release and deployment mechanisms must be simple to minimize failures.

3.3 Scoring Sensitivity Analysis

After selecting the baseline (optimal) design point (further discussed in Sections 4.3 and 4.4), a scoring sensitivity analysis was conducted to identify which design parameters influence GM, M2, and M3 scoring the most, and to determine the most effective levers for further score improvement. M1 was excluded because it contains no performance-based scoring criteria. Each scoring parameter was varied systematically about the baseline, providing a clear idea of which quantities should be maximized or minimized for competitive performance.

Figure 3 describes how M2 scoring inputs influence the mission score using two score-change scales: the left vertical axis reports relative change of the absolute score that was normalized to our selected baseline (a low-payload M2 configuration), while the right vertical axis reports the same absolute score changes normalized to a high-payload reference configuration that achieves a comparatively greater M2 score. The number of passengers and cargo pieces was exclusively increased since reducing them would create zero-income configurations and drive the M2 scores below the base value of 1, given the baseline of 3 passengers and 1 cargo. A notable score surge occurs when the number of cargo pieces is increased by 100% — this is driven by the design requirement of three passengers per cargo item: any cargo increment forces additional passengers, which amplifies both the M2 score contribution and the GM time penalty, as shown in Figure 4. We recognized that increasing the payload carried is only beneficial if all competing configurations are also designed for near-minimal M2 payloads since the score gains would be significant (see the left vertical axis of Figure 3). However, if even a single competing configuration would carry a high payload relative to our configuration, further payload growth would only provide a limited mission scoring improvement, as shown on the right axis of the same plot. In contrast, reducing the required battery energy while still striving to maximize the number of laps provides the most neutral and reliable way of improving the M2 score since it does not rely on favorable payload distributions in the scoring pool.

Meanwhile, Figure 5 shows the sensitivity of M3 score to its scoring parameters which varies primarily with banner length and number of laps, both of which change stepwise. The banner-length trend appears approximately linear because the predicted baseline banner length is remarkably large (236”). Wingspan has a relatively minor effect and is further limited by the 3–5 ft constraint, resulting in flat regions beyond its bounds. Consequently, M3 performance should be optimized by balancing achievable lap count against banner length, rather than targeting wingspan changes.

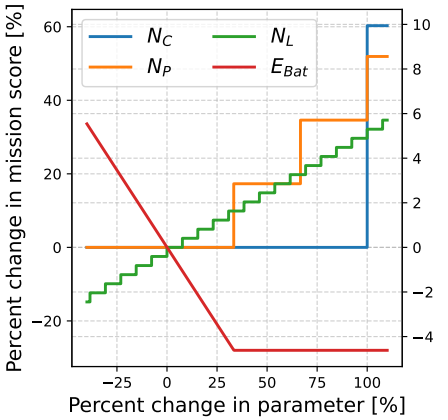

Figure 3: M2 Scoring Sensitivity

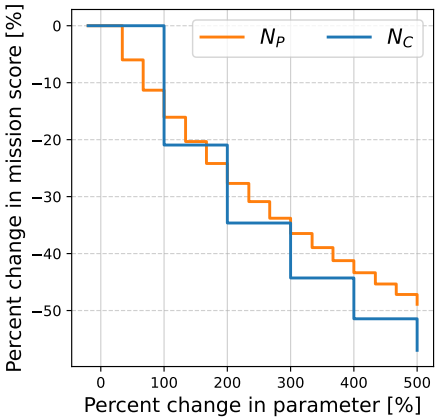

Figure 4: GM Scoring Sensitivity

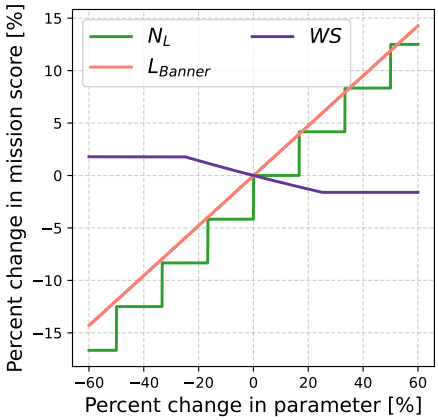

Figure 5: M3 Scoring Sensitivity

3.4 Design Selection Process

A number of design configurations were deemed suitable for further consideration. These candidates were evaluated using weighted decision matrices to identify and select the most appropriate configuration. Within the matrices, a weight rating was assigned for each Figure of Merit (FoM) by evaluating its impact on the final design, with higher weight indicating greater importance. Several sub-teams then carefully analyzed and assessed every design option on a scale from 1 to 5, where 1 indicates the least suitable and 5 the most suitable design for the specified criteria. To obtain a score for each design configuration, the weight and rating were multiplied, yielding a maximum score of 5.

3.4.1 Aircraft Configuration

The criteria studied were selected based on the sub-system requirements outlined in Section 3.2. For the different aircraft configurations shown in Table 8, stability and control were given the highest importance due to the expected unsteady and elevated wind conditions, for their effects on the banner and, consequently, the aircraft.

The other criteria studied were drag, payload integration, manufacturability, and weight, the latter being assigned the lowest level of importance, as the takeoff distance is not limited this year. After comparing the total scores of the three possible configurations, the conventional design stands out the most with great flexibility when it comes to payload integration as well as leveraging the team's experience with manufacturing this type of configuration.

Table 8: Aircraft Configuration Decision Matrix

		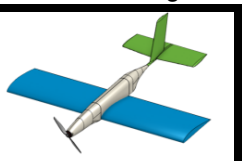	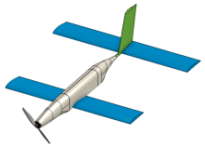	
Figures of Merit	Weight	Conventional	Tandem	Flying Wing
Stability & Control	0.3	5	3	2
Drag	0.2	4	2	5
Payload Integration	0.2	5	5	2
Manufacturability	0.2	3	3	4
Weight	0.1	4	2	5
Total	**1.0**	**4.3**	**3.1**	**3.3**

3.4.2 Propulsion

No decision matrix was created for propulsion. Following the conventional airplane and empennage configuration with low wing and taildragger landing gear, the tractor configuration was chosen as the most favorable. The pusher configuration would most likely require a twin boom design, which would have added additional complexity and weight. The twin engine configuration also adds complexity and weight to the propulsion system due to the necessary doubling of propulsion electronics. Moreover, such structure would require more motor mounting points, resulting in more reinforcements, further adding weight. Because of the pilot's experience with the tractor configuration, asymmetrical effects of a single engine on flight characteristics were not regarded as highly as system architecture simplicity.

3.4.3 Wing Placement

With GM being an important design driver, wing placement was heavily influenced by the accessibility of the internal payload and the banner, as shown in Table 9. In addition, the manufacturability and stability & control of the wing

were also considered. Based on these criteria, the low wing configuration proved to be the optimal choice, primarily because of its payload accessibility and ease of manufacture despite scoring lower in banner accessibility compared to the other considered configurations.

Table 9: Wing Placement Decision Matrix

		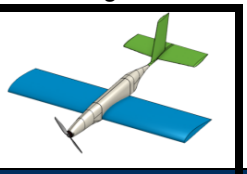	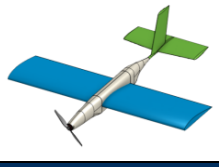	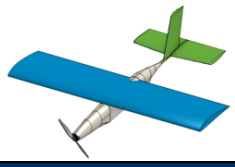
Figures of Merit	Weight	Low Wing	Mid Wing	High Wing
Payload Access	0.3	5	4	3
Banner Access	0.3	3	4	5
Stability & Control	0.2	4	4	5
Manufacturability	0.2	5	3	3
Total	**1.0**	**4.2**	**3.8**	**4.0**

3.4.4 Empennage

In the evaluation of empennage design, the team focused primarily on structural integrity and stability & control while also assessing manufacturability and weight with a reduced degree of emphasis on account of observations already discussed in Sections 3.4.1 and 3.4.3. The straight forward design of the conventional empennage in Table 10 proved to be the best-scoring, offering exceptional structural integrity, manufacturability and stability without the complexity of the T-tail or lack of stability & control of the V-tail design.

Table 10: Empennage Decision Matrix

		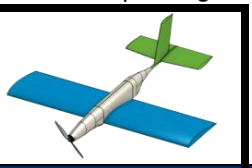	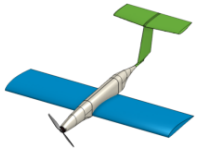	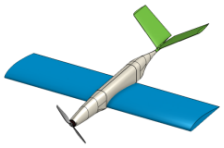
Figures of Merit	Weight	Conventional	T-Tail	V-Tail
Structural Integrity	0.3	5	3	4
Stability & Control	0.3	5	3	2
Manufacturability	0.2	5	3	4
Weight	0.2	4	3	5
Total	**1.0**	**4.8**	**3.0**	**3.6**

3.4.5 Landing Gear Placement

Three variants were analyzed when considering the landing gear design. Table 11 shows the results, as the tricycle design prevailed. Banner accessibility was prioritized with the highest weighting, because the landing gear design is a primary driver of banner-mounting efficiency during GM, which correlates directly with mission scoring. Simplicity was analyzed next, encompassing ease of manufacture and reliability. Impacting the efficiency of the aircraft, and thus M2 and M3 score, the influence of weight and drag was also studied. Ease of handling, which is based on the pilot's feedback and considerable experience, contributed to the final score with the lowest weight. Additional care was taken to ensure the banner release mechanism is sufficiently clear of the ground.

Table 11: Landing Gear Placement Decision Matrix

		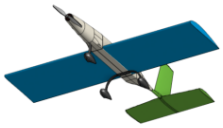	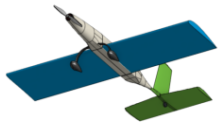	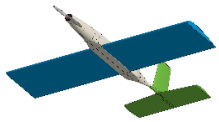
Figures of Merit	Weight	Tricycle	Taildragger	Retractable
Banner Access	0.3	5	2	5
Simplicity	0.2	4	5	1
Weight	0.2	4	5	2
Drag	0.2	3	4	5
Ease of Handling	0.1	5	2	5
Total	**1.0**	**4.2**	**3.6**	**3.6**

3.4.6 Cargo Mechanism

Multiple cargo mechanisms were studied due to their critical importance for GM scoring and the necessity for reliable securing during flight. The first mechanism considered was a puck-shaped box with a snap-on lid to secure the puck. Testing revealed several shortcomings, including unreliable lid attachment and poor time efficiency. Therefore, a simpler concept was developed, consisting of only one part: the 3D-printed puck-shaped clamps with integrated springs secure the puck radially, whereas the side walls prevent axial movement. This resulted in a faster and more reliable method for securing the cargo. Fast removal was also streamlined by the addition of U-shaped slits for fingers in the side wall. This concept, shown in Figure 6, was used as the foundation for further development.

3.4.7 Passenger Mechanism

To decrease loading and unloading time, two different working principles were analyzed. One secured the ducks with 3D-printed hooks that have a compliant base, providing enough flexibility to conform to and secure differently sized ducks (Figure 8). The other secured them with wooden hooks that snap over the duck with an over-center mechanism and extension springs (Figure 7). We decided to focus on the former mechanism, because it proved to be more reliable during testing, easier to manufacture and thus also iterate.

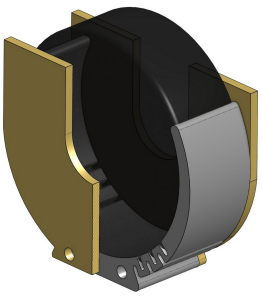

Figure 6: Cargo Mechanism with U-Shaped Slits

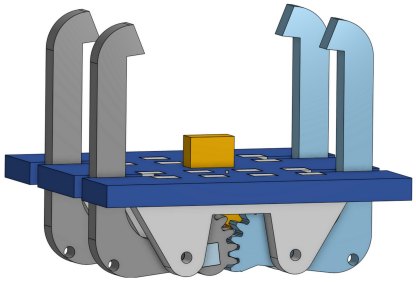

Figure 7: Over-Center Passenger Mechanism

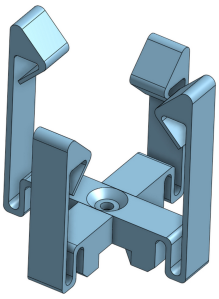

Figure 8: Compliant Hook Passenger Mechanism

3.4.8 Banner Deployment, Towing and Release Mechanism

During the conceptual design phase, several banner mechanism concepts were developed and evaluated with two primary objectives: reliable deployment during M3 and rapid installation during GM. Each concept included two independent, servo-actuated sub-mechanisms; one for releasing the folded banner for deployment, and another for releasing the towline to fully detach the banner.

The initial concept (Figure 9) used a large 3D-printed pyramid structure as the tow-line attachment element. While this configuration allowed very rapid installation and performed well for GM, testing (discussed in Section 7.1) revealed insufficient reliability in M3, as the towline release occasionally failed. Because of the critical nature of banner release, this concept was deemed unsuitable despite its installation advantages. A revised concept (Figure 10) simplified the tow-line release by eliminating the pyramid structure while retaining the same banner deployment approach. This configuration significantly improved release reliability during flight testing and was therefore selected as the baseline concept for further testing and refinement.

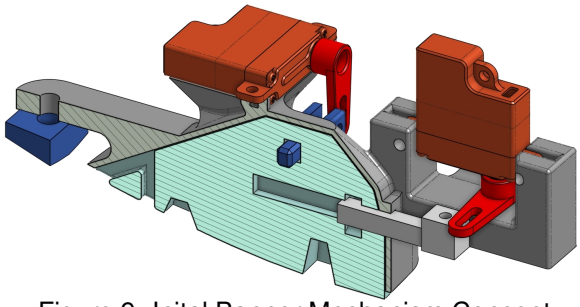

Figure 9: Inital Banner Mechanism Concept

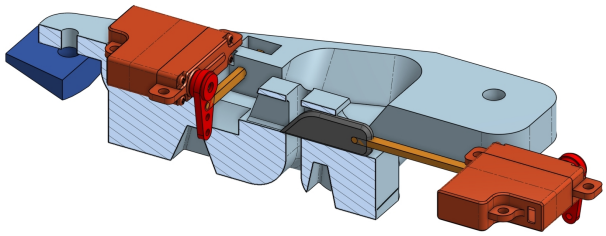

Figure 10: Revised Banner Mechanism Concept

3.4.9 Banner Material and Rigging

During the banner material selection process, several candidate materials commonly used in parachuting, gliding and aviation were evaluated. The assessment considered material density, porosity, estimated drag coefficients and tensile strength. Materials with the lowest density and porosity were each assigned a rating of 5, since lighter and less porous fabrics were expected to induce the least amount of drag. Based on these evaluations, the decision was made to proceed with further testing and evaluation of six materials, which demonstrated the most promising combination of aerodynamic performance and structural properties: Icarex, polyester, peel ply, Dacron, and two types of ripstop nylon with different densities. Based on the results presented in Table 12, Icarex was identified as the material with the greatest potential, therefore, its estimated drag coefficient range of 0.02–0.04 was used in Section 4 for banner-towing performance calculations and banner sizing. The final banner material was selected based on test results, described in Section 8.1.

Table 12: Banner Material Decision Matrix

Figures of Merit	Weight	Icarex	Dacron	Peel Ply	Polyester	Ripstop Nylon (High Density)	Ripstop Nylon (Low Density)
Density	0.2	5	4	2	3	3	5
Porosity	0.2	4	4	1	2	5	3
Drag	0.3	5	4	2	3	2	4
Tear Resistance	0.3	4	5	3	3	2	4
Total	**1.0**	**4.5**	**4.3**	**2.3**	**2.8**	**2.8**	**4.0**

Furthermore, different banner rigging methods were analyzed. The main rigging configurations considered were the asymmetric Y, single-line and triangular setups. Three main criteria were evaluated: reliability of proper deployment, simplicity, and banner stability, with the latter being weighed as most important. As shown in Table 13, asymmetric Y rigging with a longer bottom line scored the highest and was thus selected as the final design, as it offers the best towing stability and deployment reliability, which are both directly tied to success in GM and M3.

Table 13: Banner Rigging Decision Matrix

Figures of Merit	Weight	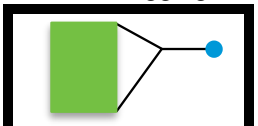 Asymmetric Y	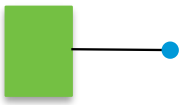 Single-Line	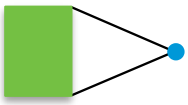 Triangular
Banner Stability	0.4	5	2	3
Simplicity	0.3	3	5	4
Reliability	0.3	4	2	4
Total	**1.0**	**4.1**	**2.9**	**3.6**

3.5 Final Conceptual Design

Figure 11 depicts the final conceptual design of the aircraft. The wing is placed under the fuselage and the conventional tail has been sized using tail volume coefficients. A single motor is mounted at the front of the fuselage, followed by a battery. Passengers and cargo are stored in the middle of the fuselage in two separated compartments, easily accessible through hatches on the top. Tricycle landing gear gives ample space for stowed banner to be attached and safely released. Banner mechanism is placed behind the main landing gear and is accessed from below.

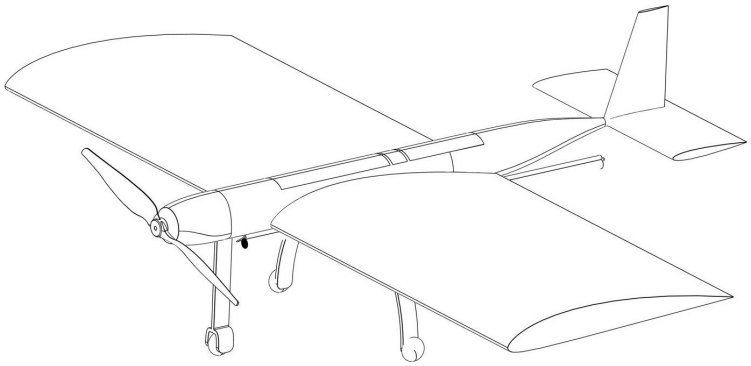

Figure 11: Conceptual Aircraft Design

4 Preliminary Design

The primary objective of the preliminary design phase was to define the aircraft's key geometry and aerodynamic performance, size the propulsion system, and determine payload capacity and banner size to maximize the Total Mission Score. Parameter trade studies were performed to interpret simulation results and estimate flight/mission metrics, such as energy consumption, lap times, maximum loads, and top ground speed. These results established the foundation for the Detail Design phase.

4.1 Design and Analysis Methodology

The design methodology followed an iterative process based on a custom aircraft flight simulation program developed in the Python programming language [2] and the team's previous experience. All simulations were based on the parameters listed in Table 14. The simulation process began by defining arrays of discrete values (or strings in the case of motors, propellers and airfoils) for each parameter. Since airfoil selection was not the focus at this stage, a single set of well-characterized and forgiving airfoils was fixed to reduce the number of simulated configurations:

CLARK Y for the wing and NACA 0010 for the tail surfaces. These discrete inputs were then systematically combined into unique aircraft configurations, which were subsequently individually evaluated through our mission model, further described in Section 4.2.

Table 14: Simulation Input Parameters

Parameter	Brief Clarification	Defined Range
Motor Name	Database key used to retrieve motor performance data	/
Number of Motors	Number of motors (i.e., number of propulsion units)	1–2
Propeller Name	Database key used to retrieve propeller performance data	/
Throttle	Fixed throttle setting **[%]**	60–100
Battery Cells	Number of in-series cells (S) used in the propulsion model	6–12
Battery Energy	Total nominal battery energy of the propulsion model **[Wh]**	60–100
Wingspan	Wingspan **[in]**	36–60
Wing Chord	Wing chord **[in]**	11.7–19.7
Wing Airfoil Name	Database key used to retrieve wing airfoil aerodynamic data	/
Tail Airfoil Name	Database key used to retrieve tail airfoil aerodynamic data	/
Passengers	Number of passengers carried	0–150
Cargo Items	Number of cargo items carried	0–40
Banner Length	Banner length **[in]**	0–470

The mission model operates using propulsion, aerodynamic and mass models, which are generated for each configuration, based on the defined input parameters and assembled into a single aircraft model. The aircraft model construction process begins with the creation of the propulsion system model, constituting of the provided propeller, motor, throttle setting and battery characteristics. The model's key parameter relationships, such as thrust-airspeed, electric current-airspeed, and battery voltage-state of charge (SoC), were derived from manufacturer-provided motor, propeller and battery data, together with required parameters (KV-rating, electrical resistance, efficiency etc.).

The aerodynamic model is then generated from the lifting-surface geometry and airfoil selection (wingspan, chord, and airfoil name). Each surface (wing and both tail stabilizers) inherits its aerodynamic properties from the given airfoil from airfoil polar data, providing lift and drag characteristics. The banner is modeled as a separate aerodynamic component that contributes to the total drag force, computed using a simple drag model. It is defined by the given length, while its height is computed from a prescribed aspect ratio of 5. The aerodynamic surfaces and banner are then combined into a single aerodynamic model.

Finally, the fuselage is built using basic geometric primitives, such as cones, pyramids and cuboids, to keep calculations simple and less numerically demanding. Its dimensions follow specific team-defined design guidelines to account for mission-specific requirements and design constraints (Section 3.2). Once the primary aircraft components are created, their mass reference points are positioned relative to one another according to the design guidelines, forming the aircraft's base mass model. Mission-dependent payloads (passengers, cargo and the banner) are then introduced to achieve the desired mission configuration, after which the aircraft is balanced by adding an additional balance mass point.

The mission model was used to evaluate performance of each aircraft configuration across M2, M3 and GM. After all configurations were assessed, the program computed the projected mission scores and TMS for each, enabling detailed trend analyses to identify optimal design and mission parameters. Based on the results, design trade studies described in Section 4.3 were conducted, from which the final design strategy, mission and key design parameters were chosen. Based on the simulation results, suitable airfoils were selected for the aircraft design. Subsequently,

detailed analyses of the wing and tail configuration as well as lift-to-drag and stability characteristics were conducted using the XFLR5 [3] and OpenVSP [4] software tools. These analyses provided a comprehensive assessment of the aerodynamic performance and stability properties of the aircraft, enabling further refinement and optimization of its design. In addition, the obtained results allowed for more accurate determination of the aircraft geometry and key dimensional parameters.

To validate the design, propulsion, banner, ground mission and prototype flight tests, detailed in Section 7, were performed. The resulting data was used to update key model characteristics, such as motor thrust and power performance as well as banner drag, thereby improving simulation predictions, their reliability and further optimizing the final design. The full design methodology is summarized in Figure 12.

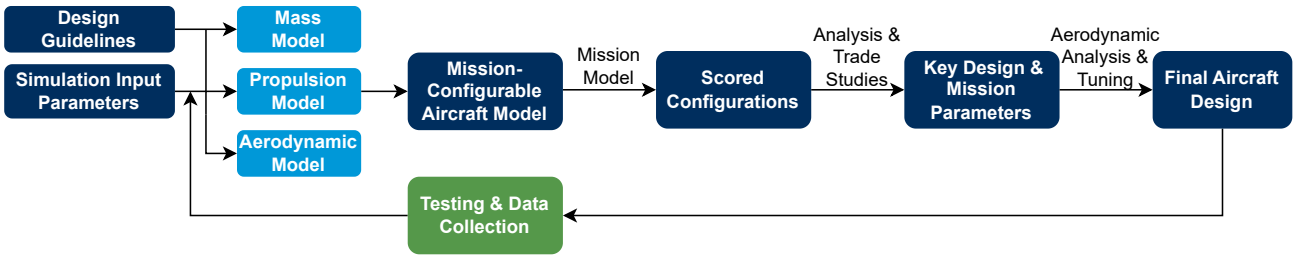

Figure 12: Design Methodology Diagram

4.2 Mission Model

Our mission model is a numerical level-flight simulator based on flight mechanics, in which each lap consists of straight and banked-turn segments. To reduce computational cost, the equations of motion are integrated in a 2-dimensional, 3-DoF formulation (planar position in X–Y and heading φ). Although pitch and bank kinematics are not directly integrated as state variables, their influence on aircraft motion is still inherently represented because the model is fundamentally constrained to level flight, which allows the attitude to be inferred from an equilibrium force balance and solved implicitly at each time step. Propulsive and aerodynamic forces are resolved into axial components (see Figure 13), which allows the required angle of attack α and bank angle θ to be determined at each integration step by enforcing vertical (Z axis) force equilibrium. Since level flight is imposed as the fundamental principle, altitude along the Z axis can be excluded from the mission model. This approach significantly reduces per-mission simulation time without sacrificing result integrity, allowing us to accurately simulate large batches of aircraft configurations in a substantially shorter time span.

Straight segments were simulated using Eq. (12), whereas turn maneuvers were simulated using Eq. (13), (14) and (15), where ω_{cmd} is the commanded heading (yaw) rate, g is gravitational acceleration, θ is the bank angle, and V is the aircraft's total airspeed magnitude. To avoid an unrealistically instantaneous change in turn rate at segment transitions, the actual heading rate $\dot{\varphi}$ is modeled with a first-order response (time constant τ), so that $\dot{\varphi}$ smoothly tracks ω_{cmd} during turn-in and turn-out. The equations were integrated over time using the 3rd order Runge-Kutta method [5] written in Python [2].

$$\ddot{x} = \frac{1}{m}(T_h - D) \tag{12}$$

$$\ddot{x} = \frac{1}{m}(T_h \cos\varphi - S \sin\varphi - D \cos\varphi) \tag{13}$$

$$\ddot{y} = \frac{1}{m}(T_h \sin\varphi + S \cos\varphi - D \sin\varphi) \tag{14}$$

$$\omega_{cmd} = \frac{g \cdot tan\theta}{V}, \qquad \ddot{\varphi} = \frac{\omega_{cmd} - \dot{\varphi}}{\tau} \tag{15}$$

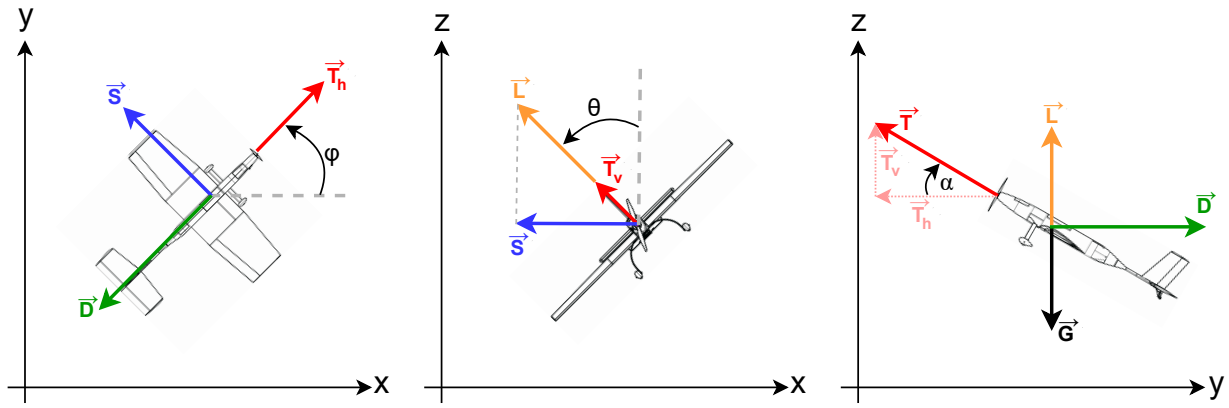

Figure 13: Mission Model Force Decomposition

The propulsion model computes thrust T and electrical current at each integration step. The mission model then uses the current to compute the battery consumption rate and update the battery state in parallel. Motor, propeller, electronic speed controller (ESC), battery parameters and performance data were taken from manufacturer-provided data, resulting in each unique propulsion configuration being characterized by its own performance curves. Thrust T is primarily a function of airspeed, but is also dependent on input voltage. Because the thrust vector is not necessarily aligned with the flight plane, it was broken down into vertical and horizontal components, T_v and T_h, as functions of T and the angle of attack. Similarly, the aerodynamic model computes total lift L and drag D using airfoil polar data obtained from the Airfoil Tools online database [6]. Both are functions of airspeed and angle of attack. The T_v contribution is added to the L vector. During banked turns, the resulting lift is distributed between its vertical and horizontal components, according to the given bank angle: the vertical component is responsible for maintaining level flight, while the horizontal component produces the side force S that drives the turn. By design, the aircraft always executes the largest bank angle that still allows the aircraft to remain in level flight, resulting in the tightest possible turns. Because the bank angle is directly linked to the maximum load factor, it was limited to 84.25°, corresponding to a maximum load factor of approximately 10 g. The banner drag contribution D_B was computed using a simple drag model (Eq. 16), where A is the banner reference area, ρ is air density, V is the airspeed magnitude, and $C_{D,\text{banner}}$ is the banner drag coefficient. $C_{D,\text{banner}}$ was initially modeled as a constant and later reworked into an airspeed-dependent function based on banner test data (Section 7.1). The flight mission model also accounted for wind effects on the aircraft's airspeed. The wind vector was assumed to align with the straight segments of the lap. Unless stated otherwise, simulations were performed with a wind speed of 13.5 kt, selected as the average late-April wind speed in Wichita based on past weather records [7].

$$D_B = \tfrac{1}{2}\,\rho\,V^2\,A\,C_{D,\text{banner}} \tag{16}$$

The model also detects configurations that are unfit for flight, which is particularly useful when simulating large batches since infeasible cases can be discarded automatically. Configurations were rejected if they could not satisfy the required vertical force balance within the valid angle-of-attack range (bounded by the available aerodynamic data to avoid stall) and within the allowable bank-angle limit (corresponding to a maximum load factor of 10 g and a minimum angle of 10°). The model also monitored the battery SoC. If the battery ran out before the mission time limit, the

number of laps completed up to that point was assumed as the configuration's result.

The approach described above has also some uncertainties and limitations. As mentioned, the forces are modeled in three dimensions, but the movement of the aircraft itself is strictly two-dimensional to reduce the numerical cost and does not account for altitude changes. Loss of time and energy due to aircraft climb is therefore neglected. Furthermore, straight flight segments are exactly 1000 ft long, followed by instantaneous aircraft roll. With this assumption, the pilot's reaction time and transient of the aircraft roll are ignored. In addition, the model does not solve rotational equations of motion. Therefore, the aircraft moments of inertia are not used, and attitude changes are represented through imposed bank angles and quasi-steady force equilibrium rather than through applied moments and angular accelerations. Lastly, uncertainties and errors in lift, drag, thrust and banner drag prediction could further affect the mission model. The biggest uncertainties being the banner drag prediction, unsteady tow conditions, and lift and drag predictions during takeoff, as well as the subsequent effects of flaps, which were not modeled. To address these challenges, the team undertook a series of comprehensive studies of aerodynamic effects, complemented by real-world testing and validation efforts.

4.3 Mission and Design Parameter Trade Studies

4.3.1 Passenger and Cargo Counts

Figures 14 and 15 show the influence of the passenger and cargo counts on mission performance, using normalized score contours to outline trends across the design space. The blank region at the upper boundary of both plots corresponds to infeasible configurations that were automatically discarded by the mission model.

Figure 14 presents the normalized M2 score as a function of passenger and cargo counts. As expected, M2 scoring generally increases with payload capacity, since both passengers and cargo carried contribute directly to the mission income (Eq. 6), thus increasing net income. The highest M2 scores are around the high-payload region, where both passenger and cargo counts are high. However, maximizing M2 alone does not maximize overall performance. In contrast to the M2 trend, Figure 15 reveals two distinct high-scoring regions: one clustered around minimal payload and a second at moderate payload. These regions represent two viable but fundamentally conflicting mission strategies that achieve a similar TMS ceiling (approximately 86%), corresponding to 6 out of 7 mission points. The origin of this conflicting behavior is the opposing incentive structure of M2 and GM. M2 rewards higher passenger and cargo capacity, encouraging larger N_P and N_C to maximize payload-related scoring. GM, however, is dominated by ground-handling and configuration time, and therefore favors minimal allowable N_P and N_C to reduce loading and setup time between mission phases.

The absence of a single broad optimum between these two regions indicates that a practical compromise is not achievable. Increasing payload improves M2 performance, but it simultaneously increases the time required to reconfigure the aircraft for GM, which directly opposes the M2 gains and prevents a unified optimum. Preliminary GM timing tests further suggested that the M2 configuration time could not be reduced sufficiently to satisfy both objectives simultaneously, and as a result, the trade study is effectively reduced to a strategic choice between an M2-oriented payload-maximization approach and a GM-oriented low-payload approach.

Given that flight missions present a wider range of uncertainties and possible failure modes compared to ground-

handling, the team decided to adopt the GM-oriented design strategy. This decision accepts an intentional trade-off in M2 scoring in exchange for reduced handling time, repeatable GM execution, M3-focused design approach and a more compact aircraft design, which also streamlines the manufacturing process.

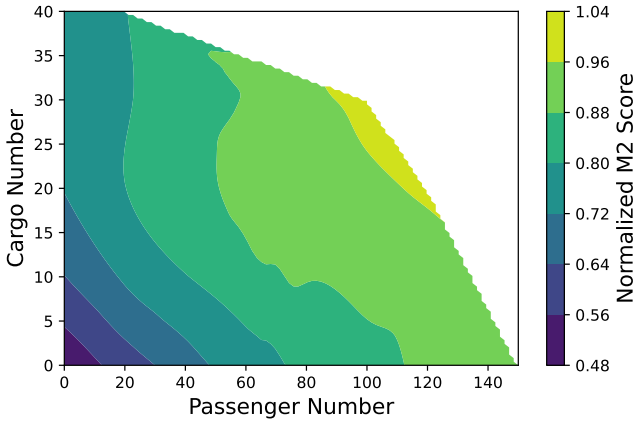

Figure 14: M2 Scoring Based on Passengers and Cargo

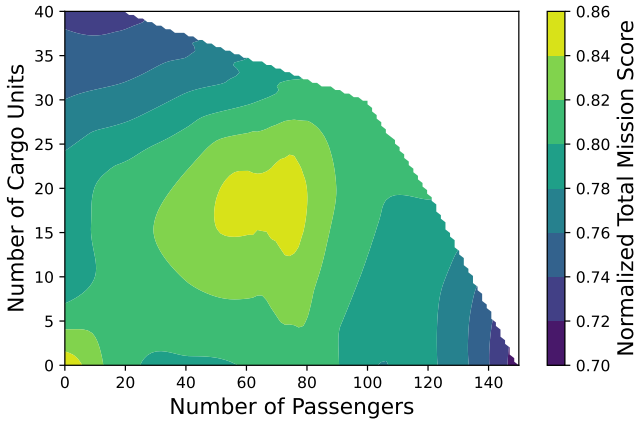

Figure 15: TMS Based on Passengers and Cargo

4.3.2 Banner Length

Figure 16 outlines the role of banner length as the primary M3 design driver. Increasing banner length L_{banner} also increases tow drag, which reduces achievable performance and generally lowers the number of completed laps N_L. As a result, M3's Primary Score Factor (PSF), $N_L \cdot L_{banner}$, exhibits a characteristic sawtooth trend: each vertical drop corresponds to the loss of one lap, which causes an instantaneous reduction in the PSF multiplier. For a fixed configuration, the practical optimums therefore occur just before a lap-loss threshold, where L_{banner} has been increased as much as possible while maintaining the higher feasible N_L. The figure also shows the influence of the banner drag coefficient $C_{D,\text{banner}}$, whose value range was based on the material selected in Section 3.4.9 and its predicted in-flight shape, behavior and stability. Lower $C_{D,\text{banner}}$ preserves lap capability at longer banners, shifting the curve upward and yielding higher attainable M3 scores.

Figure 17 expands this study by comparing the raw PSF of the $C_{D,banner} = 0.02$ characteristic to the normalized M3 score. It is important to note that the M3 score peaks do not perfectly align with PSF optimums, because the normalized score is not only driven by N_L and L_{banner} but is also scaled by the penalty factor RAC, which is a function of wingspan (Eq. 9). For shorter banners, the aircraft can sustain the required lap count N_L with the minimum allowable wingspan (3 ft), keeping RAC low and yielding early score peaks. As banner length is increased further, tow drag rises and as a consequence achievable airspeed decreases. Lower airspeeds reduce the lift margin, requiring higher lift coefficients and higher angles of attack to maintain level flight. Once the required lift approaches the configuration's maximum lift capability, increasing the wing area becomes necessary to compensate for lift loss due to the airspeed decrease. Wing area can first be increased by enlarging wing chord, but after the chord reaches its upper bound in the defined design space (Table 14), further increases are only possible through increasing the wingspan. This increases RAC, which partially offsets the gains from a higher PSF. The score peaks therefore represent the longest banner that can be towed while still sustaining the target lap count using the smallest feasible wing geometry. Beyond this point, maintaining feasibility requires wingspan increases that raise RAC, so the normalized M3 score slightly declines even

if the raw *PSF* continues to grow. Nevertheless, the overall TMS is not strongly penalized by this effect, consistent with the relatively low sensitivity of wingspan observed in Section 3.3. This allows the wingspan to be increased later in the design process if required, with only a minimal impact on the overall score.

In practice, this trade study indicates that the optimal banner strategy is to minimize $C_{D,\text{banner}}$ through banner design, and select L_{banner} near a lap-loss threshold while maintaining the smallest wingspan that reliably sustains the required N_L in tow.

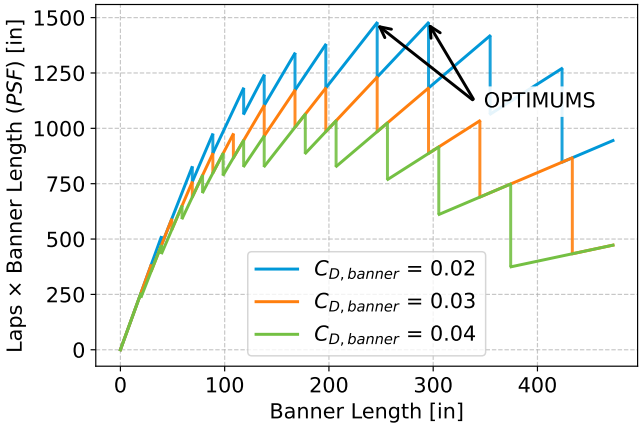

Figure 16: *PSF* vs. Banner Length for Varying $C_{D,banner}$

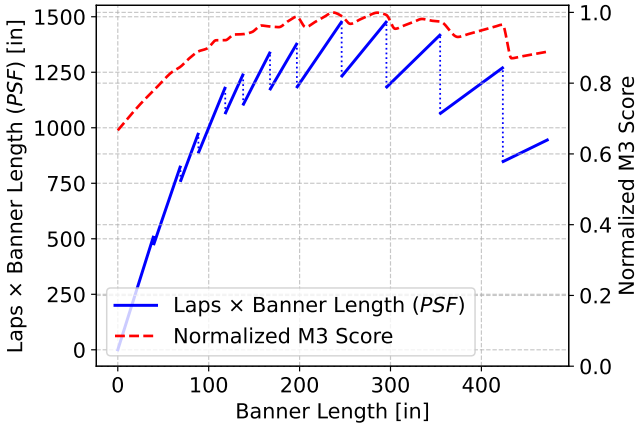

Figure 17: *PSF* vs. M3 Scoring for $C_{D,banner} = 0.02$

4.3.3 Wing Sizing

Figures 18 and 19 summarize the wing sizing study by showing the normalized M2 and M3 scores as functions of wingspan and wing chord. As expected, M2 generally favors larger wings, since increased wing area improves payload capability, which would allow the aircraft to carry higher passenger and cargo counts, resulting in a direct increase in M2 score. In contrast, M3 shows a different preference: because the M3 score is scaled by the *RAC* penalty term, shorter wingspans tend to be more favorable from a scoring perspective. At the same time, towing longer banners increases total drag and shifts the airspeed operating range lower, which requires additional wing area to maintain level flight without exceeding stall limits. The wing area can be provided efficiently by increasing chord, resulting in a preference for relatively short but thicker wings with a lower aspect ratio for M3.

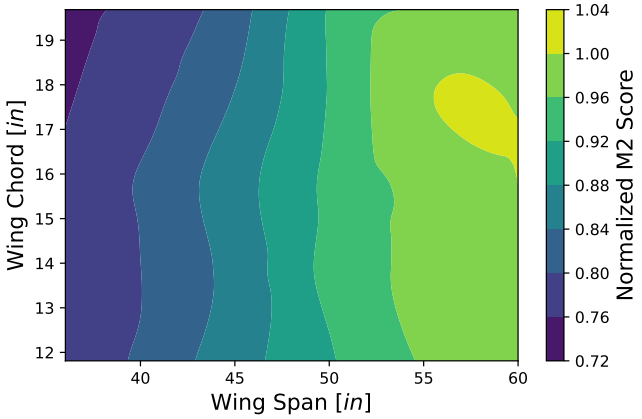

Figure 18: M2 Wing Sizing Scores

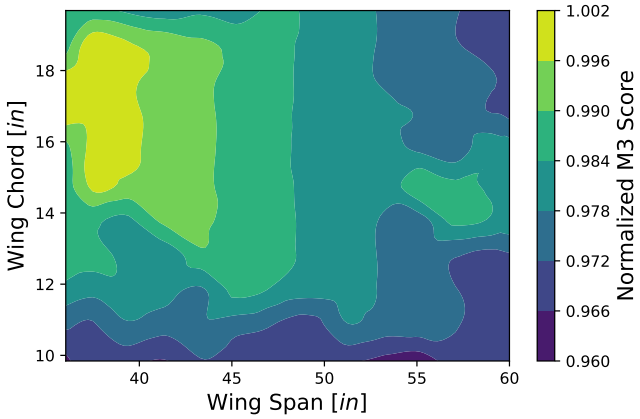

Figure 19: M3 Wing Sizing Scores

Given the adopted GM-oriented strategy, the design emphasis was placed on robust flight mission performance, particularly M3, while accepting a reduced M2 score. Notably, the score contours in Figure 19 indicate that wingspan has only a minor influence on M3 scoring across the explored range, which is consistent with the sensitivity analysis (Section 3.3) and the banner length trade study (Section 4.3.2). Consequently, the final design choice should de-prioritize the RAC penalty and adopt a larger wingspan to improve aircraft stability, its handling margins and in-flight reliability, which is beneficial especially under the expected windy weather conditions in Wichita.

4.3.4 Propulsion Configuration

A total of 155 100 unique propulsion configurations were generated during the simulations, comprising 110 electric motors, 47 APC propellers [8], three battery cell configurations (6S, 8S and 12S), and five battery energy ratings, evaluated in both single and dual-motor arrangements across all possible combinations. Configurations that exceeded the rule-defined current limit of 100 A or the maximum motor current limit within a tolerance of 2.5% were eliminated, as were configurations that did not retain a 400 mAh charge reserve for landing. The main focus of this study was to identify the best suited propulsion configuration for M3, since M2 performance was given lower priority with the adoption of the GM-oriented design strategy.

Simulation results clearly showed that the optimal battery cell configuration is 6S, with 8S and 12S scoring significantly lower. Because M3 is an endurance flight mission, the 100 Wh battery energy cap penalizes higher battery cell counts by reducing the configuration's maximum battery capacity, leading to earlier battery depletion, fewer completed laps and failing to utilize the full 5-minute mission time. This trend highlights the importance of maximizing battery capacity rather than operating at higher voltages, which is one of the key propulsion drivers for M3. Similarly, dual-motor configurations also performed badly due to lower propulsive efficiency.

Finally, the problem was reduced to identifying the optimal electric motor and propeller combination. The top two propulsion configurations are presented in Table 15 and are effectively equivalent, since their projected M3 scores only differ marginally. On the other hand, they do not exhibit identical mission behavior; differences in available tow thrust and efficiency shift the feasible M3 operating point, thus affecting the optimal banner length, the achievable number of laps and remaining battery capacity reserves for landing in said conditions. While wind speed changes did not affect the top configurations themselves, it did affect optimal banner length and number of laps.

Table 15: Optimal Propulsion Configurations

No.	Electric Motor	Propeller	Battery Cells	Battery Capacity	Remaining Capacity	Number of Laps in M3	Banner Length	Projected M3 Score
Wind Speed = 0 kt								
1	Kontronik PYRO 700-34	18 x 12	6	4500 mAh	700 mAh	5	335.75”	3
2	Kontronik PYRO 700-45	15 x 10E			600 mAh	5	324.75”	2.97
Wind Speed = 13.5 kt								
1	Kontronik PYRO 700-34	18 x 12	6	4500 mAh	700 mAh	5	285.50”	3
2	Kontronik PYRO 700-45	15 x 10E			700 mAh	6	236.25”	2.99

As mentioned, M2 was not a primary focus in this study, but we did explore different 6S configurations with variable battery capacity, since the Sensitivity Analysis presented in Section 3.3 implied that lowering the total battery energy held the greatest potential for M2 score improvement. The lowest battery energy at which both optimal propulsion

configurations still retain their projected number of M2 laps at full battery capacity was 50 Wh, establishing this as the M2 battery optimum.

Figures 20 and 21 show predicted thrust profiles based on airspeed and battery SoC for both optimal propulsion configurations. Given their nearly identical performance and characteristics, both configurations were considered viable candidates, prompting real-world validation (Section 7.2) to ultimately choose the final design.

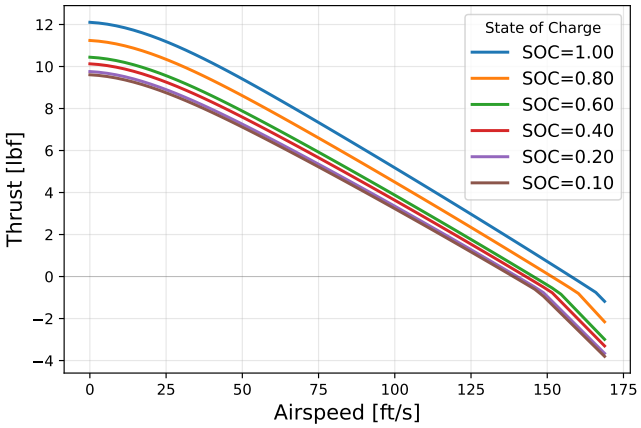

Figure 20: Predicted Thrust Based on Airspeed and SoC for Propulsion Configuration No. 1

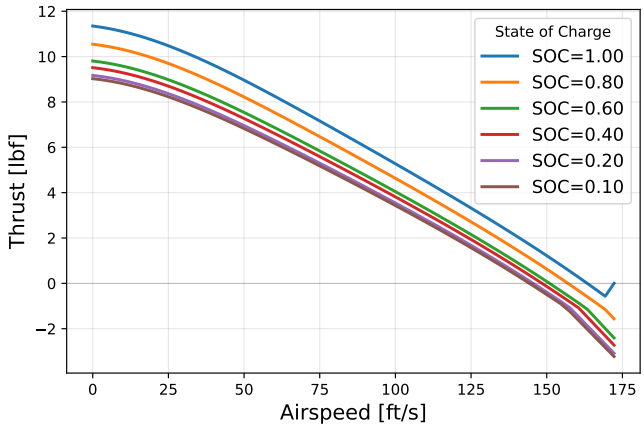

Figure 21: Predicted Thrust Based on Airspeed and SoC for Propulsion Configuration No. 2

4.4 Optimal Mission Design Parameters and Wing Size

Following the adoption of the GM-oriented design strategy, payload counts were decreased to the minimum of 3 passengers and 1 cargo unit. To maximize M2 performance while preserving a comfortable landing reserve, the available propulsive energy was reduced to 50 Wh; for M3 endurance, the full 100 Wh limit was selected (6S – 4500 mAh). The final banner length could not be selected at this design stage as real-world testing was yet to be conducted, but the feasible optimal range could be narrowed down to 236.25”–335.75”. Since the aircraft design prioritizes M3 performance, the wing design adheres to the *RAC* penalty, therefore the optimal wing design is driven by minimizing the *RAC* penalty, favoring shorter wingspans with low aspect ratios *AR*. Optimal wing sizing ranges are provided in Table 16, along with a summary of the optimal design point. The reported banner length range is based on simulations assuming a wind speed of 13.5 kt.

Table 16: Optimal Mission Parameters and Wing Size

M2			M3		Wing Size		
Passenger Number	Cargo Number	Battery Energy	Banner Length	Battery Energy	Wingspan	Wing Chord	Wing AR
3	1	50 Wh	236.25"–285.50"	100 Wh	36”–40”	15”–19”	1.89–2.67

4.5 Aerodynamic Characteristics

4.5.1 Airfoil Analysis

In the initial phase of selecting the airfoil for the main wing and tail surfaces, a broad range of candidate airfoils was considered based on previous experience, relevant literature and mission requirements, with particular emphasis on airfoils demonstrating good performance at low Reynolds numbers, a slightly negative pitching moment coefficient and predictable stall characteristics. From this initial set, 6 of the most suitable airfoils were selected and further analyzed

as shown in Table 17. Airfoil geometric and aerodynamic data were obtained from the Airfoil Tools online database [6]. The key aerodynamic characteristics, such as the lift coefficient (C_L), drag coefficient (C_D), pitching moment coefficient (C_m), and stall behavior, were evaluated, using the XFLR5 [3] software, employing a simple linear-vorticity stream function panel method, which enables batch analysis of multiple airfoils simultaneously. The analyses were performed for Reynolds numbers corresponding to the expected flight speeds of the aircraft obtained from simulations, within the range of 200 000 to 1 500 000.

Based on the results of the analyses, the NACA 4412 airfoil was selected for the main wing. At low aircraft speeds, this airfoil still provides a stable lift development and a sufficiently high maximum lift coefficient, which contributes to an improved lift-to-drag ratio. Due to its moderate camber, it enables flight at relatively low angles of attack and exhibits gradual and non-aggressive stall behavior that provides the pilot with more handling cues and time for corrective action, which is particularly important in competitive flight operations, especially in M3. In addition to its aerodynamic performance, practical aspects were also considered. The airfoil is well documented, easy to analyze numerically, and relatively easy to manufacture, which reduces the risk of deviations between the design and the actual wing geometry.

Table 17: Dataset of Best Wing Airfoils

Re 200 000						
Airfoil name	C_{Lmax}	AoA for C_{Lmax}	C_{Dmin}	C_L/C_D	AoA for C_L/C_D	C_m
SD 6060	1.1039	10.75	0.0167	51.6	6.5	-0.0698
NACA 6409	1.4565	8.75	0.0193	61.59	8.5	-0.1371
NACA 4412	1.4783	14.25	0.0182	56.09	8.5	-0.1041
Clark Z	1.5245	14.75	0.0180	54.02	7.5	-0.0975
USA–35B	1.4499	9.75	0.0156	53.35	6.75	-0.0933
NACA 0012	0.9917	10.75	0.0143	36.68	5	0

The NACA 0012 airfoil was chosen for both the horizontal and vertical stabilizers because of its symmetrical design, which provides neutral and consistent aerodynamic behavior for control surface deflections in either direction. Its geometry inherently ensures a stable and linear response without the generation of additional lift at zero angle of attack, which is particularly desirable for the tail surfaces. This airfoil also demonstrates reliable performance throughout the range of Reynolds numbers anticipated for the aircraft and allows the control surfaces to remain effective even at large deflection angles, which is essential for maintaining stable flight during banner operations.

4.5.2 Lifting Surface Analysis

To identify the optimal aerodynamic configuration, a comprehensive analysis was performed on five wing geometries: a rectangular wing, an asymmetrical tapered wing, a wing with a constant-chord inboard section and tapered outboard sections, a wing with a tapered leading edge and straight trailing edge, and a wing with a straight leading edge and tapered trailing edge. The evaluation focused on aerodynamic performance and stability-related parameters, including lift, drag and moments about the principal aircraft axes (pitch, yaw and roll). The primary objective was to select the most stable and aerodynamically efficient wing configuration for the aircraft while adhering to the 5 ft length constraint, as specified in Table 5. Based on the analysis of all wing geometries, an asymmetric tapered wing configuration was selected, since it provided the best compromise between the previously discussed aerodynamic characteristics and structural design considerations. The tapered wing configuration allows the use of a straight main wing spar because

of its asymmetrical shape. This significantly simplifies the wing structure and manufacturing process, and at the same time enables high lift generation while maintaining reduced aerodynamic drag.

Based on conclusions, drawn from Section 4.3.3, the wing span was extended to the maximum allowable length of 5 ft despite the associated penalty in the scoring system. This decision was primarily driven by the significantly improved aerodynamic characteristics of a longer and narrower wing compared to a wing with lower aspect ratio. A longer and narrower wing provides lower induced drag, higher aerodynamic efficiency (C_L/C_D), a more favorable lift distribution along the wing span, and improved low-speed performance resulting in enhanced overall aircraft efficiency and stability.

Based on the analysis of the lift distribution results in XFLR5 [3], a root chord of 11.02” and a tip chord of 7.87” were selected. When defining the taper of the leading and trailing edges, the primary design driver was the placement of the main wing spar. Consequently, the wing was designed with a leading edge sweep of 1.8° aft, while the trailing edge was designed with a sweep of 5.3° forward.

As indicated by the criteria outlined in Section 3.4.4, the conventional tail represents the more favorable configuration, from an aerodynamic standpoint, primarily due to its lower susceptibility to deep stall and its superior control effectiveness at low airspeeds compared to T-tail configuration. The sizing of the horizontal and vertical stabilizers was performed using the tail volume coefficients, which establishes the relationship between the wing reference area, mean aerodynamic chord (MAC) and the respective tail volume coefficients. The values of these coefficients were adopted from literature [9]. Following these calculations, the horizontal stabilizer was designed with a tapered leading edge and a straight trailing edge, having a span of 8.66”, a root chord of 7.09” and a tip chord of 5.51”. The vertical stabilizer was configured with a span of 9.45”, a root chord of 5.91” and a tip chord of 4.33”.

4.5.3 Wing Control Surface Analysis

For the design and evaluation of wing control surfaces (flaps and ailerons), a structured simulation workflow was used to size the surfaces and compare configurations consistently. Based on previously conducted airfoil analyses, hinged control surfaces were added, with relative flap chord length of 35%, 25% and 15%, and relative aileron chord length of 25%, 20% and 15%, simulating deflections of 5° and 35° to capture both trimming behavior and performance limits.

To account for planform scaling effects, all configurations were tested at two distinct flap-to-airfoil size ratios (1:1 and 2:3). The control surfaces spanned nearly the full wing, with the exception of the fuselage intersecting region. A parametric optimization was conducted in which the deflection angle was systematically varied to determine the configuration providing the greatest aerodynamic efficiency. Initial increments of 2° (30°–50°) narrowed the promising range, which was then refined in 1° steps (42°–46°).

The results indicated that the 2:3 flap-to-airfoil size ratio provided the most suitable overall behavior, particularly in terms of producing predictable control authority. Within that geometry, the most favorable configuration was identified as an aileron sized at 20% of the chord and a flap sized at 25% of the chord. This combination was shown to offer the best balance between generating the required aerodynamic response and was therefore selected as the most optimal configuration for the aircraft.

4.5.4 Lift and Drag Analysis

The aircraft drag analysis was performed using a combination of established empirical methods and numerical analysis. The overall drag coefficient (C_D) was evaluated using the OpenVSP [4] software, which provides an efficient and reliable framework for aerodynamic geometry modeling and drag estimation.

The zero-lift drag coefficient was calculated using Eq. 17, which includes the skin friction coefficient C_f, the form factor FF, the wetted surface area S_{wet}, and the reference surface area S_{ref}. The Torenbeek method [10], implemented within OpenVSP, was used to determine the form factor and skin friction coefficient for each aircraft component. Induced drag was calculated using the Lifting-Line Theory (LLT) [10].

$$C_D = \frac{C_f \cdot FF \cdot S_{wet}}{S_{ref}} \tag{17}$$

Due to the nature of M3, it was also necessary to account for the drag of the banner in addition to the aircraft's drag. As detailed in Section 3.4.9, the banner drag coefficient was approximated at 0.02, as banner testing was not yet conducted at this stage. The flag's drag coefficient was first predicted using numerical simulations and subsequently subjected to experimental validation (Section 8.1). The drag of the banner was evaluated independently from the aircraft using its own appropriate reference area. For each component, the drag force was calculated with Eq. 18

$$D = \frac{1}{2}\rho V^2 C_D A_{\text{ref}} \tag{18}$$

where the aircraft drag was based on the wing reference area and the banner drag was based on the banner's projected frontal area. The two drag forces were then summed to obtain the total system drag. For performance analysis, the combined drag was finally expressed in terms of the aircraft wing reference area, allowing the total drag coefficient to be compared consistently with the baseline aircraft configuration. This approach resulted in predicted drag profiles for the aircraft under the considered mission scenarios. Figure 22a presents the predicted drag profile of the aircraft during missions M1 and M2 at the airspeed of 100 ft/s. Figure 22b shows the corresponding drag profile for mission M3 at the airspeed of 72.91 ft/s.

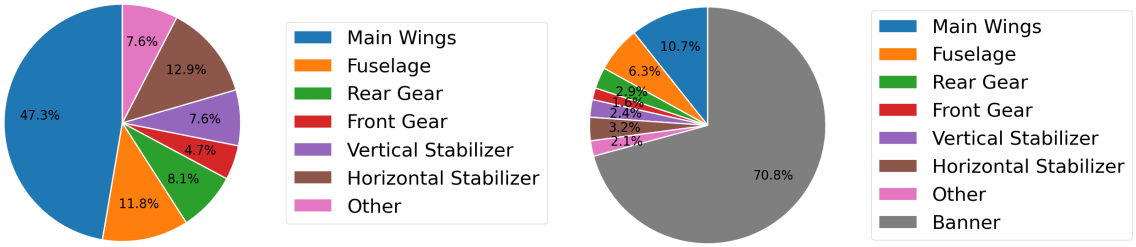

(a) Mission 1 and 2 (b) Mission 3

Figure 22: Drag Pie Chart

To evaluate the lift distribution along the wing, aerodynamic simulations were conducted using LLT. The calculations were based on the actual wing geometry, taking into account key parameters such as the aspect ratio, taper ratio and aerodynamic loading. The lift distribution was evaluated at multiple spanwise stations to assess how aerodynamic loading develops from root to tip. The results indicated regions of elevated sectional lift coefficients toward the outer span, which may increase the likelihood of tip stall at higher AoA. Such behavior can reduce aileron effectiveness and adversely affect lateral control near stall. Based on these observations, the wing design was selected to promote a more favorable root-first stall progression, thereby preserving controllability and ensuring predictable stall characteristics.

4.5.5 Drag Reduction Through Winglets

With M3 being the primary flight mission, as previously discussed in Section 4.3.1, additional focus was given to the optimization of the airplane's drag. The largest contributor to the total drag for all three flight missions was the main wing drag, only surpassed by the banner drag in M3, as seen in Figure 22. Therefore, it was decided to consider reducing the wing drag with winglets. After the thorough review of the relevant literature, raked and blended winglets were selected for further research. Based on studies by Lopez [11], Prieto et. al. [12] and Teschner [13], vortex lattice method (VLM) based workflow with Flow5 [14] was chosen to obtain the necessary aerodynamic data. To maintain proper airplane control and sizing of the flight control surfaces, two cases of winglet spans were investigated, one with 10% and the other with 15% of the wingspan. Similarly, maximum height and sweep were defined, forming a type of 3D design space box at the wingtip. To aid with the non-planar geometry input into the VLM solver, a custom Python script was written to populate all of the necessary values, which were also used to create geometrical representations shown in Figure 23.

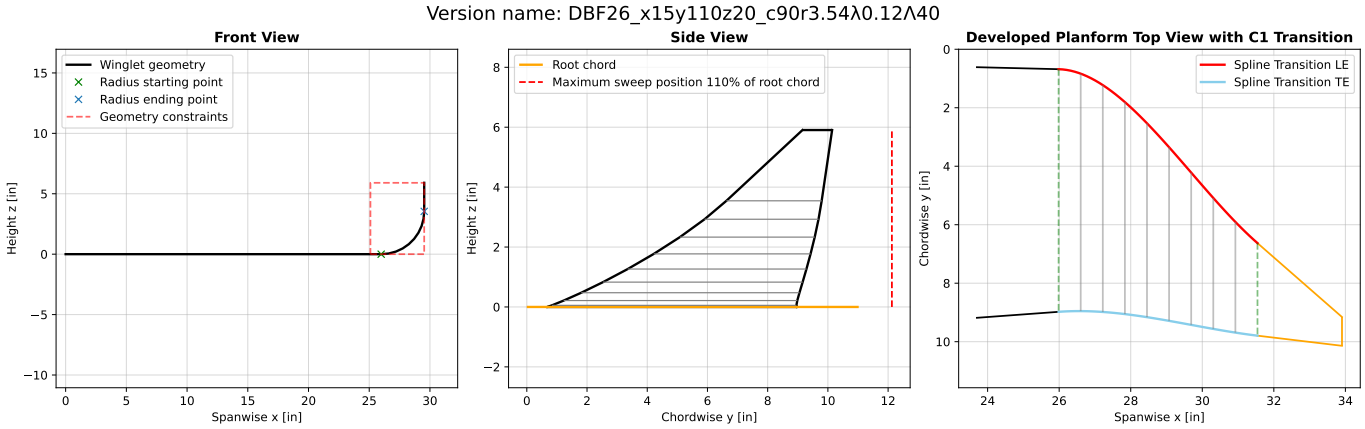

Figure 23: Discretized Winglet Geometry

To calculate the winglet operating point for M3, the speed profile was taken from the simulations and averaged for the level and turning flight conditions, with the wing's AoA calculated for both. Flow5's triangular uniform-density panel method was then used for analysis at both speeds, due to its reliability, fast calculations and the triangular mesh better conforming to the complex geometry at the wingtip to winglet junction. The resulting data was then interpolated between discrete AoA values, to ensure correct values for both flight conditions. The final values were obtained with the summation of weighted aerodynamic parameters, namely C_L and C_D, where the weights represented the proportion of time spent in the specific flight regime.

Initially, 126 different combinations were studied, varying the cant angles from 0° (raked winglet) to 90° with a step of 15°, blending radii between 30%, 60% and 90% of the maximum radius and three different sweep angles, one forming a winglet with a straight trailing edge, one limited by the rear sweep limit, and an in-between sweep angle. First simulations showed largest improvements in aerodynamic efficiency (C_L/C_D) for winglets of 15% wingspan and higher cant angles, so cases with cant angles between 75° to 90° were studied in more detail. Results in Figure 24a show a clear trend that a larger cant angle and sweep both improve efficiency, while similar trends were not observed for the blending radii.

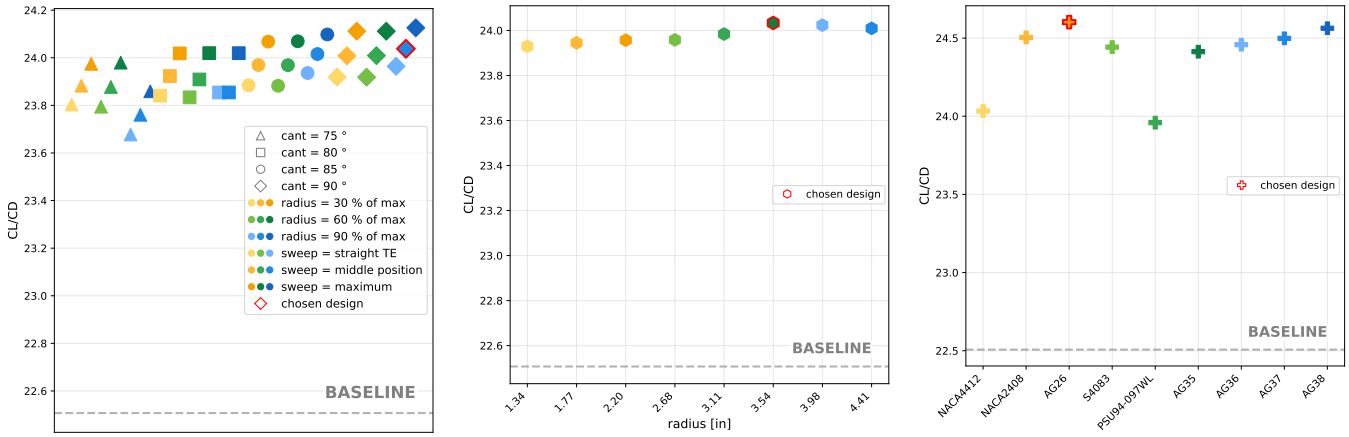

(a) Cant, Radius and Sweep Variation (b) Radius Variation (c) Airfoil Analysis

Figure 24: Analysis of Winglet Geometric and Aerodynamic Parameters

Based on the data presented in Figure 24a and Maughmer's research [15], a winglet with a 90° cant angle and a sweep of 40° was chosen as the optimal. Following that, two additional design iterations were performed, first varying the blending radius and second the winglet airfoil, as shown in Figures 24b and 24c, respectively. Due to the very different flow conditions across the winglet compared to the wing, more than 20 different airfoils (mainly chosen for their performance at low Reynolds numbers) were studied, with some of them presented in 24c. Finally, AG26 airfoil with a 3.54" radius was selected as the optimal. The last parameter studied was the tip twist, although its variation showed a minimal impact on the aerodynamic efficiency, thus a value of 0° was selected to simplify the manufacturing process. However, if the flight testing phase shows that the winglet stalls prematurely, tip twist could be added in the future.

4.6 Static Stability

Static stability analysis was performed to evaluate the inherent aerodynamic stability of the aircraft in all three axes. Since the banner towing configuration represents the most demanding operating case in terms of aerodynamic loading, the drag contribution of the banner was included in the model as an equivalent concentrated drag force acting at the towing attachment point. This additional drag was taken into account in the trim condition and in the computation of the stability derivatives.

Longitudinal static stability describes how the aircraft reacts to small disturbances in pitch. This behavior is evaluated through the derivative C_{m_α}, which represents the change in pitching moment with respect to angle of attack. For a statically stable aircraft, this derivative must be negative, meaning that an increase in angle of attack produces a restoring nose-down pitching moment. As shown in Figure 25a, the pitching moment coefficient C_m has a clear negative slope over the analyzed range of angles of attack. This confirms that the aircraft is longitudinally statically stable and naturally tends to return to its trimmed flight condition after small pitch disturbances.

Lateral static stability describes the aircraft response to a sideslip disturbance in terms of rolling motion. This behavior is evaluated using the derivative C_{l_β}, which represents the rolling moment generated by a sideslip angle. For positive lateral stability, this derivative must be negative so that a sideslip produces a restoring rolling moment. The rolling moment coefficient C_l shown in Figure 25b decreases with increasing sideslip angle, confirming negative C_{l_β}

and therefore positive lateral static stability. This means that the aircraft naturally resists roll deviations and tends to maintain a stable wings-level attitude.

Directional static stability describes how the aircraft reacts to sideslip in terms of yaw motion. This behavior is described by the derivative C_{n_β}, which represents the yawing moment generated by a sideslip angle. For a directionally stable aircraft, this derivative must be positive, meaning that a sideslip produces a restoring yawing moment that aligns the aircraft with the airflow. As observed in Figure 25c, the yawing moment coefficient C_n increases with the sideslip angle, indicating positive C_{n_β} and good directional static stability. This ensures stable heading control and predictable directional behavior, especially important when external disturbances, such as the banner, are present.

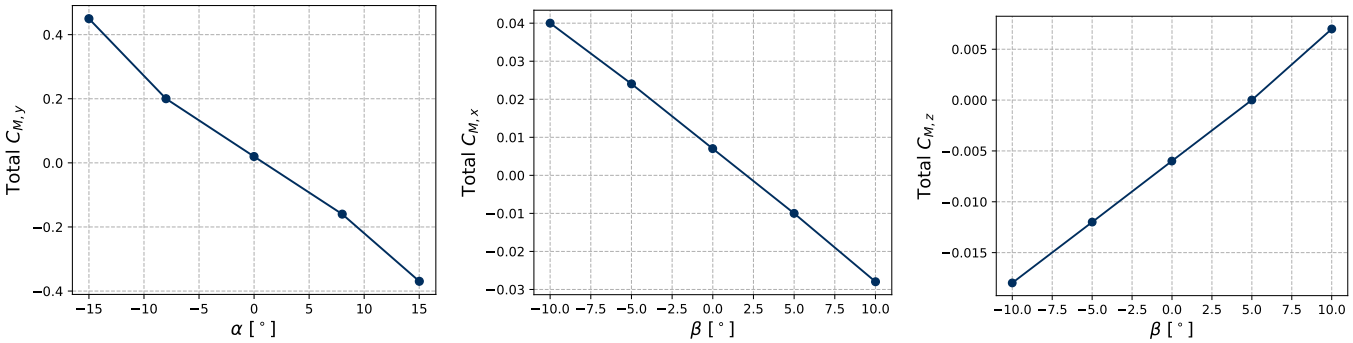

(a) Longitudinal (b) Lateral (c) Directional

Figure 25: Static Stability Characteristics Around Three Axes

4.7 Dynamic Stability

Dynamic stability analysis was performed in order to evaluate the time response of the aircraft to small disturbances around the trimmed flight condition. The same aerodynamic model and banner representations, used in the static stability analysis, were also applied here, meaning that the banner was included as an additional steady drag force acting at the towing attachment point. The dynamic response was analyzed by examining the longitudinal motion, focusing on the two dominant modes: the short-period mode and the phugoid mode.

Short-period mode represents the fast longitudinal response of the aircraft, mainly associated with rapid changes in angle of attack and pitch rate. This mode is primarily related to the aerodynamic characteristics of the wing and tail, and is important for handling qualities and pilot control. As shown in Figure 26a, the short-period response is highly damped, with oscillations that decay rapidly within a short time. This indicates that the aircraft reacts quickly to pitch disturbances and returns to equilibrium without sustained oscillations. Such behavior is desirable, as it ensures good pitch controllability and prevents aggressive or uncomfortable motion during small control inputs.

Phugoid mode represents the slow longitudinal motion involving the exchange between kinetic and potential energy, and is mainly associated with variations in airspeed and altitude. Compared to the short-period mode, the phugoid has a much lower frequency and longer time scale. As shown in Figure 26b, the phugoid response exhibits lightly damped oscillations that decay gradually over time. This confirms that the phugoid mode is dynamically stable, meaning that airspeed and altitude disturbances are naturally attenuated. Although this mode is slow, its stability is important for long steady flight segments, ensuring that the aircraft does not diverge in airspeed or flight path over time, especially during the banner is deployed.

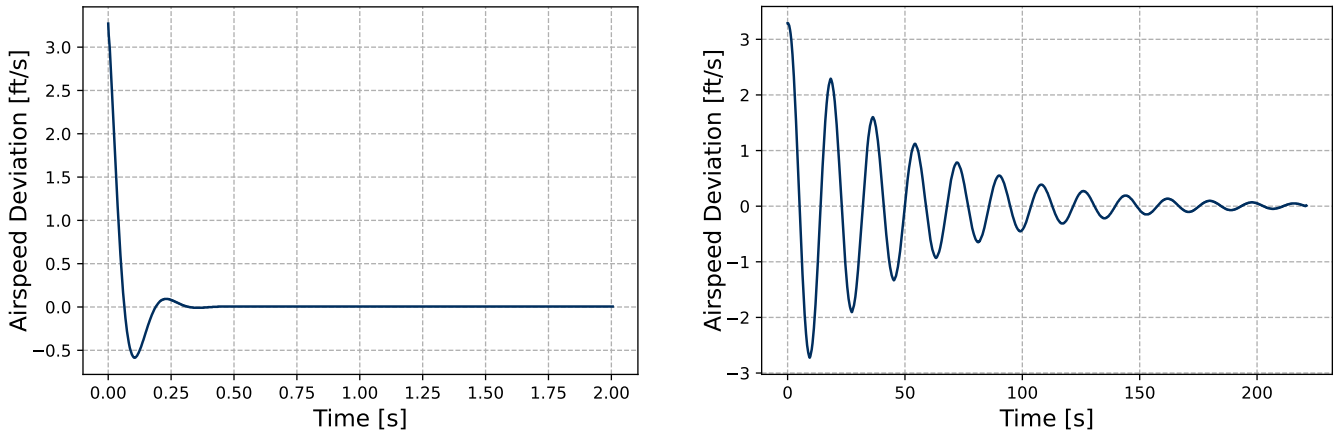

(a) Short-Period Mode Response (b) Phugoid Mode Response

Figure 26: Dynamic Longitudinal Response

4.8 Estimated Mission Performance

All performance characteristics were calculated using our mission model, which was refined using the insights from Section 4.5. Table 18 shows the predicted aircraft performance in each mission. All performance metrics were computed using the propulsion configuration consisting of a Kontronik PYRO 700-45 motor and APC 15×10E propeller, except the M3 banner length and number of laps, which are reported as ranges spanning both viable propulsion configurations identified in Section 4.3.4.

The optimal M2 payload consists of 3 passengers and 1 cargo unit, consistent with the adopted GM strategy. The adoption of the NACA 4412 airfoil did not affect the optimal banner length range, however it did offer better lift, drag and stall characteristics than the previously simulated CLARK Y airfoil. Since banner stowing is part of the GM and teams are allowed to bring two different banners to the competition, we reserved one banner exclusively for the GM. To minimize stowing time, and therefore overall GM time, we selected the minimum allowable length of 10” for this banner.

Table 18: Preliminary Design Mission Performance Characteristics

Performance Parameter	M1	M2	M3	GM
C_{Lmax}	1.48	1.48	1.48	/
$C_{Lcruise}$	0.065	0.070	0.368	/
$C_{Dcruise}$	0.017	0.018	0.352	/
L/D_{cruise}	3.82	3.89	1.05	/
Wing Loading [lbs/ft^2]	1.31	1.41	1.58	/
v_{cruise} [ft/s]	125.9	125.7	58.2	/
v_{stall} [ft/s]	27.29	28.27	29.94	/
Aircraft MTOW [lbs]	5.92	6.35	7.13	Varied
Carried Payload	/	3 passengers, 1 cargo unit (0.50 lbs)	1 banner (1.39–2.03 lbs)	3 passengers, 1 cargo unit, 1 banner (0.53 lbs)
Banner Length [in]	/	/	236.25–285.50	10
Number of Laps	3	13	5–6	/
Mission Time [s]	67	288	295	28
Mission Score	1.0	1.02	3.0	1.0

Figures 27 and 28 show predicted M2 and M3 ground speed profiles, using the propulsion configuration consisting of the previously mentioned propulsion configuration. For both profiles, a wind speed of 13.5 kt was assumed. For M3, the banner length was set to 236.25”. Decreases in ground speed correspond to turn maneuvers. Because the wind effect was accounted for, the first 180° upwind turn of each lap exhibited only a minimal reduction in ground speed,

whereas the second 180° downwind turn shows a larger and sharper decrease. The first sharp drop in M3 ground speed marks the moment the banner was deployed, which caused a sudden increase in drag.

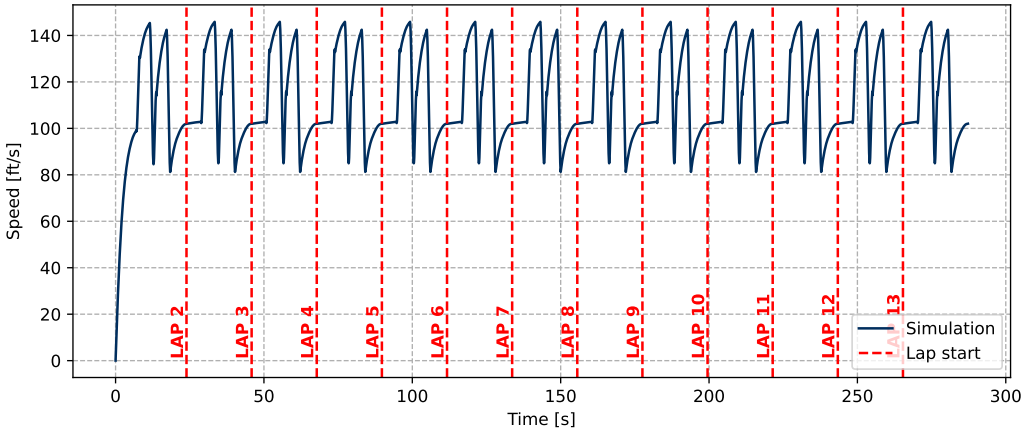

Figure 27: M2 Ground Speed Profile

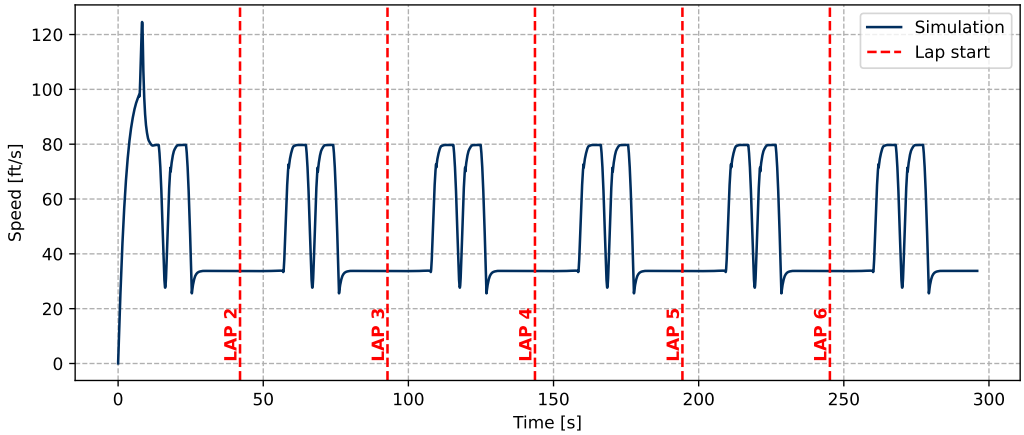

Figure 28: M3 Ground Speed Profile

5 Detail Design

5.1 Dimensional Parameters

Table 19 shows the main aircraft dimensions and characteristics the team deemed ideal for this year's competition.

Table 19: Aircraft Dimensions

Fuselage		Vertical Tail	
Fuselage length [in]	56.60	Airfoil	NACA 0012
Maximum width [in]	3.94	Span [in]	8.27
Maximum height [in]	4.72	Chord-base [in]	5.51
Wing		Chord tip [in]	3.54
Airfoil	NACA 4412	Wing Area [ft^2]	0.26
Span [in]	59.06	Aspect Ratio	1.83
Chord-base [in]	11.02	Horizontal Tail	
Chord tip [in]	7.87	Airfoil	NACA 0012
Wing Area [ft^2]	3.94	Span [in]	17.32
Aspect Ratio	6.14	Chord-base [in]	7.09
Angle of Incidence [°]	1.5	Chord tip [in]	5.51
Dihedral Angle [°]	0	Wing Area [ft^2]	0.76
Twist [°]	0	Aspect Ratio	2.75

5.2 Systems and Sub-Systems Integration

5.2.1 Fuselage and Payload Integration

The fuselage features a monocoque structural design integrating the avionics system, banner mechanism, and separated payload compartments, as illustrated in Figure 29. The passenger compartment is positioned above the low-mounted wing and is designed to accommodate three ducks. The cargo compartment is located forward of the wing and houses the puck restraint mechanism with a single puck. Both compartments are accessible through dedicated upper fuselage hatches, equipped with a quick-release mechanism to minimize GM loading and unloading time. The banner mechanism is located at the bottom of the fuselage, behind the wing and the main landing gear sub-assembly. In its stowed configuration, the banner is mounted externally under the fuselage, extending from the front landing gear to the tail section. The propulsion battery is mounted on a tray, located aft of the front landing gear, while the receiver is positioned behind the banner mechanism. Both components are secured using Velcro.

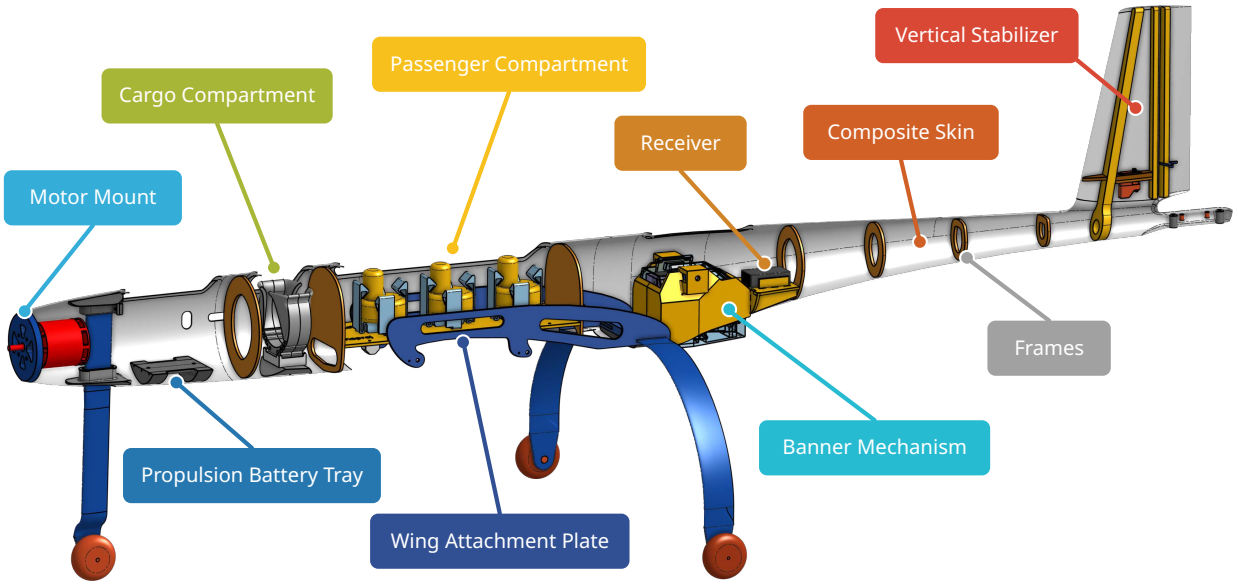

Figure 29: Fuselage Design

The fuselage skin is made from fiber-reinforced composite sandwich structure with an aramid honeycomb core. A 0.08” thick carbon fiber wing attachment plate is incorporated within the fuselage skin and serves as the primary structural interface between the fuselage, wing and main landing gear fixture. This configuration ensures efficient load transfer and distribution across the airframe during all flight phases. The banner mechanism is structurally linked to this rib via the landing gear fixture, providing a continuous load path. Internal Airex or Airex-fiberglass composite frames provide local support and geometric stability to the fuselage shell and support internal subsystems. With the motor installed internally, the motor loads are transferred into the fuselage structure through a carbon-fiber-reinforced medium-density fiberboard (MDF) motor mount located at the front of the fuselage. Additional service hatches are incorporated on the upper fuselage surface to provide access to the avionics and banner mechanism.

The fuselage structure also integrates the vertical stabilizer, reducing structural complexity and weight while improving rigidity and manufacturability. The servo motor for the control surface is fastened to 0.12” thick plywood rib, and the hinge is integrated directly into the skin using an aramid laminate hinge.

5.2.2 Horizontal Stabilizer

The horizontal stabilizer, shown in Figure 30, is positioned slightly behind the vertical stabilizer to simplify assembly and mounting. It is secured to the empennage using two bolts, threaded into a central 3D-printed rib in the horizontal stabilizer. These bolts can also accommodate ballast to adjust the center of gravity (CG) for different missions. The servo motor is fastened to the central 3D-printed rib. Additional 0.39" Airex spars and 0.12" Airex-fiberglass composite ribs are added to support the structure.

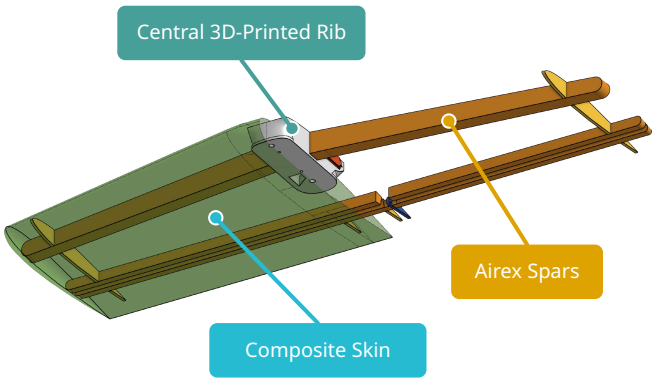

Figure 30: Horizontal Stabilizer Design

5.2.3 Wing

The wing, shown in Figure 31, has a tapered planform with an aspect ratio of 6.14. The primary load-bearing structure consists of a composite skin, the front spar and the rear spar. Together they form a torsionally stiff structure and provide an efficient load path into the fuselage through fuselage attachment ribs bonded directly to the spars. These ribs are cut out from 0.08" thick carbon fiber sheets and secured to the fuselage structure using four M4 bolts. The skin forms the airfoil shape and is manufactured from a carbon fiber and foam sandwich structure, which provides torsional stiffness to the wing. Each spar is composed of an Airex foam shear web, reinforced with fiberglass laminate and unidirectional (UD) carbon fiber strips that form the spar caps. The web and caps thus form a rigid beam that carries bending and shear loads.

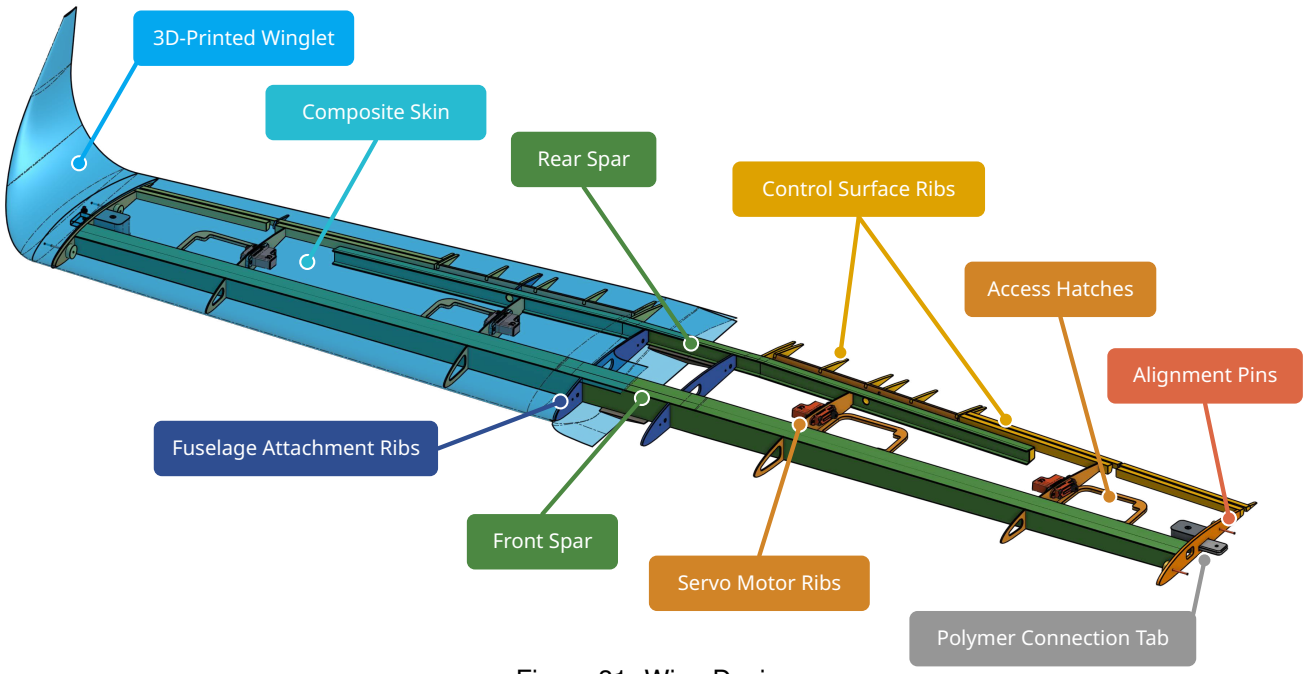

Figure 31: Wing Design

The control surfaces pivot around an aramid laminate hinge integrated directly into the wing skin and are reinforced with a combination of 0.39” Airex and 0.12” Airex-fiberglass composite ribs. The servo motors are fastened to 0.12” thick plywood ribs, which provide a precise and reliable mounting point, and helps evenly distribute the actuator-induced moments into the wing structure. Removable service hatches are incorporated into the lower skin to allow inspection and maintenance access to the servos and control linkages. The tip of the wing has a 3D-printed winglet, mounted via two alignment pins and a fastened polymer connection tab, which also serves as a controlled failure point in case of a wing strike.

5.2.4 Landing Gear

The tricycle landing gear, shown in Figure 32, is manufactured using a forged carbon technique and provides 1.58” of ground clearance for the propeller. The front landing gear is located aft of the motor and attached to both the upper and lower fuselage skins to counter landing-induced moment loads. Both fixtures feature a large surface area with a central hole for the strut to pass through, ensuring distributed load transfer to the fuselage. The lower front-gear fixture is 3D-printed, while the upper fixture is made of forged composites to prevent the strut from penetrating the fuselage skin under expected loads. A deformable 3D-printed thermoplastic polyurethane (TPU) ring is placed between each fixture and the strut to act as a dampener. To prevent movement of the strut along the Z-axis, a 3D-printed blocker is bolted to the upper fixture.

The main landing gear, shown in Figure 32, is split into two halves and secured to the fuselage via an H-shaped forged carbon fixture. This fixture efficiently counters landing-induced moments and transfers loads through the wing attachment plates. Additionally, it provides a rigid attachment point for the banner mechanism, allowing its loads to be transmitted to the wing attachment plates. Both the front and main struts feature an airfoil-shaped cross-section to minimize aerodynamic drag.

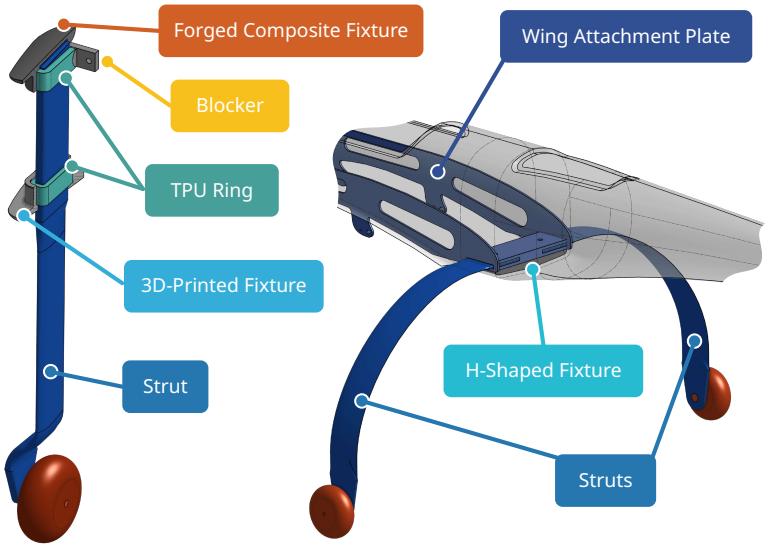

Figure 32: Front Landing Gear (left) and Main Landing Gear (right) Design

5.2.5 Passenger and Cargo Mechanisms

Since the GM-oriented strategy was adopted (Section 4.3.1), significant effort has been dedicated to cargo and passenger mechanisms to ensure fast installation and removal while safely securing the puck and ducks. To improve

GM time, the mechanisms are located at the center of the fuselage for easy access.

The cargo mechanism, based on the concept presented in Section 3.4.6, consists of 3D-printed circular clamps with integrated springs that deform during loading and unloading of the puck. The shape was optimized to better secure the cargo, and the side walls are now integrated into the clamps. A funnel-shaped top was added to mitigate human error during installation, allowing angled insertion and minimizing installation failures. The springs store energy and clamp the puck once it is fully inserted. The final mechanism is shown in Figure 33.

The passenger mechanism also underwent several iterations, with changes to parameters such as the number of hooks, their size and angle, and spring dimensions, to find the best version for securing the variable shape of ducks. The passenger mechanism works similarly to the cargo mechanism, with compliant hooks that bend during loading and unloading of ducks and remain bent, providing constant force to secure them in place. The final design, shown in Figure 34, allows us to secure a wide range of duck shapes and enables quick loading and unloading.

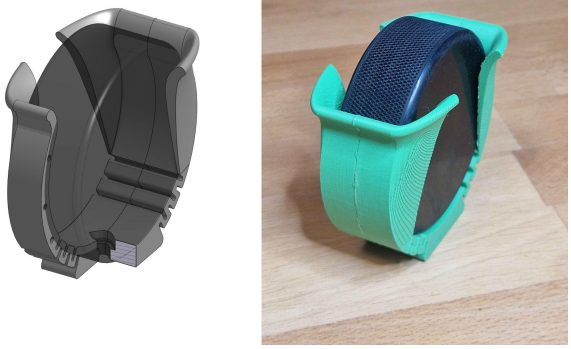

Figure 33: Final Cargo Mechanism

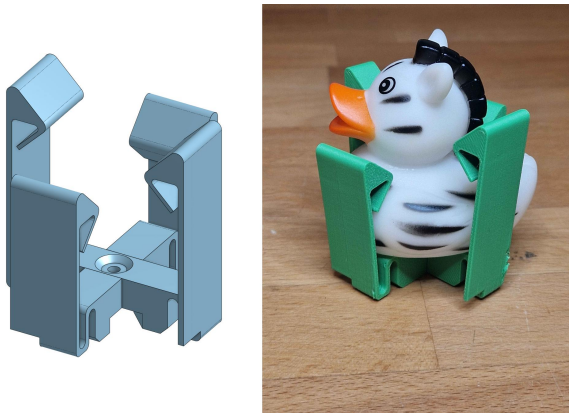

Figure 34: Final Passenger Mechanism

The two mechanisms give the GM crew member easy access to the fuselage to quickly remove cargo or passengers. The team also conducted extensive GM testing, discussed in Section 7.4, to ensure the mechanism's reliability.

5.2.6 Banner Deployment, Towing and Release Mechanism

The final banner mechanism combines the release principle chosen in Section 3.4.8 with a removable design that was introduced after Q&A #2 [16]. The clarified rules require installation of the mechanism during GM, making the previously permanently attached mechanism unsuitable. To retain the proven concept while adhering to the rules, the mechanism was redesigned as a fully self-contained module.

The system consists of two main elements: fuselage-integrated guides, and a deployment, towing and release mechanism. The guides create an empty space within the fuselage, allowing the mechanism to be inserted from the underside. A spring-loaded pin automatically engages during insertion, locking the mechanism in place as illustrated in Figure 35.

The deployment, towing and release mechanism contains two independent sub-mechanisms: one for banner deployment and one for release. The deployment sub-mechanism secures the stowed banner with a Velcro strap. One end of the strap is attached to the mechanism via Velcro, while the opposite end, which incorporates a metal loop, is retained by a movable pin. Actuation of the deploy servo retracts this pin, releasing the strap and allowing the banner

to unfold. The towline release sub-mechanism retains a loop at the end of the towline with a second servo-actuated pin. When commanded by the pilot, the pin is retracted, detaching the banner from the aircraft (illustrated in Figure 35). Both locking pins are 3D-printed from acrylonitrile styrene acrylate (ASA) filament and are connected to servo arms using standard clevises and push rods. For accurate positioning, pyramid-shaped alignment features on the mechanism (seen in Figure 36) interface with a matching 3D-printed element on the banner leading edge, ensuring precise and repeatable alignment.

The entire module is electrically self-contained, incorporating its own 2S battery and a receiver. This eliminates the need for electrical connections during installation, reducing ground handling complexity and improving robustness during GM operations.

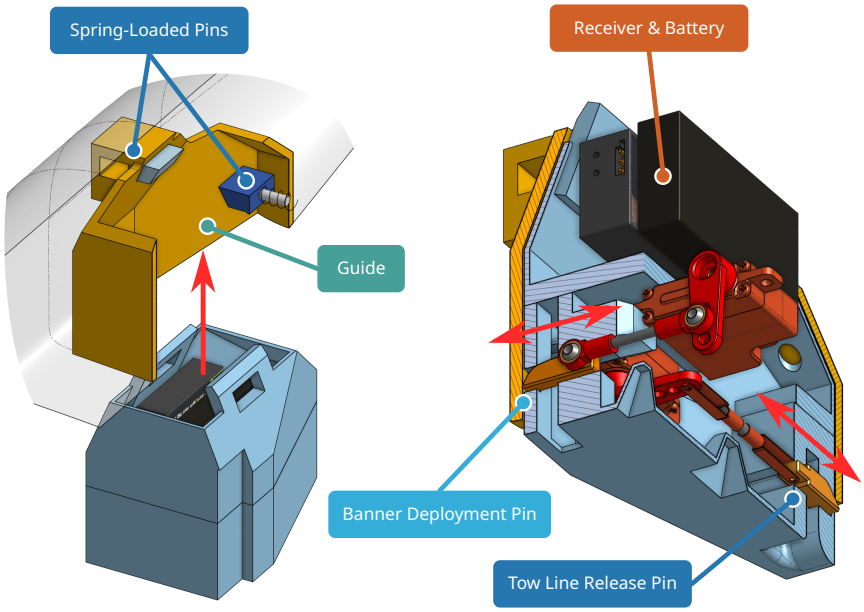

Figure 35: Banner Mechanism Design

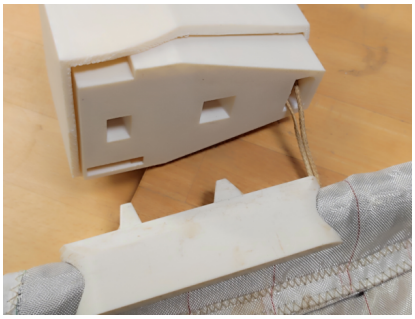

Figure 36: Pyramid Shapes for Alignment

5.2.7 Banner Rigging

The banner's leading edge is attached to a carbon fiber tube to maintain the rectangular shape. A ballast weight is inserted into one end of the tube to help keep a stable upright orientation during flight. To ensure reliable deployment, a spool was added to the towline to prevent tangling during release.

5.2.8 Propulsion

The aircraft is powered by a Kontronik PYRO 700-45 brushless motor, capable of producing up to 2.5 kW of continuous power. It was selected based on testing results, detailed in Section 7.2, which established a lower battery consumption compared to the other propulsion candidate, making it more suitable for this year's endurance nature of M2 and M3. It is controlled by the APD 120F3 v2 ESC, which was chosen for its light weight compared to other ESC-s of similar capabilities as it has no heat sink. Therefore, it had to be mounted outside of the fuselage to ensure sufficient cooling. One 4500 mAh 6S 22.2 V lithium-polymer (LiPo) battery is connected through an externally mounted 100 A fuse to the ESC, supplying the entire propulsion system. All of the components are placed at the front of the aircraft to move the CG forward, and are easily accessible through a hatch.

5.2.9 Avionics

The avionics system, consisting of a receiver, four Chaservo HV95 and two Chaservo HV75 servo motors, is powered by a 1000 mAh 2S 7.4 V LiPo battery. The signal integrity of the radio connection is ensured with a dual-band FrSky Tandem TD SR10 receiver, which provides low latency and reliable signal integrity as it works on both 2.4 GHz and 900 MHz simultaneously. With its built-in advanced stabilization functions, it facilitates the pilot's control during flight. Furthermore, the ESC offers voltage, current and motor RPM telemetry, which will help us adjust our strategies during the competition to ensure optimal performance. The banner mechanism is an independent system to enable quick installation during the GM. It consists of a FrSky Archer SR8 PRO receiver, two Chaservo HV95 servos and is powered by a 650 mAh 2S 7.4 V LiPo battery. The wiring diagram is shown in Figure 37.

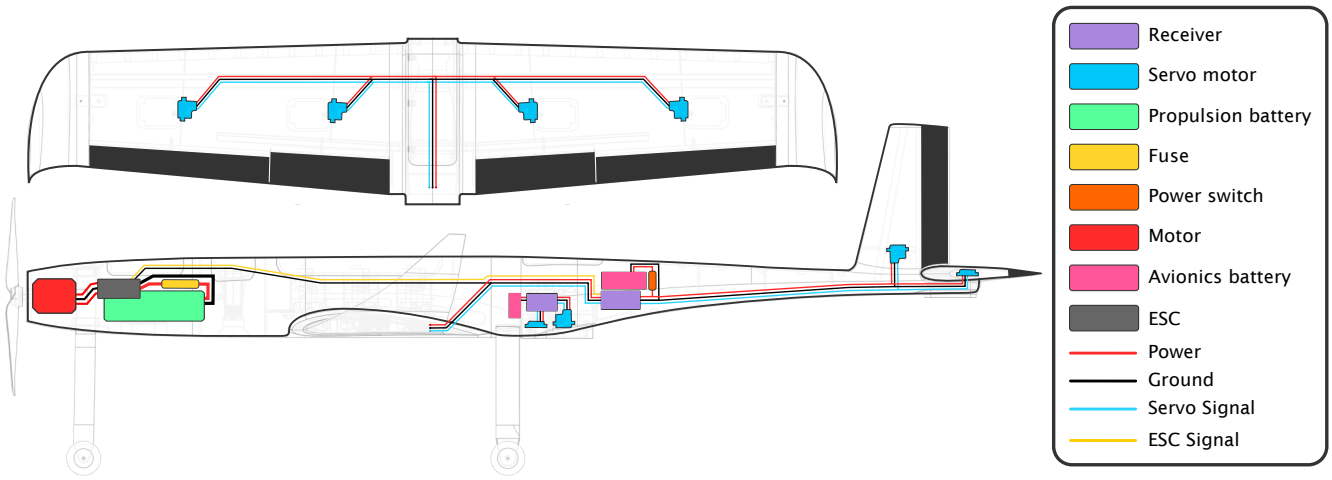

Figure 37: Wiring Diagram

A separate independent data-logging system is used to collect data exclusively during testing. It consists of a CubePilot Cube Orange+ flight controller (FC), a Here4 GPS and a Mauch power meter, and is running ArduPilot firmware with Plane BlackBox Logger build [17]. All data is logged on an SD card and analyzed after test flights.

5.2.10 Structural Characteristics

The aircraft's structure is engineered to transfer all the aerodynamic, ground and propulsion forces acting upon the airplane to the primary load-bearing components as illustrated in Figure 38. The center piece of the aircraft's structure are two carbon fiber wing attachment plates, serving as the mounting point for the wing and landing gear. Furthermore, the main landing gear fixture also serves as a base for the banner mechanism. Composite fixtures and frames distribute the loads across the fuselage skin, while the propulsion forces and torque are carried through the motor mount, bonded to the reinforced laminate. The wing's horizontal and vertical aerodynamic loads are transferred through the skin to the spars and ultimately to the fuselage attachment ribs. Loads generated by the empennage are likewise transferred into the fuselage skin structure. The inertial and aerodynamic forces of the banner are directed through the banner mechanism into the main landing gear fixture.

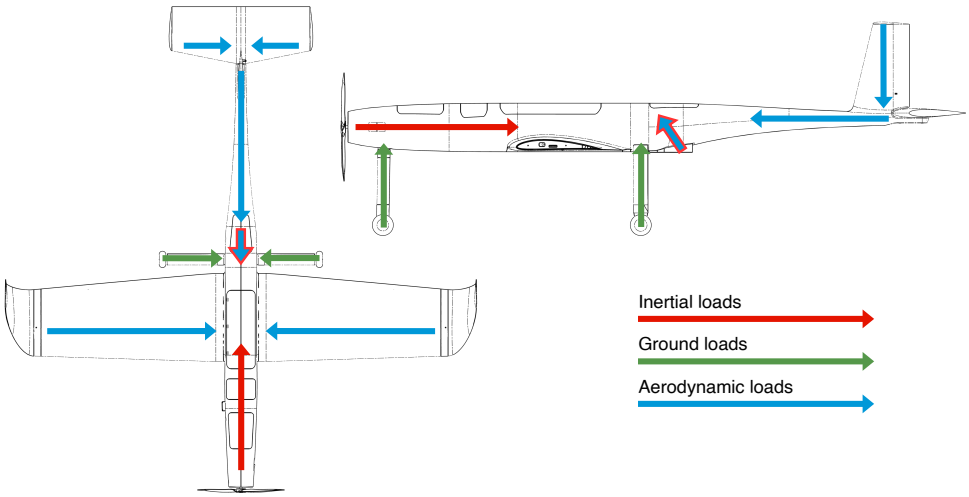

Figure 38: Load Path Diagram

A finite element analysis (FEA) was performed in Ansys [18] to evaluate the wing's ability to withstand expected loads during flight. To improve computational efficiency, only half of the wing was analyzed, taking advantage of its symmetry. The wing's surface was first split into the upper and lower half. Each half was then divided into five chordwise regions and each chordwise region was further divided into five spanwise regions, totaling 50 elements. A computational fluid dynamics (CFD) analysis in Ansys was used to calculate lift in each of the 50 elements during a 10 g turn at the aircraft MTOW of 8.05 lbs. The obtained lift was then multiplied with a safety factor of 2 and applied as pressure on the structural model. Fixed support boundary conditions were applied to the rib where the wing is fastened to the fuselage and at the wing root where symmetry was applied. The mesh was composed of finite elements sized at 0.25". The analysis was static, excluding vibrations and dynamic effects.

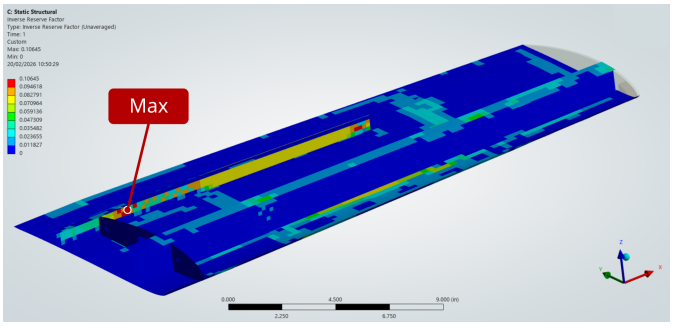

Figure 39: Inverse Reserve Factor of the Wing

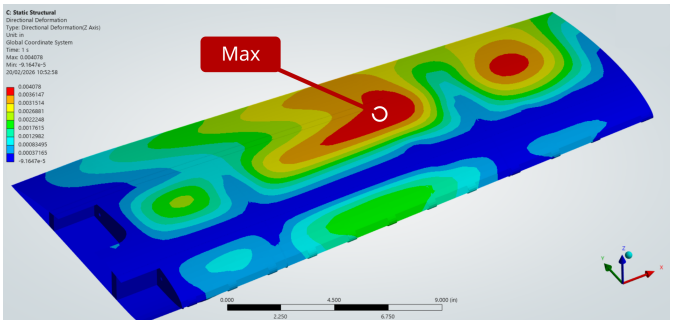

Figure 40: Total Deflection of the Wing

The analysis confirmed that the wing can withstand the required loads without sustaining any structural damage, as shown in Figure 39. The inverse reserve factor (IRF) measures proximity to failure in composite elements, with values above 1 indicating failure. The highest IRF recorded was 0.11, meaning that the structure can endure significantly higher loads than required. This indicates that less material can be used for the competition aircraft's wing and thus lowering its weight. The maximum recorded wing deflection was 0.04" (Figure 40).

A FEA in Ansys [18] was also performed on the main landing gear to verify its structural characteristics during ground operations. Adequate ground clearance has to be maintained while remaining as lightweight as possible. The

analysis showed that the landing gear's deformation in vertical direction experiencing 4 g landing at MTOW is 1.15" (Figure 41), which is sufficient for maintaining required ground clearance. The failure was predicted at 56 lbf.

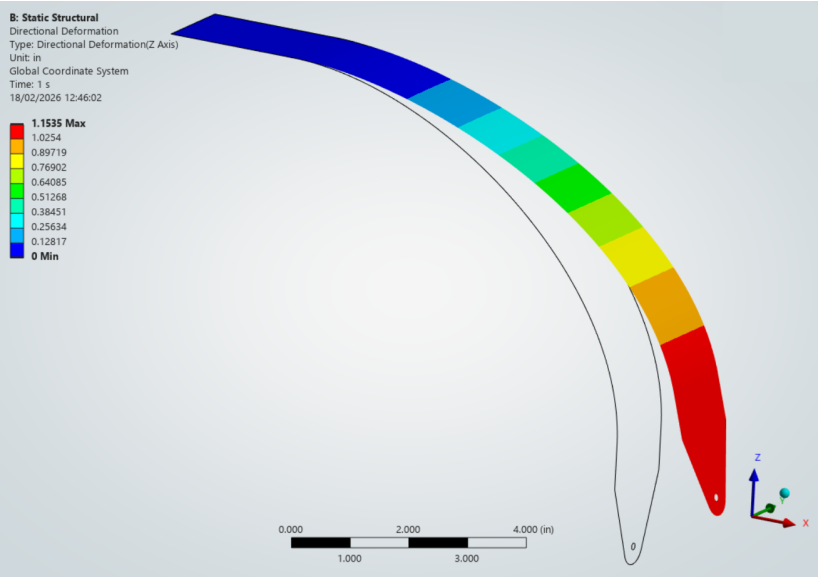

Figure 41: Deflection of Landing Gear in Vertical Direction

5.2.11 Weight and Balance

To ensure stability and planned aerodynamic behavior of the final aircraft, Table 20 was created. The planned CG location is set at 30% MAC of the main wing. Component's locations were measured from the computer-aided design (CAD) model in regards to the datum set at the front surface of the motor mount, where Y denotes the distance along the airplane's longitudinal axis. First, weight estimates were used to determine the CG, which was later adjusted as every sub-component was weighed after it was manufactured. Mission specific CG location in relation to MAC is presented for every mission. Counterweights are added to the tail for M1 and M2, as the aircraft CG was optimized for M3. Due to the significant weight of the banner, relative to the aircraft, the CG location following the release of the banner in M3 was also analyzed to ensure it stays within an acceptable range.

Table 20: Weight & Balance

Aircraft Component	Weight [lb]	Y [in]	Aircraft Component	Weight [lb]	Y [in]
M1 — 28.62% MAC					
Propeller	0.10	−0.48	Fuselage	1.23	24.25
Motor	0.86	1.48	Wing	1.87	22.87
ESC	0.11	4.94	Horizontal stabilizer	0.29	56.57
Propulsion battery	1.52	8.48	Transmitter and battery	0.15	34.25
Front landing gear	0.18	3.54	M1 ballast weight	0.17	57
Rear landing gear	0.35	28.54	**Total M1**	6.83	18.90
M2 — 28.91% MAC					
Passenger	0.04	16.54	Puck	0.38	12.24
Passenger	0.04	19.69	M2 ballast weight	0.24	57
Passenger	0.04	22.83	**Total M2**	**7.40**	**18.93**
M3 towing phase — 37.53% MAC					
Banner	1.39	29.25	**Total M3 towing phase**	**8.05**	**19.89**
M3 landing phase — 21.43% MAC					
/	/	/	**Total M3 landing phase**	**6.66**	**17.93**

5.3 Flight and Mission Performance

Flight performance characteristics as well as mission results of the final aircraft were determined and are shown in Table 21. These predictions account for all changes made to the mission model based on testing inputs, described in Section 8. Banner lengths, mission times, lap counts and scores were calculated assuming a wind speed of 13.5 kt.

Table 21: Detailed Mission Performance Characteristics

Performance Parameter	M1	M2	M3	GM
C_{Lmax}	1.42	1.42	1.42	/
$C_{Lcruise}$	0.160	0.163	0.369	/
$C_{Dcruise}$	0.042	0.042	0.352	/
L/D_{cruise}	3.81	3.89	1.05	/
Wing Loading [lbs/ft^2]	1.73	1.88	2.04	/
v_{cruise} [ft/s]	137.0	136.6	64.6	/
v_{stall} [ft/s]	32.25	39.23	34.94	/
Aircraft MTOW [lbs]	6.83	7.40	8.05	Varied
Carried Payload	/	3 passengers, 1 cargo unit (0.50 lbs)	1 banner (1.39 lbs)	3 passengers, 1 cargo unit, 1 banner (1.89 lbs)
Banner Length [in]	/	/	226.25	10
Number of Laps	3	13	5	/
Mission Time [s]	66.80	287.25	234.70	26.3
Mission Score	1.0	1.02	3.0	1.0

5.4 Drawing Package

The following section contains the 3-view drawing, the structural arrangement drawing, the system's layout drawing and the payload accommodation drawing. The first sheet shows the 3-view drawing with dimensions of all configurations, the following two sheets show structural arrangement and the system's layout. The last page in this section shows the passenger and payload accommodation with detail views of the passengers, cargo and banner deployment, towing and release mechanisms.

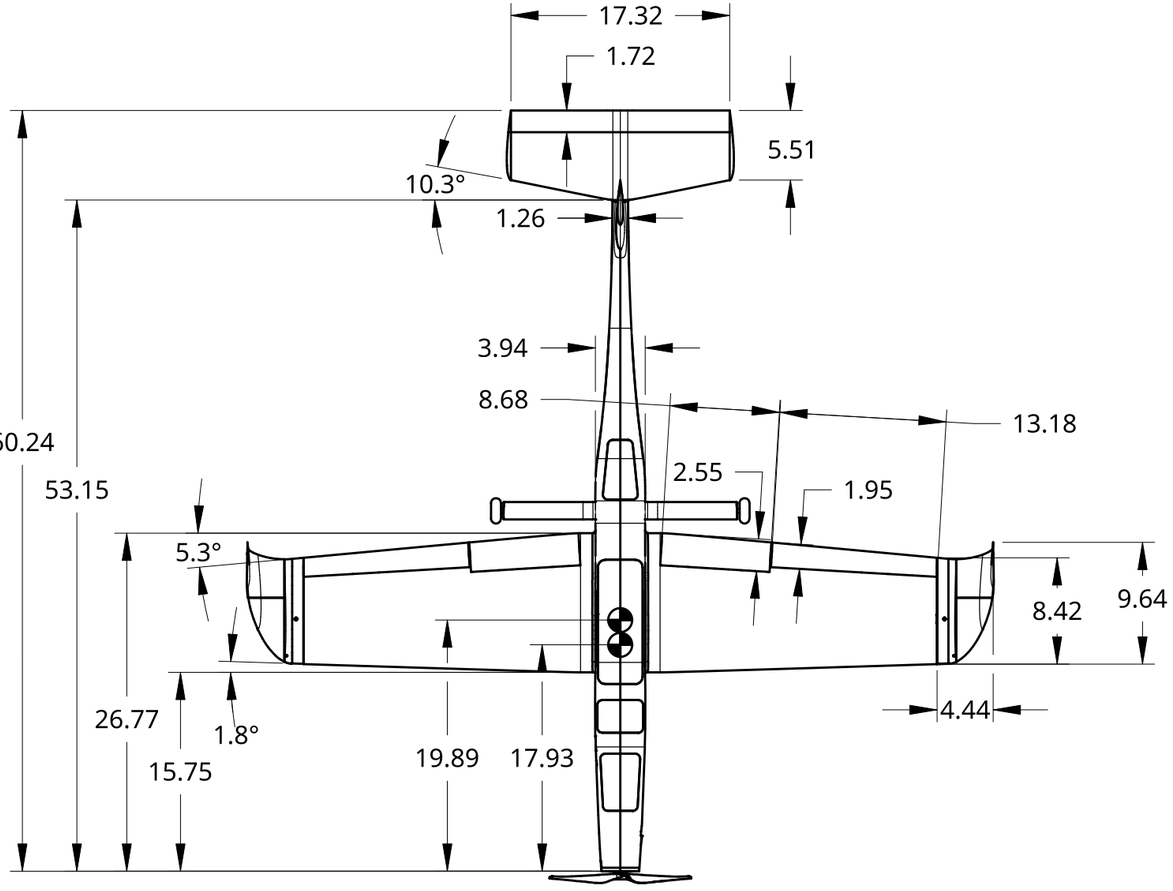

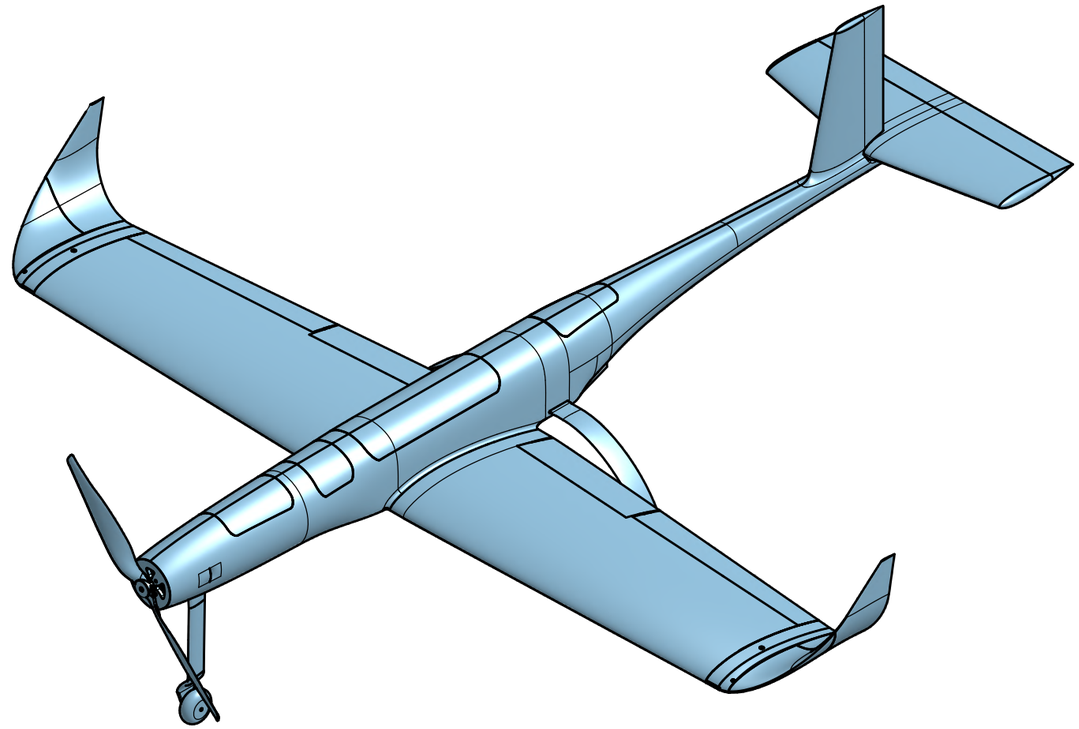

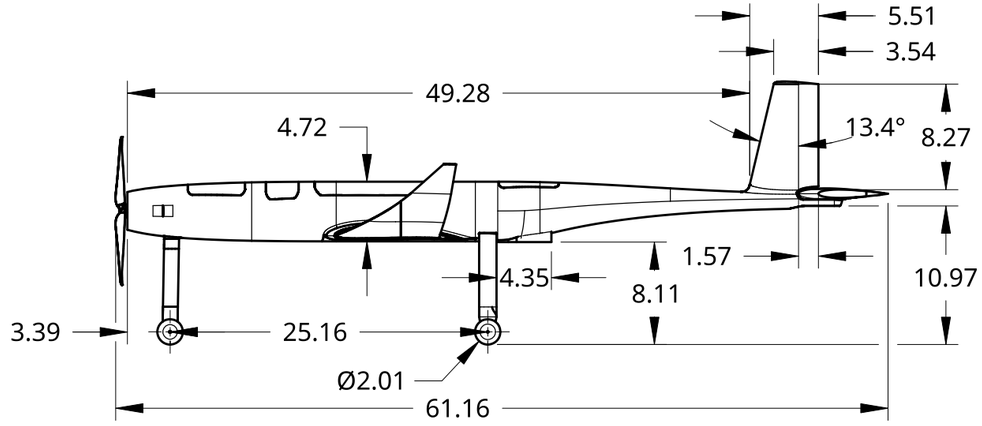

NOTE: AFTMOST CG IS AT 19.89 IN
FORWARDMOST CG IS AT 17.93 IN

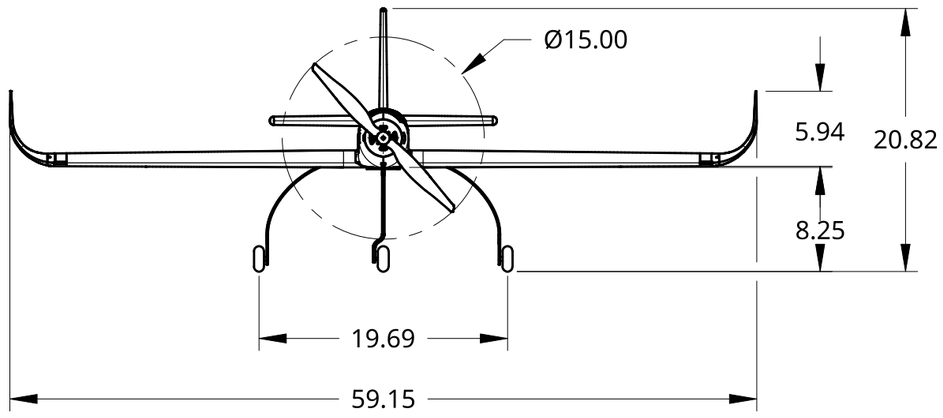

	NAME	DATE
DRAWN	BORUT PURGAR	02/14/2026
CHECKED	MATEJ MARKUŽA	02/20/2026
APPROVED	MATEJ MARKUŽA	02/20/2026

ALL DIMENSIONS IN INCHES
UNLESS SPECIFIED OTHERWISE

THIRD ANGLE PROJECTION

UNIVERSITY OF LJUBLJANA
EDVARD RUSJAN TEAM

TITLE

3 POINT VIEW

SIZE	DWG NO.	REV.
B	ERT2026-1	

SCALE	WEIGHT	SHEET
1:12	6.83 lbs	1 of 1

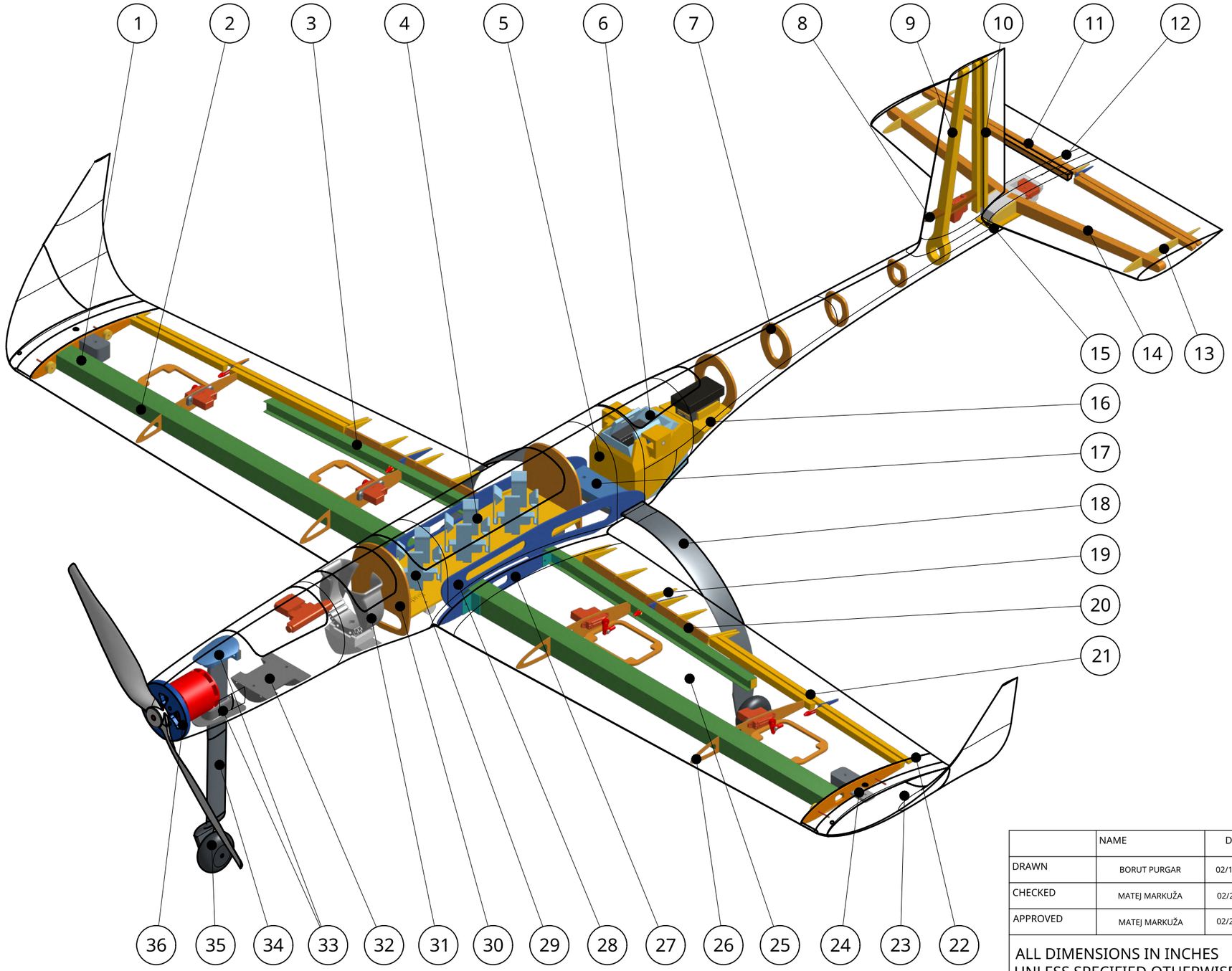

ITEM	QTY.	DESCRIPTION	MATERIAL
1	2	Front Wing Spar Cap	UD CF
2	1	Front Wing Spar Web	GF + Airex
3	1	Rear Wing Spar	UD CF + GF + Airex
4	1	Passenger Compartment Floor	Plywood
5	2	Banner Mechanism Guide	ASA
6	1	Banner Mechanism	ASA
7	4	Tail Structural Frame	GF + Airex
8	1	Vertical Tail Rib	Plywood
9	1	Vertical Tail Spar	Airex
10	1	Rudder Spar	Airex
11	2	Elevator Spar	Airex
12	4	Elevator Rib	GF + Airex
13	2	Horizontal Tail Rib	GF + Airex
14	2	Horizontal Tail Spar	Airex
15	1	Horizontal Tail Interface	CF + Plywood
16	1	Electronics Tray	Plywood
17	1	Main Landing Gear Fixture	CF + PETG
18	2	Main Landing Gear Strut	CF
19	12	Flap Rib	GF + Airex
20	2	Flap Spar	Airex
21	8	Aileron Spar	Airex
22	6	Aileron Rib	GF + Airex
23	2	Winglet	ASA
24	2	Winglet Interface	PETG + Plywood
25	/	Aircraft Skin	CF + GF + Airex
26	4	Servo Motor Rib	Plywood
27	2	Fuselage Attachment Rib	CF
28	2	Wing Attachment Plate	CF
29	3	Passenger Mechanism	PETG
30	2	Fuselage Frame	CF + Airex
31	1	Cargo Mechanism	PLA
32	1	Propulsion Battery Tray	PLA
33	2	Front Landing Gear Fixture	CF + PETG + TPU
34	1	Front Landing Gear Strut	CF
35	3	Wheel	Rubber
36	1	Motor Mount	CF + MDF

	NAME	DATE
DRAWN	BORUT PURGAR	02/14/2026
CHECKED	MATEJ MARKUŽA	02/20/2026
APPROVED	MATEJ MARKUŽA	02/20/2026

ALL DIMENSIONS IN INCHES
UNLESS SPECIFIED OTHERWISE

THIRD ANGLE PROJECTION

UNIVERSITY OF LJUBLJANA
EDVARD RUSJAN TEAM

TITLE

STRUCTURAL ARRANGEMENT

SIZE	DWG NO.	REV.
B	ERT2026-2	

SCALE	WEIGHT	SHEET
1:5	6.83 lbs	1 of 1

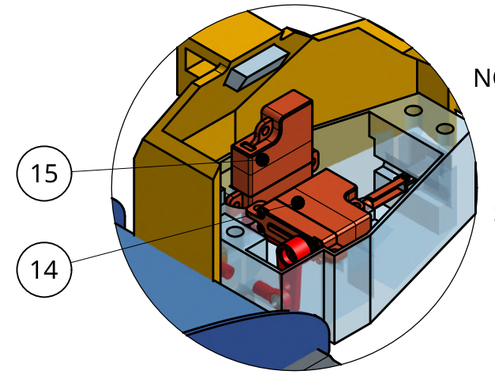

DETAIL A
SCALE 1:2

NOTE: SOME PARTS ARE HIDDEN FOR CLARITY

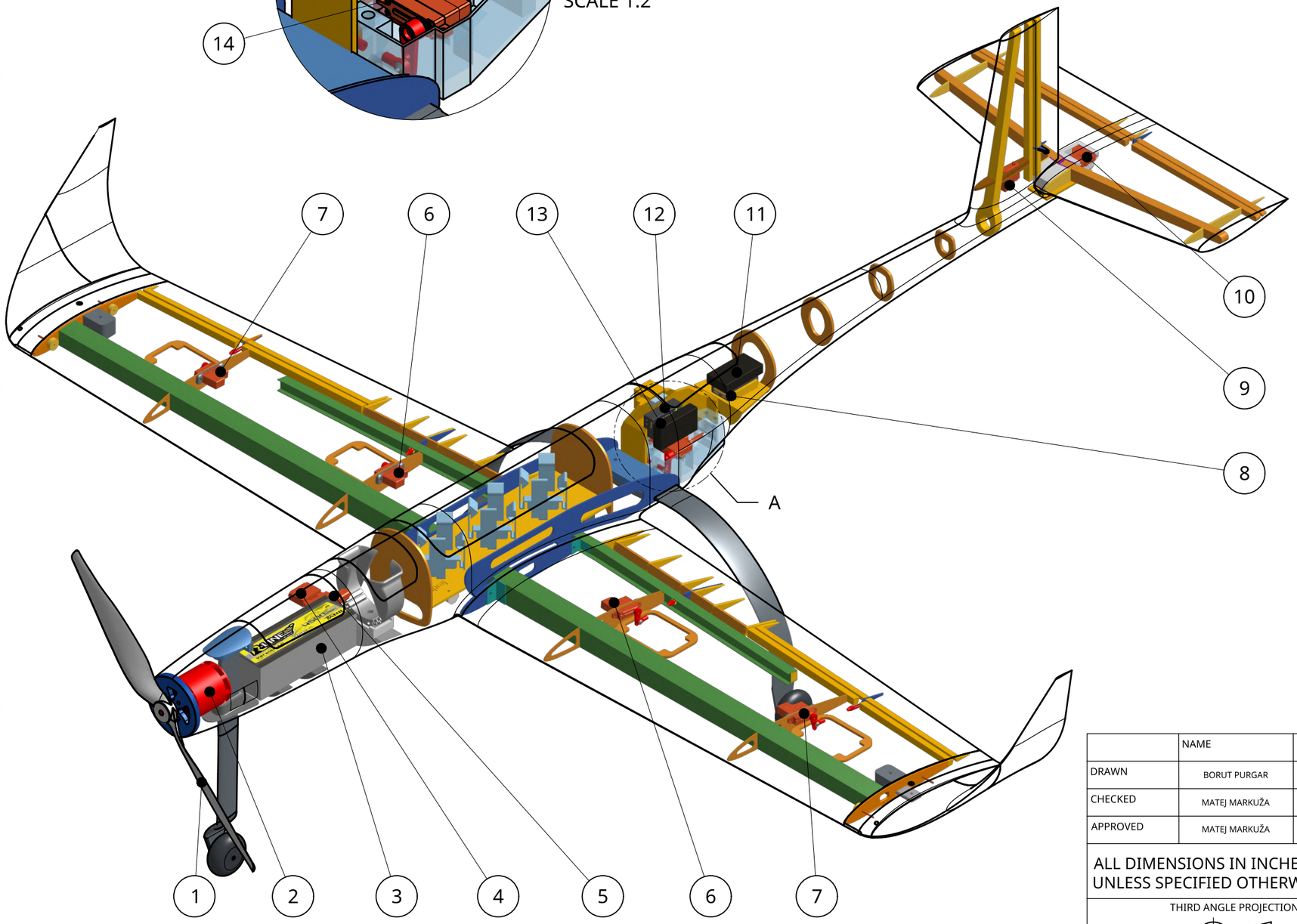

ITEM	QTY.	SYSTEM	DESCRIPTION
1	1	Propeller	APC 15x10E
2	1	Electric Motor	Kontronik PYRO 700-45
3	1	Propulsion Battery	4500 mAh 6S 22.2 V LiPo
4	1	Fuse	100 A fuse
5	1	ESC	APD 120F3 v2
6	2	Flap Servo	Chaservo HV95
7	2	Aileron Servo	Chaservo HV95
8	1	Receiver	FrSky Tandem TD SR10
9	1	Rudder Servo	Chaservo HV75H
10	1	Elevator Servo	Chaservo HV75H
11	1	Receiver Battery	1000 mAh 2S 7.4 V LiPo
12	1	Banner Mech. Receiver	FrSky Archer SR8 PRO
13	1	Banner Mech. Battery	650 mAh 2S 7.4 V LiPo
14	1	Banner Deploy Servo	Chaservo HV95H
15	1	Banner Release Servo	Chaservo HV95H

	NAME	DATE
DRAWN	BORUT PURGAR	02/14/2026
CHECKED	MATEJ MARKUŽA	02/20/2026
APPROVED	MATEJ MARKUŽA	02/20/2026

ALL DIMENSIONS IN INCHES
UNLESS SPECIFIED OTHERWISE

THIRD ANGLE PROJECTION

UNIVERSITY OF LJUBLJANA
EDVARD RUSJAN TEAM

TITLE

SYSTEM ARRANGEMENT

SIZE	DWG NO.	REV.
B	ERT2026-3	

SCALE	WEIGHT	SHEET
1:5	6.83 lbs	1 of 1

LOADED PASSENGERS & CARGO DURING M2

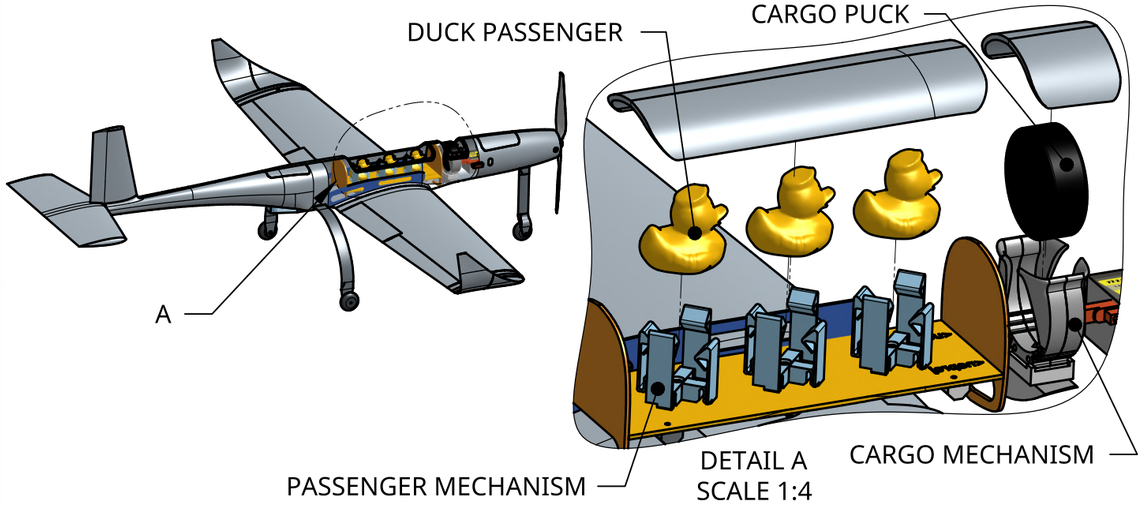

INSTALLED BANNER DEPLOYMENT, TOWING & RELEASE MECHANISM

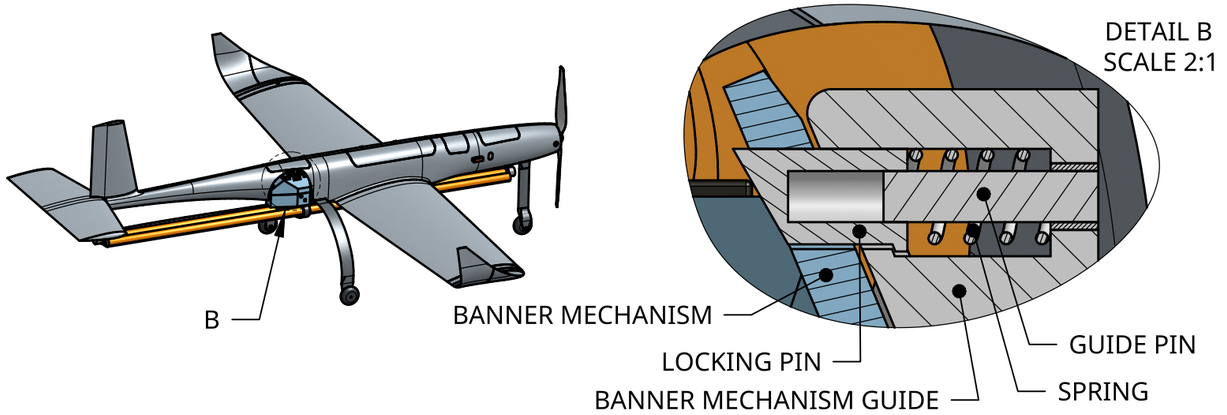

FOLDED BANNER DURING M3

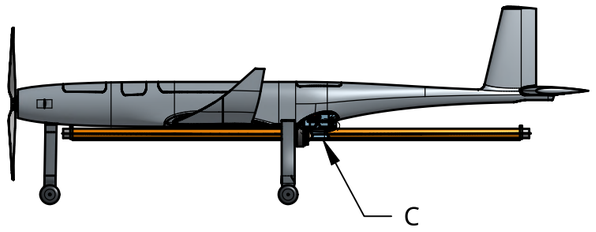

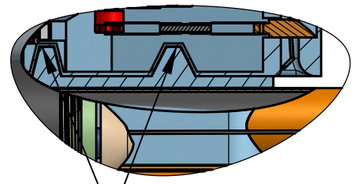

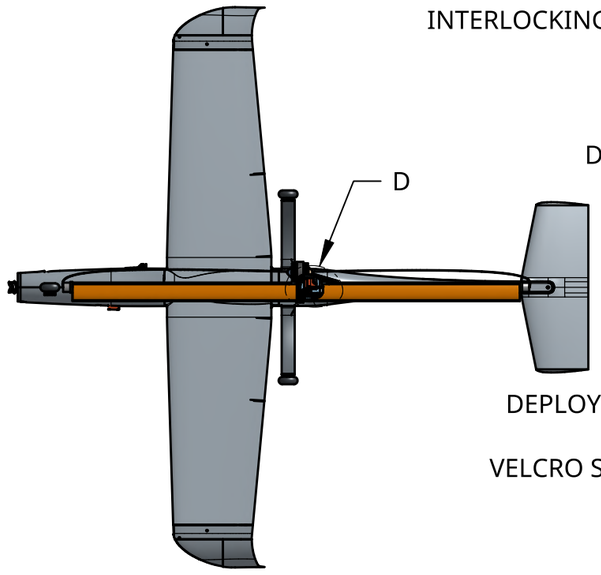

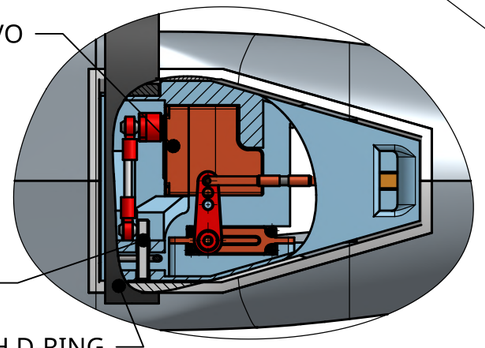

NOTE: DEPLOYMENT PIN RETRACTS TO DEPLOY BANNER

BANNER TOWING DURING M3

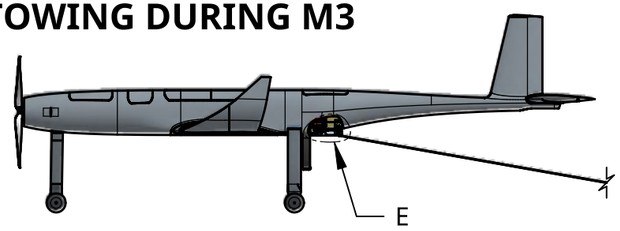

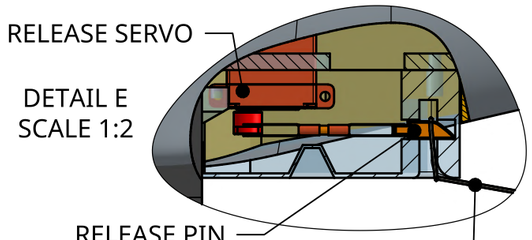

NOTE: RELEASE PIN RETRACTS TO RELEASE BANNER

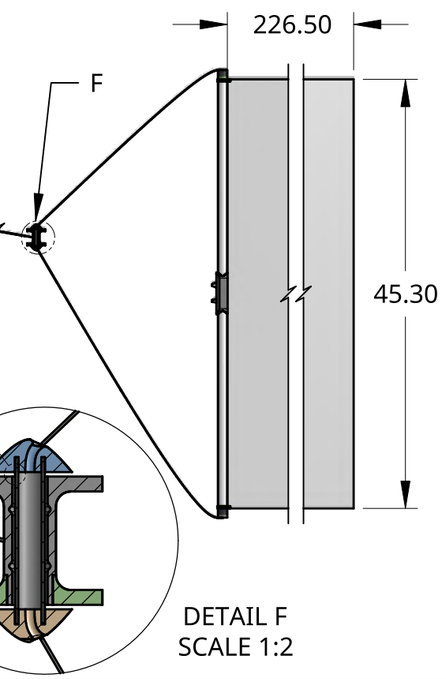

	NAME	DATE
DRAWN	BORUT PURGAR	02/14/2026
CHECKED	MATEJ MARKUŽA	02/19/2026
APPROVED	MATEJ MARKUŽA	02/19/2026

ALL DIMENSIONS IN INCHES UNLESS SPECIFIED OTHERWISE

THIRD ANGLE PROJECTION

UNIVERSITY OF LJUBLJANA
EDVARD RUSJAN TEAM

TITLE

PAYLOAD ACCOMODATION

SIZE	DWG NO.	REV.
B	ERT2026-4	

SCALE	WEIGHT	SHEET
1:16	8.05 lbs	1 of 1

6 Manufacturing

6.1 Manufacturing Plan

Table 22 shows our manufacturing schedule to ensure the optimal distribution of workload.

Table 22: Manufacturing Schedule

UL DBF 2025–26 Manufacturing Schedule	September				October					November				December				January					February				March				April		
	1	2	3	4	5	6	7	8	9	10	11	12	13	14	15	16	17	18	19	20	21	22	23	24	25	26	27	28	29	30	31	32	33
Preparations																																	
Testing Manufacturing Techniques	//////////////////////////////////////																													Planned Task			
Workshops				////////////////////////																									////	Progress			
Prototype Plane																																	
Horizontal Stabilizer Molds Preparation														////																			
Horizontal Stabilizer Lamination															////																		
Horizontal Stabilizer Assembly & Wiring																////																	
Wing Molds Preparation																////																	
Wing Lamination																	////																
Wing Assembly & Wiring																		////															
Fuselage Molds Preparation																	////																
Fuselage Lamination																		////															
Fuselage Assembly & Wiring																			////														
Landing Gear																			////														
Mechanisms																		////////															
Final Assembly																			////////	////													
Final Model Plane																																	
Horizontal Stabilizer Molds Preparation																								////									
Horizontal Stabilizer Lamination																									////								
Horizontal Stabilizer Assembly & Wiring																																	
Wing Molds Preparation																									////								
Wing Lamination																																	
Wing Assembly & Wiring																																	
Fuselage Molds Preparation																																	
Fuselage Lamination																																	
Fuselage Assembly & Wiring																																	
Landing Gear																																	
Mechanisms																																	
Final Assembly																																	
Banner																																	
Banner								////////											//////////														

6.2 Manufacturing Processes Investigated

Various manufacturing processes were investigated during the plane's design phase to determine the best building techniques for each component of the aircraft and achieve optimal performance. The team's experience, financial resources, and technological capabilities were all considered. An overview of the techniques used is provided below.

6.2.1 CNC Milling

Computer numerical control (CNC) milling is a widely used and versatile cutting process. This technique offers high accuracy, efficiency, consistency and reliability. On the other hand, CNC mills call for skilled operators and can be a great financial strain to acquire and maintain. With access to a CNC machine at the university, it is possible to machine parts with complex shapes, such as ribs made from carbon fiber and molds for the aircraft, as well as post-process aircraft components.

6.2.2 Foam Core Modeling

Foam core modeling is a simple and cost-effective method for manufacturing various airplane components. A CNC hot wire cutter enables rapid and precise cutting of foam, making it particularly ideal for fabricating airfoils. However,

despite the simplicity of the foam core process, the resulting products are unsuitable for larger and more demanding aircraft, as foam lacks the strength and durability of composite materials.

6.2.3 Balsa and Plywood

Balsa, a low-density wood, can be used to create incredibly lightweight airframes for model airplanes where foil is stretched across the airframe to form the aircraft's skin. Because of its low strength, it is not always suitable for load bearing structures and demands careful consideration throughout the design process. It can be combined with plywood or other materials to increase strength, but this comes at the cost of increased weight. The fundamental advantage of wood is that it can be cut simply and accurately with a CNC laser, making it a viable option for early rapid prototyping.

6.2.4 Additive Manufacturing

3D printing, specifically fused deposition modeling (FDM), is ideal for rapid prototyping and the creation of complex structures that other manufacturing processes are not capable of producing. However, the material used in FDM is not ideal for lightweight high load-bearing applications, hence this approach is usually limited to smaller components (e.g. mechanisms, connectors or adapters) and molds.

6.2.5 Composite Molding

Composite materials allow us to create structures of high strength and low weight, which makes them ideal for aircraft construction. The main drawbacks of the composite manufacturing, it being time-consuming and complicated, as well as composite materials (such as carbon fibers and epoxy resin) being expensive, are offset by the excellent properties of composites, namely great strength-to-weight ratio compared to conventional materials. In composite manufacturing, the following techniques are most commonly used: hand-laminating, resin infusion and forged composites.

Hand-laminating involves laying carbon fiber cloth wetted with resin and letting it cure, resulting in strong, lightweight parts with minimal thickness. Hand-laminated composite materials allow for the creation of monocoque designs, providing more free volume in aircraft components. To further enhance part performance, the laminate is vacuum-bagged to reduce the risk of air voids or bridging, and to remove excess resin. Additional mass reduction can be achieved by producing laminates with core materials.

Resin infusion is a technique in which dry carbon fiber fabrics are placed in a mold and resin is drawn through the fibers under vacuum bag. This process ensures uniform resin distribution and minimizes the risk of air pockets, producing strong and lightweight components. By using resin-infused composites, critical load-bearing components, such as wing spars, can be manufactured with high structural integrity and minimal defects.

Forged composites involves carbon fibers that are compression molded in multi-part mold to create strong solid geometries. Forged composites technique produces stronger parts compared to conventional 3D-printed components, but unlike some 3D-printed materials, it cannot be made hollow, which can limit weight savings. It is particularly well-suited for the production of smaller elements that need to withstand considerable structural loads, such as landing gear and landing gear fixtures, because of its ability to create complex geometric parts that require precision, stiffness and reliability.

6.2.6 Sewing and Hemming

Sewing and hemming is a widely used and reliable method for finishing fabric edges. This technique allows for better force distribution across the material, improving durability and reducing the risk of tearing compared to straight stitching. On the other hand, careful thread selection and precise stitching are required to avoid cutting or weakening the fabric. By using high-quality nylon threads with stiffness matching that of the banner material, it is possible to reinforce edges while maintaining flexibility. With this approach, the banner edges can withstand aerodynamic loads and remain structurally sound during operation.

6.3 Selection Process

The team evaluated the manufacturing processes and techniques outlined in the previous section to identify the most suitable options for the manufacture of prototypes and the final competition model. The aircraft's requirements and design, along with the team's resources and expertise, were all considered.

FoM was used to rate the processes, factoring in the following criteria using weights from 1 (lowest priority) to 5 (highest priority) as shown in Table 23.

Table 23: Manufacturing FoM for the Competition Airplane

		Manufacturing Processes				
	Weight Factor	Balsa & Plywood	Foam Core	Composite Molding	CNC Milling	Additive Manufacturing
Cost	2	3	4	2	3	4
Time	4	4	4	1	2	3
Experience	3	2	3	5	5	5
Weight	3	4	2	5	5	2
Strength	5	3	4	5	4	3
Assembly Complexity	5	2	2	4	3	4
	Total	65	69	83	79	76

Cost: The team has a limited budget but receives most of the building materials from donors, therefore the financial cost has a low weight factor.

Time: Each manufacturing process requires a certain amount of time to produce the parts required and since the overall manufacturing schedule is limited the production time has a moderate weight factor.

Experience: Throughout the years, the team has mastered certain techniques, which makes those manufacturing processes more time-efficient, and produces reliable and higher quality results.

Weight: With no limiting effect on takeoff performance and no significant impact on the mission score, weight has been assigned a moderate priority in the competition aircraft design, as reducing mass still improves overall flight performance.

Strength: The airframe has to withstand significant forces, thus strength has a high priority factor.

Assembly Complexity: A simpler aircraft assembly with fewer components allows the team to design, assemble and repair the airplane more quickly, leading to earlier test flights and fewer potential delays in the schedule.

The team determined that composite molding with CNC-milled molds enables the production of an aircraft that meets the performance objectives highlighted in the FoM analysis. For smaller components, such as mechanisms and internal structures, laser cutting and additive manufacturing were also identified as suitable techniques. Molds for

smaller parts, such as landing gear and landing gear fixtures, are produced using additive manufacturing. Banner material was chosen based on banner drag testing covered in in Section 7.1. The final selection of materials and manufacturing techniques for each major component is summarized in Table 24.

Table 24: Materials and Manufacturing Techniques by Component

Component	Material and Technique
Fuselage	CNC-milled Purenit MD 550 molds, hand laminated carbon/glass fiber + aramid honeycomb
Wing	CNC-milled Purenit MD 550 molds, hand laminated carbon/glass fiber + Airex foam
Horizontal Stabilizer	CNC-milled Purenit MD 550 molds, hand laminated carbon/glass fiber + Airex foam
Wing Spar	CNC-milled Purenit MD 550 molds, hand laminated carbon/glass fiber + Airex foam
Ribs and Internal Reinforcements	Fiberglass reinforced Airex foam laminate, 0.04”–0.12” thick plywood or carbon sheet, 0.39” thick Airex
Front and Main Landing Gear	3D-printed molds, forged carbon fiber
Passenger, Cargo and Banner Mechanisms	Additive manufacturing
Banner	Icarex polyester, machine-sewn using a zigzag stitch with nylon thread

6.4 Composite Manufacturing of Fuselage, Horizontal Stabilizer and Wings

6.4.1 Preparation of Molds for Lamination

Negative molds for each main part were CNC-machined from Purenit MD 550 material. Material selection was based on the manufacturer’s guidelines, the team’s previous experience and budget constraints. Molds for smaller parts, such as landing gear, hatches and winglets, were 3D-printed, as CNC machining is too time-consuming and unsuitable for producing small molds with details.

Alignment slots were incorporated into the molds to ensure the precise positioning of critical fiber reinforcements. Furthermore, holes for the landing gear, wiring, hatches and air ducts that appear in the laminate were either cut out or marked in the molds to prevent placing critical reinforcements in these areas and instead positioning them in more suitable locations. Additionally, pin holes were added to accurately join the two halves of the aircraft part shell and to locate jigs for precise placement of internal structural components. Furthermore, a channel for excess resin was cut out at the end of the trailing edge. After CNC cutting, the molds were first sanded to a 400-grit finish, then cleaned and coated with resin sealant. Once sealed, a layer of surface coating resin was applied with a spray, resulting in a finish that could be polished. After polishing, a wax release agent was applied to the molds. A polyvinyl alcohol (PVA) release agent was also added to regions where part release could be problematic.

6.4.2 Internal Structure

The internal structure of molded parts is essential for ensuring structural integrity and functionality of the laminated components. Ribs, spars and frames are made from three different materials, each selected based on their specific structural role. The spars and frames designed to withstand compressive forces and distribute loads are cut from a 0.39” thick Airex foam sheet. The ribs that are required to carry higher loads are manufactured from 0.12” thick plywood sheets. Servo motors are mounted on these ribs, allowing stresses to be more evenly distributed through the laminate structure. In addition, some ribs and frames are constructed as sandwich composites made of 1.47 oz/yd² fiberglass layers on each side of a 0.12” Airex core, providing an excellent strength-to-weight ratio.

An exception are the structurally critical elements connecting the fuselage to the wing, which are cut from a 0.08” thick carbon fiber sheet. The motor mount, which is subjected to significant loads, is manufactured from a 0.20” MDF board, reinforced with four layers of 5.88 oz/yd² plain weave carbon fiber on each side.

The internal structural components are positioned using dedicated jigs, which are located with pins (shown in Figure 43), engaging precision-machined holes in the mold. This ensures accurate placement and repeatability of the assembly process. The internal structure is bonded to the laminated components using a structural adhesive that provides high bond strength and a short curing time.

6.4.3 Composite Manufacturing of the Fuselage

Manufacturing of the fuselage was established using a sandwich structure to optimize the strength-to-weight ratio. The outer skin was manufactured from a 1.18 oz/yd² biaxial carbon fiber layer in a $+45/-45$ degree orientation for torsional stiffness. To improve longitudinal strength under banner-towing loads, additional 1.47 oz/yd² UD spread-tow carbon-fiber strips were added along the length of the fuselage together with vertical strips to places where the internal structure attaches, as shown in Figure 42. The hinge for the vertical stabilizer was made from 8.85 oz/yd^2 aramid flat braid. For better adhesion to the core material, a thin layer of 0.74 oz/yd² plain weave fiberglass was placed over the carbon laminates. Next, 0.079" thick aramid honeycomb core was inserted and covered with an additional layer of 1.47 oz/yd² glass fiber fabric in a $+45/-45$ degree orientation. The laminates were vacuum-bagged and cured for 24 hours under 85% vacuum.

Once cured, the wing attachment plates were precisely glued in place using a structural adhesive. This was achieved by first removing the fiberglass and honeycomb sections of the laminate, and then securing the plates in all three dimensions using the mold and alignment pins. Upon completion of both fuselage parts, the internal structure was glued in place, including the reinforcement frames and motor mount, using specialized jigs to position them precisely, as shown in Figure 43. The halves were then joined and pressed together using clamps and screws that passed through dedicated holes in the mold.

After joining, the laminated fuselage was removed from the molds and underwent an 18-hour post-cure at 130 °F to ensure maximum rigidity. This was followed by post-processing, which included sanding excess laminate and adhesive, as well as hinging by cutting out the control surface for the vertical stabilizer. The internal structure was completed by attaching the landing gear fixtures, internal mechanisms and servo motor for the vertical stabilizer to the fuselage.

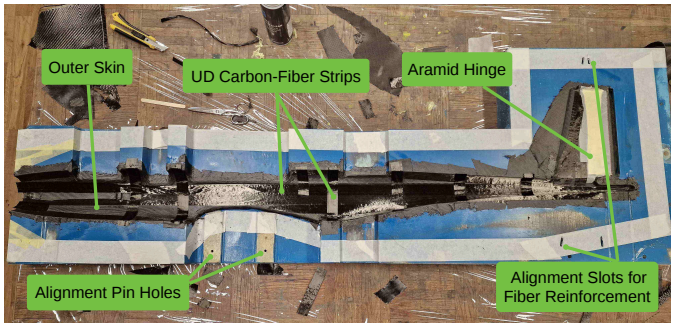

Figure 42: Fuselage Lamination

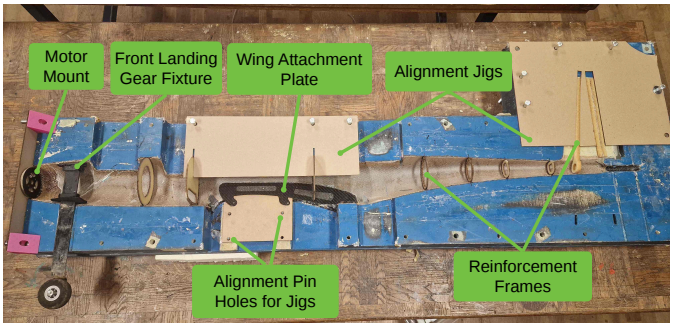

Figure 43: Positioning of the Internal Fuselage Structure

6.4.4 Composite Manufacturing of the Wing

The wing was hand-laminated using a 1.18 oz/yd^2 biaxial carbon fiber layer, applied to the mold in a $+45/-45$ degree orientation to enhance torsional stiffness. The hinges for the flaps and ailerons were made from 8.85 oz/yd^2 aramid flat braid, due to its fatigue resistance (Figure 44). Additional 2.36 oz/yd² carbon fiber reinforcements were

placed at the rib locations and at the wing center to strengthen the fuselage attachment area. 0.079” thick Airex foam was then placed over and covered with 1.47 oz/yd^2 glass fiber fabric. This layer of fabric had to be saturated with epoxy before being placed into the mold, as laminating it in the mold would cause much of the epoxy to soak into the Airex foam. The parts were vacuum-bagged and cured for 24 hours under 85% vacuum, followed by an 18-hour post-cure at 130℉.

The front and rear spars feature a U-shaped cross-section, allowing them to be manufactured in a single process while providing improved bonding between the spar web and caps. Both the front and rear spars were manufactured using resin infusion. The caps of the front spar, positioned on opposite sides of the U-profile, were made using six strips of 1.47 oz/yd² UD spread-tow carbon fiber on each side of the web, with number of strips gradually decreasing from the wing root toward the tip. For the rear spar, three of such strips were used. The webs of both spars were constructed from two layers of 1.47 oz/yd² fiberglass cloth, which extend along the entire U-profile. After curing, the spar webs were further reinforced by bonding and vacuum-bagging a 0.39” thick Airex core along the full length of the spars within the U-profile. The spars were post-cured for 15 hours at 160℉.

Before joining the two halves of the wing, the internal components, including spars, ribs and servo motors, were precisely installed using jigs, as shown in Figure 45. Post-processing included hinging by cutting out the control surfaces, as well as creating openings for the access hatches and attachment points to the fuselage using mainly CNC milling.

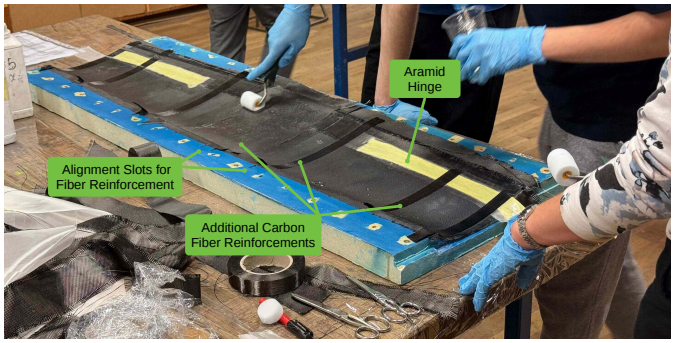

Figure 44: Wing Lamination

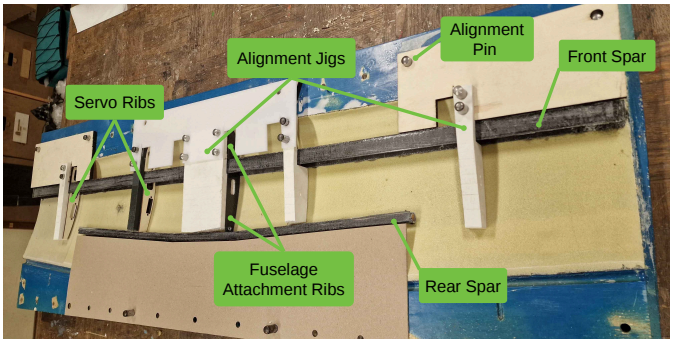

Figure 45: Internal Structure of the Wing

6.4.5 Composite Manufacturing of the Horizontal Stabilizer

Horizontal stabilizer was hand-laminated using 1.18 oz/yd^2 biaxial carbon fiber layer, laminated in a $+45/-45$ degree orientation to improve torsional rigidity. Additional carbon fiber reinforcements were placed at the connection point to the fuselage. Hinge for the control surface was laminated into the skin using 8.85 oz/yd^2 aramid flat braid. Caps of spar were laminated into the skin of the wing using two strips of 1.47 oz/yd^2 UD spread-tow carbon fiber. 0.079” thick Airex foam was then placed over and covered with 0.74 oz/yd^2 glass fiber fabric. Before joining the two halves of the horizontal stabilizer, the internal structure and servos were installed. The laminates were vacuum-bagged and cured for 24 hours under 85% vacuum, followed by an 18-hour post-cure at 130℉. Post-processing was mainly done using CNC milling, allowing us to precisely cut out the control surface and servo access hatch.

6.4.6 Composite Manufacturing of the Landing Gear

The front and rear landing gear, and their fixtures were made using the forged carbon technique. For lamination, the required amount of chopped carbon fiber was prepared based on the part's volume, which was derived from the CAD model. From this volume, the mass was calculated by multiplying the density of the carbon-epoxy laminate (0.81 oz/in^3). Using the optimal 60/40 fiber-to-resin ratio (by weight) for forged carbon, the mass of resin and carbon fiber was determined. To ensure the strength of the part, long fiber tows were primarily used, while some chopped carbon fiber was incorporated to improve mold compaction.

The lamination process began by spreading a thin layer of epoxy onto the mold and covering it with carbon fiber, which was then carefully saturated. Long fiber tows were placed in the mold and this process was repeated until all the epoxy and carbon fiber were used. The parts were then pressed together and allowed to cure for 24 hours at room temperature. The parts were later removed from the mold and post-cured at 130°F for 18 hours. Lastly, they were post-processed by fine sanding and cutting the necessary holes for attachments.

6.4.7 Manufacturing of Mechanisms

The mechanisms were manufactured using additive manufacturing with ASA filament. To improve structural strength as well as functional performance of the printed components, additional modifications were implemented, including threaded inserts and embedded carbon rods. These enhancements enable more reliable mounting of servo motors where required, and allow for easy replacement of individual components if necessary.

6.4.8 Manufacturing of the Banner

To create the banner, the fabric was first cut slightly oversized, relative to the target dimensions. The excess material was then folded two times into a reinforced hem and machine-sewn around the perimeter (Figure 46) to reduce edge tearing. The border was hemmed using a zigzag stitch and a nylon thread. The team opted for the nylon thread because its stiffness is approximately comparable to that of the chosen fabric. As a result, it does not induce localized cutting or stress concentration within the material during flight, which could otherwise occur if a thread with significantly higher stiffness than the base material were used. The team also briefly tested cutting the fabric with a hot-knife by melting and thus sealing the plastic edge to eliminate the need for stitching, however, these borders showed a significantly higher tendency to tear (as shown in Figure 47), hence the technique was omitted.

Figure 46: Banner Hemming


Figure 47: Hot-Knife Cut Edge Border After Flight

To minimize surface irregularities that could disturb the airflow and affect drag, the team chose screen printing as the most suitable marking technique for applying the university name and logo onto the banner fabric.

7 Testing

Testing was implemented to validate numerical simulation results regarding flight performance, propulsion, stability, load-bearing capabilities and banner aerodynamics. As a quality assurance procedure, additional tests were performed to confirm the functionality of the aircraft and key mechanisms. Testing was divided into three categories: preliminary testing, ground testing and flight testing. A detailed schedule, shown in Table 25, was proposed to track errors before they negatively impacted later steps.

Table 25: Testing Schedule

UL DBF 2025–26 Testing Schedule	September				October					November				December				January				February				March				April		
	1	2	3	4	5	6	7	8	9	10	11	12	13	14	15	16	17	18	19	20	21	22	23	24	25	26	27	28	29	30	31	32	33
Preliminary Testing																																	
Initial GM Simulations																																	
Ground Testing																																	
Banner Tests																																	
Propulsion Tests																																	
Wing Structural Tests																																	
Passenger & Cargo Mechanism Tests																																	
Banner Mechanism Ground Tests																																	
GM Simulations																																	
Electronics & Systems Tests																																	
Flight Testing																																	
Fine-Tuning																																	
Performance Tests																																	
M1 & M2 Simulations																																	
M3 Simulations																																	
Banner Mechanism Flight Tests																																	

Planned Task

Progress

7.1 Banner Testing

The primary objectives of this test were to measure drag coefficients of different banner fabrics to select the final banner material, validate simulation results as well as refine the mission model parameters, making it more accurate.

Data acquisition (DAQ) was done with Dewesoft equipment and DewesoftX software [19], which facilitate a more convenient, fast and accurate measuring process. The banner testing rig was equipped with a Dewe-43A measurement card, S-beam load cell and a ManoAir-100 differential pressure sensor connected to a 20” pitot tube, as illustrated in Figure 48. Figure 49 shows the installed banner testing rig inside a vertical wind tunnel, which provided a controlled testing environment with homogeneous air flow, ranging from 26 ft/s to 200 ft/s.

Six banners were tested, each measuring approximately 118.11” x 23.62”, with these dimensions representing the effective surface area A_{banner}. The drag force D of each banner material was measured at different airspeeds for 30 seconds, thus eliminating random noise from rig oscillations and banner flutter. After simultaneously measuring dynamic pressure q, we could calculate the banner’s drag coefficient $C_{D,\text{banner}}$ from a derived formula shown in Eq. 19. To acquire true airspeed data we had to measure air pressure, humidity and temperature from which air density was calculated. Because of limited allocated time in the wind tunnel and a lot of repetitive work, an automated sequence was created using DewesoftX sequencer, further optimizing and streamlining the data acquisition process.

$$C_{D,banner} = \frac{D}{q \cdot A_{banner}} \tag{19}$$

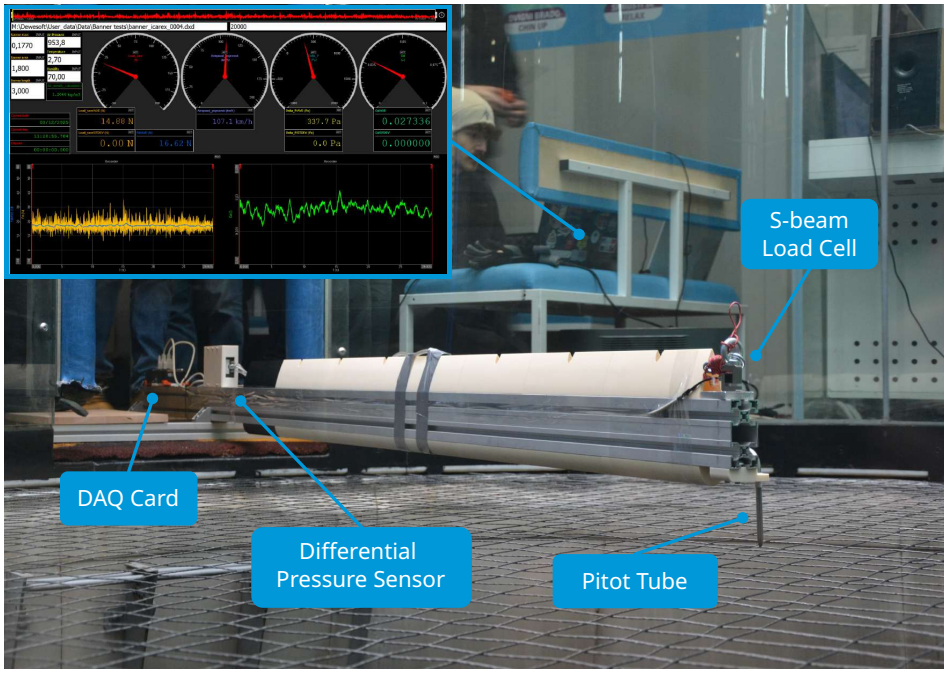

Figure 48: Banner Testing Rig

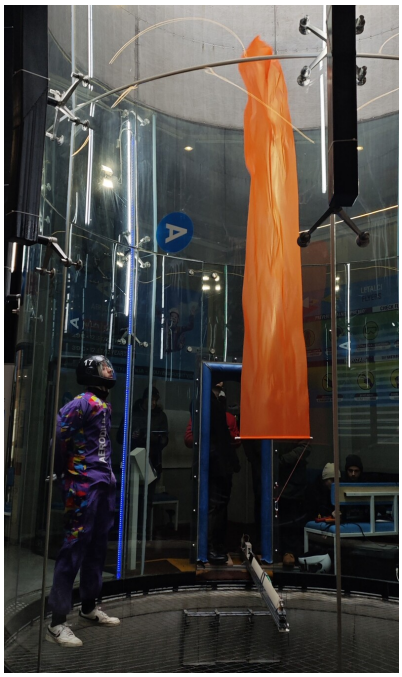

Figure 49: Banner Test

7.2 Propulsion Testing

The main goal was to select the optimal propulsion configuration from the two shortlisted options (discussed in Section 4.3.4), and to validate and improve initial propulsion calculations by comparing them to the measured characteristics.

Having no access to a wind tunnel suitable for propulsion testing, a custom propulsion testing rig that can be mounted high above the roof of a car in clean airflow (Figure 50) was used to test the two selected combinations of motors and propellers at different airspeeds. The propulsion configurations were individually mounted onto a round beam with attached strain gauges to measure the generated thrust force, while the input current and voltage were measured using DS-CLAMP-300DC hall effect current clamp combined with a Dewe-43A measurement card. Airspeed was measured using the QS-FS cup anemometer. Dynamic thrust and electric current were measured at airspeeds ranging from 0 ft/s to 100 ft/s, resulting in thrust/airspeed and current/airspeed characteristics, presented in Section 8.2.

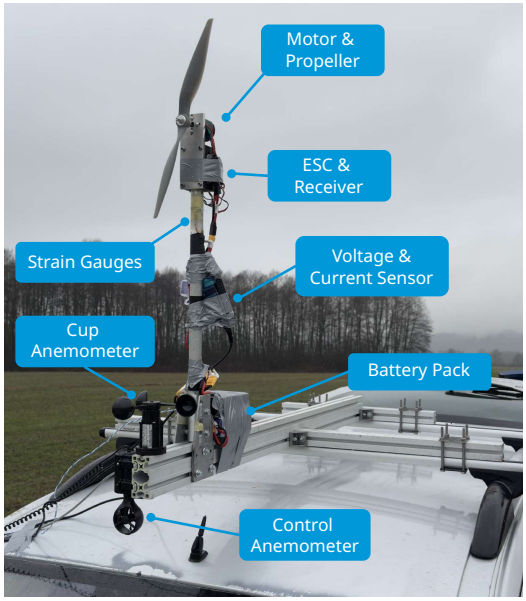

Figure 50: Propulsion Testing Rig

Two propulsion setups were tested: PYRO 700-45 with the APC 15×10E propeller and PYRO 700-34 with the APC 18×12 propeller. Both configurations were powered by the same 6S 18 Ah battery pack charged to 3.8 V, ensuring identical testing conditions. Furthermore, battery consumption was monitored to ensure that the all measurements were captured at the same voltage with a ±2% error. All tests were performed with the throttle set at 100% for 10 seconds to eliminate random error gained from the imperfect testing environment.

7.3 Wing Structure Testing

The goal of wing structure testing was to validate wing FEA results, assess manufacturing quality, and confirm the wing's airworthiness before its first flight. A non-destructive three-point bending test was performed in a controlled laboratory environment to determine wing rigidity by measuring the relationship between applied force and wing deflection.

To determine the support locations relative to the wing center, the spanwise lift distribution was estimated using Anderson's method [20]. The resulting bending moment distribution was then used to place the supports so that the bending moment induced during the test matched the bending moment acting upon the wing in flight due to lift. Torsional loads were not taken into account since they are not as critical.

The wing was rigidly clamped on an electrically actuated load applicator positioned at the wing center, as shown in Figure 51, while two bottom roller supports provided reaction forces at the edges of the wing. The test was displacement-controlled by prescribing deformation values, while the corresponding force was measured using a load cell. The load was increased incrementally up to 150 lbf, which is the expected load of the fuselage on the wing during a 10 g incorporating a safety factor of two.

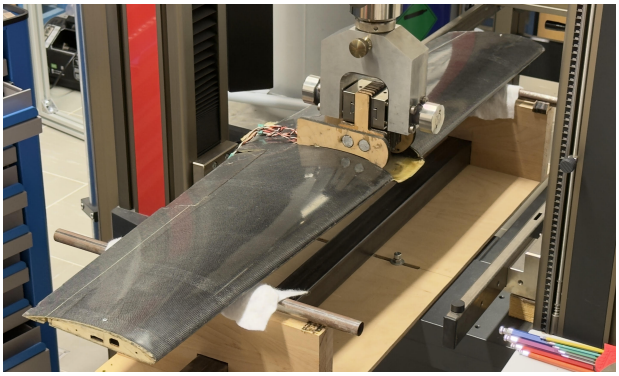

Figure 51: Three-Point Bending Test

7.4 Ground Mission Testing

The Ground Mission testing provided crucial insight into the times needed to configure the aircraft to a charter-flight configuration, and then reconfigure it for banner-towing flight. The sequence included passenger and cargo loading and unloading, hatch opening and closing, and banner installation. Segments that involved running between the start/finish line and the aircraft were each approximated as 2 seconds (as was assumed in the mission model), since the start/finish line distance from the aircraft was not specified. The main goal was to determine the optimal sequence, followed by multiple simulated runs of the complete mission. The assembly crew member configured the aircraft while another member recorded the time required to perform each task and simultaneously marked start times of each segment (eg. hatch opening/closing). During the process, notes were taken to identify possible areas of improvement and assess the time efficiency of each individual step.

7.5 Flight Testing

This year, the team did not manufacture a preliminary conceptual prototype of the competition airplane, as the mission requirements did not require exploring configurations the team was unfamiliar with. Therefore, a well-defined prototype that is capable of executing all three flight missions was developed. To gather precise telemetry data, the team mounted the flight recording system described in Section 5.2.9 behind the main battery in the fuselage.

Firstly, low and high speed taxiing was conducted at MTOW to confirm landing gear rigidity. Flight tests began with a simple pattern flight to fine-tune and trim the airplane. The team continued with M1 and M2 simulations, since the payload difference between both mission configurations is minimal. When simulating M3, the team's primary goal

was to inspect the aircraft's behavior while towing the banner. Initially, a shorter banner was used but its length was then incrementally increased as the pilot got more comfortable with banner-towing flight. Simultaneously, the banner deployment and release mechanisms were also tested in flight conditions for the first time.

7.6 Flight Checklist

Checklists are an essential part of every design and test process, which is why they were incorporated into the flight-test workflow. This was done to minimize the possibility of human errors, ensure proper data acquisition and improve test efficiency. The checklist, as seen in Table 26, was used before each flight test and designed around specific requirements of each mission. This checklist will also serve as the final check-up before each fly-off in the upcoming DBF competition.

Table 26: Flight Checklist

PREFLIGHT		
Aircraft Assembly	Avionics	Interior
CHECK airframe for damage	VERIFY charge on all batteries	SECURE payload
CHECK control surfaces	SECURE all batteries	Exterior
CHECK & SECURE wing and tail	SECURE receiver	CLOSE all hatches
SECURE landing gear	CENTER control surfaces	SECURE banner
SECURE the banner mechanisms	CHECK flaps 1 and 2	CHECK CG
CHECK servo linkages and horns	CHECK failsafe	Final walkaround
CHECK & SECURE motor, prop	CHECK range	

PREFLIGHT BANNER
CHECK mechanisms
CHECK for damage
CHECK towline
STOW compactly
SECURE on aircraft
Banner CLEAR

BEFORE TAKEOFF	
Pilot READY	INSERT arming plug
CHECK wind	Motor ARMED
TURN ON avionics	START video
Controls CLEAR	CLEAR runway
SET flaps (if needed)	START flight timer

BEFORE LANDING
CHECK wind
CLEAR runway
SET flaps (if needed)

AFTER LANDING	
STOP timer	TURN OFF avionics
STOP video	UNPLUG all batteries
Motor DISARMED	VERIFY charge on all batteries
REMOVE arming plug	Final walkaround

7.7 Banner Deployment and Release Mechanism Testing

To confirm that both mechanisms operated reliably and as intended, testing was performed in two stages. First, both mechanisms were tested on the ground by repeatedly attaching, deploying and releasing banners of varying sizes. After confirming correct operation, the mechanisms were installed on the detailed prototype and validated in flight. Onboard cameras were used to monitor the drop and release phases, allowing us to analyze all main stages of mechanism operation (stowed-flight, drop and release) in detail.

8 Test and Performance Results

8.1 Banner Test Results

Across the tested airspeed range, the measured drag coefficient $C_{D,banner}$ remained fairly stable for all materials and its characteristic showed a slight decrease with increasing airspeed. Icarex performed notably better compared to other materials, reaching drag coefficients as low as 0.018, as shown in Figure 52. This aligned well with the team's predicted $C_{D,banner}$ of 0.02, which was used in all preliminary performance calculations.

Drag force measurements and their associated deviations are presented in Figure 53. As airspeed increases, the deviations also increase, with Peelply exhibiting the largest scatter and Icarex the smallest. They are not fully consistent across runs, suggesting that the measured scatter is influenced not only by the banner material itself, but

also by test-condition variability (e.g. slight changes in towline angle, banner attitude/tension, and rig dynamics), which becomes more pronounced at higher airspeeds.

Since Icarex consistently exhibited the lowest drag coefficients and the smallest force deviations across the tested airspeed range, it was selected as the final banner material. The measured banner characteristics were then used to update the mission model by setting the banner drag coefficient to $C_{D,banner} = 0.019$, taken from the measured characteristics at the calculated M3 cruise speed of 64.6 ft/s. Because this adjustment was small, it did not change any of the previously identified optimal mission parameters, however, it slightly reduced the predicted battery consumption and therefore increased the available energy reserves for landing, which improved the team's overall confidence in the mission plan.

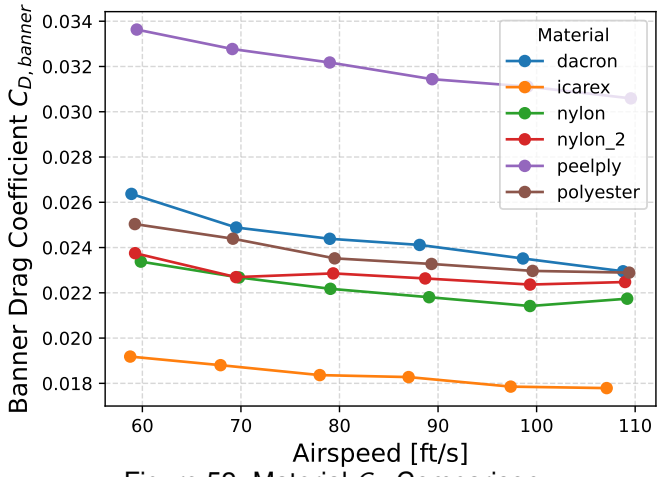

Figure 52: Material C_D Comparison

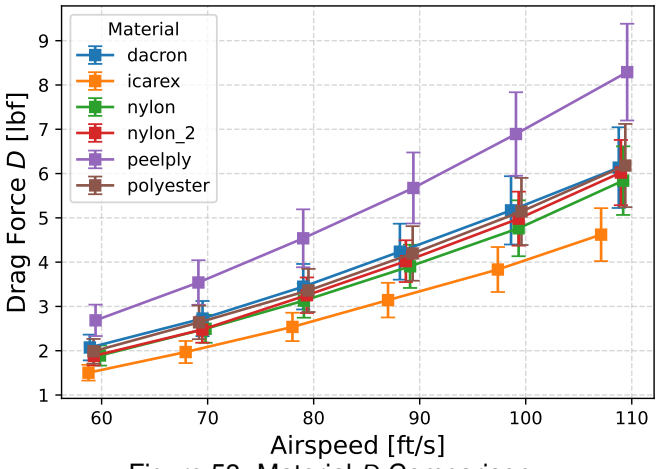

Figure 53: Material D Comparison

8.2 Propulsion Test Results

The propulsion test data presented in Figures 54 and 55 shows that both tested configurations exhibit very similar performance, as anticipated. The measured thrust characteristics align well with the predicted trends, particularly within the operating range. In contrast, the predicted current draw is consistently lower than the measured data points.

Ultimately, the propulsion configuration consisting of the Kontronik PYRO 700-45 motor and the APC 15x10E propeller was chosen for the final aircraft, since it provides similar thrust in the operating range while requiring a slightly lower current draw compared to the alternative configuration. In addition, the smaller propeller diameter allows the landing gear to be slightly shorter in height, which lowers aerodynamic drag and improves stiffness and ground handling.

Based on these results, the mission model was updated to better match the current characteristics with measured values, therefore increasing the consumption rate. This had an impact on preliminary mission performance that was predicted in Section 4.8, slightly shortening the optimal banner length and reducing M3 flight time due to greater battery consumption. Final mission performance predictions are presented in Section 5.3.

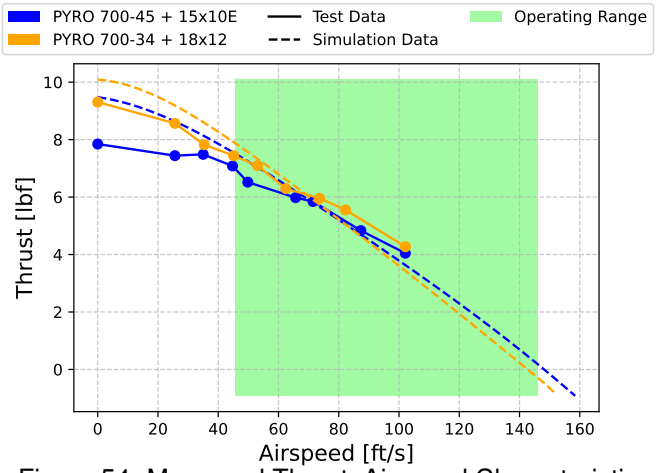

Figure 54: Measured Thrust–Airspeed Characteristic

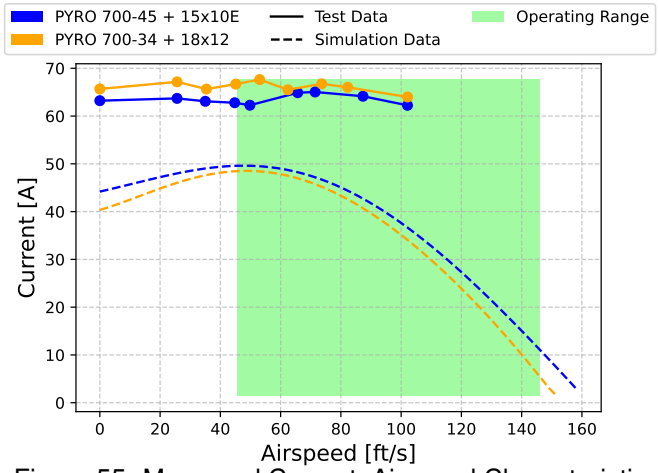

Figure 55: Measured Current–Airspeed Characteristic

8.3 Wing Structure Test Results

Following the steps described in Section 7.3, the wing's deflection/strain characteristic was measured. The results shown in Figure 56 indicate that the test wing successfully withstood a maximum load of 157 lbf without exhibiting any permanent deformations, structural failure or damage. Based on these results, the team concluded that the wing can safely withstand the load predicted by the FEA in Section 5.2.10, confirming both its structural margin and the quality of manufacture.

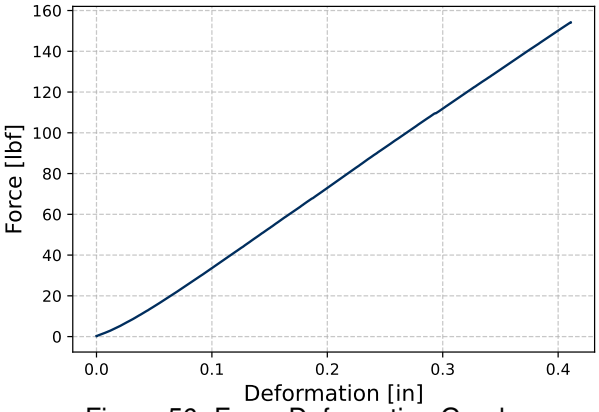

Figure 56: Force Deformation Graph

8.4 Ground Mission Test Results

Following the steps outlined in 7.4, the segment and total mission times were recorded and averaged. Final segment and total mission time averages are outlined in Table 27. Workflow optimization and the aircraft's design for rapid reconfiguration slightly reduced the expected segment times. Based on the results and assembly crew member feedback, the banner installment phase was recognized as the greatest opportunity for time savings.

Table 27: Average GM Segment Times

Segment	Run 1	Hatch Open	Pax Load	Cargo Load	Hatch Close	Run 2	Run 3	Hatch Open	Pax Unload	Cargo Unload	Hatch Close	Banner Install	Run 4	**Total**
Average Time [s]	2.0	1.0	3.1	1.6	0.7	2.0	2.0	1.1	1.4	0.9	0.7	7.8	2.0	**26.3**

8.5 Flight Performance

Performance metrics of the detailed prototype aligned well with the team's expectations. The airframe showed no visible deformation at MTOW, however, the rear landing gear initially flexed excessively, causing the aircraft to bounce during touchdown, raising concerns. This was quickly resolved by wrapping it in additional carbon-fiber sheets to increase rigidity and therefore improve landing reliability. Afterward, no issues were observed during taxiing, takeoff, or landing, even on a grass runway (Figure 57). The airplane showed excellent maneuverability and stability in all stages of flight, and achieved maximum speeds of approximately 155 ft/s, which validated our simulated predictions.

Initial flight tests were conducted in calm weather without any wind, using a Kontronik PYRO 700-45 motor and an APC 15x10E propeller. M2 and M3 flight telemetry was compared with the simulation results obtained using our mission model (presented in Section 4.2), configured with the same propulsion system and mission parameters, with the wind speed set to 0 kt.

The simulated M2 flights demonstrated that the aircraft can reliably fly with the planned payload. An average lap time of 33.4 seconds was calculated using the recorded logs. The ground speed profile comparison of a simulated and log-recorded M2 run (Figure 58) shows a close agreement of both plots in terms of ground speed magnitude, although the tested aircraft achieved slightly higher speeds along straight segments. Nevertheless, a noticeable offset along the time axis is present. This offset arises because the flight log was recorded during early testing stages, when the pilot was still becoming familiar with the aircraft. With sufficient pilot training, we expect this misalignment to be largely eliminated.

Figure 57: Testing on a Grass Runway

Since the team had no prior experience with banner towing flight, the banner length was increased incrementally, starting with a length of 40” and increasing it up to 217”. Even during tow flight, the aircraft showed no signs of structural issues or any unaccounted-for behavior. The performance remained stable and predictable, even with longer banners. Using the recorded logs, an average lap time of 59.7 seconds was calculated. Figure 59 shows the comparison between the simulated and log-recorded M3 speed profiles while towing a 217” banner. Similarly to the M2 speed profile comparison, the tested aircraft slightly exceeded the predicted ground speed along straight flight segments. However, a noticeable offset along the time axis is still present and is even larger than in M2, as the pilot does not have previous banner-towing experience.

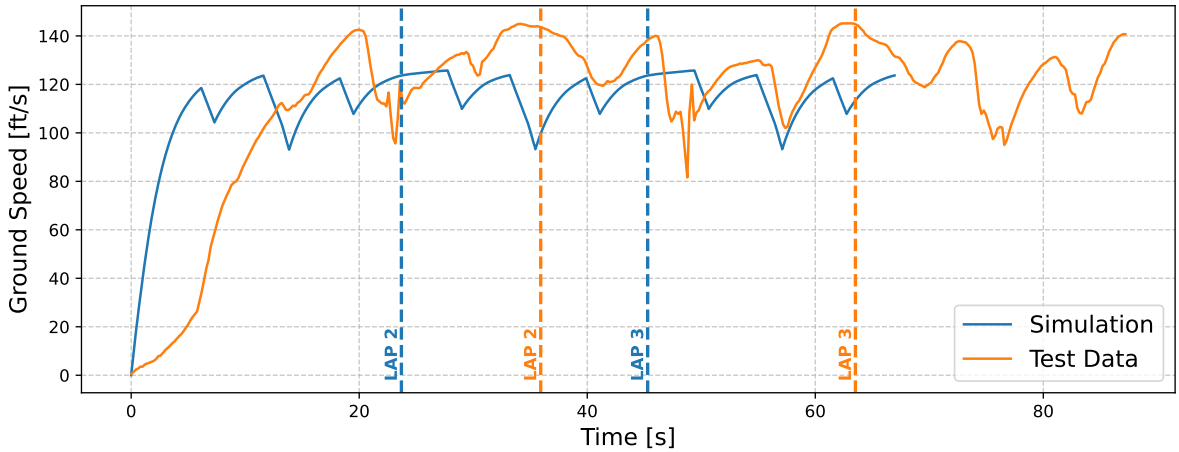

Figure 58: M2 Ground Speed Comparison for the First 3 Laps

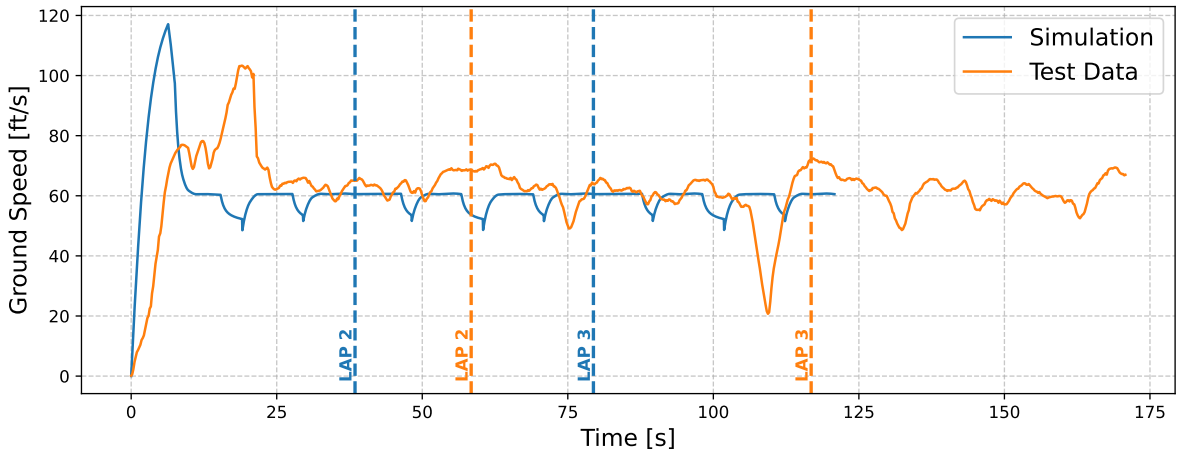

Figure 59: M3 Ground Speed Comparison For the First 3 Laps

8.6 Banner Deployment and Release Mechanism Performance

In addition to mission flight simulations, banner deployment and release mechanism testing was also conducted. Figure 60 shows a successful banner deployment and tow-flight. Initially, the release mechanism exhibited two issues. First, the banner could not be released under tow load, because it had not been accounted for in the initial design. Secondly, minor deployment issues were also observed, with occasional uncommanded banner deployments. Both issues were resolved quickly by adjusting the mechanism characteristics, and flight testing continued as planned.

The modified mechanism then operated reliably until a subsequent mishap: upon deployment, the towline got entangled around the rear landing gear, preventing proper deployment and release. This led to a rapid loss of control, which resulted in the prototype crashing (Figure 61). Although the crash halted further testing until the next iteration was manufactured, it provided valuable insights into structural weaknesses and a potential failure mode. The team used the collected data and observations to refine the design and address these issues.

Regardless of the crash, the pilot logged more than 5 hours of flight time during testing, improving his confidence in flying the aircraft, although additional training is still needed to reduce the time-axis offsets as much as possible. To further prepare for the competition, the team will also conduct several simulated competition scenarios, allowing the entire team to get ready for the fly-off.

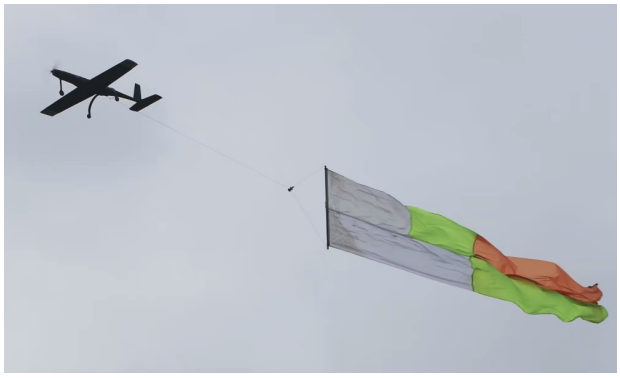
Figure 60: Successfully Deployed 217” Banner


Figure 61: Crash Aftermath

The team is proud to present the final manufactured aircraft called Brvinc to the world and the judges at the Textron Aviation Employees’ Flying Club in Wichita, Kansas.

9 Bibliography

[1] American Institute of Aeronautics and Astronautics (AIAA), "2025-26 AIAA Design, Build, Fly (DBF) Rules," https://aiaa.org/wp-content/uploads/2025/10/DBF-Rules-2026-Final.pdf, Oct. 2025, Accessed: 10-Jan-2026.

[2] Python Software Foundation, "Python," https://www.python.org/, Accessed: 16-Feb-2026.

[3] XFLR5 Team, "XFLR5," https://www.xflr5.tech/, Accessed: 22-Dec-2025.

[4] NASA, "OpenVSP: Open Vehicle Sketch Pad (open-source parametric aircraft geometry tool)," https://openvsp.org/, Accessed: 20-Dec-2025.

[5] SciPy Community, "SciPy: scipy.integrate.solve_ivp Documentation," https://docs.scipy.org/doc/scipy/reference/generated/scipy.integrate.solve_ivp.html, Accessed: 10-Feb-2025.

[6] Airfoil Tools, "Airfoil Database," http://airfoiltools.com/, Accessed: 22-Dec-2025.

[7] Weather Spark, "April 2025 Weather History in Wichita Kansas, United States," https://weatherspark.com/h/m/8281/2025/4/Historical-Weather-in-April-2025-in-Wichita-Kansas-United-States, Accessed: 19-Feb-2026.

[8] APC Propellers, "APC Propellers Performance Data," https://www.apcprop.com/technical-information/performance-data/, Accessed: 02-Feb-2026.

[9] Scholz, D., "Empennage sizing with the tail volume complemented with a method for dorsal fin layout," *INCAS Bulletin*, Vol. 13, No. 3, 2021, pp. 149–164. 10.13111/2066-8201.2021.13.3.13.

[10] Torenbeek, E., *Synthesis of Subsonic Airplane Design*, Delft University Press, Delft, 1982.

[11] Lopez, R. J., *Numerical simulation of a UAV wing and several modifications to improve range and endurance*, Master's thesis, Naval Postgraduate School, Monterey, California, Dec. 2023.

[12] Prieto, M., S. Escarti-Guillem, M., and Hoyas, S., "Aerodynamic optimization of a VTOL drone using winglets," *Results in Engineering*, Vol. 17, 2023. 10.1016/j.rineng.2022.100855.

[13] Teschner, T.-R., *A comparative study between winglet and raked wingtip wing configurations*, Master's thesis, Hamburg University of Applied Sciences, Hamburg, Germany, July 2012.

[14] Vic-Aéro, "flow5," https://www.flow5.tech/, Accessed: 16-Feb-2026.

[15] Maughmer, M. D., "Design of Winglets for High-Performance Sailplanes," *Journal of Aircraft*, Vol. 40, No. 6, 2003, pp. 1099–1106. https://doi.org/10.2514/6.2001-2406.

[16] American Institute of Aeronautics and Astronautics (AIAA), "2025-26 DBF Q&A #2," https://aiaa.org/wp-content/uploads/2026/01/QA-2.pdf, Oct. 2026, Accessed: 31-Jan-2026.

[17] ArduPilot Community, "ArduPilot Open Source Autopilot," https://ardupilot.org/, Accessed: 12-Jan-2026.

[18] Ansys, Inc., "Ansys Academic," https://www.ansys.com/academic, Accessed: 15-Jan-2026.

[19] Dewesoft d.o.o., "DewesoftX DAQ software," https://dewesoft.com/products/dewesoftx, Accessed: 22-Jan-2026.

[20] Abbot, I. H. and von Doenhoff, A. E., *Theory of Wing Sections*, Dover Publications, New York, 1959.

BUZZERANG

AIAA Design/Build/Fly Design Report 2025-2026

Georgia Institute of Technology

CONTENTS

LIST OF FIGURES

LIST OF TABLES

ACRONYMS AND NOMENCLATURE

AIAA	–	American Institute of Aeronautics and Astronautics	$C_{l,\beta}$	–	Dihedral Effect Coefficient
DBF	–	Design Build Fly	$C_{L,\alpha}$	–	Lift Curve Slope
GPS	–	Global Positioning System	$C_{m,\alpha}$	–	Pitch Stability Derivative
CAD	–	Computer Aided Design	$C_{n,\beta}$	–	Yaw Stability Derivative
GT	–	Georgia Tech	$C_{l,p}$	–	Roll Damping Coefficient
M1	–	Mission 1	$C_{m,q}$	–	Pitch Damping Coefficient
M2	–	Mission 2	$C_{n,r}$	–	Yaw Damping Coefficient
M3	–	Mission 3	L.E.	–	Leading Edge
GM	–	Ground Mission	C.G.	–	Center of Gravity
N_{Laps}	–	Number of Laps	V-n Diagram	–	Velocity-Load Factor Diagram
LiPo	–	Lithium Polymer	V_{NE}	–	Never Exceed Velocity
NiMH	–	Nickel Metal Hydride	ESC	–	Electronic Speed Controller
NiCad	–	Nickel Cadmium	OD	–	Outside Diameter
Wh	–	Wh	g	–	Gravitational Constant
V_{stall}	–	Stall Velocity	FEA	–	Finite Element Analysis
MTOW	–	Maximum Take-Off Weight	$C_{L,max}$	–	Maximum Coefficient of Lift
FOM	–	Figure of Merit	R	–	Radius
TO	–	Take-Off	V_{∞}	–	Freestream Velocity
psf	–	Pound per Square Feet	n	–	Load Factor
fps	–	Feet per Second	ω	–	Turn Rate
APC	–	Advanced Precision Composites	W/S	–	Wing Loading
UIUC	–	University of Illinois, Urbana-Champaign	V_{min}	–	Minimum Velocity
AVL	–	Athena Vortex-Lattice	V_{max}	–	Maximum Velocity
OpenVSP	–	Open Vehicle Sketch Pad	CA	–	Cyanoacrylate
$C_{D,0}$	–	Parasite Drag Coefficient	CNC	–	Computer Numeric Control
$C_{D,i}$	–	Induced Drag Coefficient	PLA	–	Polyactic Acid
C_L	–	Coefficient of Lift	PETG	–	Polyethylene Terephthalate Glycol
AR	–	Aspect Ratio	SLA	–	Stereo lithographic apparatus
e	–	Oswald Efficiency Factor	RPM	–	Revolutions per Minute
α	–	Angle of Attack			
β	–	Sideslip Angle			

1. EXECUTIVE SUMMARY

This report discusses the design, manufacturing, and testing of *Buzzerang*, the Georgia Institute of Technology's submission for the 2025-2026 AIAA Design, Build, Fly (DBF) competition. *Buzzerang* was designed to strike a balance between two commercial applications of fixed-wing aircraft: passenger flights and banner towing. The aircraft will complete a Ground Mission (GM) and three flight missions in multiple configurations: without payload, with cargo and passengers, and with a banner that must be stowed, deployed, and released in flight. *Buzzerang* is a 5-ft wingspan, low-wing aircraft with tricycle landing gear, and a maximum takeoff weight (MTOW) of 4.32 lb. It will carry an optimal payload of three rubber duck passengers and one hockey puck cargo in Mission 2 (M2), and a 75” by 15” banner in Mission 3 (M3).

1.1 Design Process

Buzzerang's design process began with a detailed scoring analysis to identify the characteristics that would most effectively contribute to an optimal score. This study guided design decisions, including wing area, optimal cargo load, passenger capacity, and banner size. Initial testing was conducted by retrofitting old aircraft with banner mechanism prototypes for early subsystem development run in parallel with preliminary aircraft design. Further analysis was performed to select a configuration, propulsion system, and empennage design for the final competition aircraft.

1.2 Key Performance Parameters and Design Features

The final design was selected based on scoring analysis and competition rules. The most important performance parameters are payload quantity, loading time, speed, endurance, and banner size. The aircraft features a conventional fuselage, low wing, and conventional tail. Cargo and passengers are arranged in a single file to allow for a narrow fuselage, thereby reducing skin friction drag. The tail is large to maintain adequate pitch and yaw authority while towing a banner at high speed. The banner is stowed underneath the fuselage and deployed by a swinging bar.

1.3 System Performance Capabilities

Overall performance for each system is determined through iterative designs in CAD programs. Modifications were made at each iteration. All mission-critical components were manufactured and tested to verify satisfactory performance. Some performance characteristics are listed in Table 1-1.

Table 1-1 Buzzerang Performance Characteristics

Performance Metric	Mission 2	Mission 3
Payload Capacity	3 Passengers, 1 Cargo	75” Banner
Lap Speed	136.4 ft/s	70.4 ft/s
Lap Time	24.8 seconds	38.8 seconds

2. MANAGEMENT

2.1 Team Organization

The Georgia Institute of Technology AIAA DBF Team is divided into two branches: the executive branch and the team member body. The team member body is further divided into four sub-teams with distinct missions and objectives: Structures, Aerodynamics, Propulsion, and Subsystems. The executive branch oversees finances and operations. The executive branch is comprised of the Faculty Advisor, a Post-Graduate Assistant, the Pilot, Chief Engineer, and Project Manager.

The Faculty Advisor and Post-Graduate Assistant provide support regarding technical analyses and decision-making, drawing on decades of combined experience in competition teams and entries. The Faculty Advisor further provides a direct link to the institution, supporting the team's logistical needs. The Pilot offers direct insight into the aircraft's handling properties and performance while mastering flying techniques to optimize mission performance. The Chief Engineer oversees the analysis, design, manufacturing, and testing of the aircraft while communicating directly with team leads to assess the team's overall operations. The Project Manager oversees sub-teams, manages team logistics, facilitates meetings, and tracks the project's timeline. The student members of the executive body work in conjunction to monitor the aircraft development process and ensure the team's competition-readiness.

The main body consists of 16 members, divided into four sub-teams. These teams are fluid and evolve over the course of the project as each team contributes to manufacturing and testing. Each team is headed by a Team Lead, a member with previous DBF experience appointed by the executive body. Each team has a specific role in the aircraft design process, completing tasks as outlined by the Project Manager and Chief Engineer. Newer members are free to choose any team and encouraged to branch out to other teams, facilitated by a close working relationship between teams. Team Leads report to the Project Manager and Chief Engineer with updates, requests, and questions as shown in Figure 2.1.

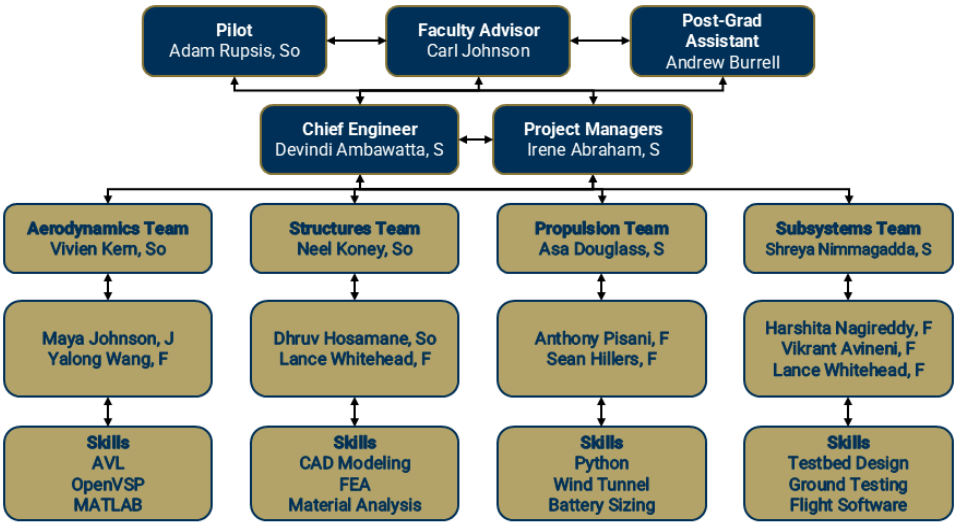

Figure 2.1 Team Organization Chart

2.2 Milestones

The Gantt Chart is organized by the Project Manager and lays out a schedule for the team leads to manage progress within sub-teams relative to the overall development of the competition plane. The schedule tracks multiple subsystems, utilizing communication between team leads to ensure proper coordination of deadlines. The initial scoring analysis and design is followed by multiple prototype constructions, with subsystem and prototype testing conducted concurrently to both validate sensitivity analysis results and inform later prototypes and the Competition Aircraft.

Team leads reconvene regularly to assess progress and reevaluate deadlines as needed. Tasks that fall behind schedule are identified and appropriately managed. The Gantt Chart in Figure 2.2 breaks down the design and manufacturing schedule Figure 2.2for easy visualization of all tasks and subtasks progress. All timelines include a margin of error to account for potential delays in progress. Subsystem design progressed slower than expected, as seen in the chart, due to iterative redesigns required after testing.

Progress through tasks and subtasks is indicated by bars overlayed on the Gantt Chart. By adhering to the schedule, the team was able to construct and test three aircraft. Prototype 1 involves manufacturing the general design of the aircraft and ensuring that flight is achievable, as well as initial tests of the banner system. Prototype 2 consists of continued testing of the banner system: collecting drag data and troubleshooting deployment systems. This culminates in a collective of design knowledge to construct the competition aircraft, ensuring all requirements are met.

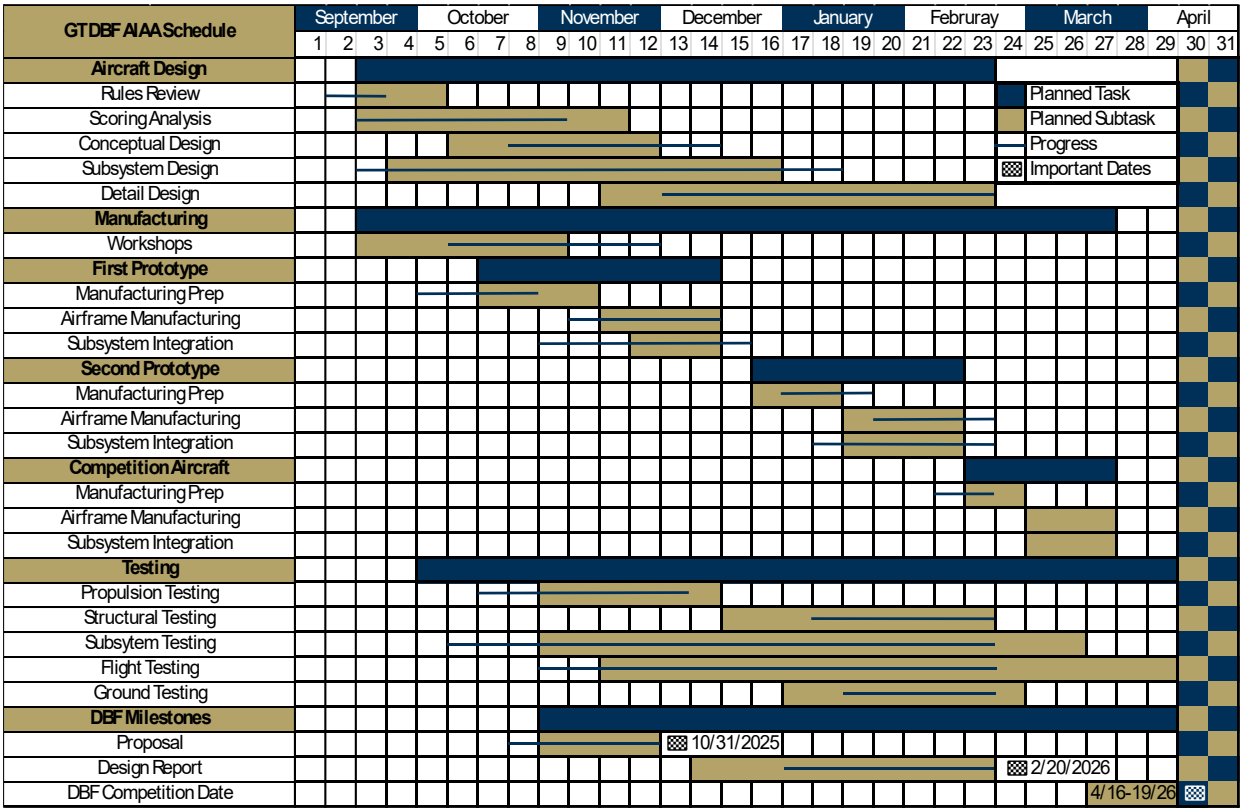

Figure 2.2 Aircraft Design and Manufacturing Schedule Gantt Chart

3. CONCEPTUAL DESIGN

The conceptual design phase involves decomposing the mission requirements and constraints to select an optimized aircraft configuration. A scoring analysis was conducted using the mission scoring equations, yielding general design parameters that maximized the total score. An iterative trade study was then employed to identify an aircraft configuration that satisfies both regulatory guidelines and optimized design parameters while maintaining manufacturability.

3.1 Mission Requirements

3.1.1 Mission Scoring

The total score of a team is mainly determined by two sub-scores: the report score and the mission score. The mission score is the sum of all three flight missions and the ground mission. The report score is a combination of the grades received on both the design report and the proposal, weighted at 85% and 15%, respectively. The total mission and report scores are multiplied together and added with a participation score of 1, 2, or 3 points for attending the fly-off, completing tech inspection, and attempting a flight mission, respectively. These equations are shown below in Equations 1-3.

$$Total\ Mission\ Score\ = M1\ + M2\ + M3\ +\ GM \tag{1}$$

$$Total\ Report\ Score\ =\ 0.85\ \times\ Design\ Report\ Score\ +\ 0.15\ \times\ Proposal\ Score \tag{2}$$

$$Competition\ Score\ =\ Total\ Report\ Score\ \times\ Total\ Mission\ Score\ +\ Participation\ Score \tag{3}$$

Each team must pass tech inspection before attempting a mission. The ground crew member will prepare and install all necessary components on the aircraft over a 5-minute staging window after passing tech inspection. The flight window for each mission begins when the aircraft throttle is advanced for the first time and lasts for 5 minutes.

A full competition lap consists of two 1,000 ft straight sections, an upwind and downwind 180-degree turn, and a 360-degree loop on the downwind straight as shown in Figure 3.1 Flight Mission CourseFigure 3.1. Teams must land successfully on the paved portion of the runway without significant damage, as determined by the Flight Line Judge, for any mission attempt to be deemed successful and to receive a score.

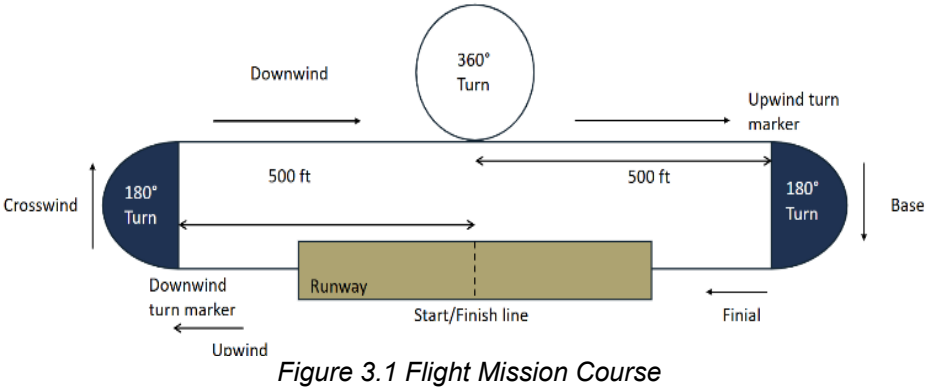

Figure 3.1 Flight Mission Course

3.1.2 Mission 1 (M1) – Delivery Flight

M1 requires the aircraft to complete 3 laps within the flight window. The team receives a score of 1.0 upon successful completion, as shown in Equation 4.

$$M1 = 1.0 \tag{4}$$

3.1.3 Mission 2 (M2) – Charter Flight

M2 requires the aircraft to complete as many laps as possible within the flight window while carrying a payload of passengers and cargo. Each team does not need to load the maximum number of passengers and cargo declared at Tech Inspection, but cannot exceed either the maximum cargo to passenger ratio or the maximum number of passengers and cargo. The team's score for M2 is a function of 1.0 points plus their net income divided by the maximum net income of all teams, as defined in Equation 5.

$$M2 = 1.0 + \frac{Net\ Income_{GT}}{Net\ Income_{Max}} \tag{5}$$

Net income is calculated by subtracting cost from income, as shown in Equation 6. Income and cost are based on the number of passengers and cargo comprising the aircraft's payload, and on the number of laps completed, as defined in Equations 7 & 8. Cost is also multiplied by the Efficiency Factor, which depends on the propulsion battery capacity in watt-hours, as shown in Equation 9.

$$Net\ Income = Income - Cost \tag{6}$$

$$Income = \left(P \times \left(6 + 2N_{Laps,M2}\right)\right) + \left(C \times \left(10 + 8N_{Laps,M2}\right)\right) \tag{7}$$

$$Cost = N_{Laps,M2} \times (10 + 0.5P + 2C) \times EF \tag{8}$$

$$EF = \frac{Q_{Battery}}{100} \tag{9}$$

3.1.4 Mission 3 (M3) – Banner Flight

M3 requires the aircraft to complete as many laps as possible within the flight window while flying a banner. The banner must be deployed on the downwind leg following the first upwind turn and released after the aircraft crosses the finish line on the last lap. The team receives a sub-score equal to the number of laps completed, multiplied by the banner length, and divided by the Rated Aircraft Cost (RAC). RAC is determined by the aircraft's wingspan in feet as shown in Equation 10. The team's score for M3 is 2.0 points plus the team's sub-score divided by the maximum sub-score of all teams as defined in Equation 11.

$$RAC = 0.05 \times b + 0.75 \tag{10}$$

$$M3 = 2.0 + \frac{(N_{Laps,M3} \times L_{Banner} \times (RAC)^{-1})_{GT}}{(N_{Laps,M3} \times L_{Banner} \times (RAC)^{-1})_{Max}} \tag{11}$$

3.1.5 Ground Mission (GM) – Charter and Banner Demonstration

GM begins with the aircraft in its flight configuration, inside a 10 ft by 10 ft "mission box," along with its uninstalled banner and the maximum number of passengers and cargo declared at Tech Inspection. Only the assembly crew member and the pilot can participate in the ground mission, and only the assembly

crew member may touch the plane. Both must start each segment of the GM behind the start/finish line and take off only when the GM official gives the signal.

The first segment of the GM begins with the assembly crew member loading the passengers and cargo into the aircraft, then running back to the start/finish line to stop the timer. The second segment involves the assembly crew member removing the passengers and cargo from the aircraft, installing the banner in the stowed configuration, and running back to the start/finish line to stop the timer again. The pilot will demonstrate that the flight controls are active before and after each segment, and that the banner is deployed and released after the second segment. The GM score for a team is its total time normalized by the lowest time recorded by any team, as defined in Equation 12.

$$GM = \frac{t_{GM}|_{Min}}{t_{GM}|_{GT}} \tag{12}$$

3.2 Translation into Design Requirements

The aircraft and its subsystems must satisfy a set of requirements derived from the mission objectives outlined in Section 3.1. These requirements are presented in Table 3-1 and served as goals during the conceptual design phase. The team derived specific subsystem and performance requirements by narrowing these high-level system design requirements to actionable items, as shown in Table 3-2.

Table 3-1 Requirements Breakdown from Ruleset

Category	Subcategory	Requirement	Requirement Identifier
Missions	M1	The airplane must complete three laps within five minutes	M1.1
		The airplane must land successfully	M1.2
	M2	The airplane must securely carry a certain number of passengers and cargo	M2.1
		The storage volume must be large enough to securely store all ducks and pucks	M2.2
	M3	The airplane must be able to deploy the banner remotely	M3.1
		The airplane must be able to release the banner remotely	M3.2
		The banner material and length must not interfere with stable aircraft flight	M3.3
		The banner must not excessively increase aircraft drag	M3.4
	GM	All hatches and access doors should be easily accessible	GM.1
		The banner must be sufficiently quick to load	GM.2
		The airplane must not be rotated or picked up during assembly or payload installation	GM.3
General	Structures	All components must be able to support the load during all parts of flight	G.1
	Aerodynamic	The aircraft must be stable in all flight conditions	G.2
	Propulsion	The aircraft must provide sufficient thrust to carry all cargo and maximize speed for the duration of the flight	G.3

Table 3-2 Subsystem Requirements Breakdown

Category	Driving Requirements	Subsystem Requirements / Performance Goals
Aerodynamics	M1.1, M3.3, M3.4, G.2	The aircraft must generate sufficient lift and maintain stable flight in all mission configurations, including banner towing and maximum payload conditions.
	M1.1	The aircraft must minimize drag to achieve three laps within five minutes.
	M1.1, M2.1, G.3	The propulsion system must provide sufficient thrust to carry maximum payload and meet lap-time requirements for the full flight duration.
Propulsion & Avionics	M3.1, M3.2	The aircraft must enable reliable remote deployment and release of the banner.
	GM.3	Avionics and control systems must allow ground installation without lifting or rotating the aircraft.
Payload Integration	M2.1, M2.2	The aircraft must securely accommodate all required passengers, cargo, ducks, and pucks without compromising CG or stability.
	M3.1–M3.4	The banner system must integrate without hindering aircraft controllability or excessively increasing drag.
	GM.1, GM.2	Payload systems must be quickly installed, demonstrated, and removed during competition operations.
Structures	G.1, M2.1, M3.3	All structural components must withstand flight loads, maneuver loads, and payload loads in all mission configurations.
	All missions	The airframe must maintain adequate strength-to-weight ratio to maximize mission performance.

3.3 Scoring Sensitivity

A thorough analysis of the scoring functions, mission profiles, and their implications were completed before the conceptual aircraft design. To understand which design parameters would most impact the aircraft's performance, a sensitivity analysis of the scoring functions was executed. This informed the configuration selection, as explored through numerous trade studies. Parametric models for key performance metrics were used within a physics-based trajectory simulation, enabling the team to better understand key design trade-offs and the systems-level interactions among scoring parameters.

A physics-based mission simulation framework was used to model all scored missions from this year's ruleset. The goal of this analysis was to identify key aircraft parameters and design trade-offs that optimize performance across all missions and maximize total competition score, while still complying with operational requirements and mission constraints. Variables used in the scoring functions were tracked throughout the mission simulations, including wing loading, payload capacity, banner length, wingspan, and M2 battery capacity.

3.3.1 Modelling

The mission simulator integrated parametric models and key performance parameters across discrete time steps, tracking state variables including position, velocity, acceleration, thrust, lift, and current draw. From these models, lap times and speeds were calculated for individual missions, which were applied to scoring functions so that general scoring trends could be plotted. Ruleset-specific models were integrated into the mission simulations as MATLAB functions to better reflect each mission's specific demands.

Ground Mission: The team set a baseline time for loading and unloading the banner, aiming to minimize the time as much as reasonably possible, on the assumption that the team could design an effective yet quick banner installation system. The team created various payload accommodation testbeds to practice loading and restraint mechanisms, enabling accurate time estimates for loading. Using this, a fixed amount of time was assigned to loading a single passenger and a single piece of cargo. This amount was scaled linearly with the number of passengers and cargo pieces being loaded, as no economies of scale could be assumed due to the lack of speed-loading mechanisms allowed. A safety margin was added to the GM timing model to allow for mechanical and human errors.

Structural Weight: Although the payload for this year's ruleset is not particularly heavy, it was still important to accurately model how increasing payload affects the aircraft's structural weight. A base empty weight was estimated for the aircraft using historical data from over 15 years of GT DBF aircraft. Using historical data from passenger- and cargo-focused rulesets, a weight regression was created to reflect how the aircraft's structural weight increases with its MTOW. Additionally, once propulsion options were narrowed down to a few realistic combinations, the propulsion system weight was also included in the overall weight calculations.

Propulsion: The propulsion system was modelled primarily using an in-house electric propulsion analysis tool developed by Whitmore, a former Georgia Tech graduate student [1]. The code integrates publicly available electric motor and propeller models into a Python tool, validated against commercially available software. Variables include motor kV rating and internal resistance, propeller diameter and pitch, and battery composition. The tool predicts the thrust and current draw of a given propulsion system across a range of velocities and throttle settings, which are passed to the larger trajectory simulation and used to calculate the thrust acting on the aircraft at each time step. Given that this year's ruleset included a penalty for higher battery capacities, the team also developed a model to track the amount of charge the battery used. Throughout a lap, the amount of current consumed can be interpolated from Whitmore [1] tool data using the model-predicted velocity at that time step. The model integrates the current consumption over time to estimate the battery charge consumed. By tracking how current is consumed over the course of competition laps, the team was able to determine the minimum capacity required, thus setting a threshold for sizing the M2 battery.

Aerodynamics: The team anticipated that a high-fidelity drag model would be crucial for understanding the performance trade-offs between M2 and M3. Separate studies were conducted to develop an accurate model. The aircraft's baseline drag coefficient was estimated to be 0.028 using OpenVSP predictions from historical competition aircraft. Historical data and OpenVSP models of conventional fuselage designs were used to develop a regression model of fuselage drag as a function of the number of passengers and cargo carried, to modify the baseline drag. However, the ratio of passengers to cargo remained fixed, as indicated by a sensitivity study analyzing net income variance across passenger-cargo ratios.

The most significant contributor to drag was the inclusion of the banner for M3, and so an additional drag model was created. Carruthers and Filippone's paper, "Aerodynamic Drag of Streamers and Flags" [2], was used to understand how banner length and aspect ratio affect drag through physical experiments. Since maximizing aspect ratio directly correlated to a reduction of drag, an aspect ratio of 5 was chosen for the banner. The banner's drag coefficient was defined using the banner's planform area (length × width) as the reference area and modeled as a function of the aspect ratio, as shown in Equation 13.

$$C_d = 0.4046\ (AR)^{-0.494} \tag{13}$$

This value was normalized against the wing area at each design point and added to the overall drag model. By incorporating the banner's drag into the mission simulation, the impact of the banner size on score versus aircraft performance was effectively evaluated.

Due to the strong winds that can be encountered in Wichita, it was important to accurately model the wind's effect on aircraft performance. This was done by implementing a wind-strength variable into the physics trajectory simulation, which maintained a constant direction throughout the flight. Crucially, the effect of wind was integrated throughout the aircraft's turns during the lap – this allowed for a better characterization of the speed lost during the turns and the changing effect of the wind on the banner.

3.3.2 Sensitivity Results

Payload, banner size, and battery capacity ultimately proved to be the most decisive sensitivity parameters across all missions, and the results of sensitivity analysis were used to determine the key goals of the preliminary design.

Banner Sizing: The overall mission score was highly sensitive to banner length, particularly for M3. Based on Carruthers and Filippone's paper [2], the banner's aspect ratio was fixed at 5, and the length was varied from 1 to 150 inches within the mission simulator. Increasing the banner length directly increased the score for M3, but the resulting drag penalty quickly degraded airspeed, thereby increasing lap time and reducing the number of laps that could be completed. This drag penalty was exacerbated by high wind conditions, especially the expected seasonal wind speed at Wichita of 30 feet per second. Figure 3.2 plots the M3 score as a function of banner length across a range of wind conditions.

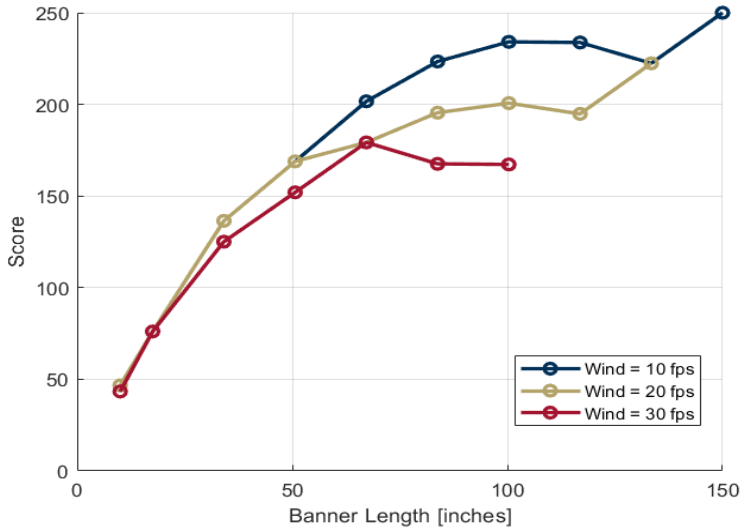

Figure 3.2 M3 Score vs Banner Length for Varying Wind Speeds

The wind speed impact was assessed using ranges from 0 to 30 fps. Each configuration has a critical banner length beyond which the marginal increase in M3 score is outweighed by performance degradation from banner-induced drag. Many longer banner lengths were eliminated in high-wind conditions due to extreme velocity loss, rendering the aircraft fundamentally non-competitive. Although this relationship between wind and critical banner length exists, the sensitivity study across all missions showed that even in high-wind conditions, M3 remains the dominant contributor to total score. As wind speed increases, the relative importance of M3 compared to M2 decreases, but it does not fundamentally alter the priority of M3 over M2. This trend is shown in Figure 3.3, which led the team to prioritize aircraft optimized for M3 rather than M2 in the preliminary design.

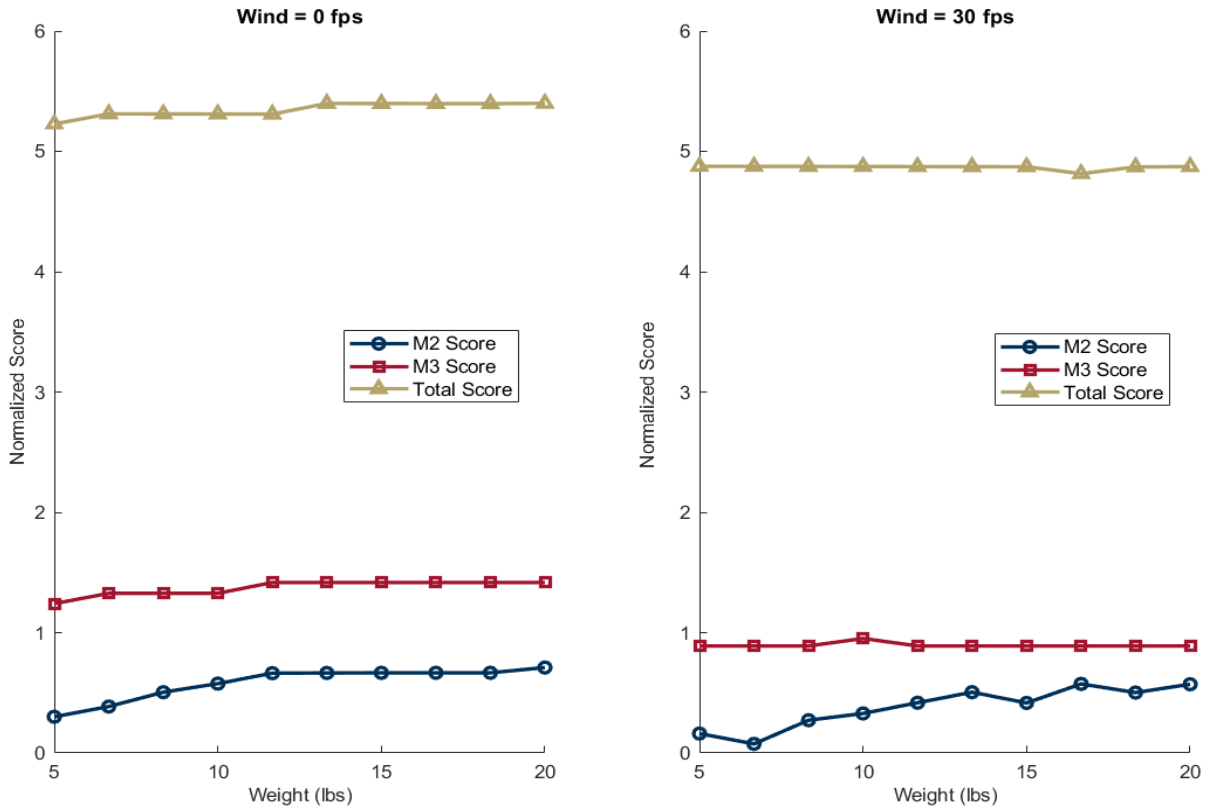

Figure 3.3 Mission Score Sensitivity to Wind Conditions

Payload: The second most important driver identified in the sensitivity analysis was the effect of the total M2 payload on aircraft performance across all missions. Although an initial sensitivity study found that, given the costs and incomes outlined in the ruleset, it was optimal to maintain a fixed ratio of three passengers to one cargo piece, the total payload still had to be determined. The sensitivity of the score to the passenger-to-cargo ratio is shown in Figure 3.4.

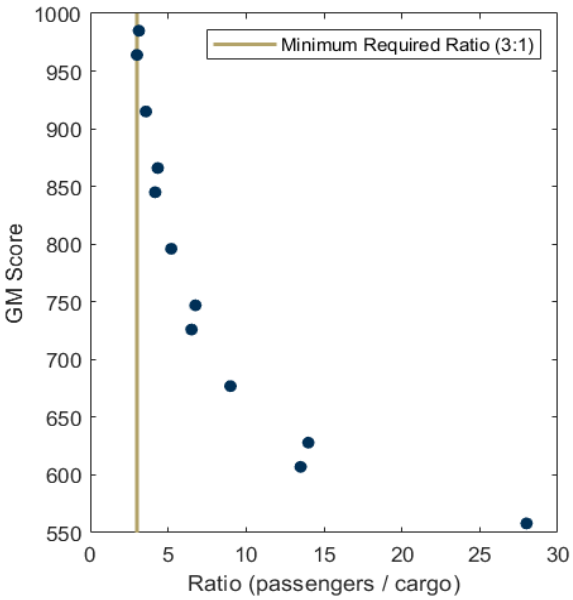

Figure 3.4 Passenger to Cargo Ratio Sensitivity

Since no speed-loading techniques are allowed for GM, it was found that GM time increases linearly with payload – therefore, maintaining the minimum of 3 ducks and 1 puck was optimal for GM. Conversely, Figure 3.5 shows a clear increase in M2 score as aircraft weight (and therefore number of payloads) increases.

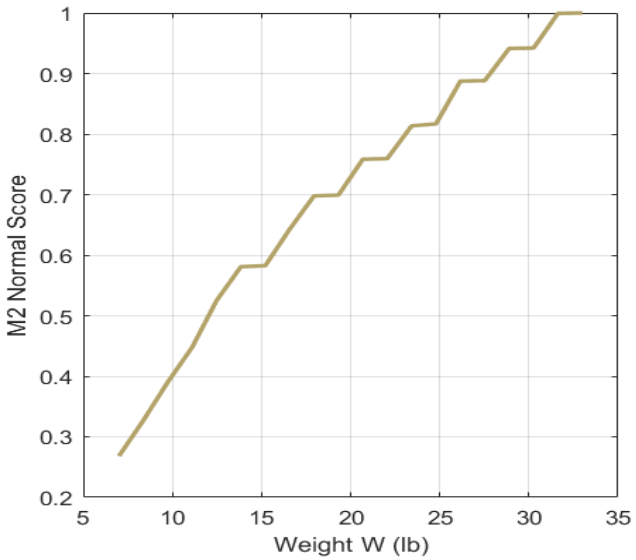

Figure 3.5 M2 Score vs Aircraft Weight

By including the drag regression for the fuselage based on payload volume, the performance of M2 and M3 can be compared to assess the effect of increasing payload volume. The marginal gain in M2 score decreases as payload volume increases, due to the growing drag penalty. As a result of this drag regression, the M3 score is strongly sensitive to payload volume, because an oversized fuselage increases the aircraft's drag during steady-level flight, on top of the existing banner drag component. Therefore, the dominance of M3 over M2 demands a lower payload for M2 to minimize fuselage drag.

Battery: By calculating current consumption over competition laps, a minimum capacity requirement was determined for M2 across all wind conditions. A margin of safety was added to account for modeling inaccuracies and to give the team greater confidence in the aircraft's safety; therefore, a 6S LiPo battery with a capacity of 75Wh was selected for M2. Although adding the margin of safety to the predicted required battery capacity had a slight negative impact on the score, the team decided that the aircraft's survivability was more important to the overall completion of M2.

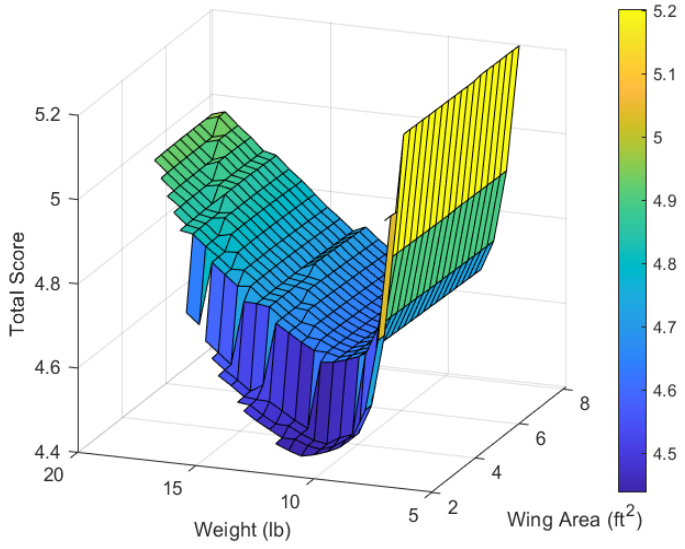

Figure 3.6 Overall Results of Sensitivity Analysis

The compiled results of the sensitivity analysis are shown in Figure 3.6. This plot displays the total score across all missions for a broad design space, covering aircraft of varying weights and wing areas. Lighter colors indicate higher scores, revealing two types of aircraft that can achieve high scores – either large aircraft carrying heavy payloads to maximize M2, or smaller, lighter aircraft built for speed in GM and M3. However, as shown in the plot, the highest scores are achieved with a low-payload design point, reflecting the greater importance of M3 and GM relative to M2.

3.3.3 Summary

Scoring analysis yielded the design point shown in Table 3-3, which informed preliminary design and sizing but remains subject to change based on testing. The sensitivity of both the GM and M3 scores to payload volume led the team to a small-fuselage, low-payload-volume design point with a large banner size. By intentionally designing for a small, light payload, the fuselage and wing structures will also be optimized for light weight, further improving M3 performance by increasing the lift-to-weight ratio. Additionally, the importance of minimizing drag for M3 drives the team to design a highly aerodynamic, low-drag banner-mounting system, so banner accommodations must be considered as early as the preliminary design phase. Sensitivity results also led the team to select very specific, lower-capacity batteries for M2, which in turn prioritized propulsion testing.

Table 3-3 Design Point from Sensitivity Analysis

Overall Aircraft Dimensions		
Wingspan	**Wing Area**	**MTOW**
5 ft	4.33 ft^2	4.32 lb
Mission-Specific Parameters		
Payload Number	**M2 Battery Capacity**	**Banner Dimensions**
3 Passengers, 1 Cargo	75 Wh	75 in. x 15 in.

3.4 Potential Configurations Explored

The team explored a variety of aircraft configurations to optimize competition performance. Both real-world aircraft as well as past AIAA competition planes were used as inspiration for *Buzzerang*'s design. Design features of high importance like wing planform, tail configuration, and banner attachment were further categorized into a weighted decision matrix. After creating the matrix in Table 3-4, the team systematically reviewed the options and selected high-scoring configurations for further development.

3.5 Configuration Selection Process

3.5.1 Pugh Matrices and Figures of Merit

This section presents the team's evaluation of the discrete configurations derived from the design alternatives in Table 3-4. A weighted Pugh matrix analysis was conducted, where each design was rated on a scale of one to five for each figure of merit. These scores were then multiplied by the respective weight of each figure of merit. After summing the weighted scores, the highest-scoring configuration was selected.

Table 3-4 Design Alternatives Matrix

Component	Subcategory	Design Alternatives		
Wing	Platform	Conventional	Delta	Flying Wing
	Attachment	Low	High	Biplane
Fuselage	Style	Singular	Double	Blended
	Cross-Section	Rectangle	Rounded Rectangle	Circular
Tail	Planform	Conventional	H-Tail	T-Tail
	Attachment	Single Boom	Double Boom	Integrated
Propulsion	Layout	Tractor	Pusher	Push-Pull

Categorical weightings were determined by careful consideration of all mission aspects. Banner stowing was considered the next most important aspect as proper storage substantially reduces drag and minimizes the event of a failed release. As seen in Table 3-5, a conventional wing-body configuration was scored higher than a blended body and delta wing because of its superiority in banner stowing and payload integration. Its rectangular fuselage is ideal for the passenger and cargo compartments to reduce GM times while providing attachment points for the banner stowing mechanism. These advantages were prioritized over the increased aerodynamic efficiency of the blended wing-body configuration.

Table 3-5 Wing-Body Configurations Weighted Pugh Matrix

		Wing-Body Configurations			
		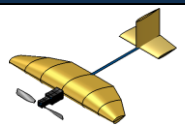	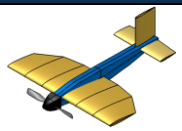	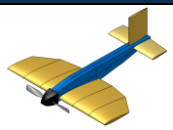	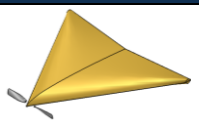
Figure of Merit	**Weight**	**Blended Body**	**Conventional High Wing and Fuselage**	**Conventional Low Wing and Fuselage**	**Delta Wing**
Ground Mission Accessibility	5	3	4	5	3
Banner Stowing	4	3	5	4	2
Banner Interference	3	3	3	3	5
Payload Integration	4	4	4	5	3
Manufacturability	2	2	4	4	5

Table 3-6 outlines the design possibilities for the tail. The primary consideration in the tail design was to prevent interference from the deployed banner. This constraint made the H-Tail and V-Tail configurations unfeasible while favoring the T-Tail configuration due to its increased separation from the banner. The Conventional Tail was selected due to its balance between maneuverability and manufacturability. This

Table 3-6 Tail Configurations Weighted Pugh Matrix

		Tail Configurations			
		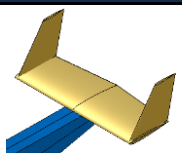	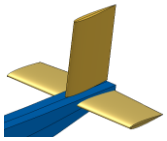	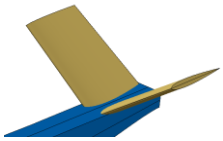	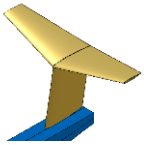
Figure of Merit	**Weight**	**H-Tail**	**Conventional Tail**	**V-Tail**	**T-Tail**
Banner Interference	5	2	4	3	5
Manufacturability	2	3	5	2	3
Weight	3	3	4	5	3
Maneuverability	4	5	4	2	3
Structural Complexity	3	3	3	5	4
Total Score	-	39	55	42	47

configuration maximizes controllability, safety, and ease of construction while still supporting effective payload integration and mission flexibility.

Table 3-7 outlines the evaluation of banner attachment and deployment mechanisms. The deployed banner's position substantially impacts the aircraft's stability by diminishing the pilot's control authority, increasing the risk of a crash. Mounting the banner near the tail increases the moment arm of the banner forces acting on the aircraft, further decreasing stability. Attaching the banner near the aircraft's center of gravity minimizes the leverage of banner drag forces, similarly reducing the generated moment after banner deployment. However, *Buzzerang's* wings and ailerons are aft of the aircraft's center of gravity, so a banner located at the CG has the potential to interfere with control systems. Drag was also prioritized due to the importance of battery management in M3. While a string-towed banner may decrease the chances that the banner gets caught in the tail, the risk of the banner rotating increases, which would create unpredictable moments on the aircraft. Ground mission accessibility is considered but not weighted as heavily as factors that compromise flight safety.

Table 3-7 Banner Attachment and Deployment Weight Pugh Matrix

Banner Attachment/Deployment				
Figure of Merit	**Weight**	**Attached at CG**	**Attached near tail**	**Towed by string**
Impact on flight stability	5	5	3	2
Impact on drag	5	4	5	3
Interference with plane during flight	4	2	3	5
Ground mission accessibility	3	2	5	3
Weight	2	4	3	5
Total Score		63	70	59

3.5.2 Aircraft Pugh Matrix and Figures of Merit

The team decided that the most critical figure of merit is maneuverability, as that most directly enables the aircraft to successfully tow, deploy, and release a banner, which significantly impacts M3 performance. Payload integration has a score of four because of its significant impact across M2 and M3 scores with cargo/passenger and banner integration, along with its impact on GM times. Drag performance is scored three because of its effect on the efficiency and speed of the aircraft through all phases of flight and during all the missions. Empty weight is also assigned three as lower projected empty weight improves performance through reducing required thrust and improving climb performance. Finally, manufacturability was weighted slightly lower than other figures but remained a consideration to ensure the aircraft could be reliably constructed and repaired in a timely manner. Table 3-8 illustrates the main figures of merit.

Table 3-8 Figures of Merit

Figure of Merit	Score				
Maneuverability					5
Payload Integration				4	
Drag			3		
Empty Weight			3		
Manufacturability		2			

3.6 Final Conceptual Design

Buzzerang is a 5-ft-wingspan, low-wing aircraft with tricycle landing gear. It features a tapered wing and a built-up fuselage that connects the wing and tail. *Buzzerang* will carry its payload of three ducks and one hockey puck in the fuselage near the CG. The banner will deploy from its mounting position, flush with the bottom of the fuselage, to a firm 90-degree angle. The final configuration is shown in Figure 3.7.

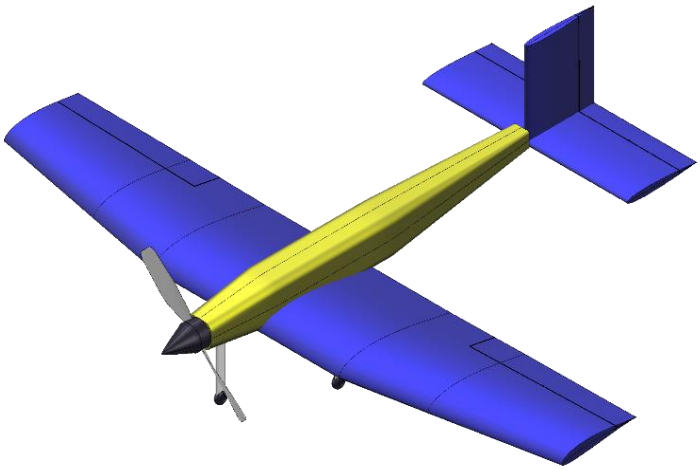

Figure 3.7 OpenVSP Sketch of Final Configuration

4. PRELIMINARY DESIGN

4.1 Design Methodology

The design methodology followed an iterative process informed by competition requirements, scoring analysis, and prior Georgia Tech DBF experience. Conceptual design began with an initial aircraft configuration, selected based on design parameters derived from scoring analysis. Based on this analysis, a low-wing, conventional-fuselage aircraft prioritizing fast GM and a long banner was selected. This layout served as the baseline for preliminary sizing and trade studies. Aerodynamic studies then selected airfoil geometry, wing loading, and a stable static margin (SM). All lifting surfaces were analyzed using the Athena Vortex Lattice (AVL) tool which was developed by Dr. Mark Drela [3]. Wing planform geometry was refined using AVL through iterations of taper, quarter-chord sweep, and tip twist to improve lift distribution and reduce tip stall tendency. The propulsion system was selected using an in-house electric propulsion analysis system, then sized and added to the aircraft's digital model. After completing initial sizing, CAD was utilized to create an outline of the aircraft and subsystem components. Space inside the fuselage and wing areas was reserved for wiring and avionics components. Completion of the design led to manufacturing, incorporating laser cutting, 3-D printing, and composite modeling. The aircraft was tested

Figure 4.1: Chosen Design Methodology

in flight tests, and designs were revised based on testing results and observations. This iterative design methodology, including feedback between analysis, testing, and refinement, is illustrated in Figure 4.1.

4.2 Design Trades

4.2.1 Constraint Sizing

Sensitivity analysis defines a target design point based on maximum takeoff weight and wing area, which is then confirmed through constraint analysis. Adapted from Mattingly's approach [4], constraint curves are plotted using an energy-based method derived from ruleset performance requirements and the team's historical data. Calculations for these curves use the heaviest expected weights and speeds from M2, with the battery capacity target set by scoring analysis as the baseline performance. The speeds for M3 assume a full 100 Wh battery but account for the expected drag from the banner. Load factors are selected based on historical aircraft limits and desired handling qualities for *Buzzerang*. The constraint analysis in Figure 4.2 yields a design point with a wing loading of 1.2 lb/ft^2, corresponding to an MTOW estimate of 4.32 lb. The design point has a power loading of about 150 Watt/lb, which is then used to determine potential propulsion system options.

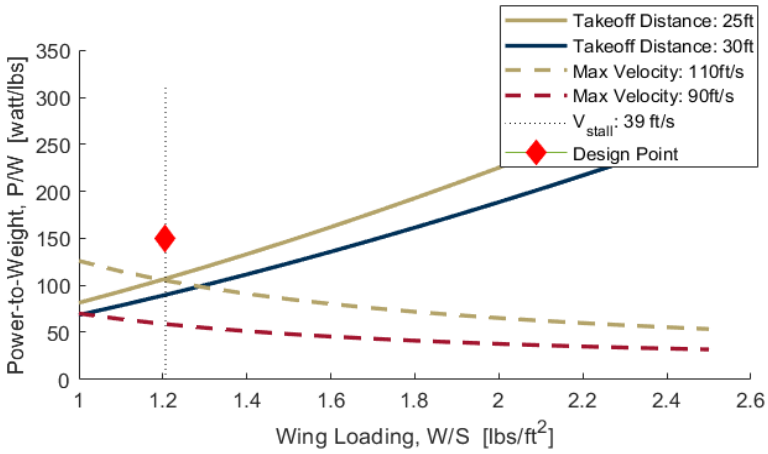

Figure 4.2 Constraint Diagram

4.2.2 Propulsion System Selection

The Whitmore Tool [1] was used to analyze the possible propulsion systems. Using parameters such as motor resistance, operating current, KV, battery values (capacity and internal resistance), and the propeller's pitch and diameter, the team evaluated over 150 propulsion system combinations from various vendors. APC propellers with 16 to 20-inch diameters and 8 to 12-inch pitches were analyzed with various motor/battery pairs. Hacker Motor, Badass Power Systems, and T-Motors were preferred, given the team's historical use and trust in these manufacturers. The best candidates and their performance metrics are summarized in Table 4-1 below.

Table 4-1 Comparison of Propulsion System Candidates

Motor	Battery	Propeller	Current (A)	Static Thrust (lbf)	Thrust at 90 fps (lbf)	System Weight (lb)
T-Motor AT4130 KV300	6S (3300mAh)	APC 17x10E	55.72	14.50	2.31	1.1
T-Motor AT4130 KV450	6S (3300mAh)	APC 17x10E	74.27	14.41	8.14	1.1
T-Motor AT4130 KV450	6S (3300mAh)	APC 18x8E	72.70	15.47	7.91	1.1

M2 features an Efficiency Factor in the scoring function that penalizes teams for higher battery capacity ratings. Therefore, the battery capacity limitation motivated the evaluation of the propulsion system candidates. The primary metrics used are peak current draw, static and dynamic thrust at 90 feet per second, and overall propulsion system weight, leading the team to select the AT4130 KV450 with a 17x10E propeller.

4.3 Aerodynamic Characteristics

4.3.1 Airfoil Selection

Lift coefficient, aerodynamic efficiency, manufacturability, and thickness were paramount to *Buzzerang*'s airfoil selection. Candidate airfoils were analyzed using XFOIL [5], an open-source, low turbulence airfoil analysis and design software. The team also compared XFOIL's predictions to the UIUC airfoil database's [6] wind tunnel testing results. The following airfoils were chosen for further analysis: SD 7062, SD 7032, NACA 4412, and NACA 23015, shown in Figure 4.3.

Metrics used to evaluate each airfoil include the following:

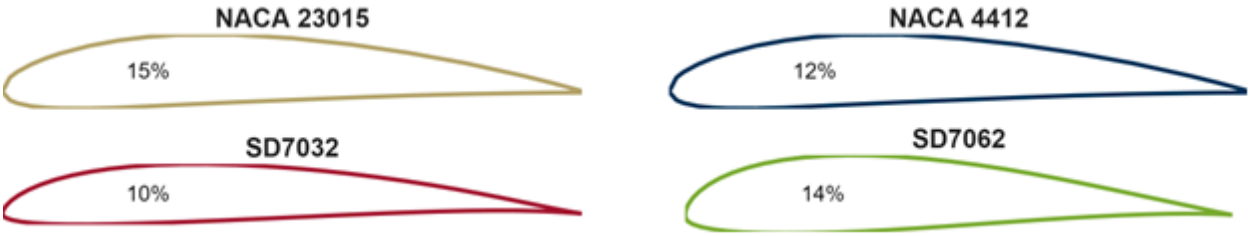

Figure 4.3 Airfoils Selected for Further Analysis

- *Lift Coefficient:* Lift coefficient was a key factor in selecting Buzzerang's airfoil because it determines how much lift the aircraft can generate during demanding maneuvers. A higher maximum lift coefficient allows the airplane to execute tighter turns and sustain higher loads without stalling, which is critical during M2 and especially M3. The lift curves for the airfoils evaluated can be found in Figure 4.4– this plot demonstrates that the SD7062 has the highest $C_{L,max}$ occurring at a sufficiently high angle of attack.
- *Aerodynamic Efficiency:* M2 and M3 both emphasize speed over a longer duration of time. Given that M3's banner will be a

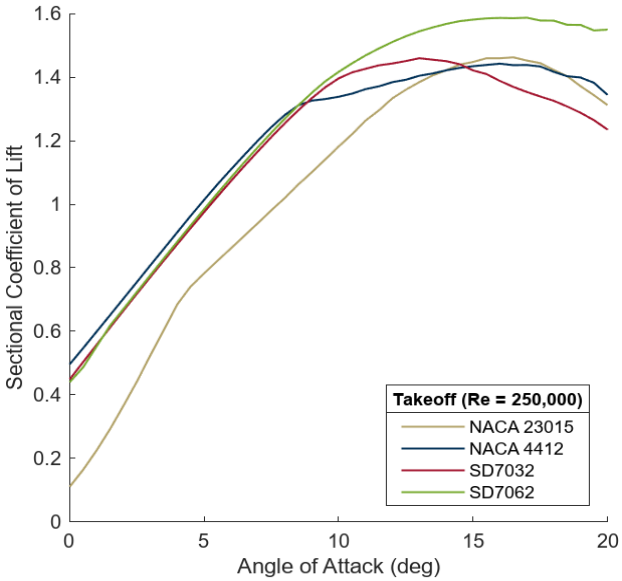

Figure 4.4 XFLR5 Airfoil Lift Curves

significant source of drag, it was important to minimize aircraft drag and therefore necessitates a high lift-to drag ratio. Although the SD 7062 has a slightly higher sectional drag coefficient (shown in Figure 4.5), the SD7062 was chosen since it maintains a high $C_{L,max}$ at high angles of attack (shown in Figure 4.4) which maximizes efficiency and prevents premature stall.

- *Manufacturing:* From prior experience, the team knew that airfoils with complex geometry and thin trailing edges are harder to CAD and manufacture. When the wing is relatively small in comparison to those built by the team previously, errors and inconsistencies in manufacturing have manifested as poor flight performance. Hence, it became important to balance aerodynamic demands with geometric simplicity.

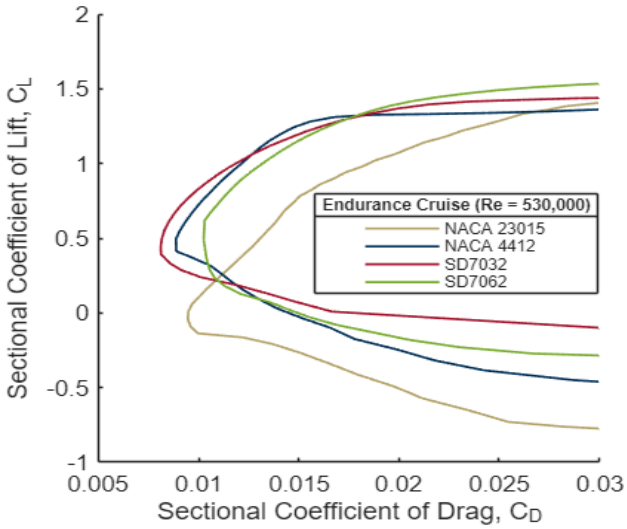

Figure 4.5 XFLR5 Drag Polars

- *Thickness:* The selected airfoil must have thickness at the root section to allow for fuselage attachment options. When the wing area is relatively small but the wingspan remains at five feet, the chord is small, increasing the risks associated with the wing being too thin. Lastly, increased thickness improves structural stiffness of the aircraft and is important under high loading conditions.

Utilizing these criteria, the team selected the SD 7062 airfoil for the wing. The team compared the predicted XFLR5 values to UIUC wind tunnel data as shown in Figure 4.6 to validate the accuracy of the aerodynamic models, and it has excellent agreement the test data.

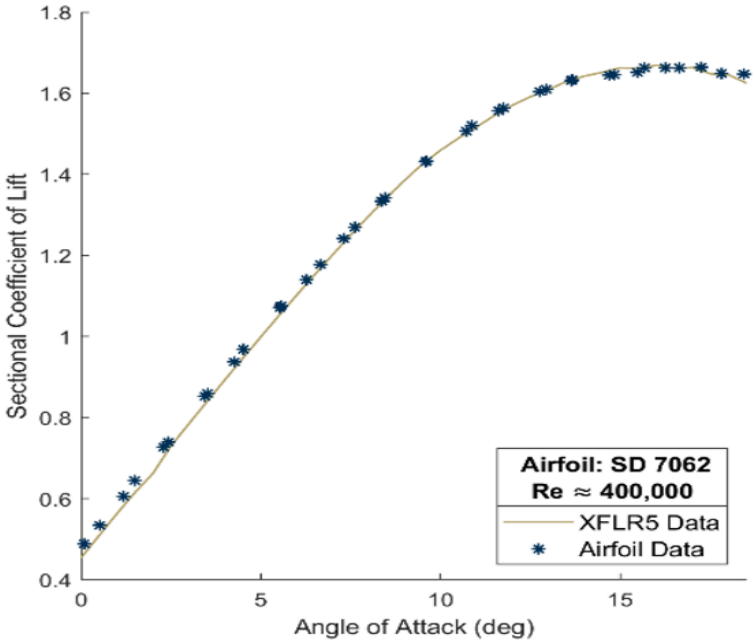

Figure 4.6 Lift Curves for XFLR5 Prediction vs UIUC Wind Tunnel Data

4.3.2 Lifting Surface Analysis

Following airfoil selection, the wing was designed using the area and AR from initial sizing. Then the wing sweep, taper, and twist were selected for a low induced drag and to maintain an unswept trailing edge to simplify manufacturing of control surfaces. After that, the tail surfaces were sized based on empirical stability targets. The total configuration is then analyzed and the results are visualized. By modeling the lifting surfaces as an infinitely thin vortex sheet in AVL [3], the software can calculate aerodynamic characteristics such as lift and drag coefficients, stability derivatives, and trim conditions. The horizontal and vertical stabilizers of the aircraft were designed using this method to ensure the necessary amount of stability and controllability. The margin for stability parameters was chosen based on previously flight-tested competition aircraft. The wing's taper and sweep were designed using AVL [3] to obtain an optimal elliptical lift distribution. Figure 4.7 displays the trimmed lift distribution overlayed across the geometry of the lifting surfaces when at $C_{L,max}$.

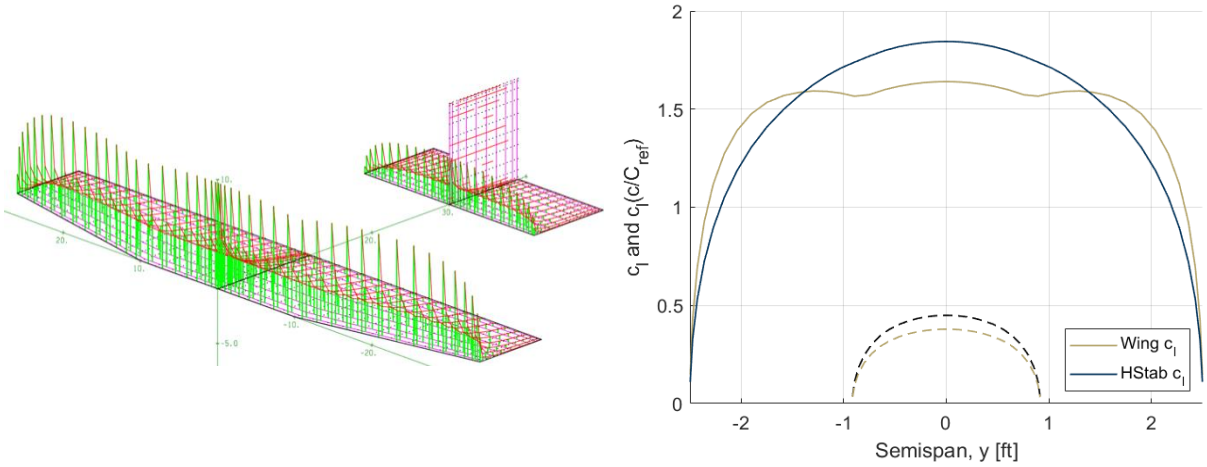

Figure 4.7 AVL loading distribution imposed on vehicle geometry (left) and Trefftz plot (right)

4.3.3 Drag Analysis

Using OpenVSP's Parasite Drag Analysis tool [7], the team obtained an initial estimate of parasitic drag for the aircraft. The OpenVSP model applies form factor relationships explained in Hoerner's Fluid Dynamic Drag [8] and normalizes each component to the wing reference area. Table 4-2 separates the parasitic drag contribution of each component, including the methodology used to derive each component's estimate.

Table 4-2 Drag Component Breakdown

Component	Method	$\Delta C_{D,0}$	%
Wing	OpenVSP Parasite Drag (DATCOM)	0.0086	56.25
Fuselage	OpenVSP Parasite Drag (DATCOM)	0.00157	10.27
Empennage	OpenVSP Parasite Drag (DATCOM)	0.00242	15.83
Landing Gear	Wind Tunnel Experiment	0.0024	15.69
Banner	Hoemer's Method for Lifting Surfaces	0.0003	1.96

4.3.4 Banner Aerodynamics

The team expects significant drag to be generated by a large banner. As referenced for the preliminary scoring analysis, the team utilized prior research to obtain empirical relationships for banner size and resulting drag. The team also referenced literature regarding the banner material's contribution to drag.

Wilk and Skuta's [9] laboratory test found that the textiles with the lowest drag coefficients were smooth materials, across a variety of stiffnesses. This influenced the team to test both lightweight and smooth fabrics. The team also explored how additions and alterations to the banner such as streamers, slits, and sewn-in rigid objects would affect performance. Carruthers and Filippone [2] found that streamers increase drag, however the team wanted to see how input and stabilization would affect the system entirely, which is discussed further in Section 8.

4.4 Stability and Control

4.4.1 Static Stability

The aircraft's static stability was evaluated using AVL [3] in a condition of zero sideslip and 16.1-degree angle of attack (the aircraft's approximate stall angle). In this condition, the aircraft achieves a lift coefficient of 1.58. Table 4-3 summarizes the results of the static stability analysis, including aerodynamic parameters and damping derivatives. Using historical data from previous competition aircraft, the team deemed all derivatives within acceptable handling qualities. These predictions were validated by pilot feedback following the flight of the first prototype aircraft.

Table 4-3 Static Stability Results

Parameter	AVL Results	
Aerodynamic Parameters	C_L	1.58
	α (deg)	16.10
	β (deg)	0.00
Stability Derivatives	$C_{L,\alpha}$ (rad^{-1})	4.28
	$C_{m,\alpha}$ (rad^{-1})	-0.61
	$C_{n,\beta}$ (rad^{-1})	0.14
	$C_{l,\beta}$ (rad^{-1})	-0.15
Damping Derivatives	$C_{m,q}$ (rad^{-1})	-12.35

4.4.2 Dynamic Stability

Dynamic stability characteristics were predicted using the static stability analysis results. The calculations used to derive dynamic stability from static stability are taken from Phillips' Mechanics of Flight [10] using the six degree of freedom linearized differential equations. The eigenvalues of Phillips' plant matrix describe the five longitudinal and lateral dynamic modes. Like static stability analysis, dynamic

Table 4-4 Dynamic Stability Results

	Longitudinal Modes			Lateral Modes	
Mode	**Short Period**	**Phugoid**	**Dutch Roll**	**Roll**	**Spiral**
Damping Rate (s^{-1})	6.92	-0.12	0.48	4.67	-0.19
Time to Double/Half (s)	0.10	5.95	1.44	0.15	3.57
Damping Ratio (~)	0.81	-0.11	0.10	~	~
Damped Natural Frequency (s^{-1})	5.03	1.05	4.79	~	~
Undamped Natural Frequency	8.55	1.05	4.82	~	~

stability was evaluated at MTOW and assumed an airspeed of 1.2 times the stall speed. Table 4-4 displays the results of the dynamic analysis, showing that the aircraft is predicted to be stable in Roll, Short Period, and Dutch Roll modes as seen by their positive damping rates. Although the Dutch Roll mode's damping ratio is relatively small, the time to double is sufficiently long such that the team remains confident in the aircraft's Dutch Roll mode stability. The aircraft is unstable in Phugoid and Spiral modes, yet their time to double is also sufficiently long, allowing for instability to be easily controlled and suppressed by the pilot.

4.4.3 Control Surface Sizing

The control surfaces were sized using AVL [3] to ensure that there would be adequate handling quality for the pilot within their deflection ranges under all flight conditions.

Elevator: *Buzzerang* was designed to maintain a neutral pitching moment during all phases of flight. During takeoff, the aircraft operates near its stall angle of attack at a low velocity, making it one of the most challenging phases to maintain pitch moment neutrality. The team used AVL to determine the required elevator deflection at $C_{L,max}$ for various elevator sizes. A 15˚ trim limit was set to ensure sufficient maneuverability. The team iterated through different combinations of horizontal stabilizer and elevator sizes until the required trim deflection fell below that limit at a chord percentage of 30%.

Rudder: The team designed *Buzzerang* to withstand significant crosswind conditions given Wichita's history of high winds. The design condition was set at a 15-mph direct crosswind, a 25˚ sideslip angle, and a 30˚ deflection limit in AVL [3]. Given a chord ratio of 30%, AVL predicted a deflection of 14.5˚ to be sufficient. The rudder was oversized slightly to account for any unpredictable dynamics from the banner, resulting in a final chord ratio of 35%.

Aileron: Faster turns will help to reduce mission lap times, which will especially compound to save time across the entire 5-minute window. The team targeted a minimum bank rate of 90 degrees within 0.5 seconds, using a conservative 12˚ aileron deflection during all critical flight phases, primarily low speed takeoff and landing. Figure 4.8 illustrates the simulated time to 90-degree bank angle.

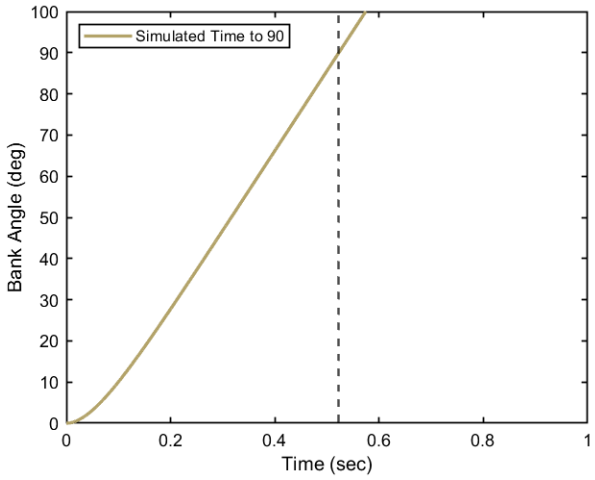

Figure 4.8 Simulated Roll Speed

4.5 Mission Performance

4.5.1 Mission Model

The team created a model to predict overall mission performance, using it to further validate and refine the preliminary design point obtained from the initial scoring sensitivity analysis by providing a more accurate mission score prediction.

The team created this mission model as a physics-based simulation in MATLAB, incorporating the preliminary aerodynamic and propulsion analysis results. The aircraft is modeled as a point mass, and the equations of motion are integrated over time to compute the trajectory across various lap segments. Climb, cruise, and turn segments are evaluated individually and then strung together to simulate a full mission for each of the three flight missions.

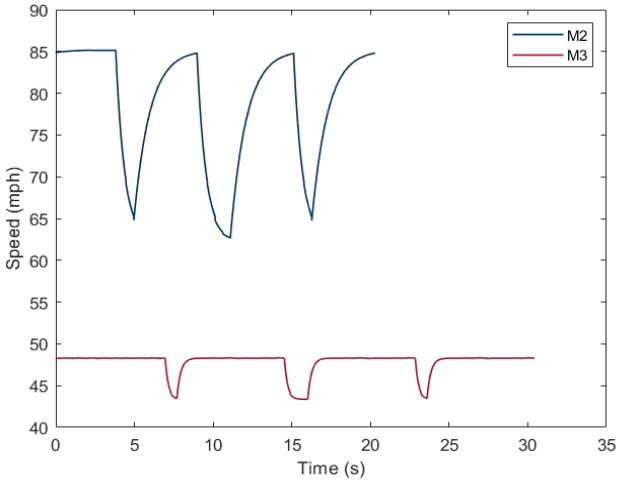

Figure 4.9 Predicted Airspeeds for 1 Lap of M2 and M3

Level flight is assumed and occurs at the lower of the stall-limit load factor or the design structural-limit load factor. Battery energy consumption, a measure of endurance, is tracked over the course of the mission using power draw predictions from the Whitmore propulsion tool [1]. Figure 4.9 shows the mission model's prediction of how airspeed varies over time for each mission. The dips in the airspeed curves represent sudden deceleration during the 180 and 360 degree turns in a standard lap profile.

4.5.2 Operating Conditions

With the competition taking place in Wichita, KS in April, historical weather conditions were analyzed to predict their impact on flight performance. Table 4-5 compares average conditions in Wichita during April with those experienced during testing in McDonough, GA. As shown in this comparison and Figure 4.10, conditions at the competition are expected to be significantly windier than those during testing, with historical average wind speeds of 12.2 mph compared to 6.7 mph in McDonough.

Table 4-5 Comparison of Weather Conditions in Wichita, KS and McDonough, GA

Condition	TAEFC Wichita, KS	HCRCC McDonough, GA
Month	April	February
Environment	Humid Subtropical Climate	
Average High Temperature (°F)	69	58
Average Wind Speed (mph)	12.2	6.7
Average Humidity (%)	67	60
Elevation (ft)	1300	814

The team anticipates that these higher wind speeds will hinder taxiing ability but increase takeoff performance at MTOW. For M3, the higher wind speeds will cause an increase in drag generated by the banner. Additionally, the increase in altitude and temperature correlates with lower air density, which is expected to reduce lift and thrust. As such, the team accounted for expected decreases in performance relative to test data in its prediction models.

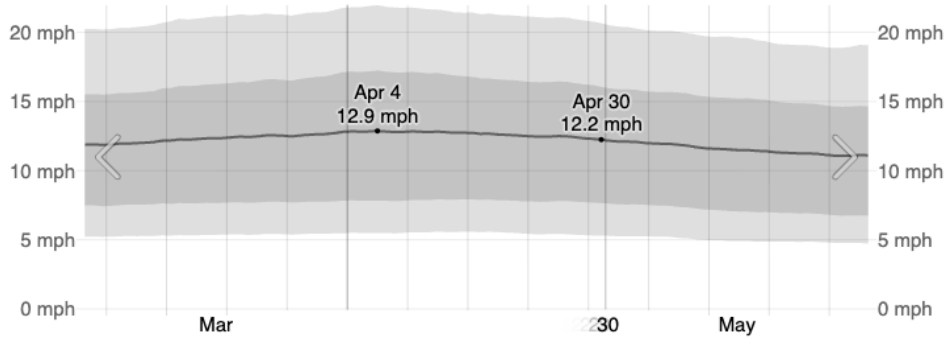

Figure 4.10 Average Wind Speed in April in Wichita, KS from WeatherSpark [11]

4.5.3 Uncertainties

The team sought to balance a relatively accurate mission model, with the need to start prototyping early in the competition timeline to maximize the amount of possible flight testing. To do so, the mission model simplifies some aspects of the flight profile. During the mission, it is unrealistic that turns maintain constant altitude or velocity, even though stall conditions are not approached. Propulsion estimates are notably uncertain, as in prior years the team has observed higher airspeeds. The models for point performance are also approximations, albeit chosen to mitigate uncertainty. The mission model also cannot accurately represent the effects of the strong and unsteady winds present in Wichita.

4.5.4 Mission Performance Summary

The team's MATLAB-based mission simulation evaluates competition performance by integrating the aircraft's equations of motion across each phase of flight and estimates battery endurance. This model links aerodynamic and propulsion characteristics to scoring functions and takes into account the predicted adverse atmospheric conditions in Wichita. The team has also recognized the assumptions made in the simulation, which were incorporated to balance early prototyping and accurate mission modeling. Key preliminary aircraft dimensions, propulsion selections, aerodynamic parameters, and predicted mission performance resulting from this process are summarized in Table 4-6.

Table 4-6 Preliminary Aircraft Design and Performance Parameters

Primary Aircraft Dimensions				Propulsion System Specifications		
Component	**Span**	**MAC**		**Component**	**M2**	**M3**
Wing	60 in	10.67 in		Motor	AT4130 KV450	
Horizontal Tail	22 in	9 in		Propeller	17x10E	
Vertical Tail	9.25 in	9 in		Battery Chemistry	LiPo	
Fuselage	**Length**	**Width**		Battery Cells	6S	6S
	39 in	4 in		Battery Capacity	3300 mAh	4500 mAh
Aerodynamics				**Predicted Aircraft Performance**		
Parameter	**AVL Value**			**Parameter**	**M2**	**M3**
$C_{L,max}$	1.58			Lap Speed	85 mph	48 mph
Stall Angle	16.1 °			Lap Time	20.68 s	30.43 s
Static Margin	15.20%			Payload Capacity	3 Pass. 1 Cargo	75" x 15" Banner
1/4 Chord Sweep	8.5 °					
Tip Twist	3 °			Scoring Variables	EF - 0.75	RAC = 0.77

5. DETAILED DESIGN

5.1 Structural Characteristics

Buzzerang's overall design is a conventional aircraft configuration with a tapered wing, conventional fuselage, and conventional tail. Table 5-1 includes key dimensional parameters of the aircraft, defined from the leading edge of the wing.

Table 5-1: Key Dimensions of Buzzerang

Dimensions			
Component	**Attribute**	**Value**	**Unit**
Overall	**Length**	44.20	**in**
	LE X-Location	5.72	**in**
	M1 CG X-Location	10.72	**in**
	Static Margin	15.76	**%**
Wing	**Span**	59.90	**in**
	Mean Aerodynamic Chord	9.40	**in**
	Aspect Ratio	5.60	**~**
	Area	640.00	**in²**
Vertical Tail	**Span**	9.25	**in**
	Chord	9.30	**in**
	LE X-Location	35.11	**in**
	Planform Area	86.49	**in²**
Horizontal Tail	**Span**	22.00	**in**
	Chord	9.25	**in**
	LE X-Location	35.11	**in**
	Area	198.00	**in²**

5.1.1 Layout and Design

The aircraft is designed to keep in mind aerodynamic, ground, and motor loads. Figure 5.1 depicts the load transfer path for each type of load.

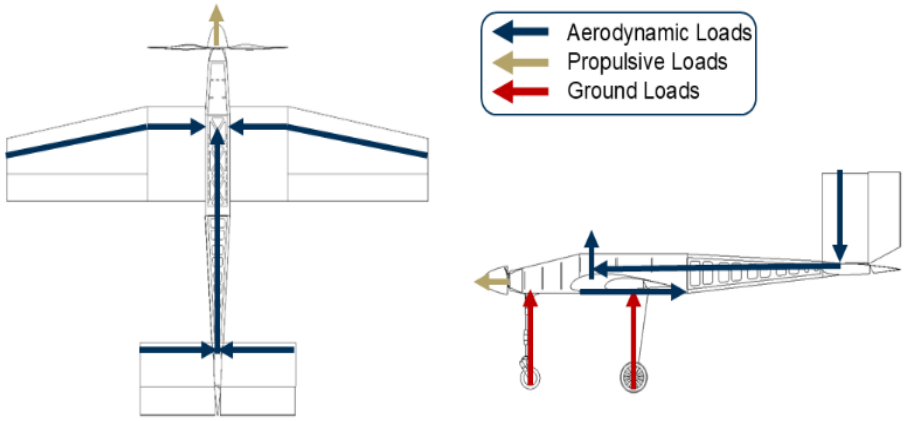

Figure 5.1: Load Path Diagram

- *Aerodynamic Loads:* Aerodynamic loads consist of lift and drag acting on the wing and tail. Carbon fiber capping strips near the quarter chord reinforce the wing, in addition to the shear webbing that resists bending loads. D-box structures are also designed to increase torsional stiffness. Any attachment point to the fuselage is reinforced with plywood doublers. The tail is similarly built, omitting the additional carbon fiber capping strips and using only the shear webbing structure, given its small size. The fuselage is built up to the tail (rather than using a tail boom) to minimize weight. The tail-fuselage connection is made of plywood.

- *Ground Loads:* Ground loads are primarily concerned with the impulses from landing impact and are therefore managed by the landing gear. The landing gear connects to carbon-reinforced plywood bulkheads, which transfer the loads to the fuselage structure.

- *Motor Loads:* The motor generates an axial thrust force and moment; this imparts a rapid change in torque when the motor is pushed to maximum power for takeoff. These motor loads are supported by a plywood bulkhead connecting to other built-up fuselage structure.

5.1.2 Flight Envelope

The aerodynamic and structural characteristics of *Buzzerang* help determine the safe operating limits before structural failure. A spar deflection calculation was performed to determine a safe loading operating range. The V-n diagram in Figure 5.2 shows the flight envelopes for the mission profiles. The maximum load factors are determined by the maximum lift coefficient ($C_{L,\,max}$) before stall.

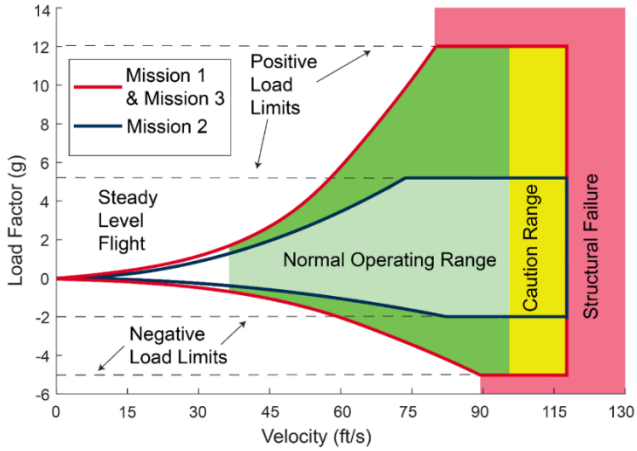

Figure 5.2 Diagram of the Aircraft's Operating Range

5.1.3 Fuselage-Wing Connection

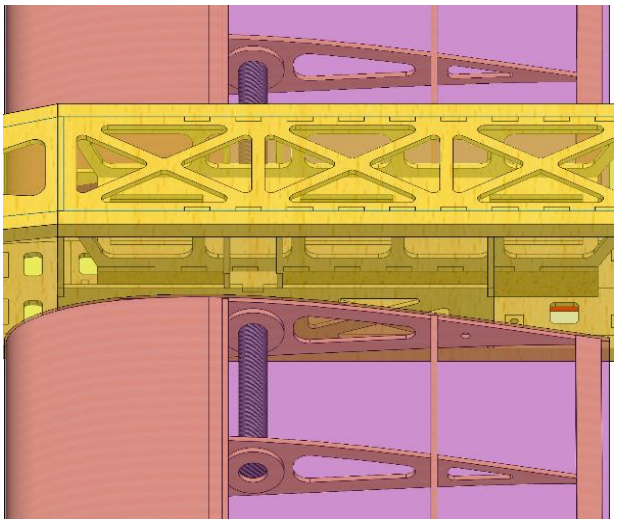

Figure 5.3 Wing Fuselage Connection Spar Connection in CAD

The wings are connected to the fuselage via a 12-inch spar that runs through the fuselage and the first two ribs of each wing. The wings slide on the spar and are secured by two bolts on each wing–one near the trailing edge and the other near the leading edge–to ensure torsional rigidity. Local plywood plates are glued to the ribs around the spar to provide adequate surface area for the wings to transfer their load to the spar and fuselage. Figure 5.3 shows the wing–fuselage connection.

5.2 System and Subsystem Design and Implementation

Buzzerang's major subsystems include the center body, empennage, landing gear, and propulsion systems. Other crucial subsystems include the banner deployment system, the cargo storage container, the passenger container, and avionics. This section outlines each subsystem and its compliance with performance requirements, highlighting their integration with other systems to improve the aircraft's overall performance.

5.2.1 Fuselage

The fuselage serves as the primary load-bearing body, while also accommodating the passengers, cargo, and banner mechanism. The primary structure consists of multiple plywood and balsa bulkheads connected by balsa sticks and reinforced by a balsa floor running through the bulk of the fuselage. Because *Buzzerang* features a high tail, the floor stops when the fuselage begins to taper upward. To support the

empennage, the fuselage utilizes a semi-monocoque construction with several bulkheads and balsa sheeting. To attach the wings, the fuselage features a short spar running through two connected plywood plates in the middle section. The main landing gear are mounted to a quarter inch plywood plate connected to the floor, and the nose gear is bolted on to the firewall. The avionics, battery, passengers, and cargo are also stored inside the fuselage, and hatches on the sides and top provide convenient access to all internal systems and wing mounting screws. An aerodynamic fairing around the motor and curved edges are used to reduce the drag produced by the fuselage which is displayed in Figure 5.4.

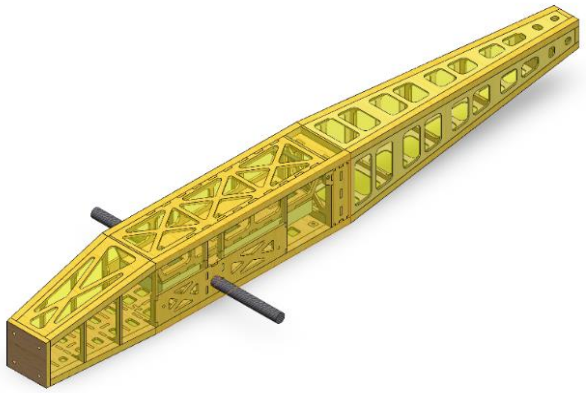

Figure 5.4: Fuselage CAD

5.2.2 Empennage

The empennage, shown in Figure 5.5, is a conventional tail configuration with one vertical stabilizer and one horizontal stabilizer. The center of the horizontal stabilizer features a protruding plywood box that extends a few inches in front of the empennage and slots into a hole at the back of the fuselage. Both stabilizers feature quarter-inch balsa sticks and shear webbing (thin balsa sticks) that run spanwise for added stiffness. The vertical stabilizer's shear webbing extends from the vertical stabilizer and through the plywood box at two points to resist shear loads during flight.

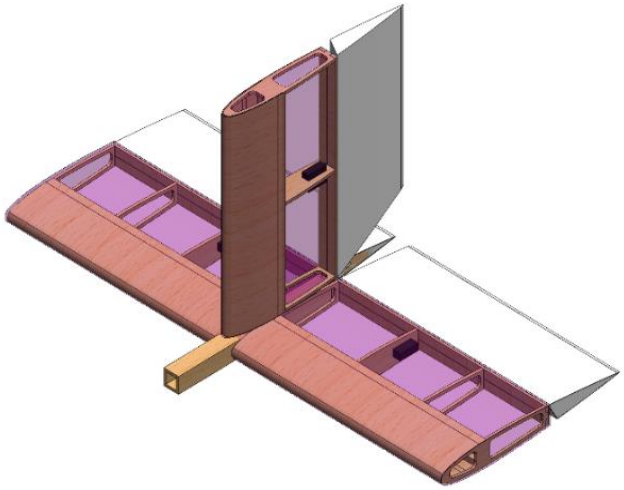

Figure 5.5: Empennage CAD

The horizontal stabilizer includes multiple shear webbing pieces that run continuously through the entire horizontal stabilizer, ensuring a strong connection to the fuselage connection box. The front portions of the horizontal and vertical stabilizers include thin balsa sheets that wrap around the leading edges to ensure resistance to torsional loads. The stabilizers are both rectangular and feature symmetric airfoils.

5.2.3 Wing

The wing consists of two different halves, which slide onto the carbon fiber tube in the fuselage and bolt on to the side plates. A non-tapered section extends 8 inches from the fuselage, followed by a 20-inch-long section with an 11.3-degree taper. Shear webbing runs along the quarter chord and is

reinforced by two thin rectangular carbon fiber rods. These provide most of the stiffness in the wing which is designed to carry a load of up to 8g at MTOW. The wing is shown in Figure 5.6.

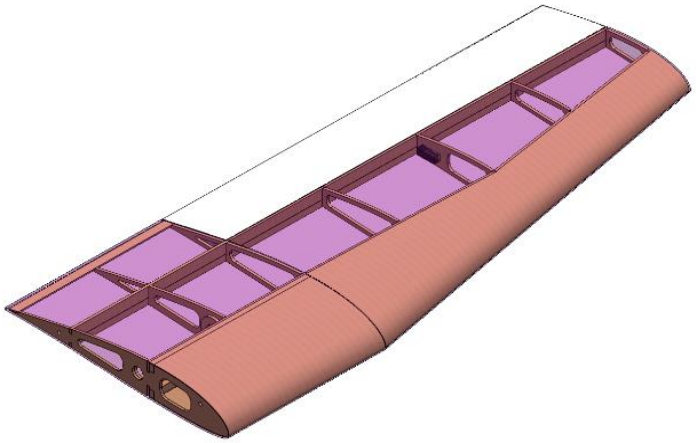

Figure 5.6: Wing CAD

5.2.4 Landing Gear

Buzzerang's tricycle landing gear consists of a carbon fiber main gear and an aluminum nose strut, as shown in the drawing package. Their placement was designed to provide proper propeller clearance, load distribution, and ground maneuverability. The main strut is an off-the-shelf bowed carbon fiber gear combined with two foam wheels. Together, they support the entire landing load. The main struts are mounted to the landing gear plate and the locally reinforced floor within the fuselage using 3 bolts. The lightweight aluminum nose strut is steered via a Corona DS939HV servo, which allows ±45 degrees of rotation to handle the windy conditions in Wichita. Figure 5.7 shows the landing gear configuration.

Figure 5.7 Landing Gear CAD

5.2.5 Propulsion

The main propulsion system is comprised of a motor, ESC, battery, and propeller. Since the M2 score depends on battery capacity, and M3 does not, a larger battery will be used in M3 to allow a higher sustained throttle setting to overcome the banner drag. An Ovonic 6S 3300mAh (73.26Wh) battery was chosen for M2, and an HRB 6s 4500mAh (100Wh) battery was selected for M3. These batteries will power a T-Motor AT4130 450kV motor with a BadAss 120A ESC in combination with a 17x10E propeller. Additionally, a fuse/arming plug is used between the battery and ESC. Details of each component are described in Table 5-2.

Table 5-2: Components for Buzzerang's Propulsion System

Components	Description
Motor	T-Motor AT4130 450kV
Propeller	APC 17x10E
Battery (M1 and M2)	6S Ovonic 3300mAh LiPo
Battery (M3)	6S HRB 4500 mAh LiPo
Speed Controller	BadAss ESC 120A

5.2.6 Passenger and Cargo Accommodation

As shown in Figure 5.8, the fuselage contains a removable box that carries a single piece of cargo, which slots into the fuselage from the side. To accommodate the passengers, a balsa box that hinges on one edge compresses the three passengers using foam attached to the top. The compartment's hatch has holes on the bottom where the passengers' heads stick out, restraining them. The compartment is part of the fuselage and fastens with C-shaped 3D-printed clasps that wrap around a small carbon-fiber tube. The fuselage is fastened to facilitate loading from the top, as sideloading would interfere with wing placement. The cargo bay is at the back of the non-tapered section of the fuselage because wing placement constricts viable locations.

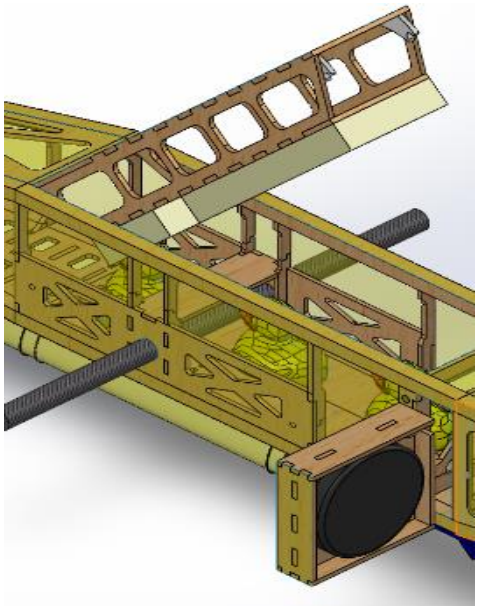

Figure 5.8 Payload and Cargo Accommodation

5.2.7 Banner Deployment and Release Mechanism

The final banner subsystem for M3 consists of a 75-inch-long by 15-inch-tall banner integrated with an under-fuselage storage and deployment system. The banner dimensions were selected to meet competition requirements while maintaining stable towing performance and acceptable aircraft handling characteristics. The banner is fabricated from 30-denier ripstop nylon, providing a lightweight, durable solution suitable for repeated deployment and release. This material offers sufficient tear resistance while minimizing aerodynamic penalties during towing. The banner is stowed beneath the fuselage and deployed using a remotely actuated swinging bar mechanism. This system securely retains the banner during takeoff and climb, enables controlled deployment during the downwind segment, and allows full release prior to landing

in accordance with M3 requirements. Before flight, the banner is wrapped around the swinging bar and securely attached. During flight, a servo releases the rubber bands which hold the banner in place, allowing the bar to swing down and the banner to unravel. To fully release the rigging, a servo actuates a pin, allowing the bar and banner to drop. The mechanism is mechanically simple, lightweight, and integrates cleanly with the fuselage, supporting reliable operation and efficient GM installation. Figure 5.9 shows the finalized banner system configuration.

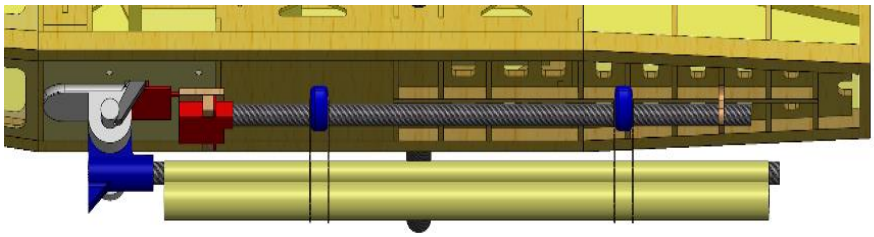

Figure 5.9: Banner Mechanism

5.2.8 Avionics

Eight servos actuate all control surfaces and the banner deployment and release mechanism. The main considerations in servo selection were size, torque, weight, and response time. The servos must fit within the ribs of the empennage surfaces, have a high torque-to-weight ratio, and have a short response time to ensure precise control at high speeds. The MKS HV6120H and Corona DS939HV servos were selected. Their specifications are compared in Table 5-3.

Table 5-3: Servos Used in Buzzerang

Servo	Servo Torque (oz-in)	Size (in)	Response Time (s)	Weight (oz)
MKS HV6120H	59.6	0.90 x 0.32 x 1.04	0.11	0.388
Corona DS939HV	36.1	0.88 x 0.45 x 0.96	0.13	0.44

The MKS HV6120H servos are used in all control surfaces for their thin profile, high torque, and low weight. The Corona DS939HV servos are used for nose wheel steering and the banner mechanism. Using a Futaba R7014 receiver and a Futaba T14SG radio, the pilot can actuate all control systems and throttle in flight. Table 5-4 shows all the avionics components.

Table 5-4: Major Avionics Components

Components	Description
Receiver	Futaba R7014
Transmitter	Futaba T14SG
Control Surface Servos	MKS HV6120H
Nose Wheel Steering	Corona DS939HV

5.3 Weight and Balance

Determining the center of gravity (CG) is crucial for longitudinal control and stability. A weight and balance analysis was conducted by modeling individual components in SolidWorks and applying appropriate material densities. The weight of fixed subcomponents was estimated using previous aircraft data. Lateral (Y-axis) and vertical (Z-axis) CG locations were briefly considered but deemed negligible due to their small moment arms. Table 5-5 displays the predicted weights and CG locations of all major components of the aircraft's empty-weight structure as it would fly in M1, along with the resulting CG and total weight. The datum for CG measurements is the wing's leading edge at the root.

Table 5-5: Weight and Balance of Empty Aircraft

M1 (Empty Aircraft)				
Category	**Components**	**Weight (lb)**	**X-CG Location (in)**	**Moment (lb-in)**
Structure	Nose Landing Gear	0.1	-5.6	-0.56
	Main Landing Gear	0.4	8	3.2
	Tail	0.3	32.25	9.675
	Fuselage	1.2	11	13.2
	Wing	0.71	3.33	2.3643
Propulsion	Propellor	0.1	-7	-0.7
	Motor	0.4	-6.3	-2.52
	ESC	0.1	-5.8	-0.58
Avionics	Receiver	0.05	-4	-0.2
	Aileron Servos	0.04	5	0.2
	Tail Servos	0.04	36	1.44
	Wiring/Connectors	0.1	12	1.2
Batteries	Receiver Battery	0.05	-5	-0.25
	Main Battery	0.89	-2.675	-2.38075
M1	-	**4.48**	**5.38**	**24.08855**
Neutral Point (in)		**6.7**		
Static Margin (%)		**15.01%**		

M2 and M3 introduce mission-specific payloads, namely passengers and cargo for M2 and the banner for M3. Adding the payload in M2 shifts the CG slightly aft, but not enough to significantly affect the airplane's stability. The static margin during M1 is 15.01%, and after adding the passengers and cargo it is 15.5%, ensuring stability and high performance across both missions. When the banner is deployed in M3, the center of mass shifts from directly under the CG of the plane to aft of it, causing a slight rearward shift in CG. However, because the banner drag increases the static margin and the banner is relatively light, this effect was deemed insignificant for CG calculations. The weight and balance for M2 and M3 are shown in Table 5-6.

Table 5-6: Weight and Balance for M2 and M3

Mission 2					Mission 3			
Category	**Component**	**Weight (lb)**	**X-CG (in)**	**Moment (lb-in)**	**Component**	**Weight (lb)**	**X-CG (in)**	**Moment (lb-in)**
Payload	Rubber Ducks	0.1125	6.5	0.73	Banner Deployment/Release Mech (Deployed)	0.5	7.5	3.75
	Hockey puck	0.375	13	4.88				
Battery	6S 3300mAh LiPo	1.04	-4.4	-4.58	6s 4500mAh LiPo	1.35	-4.4	-5.94
Empty Aircraft	-	3.43	6.11	20.957	-	3.43	6.11	20.957
M2 Configuration		4.958	4.43	21.987	**M3 Configuration**	5.28	3.55	18.767
Neutral Point (in)		**6.7**			**Neutral Point (in)**	**~6.7**		
Static Margin		**15.50%**			**Static Margin**	**~15.01%**		

5.4 Performance

5.4.1 Flight Performance

The performance of the aircraft was determined from the propulsion model, drag polar, and equations from Anderson's Aircraft Performance and Design [12]. The team used a combination of XFOIL and AVL to determine $C_{L,max}$ and determine wing loading and stall speed. Equations 14 and 15 were used to determine the turn radius and rate, respectively to determine the time necessary to complete the 360-degree turn. The results from these equations are summarized in Table 5-7.

$$R = \frac{V_\infty^2}{g\sqrt{n^2-1}} \tag{14}$$

$$\omega = \frac{g\sqrt{n^2-1}}{V_\infty^2} \tag{15}$$

Table 5-7 Flight Performance Estimates

Parameter	M1	M2	M3
Weight (lb)	4.48	4.96	5.28
Wing Loading (psf)	1.03	1.15	1.22
Stall Speed (fps)	23.04	23.04	23.04
Max Speed (fps)	85	85.1	48
Lap Time (s)	25.56	20.68	30.43
Max. Turn Load Factor, n	8	8	8
Min. Sustained Turn Rad. (ft)	28.27	28.34	9.01
Min. Time for 360 deg (s)	3.1	2.7	3.8

The stall characteristics of the aircraft are the limiting factors for the maximum instantaneous turn rate and turn load factor for a given airspeed. The selected propulsion system provides sufficient thrust to sustain turns across the entire operational velocity. The intersection of the instantaneous and sustained turn rates in the doghouse plot in Figure 5.10 determines the maximum sustained turn rate.

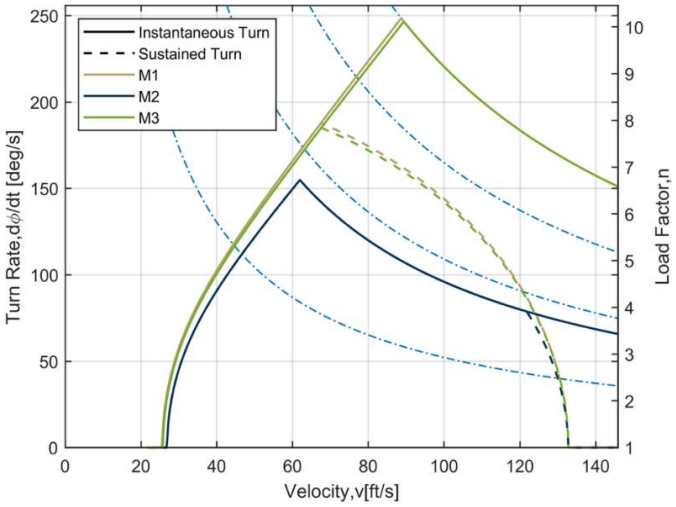

Figure 5.10: Doghouse Plot for M1, M2, and M3

A thrust available and required versus velocity plot was generated for M2 and M3, as shown in Figure 5.11. The propulsion system was chosen so that both missions could be flown at full throttle for the five-minute duration. To generate the thrust versus velocity curves, the Whitmore Propulsion Tool was run at full throttle with a 6s battery. The drag curves are based on the drag polar and flight test data on the drag created by the banner when deployed. The intersection of the thrust and drag curves determines the maximum velocity.

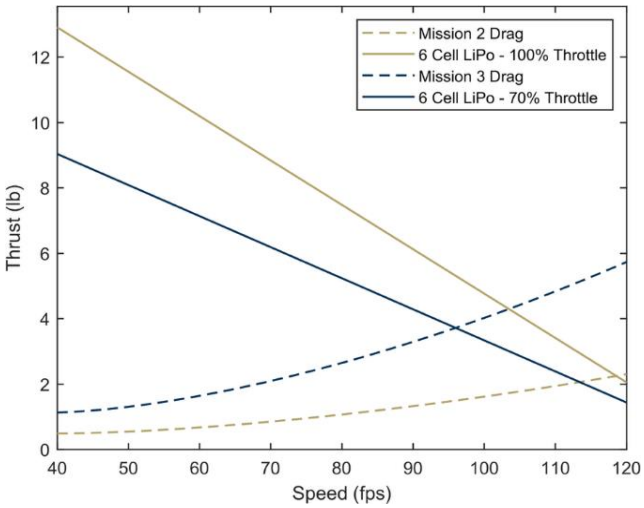

Figure 5.11: Thrust Available and Required

5.4.2 Mission Performance

The mission model developed in Section 4.5 was used to predict mission performance. A performance simulation was run, integrating lift and drag data from OpenVSP and AVL and yielding data for the aircraft's airspeed over time. The predicted airspeed over one lap of M2 and M3 is shown in Figure 5.12.

The aircraft demonstrates lower cruise velocity in M3 than in M2 due to the large drag force generated by the banner. M2 does not have the same drag penalty but is flown at a lower power setting to maximize propulsion system efficiency. Because M1 score does not depend on lap times, it will be flown at a lower and safer velocity to minimize risk of failure.

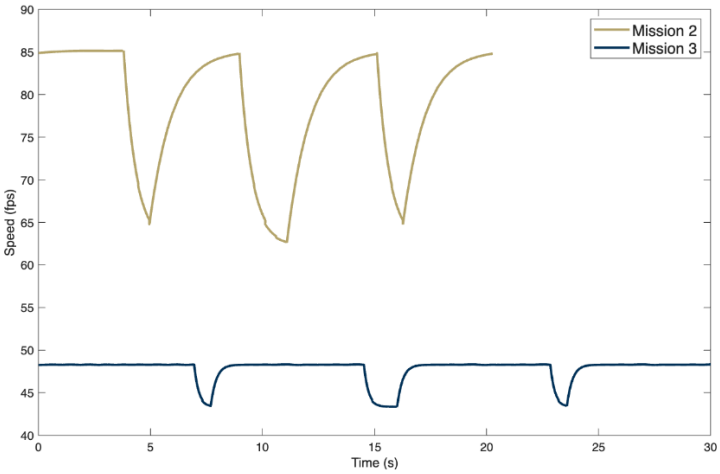

Figure 5.12 Predicted Airspeed Through One Lap of M2 and M3

5.5 Drawing Package

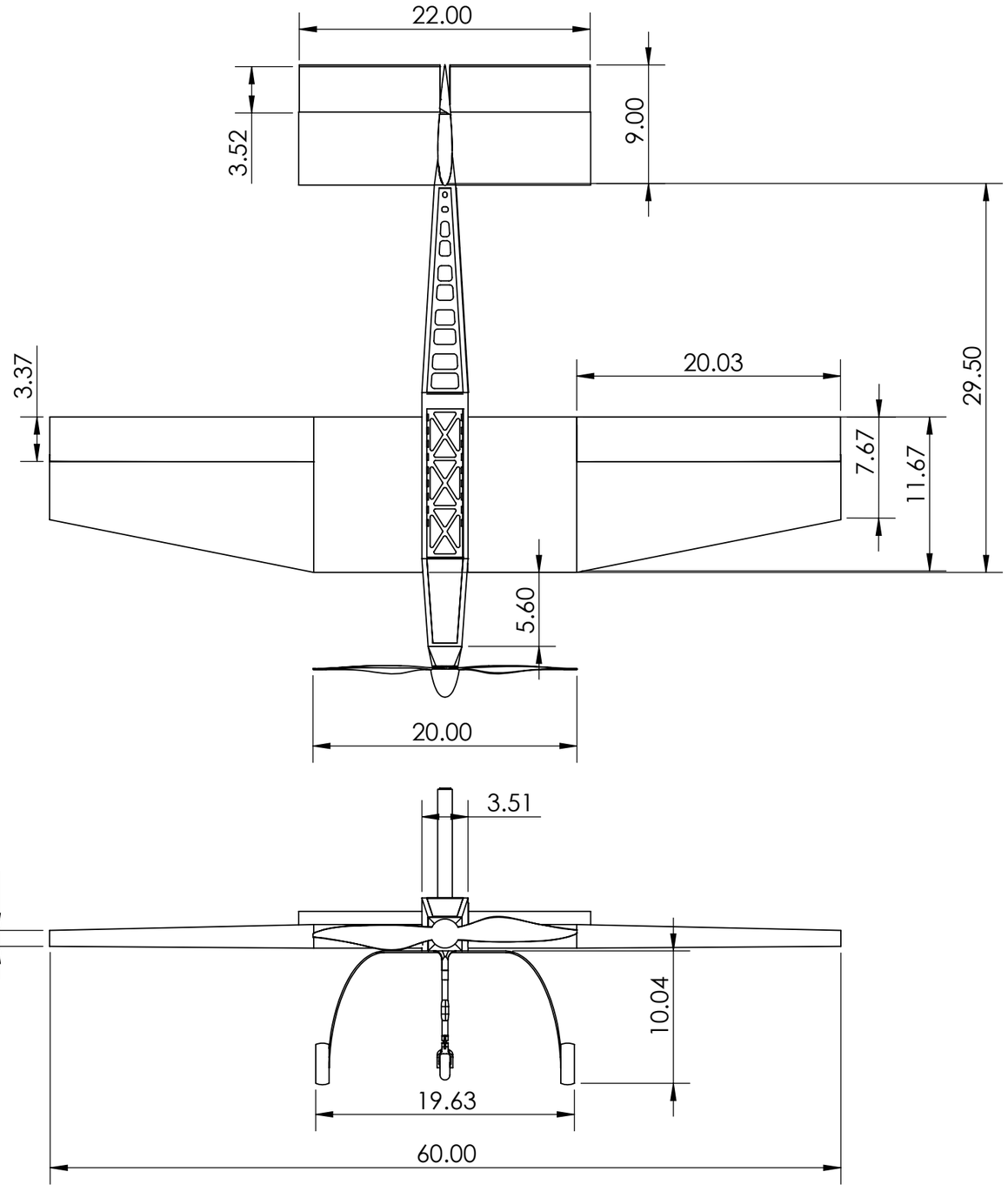

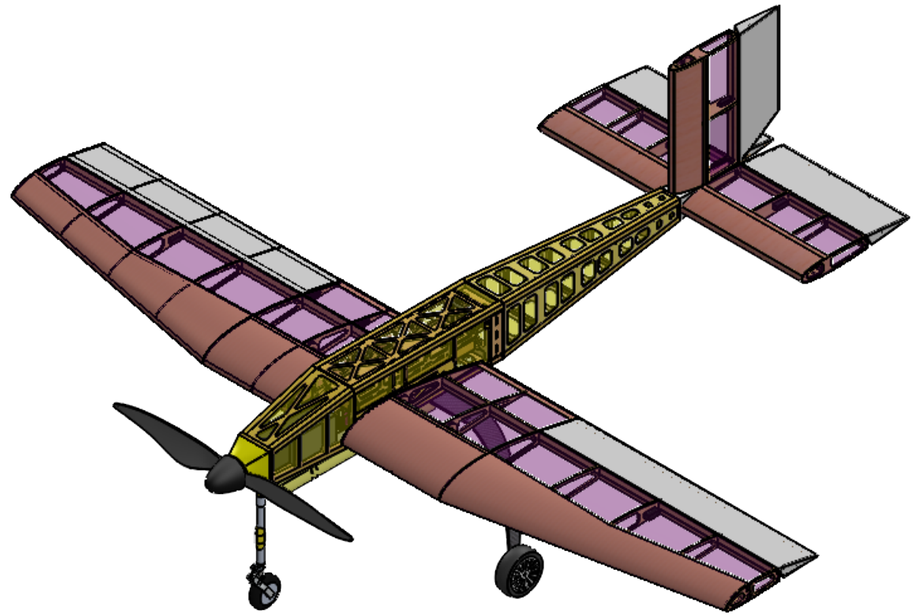

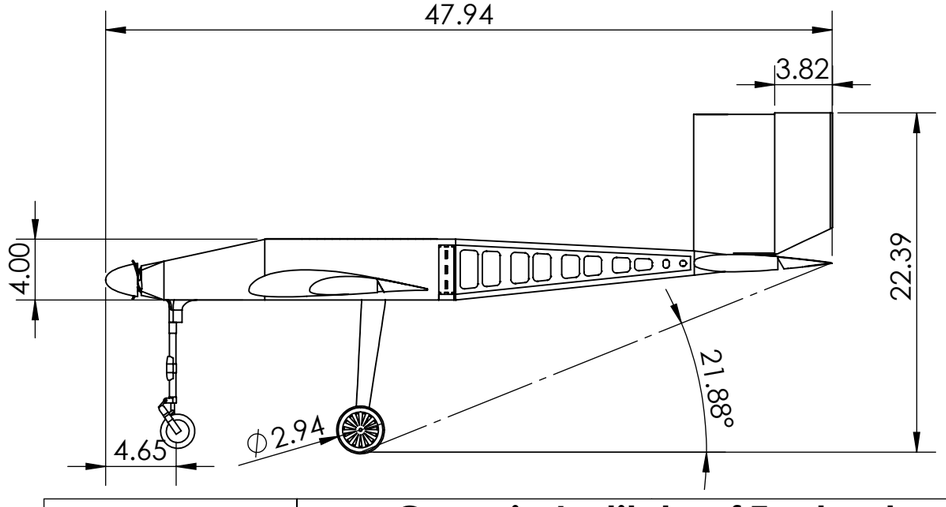

2/15/2026	**Georgia Institute of Technology**	
Drawn by: Neel Koney	Buzzerang	
Checked by: George P. Burdell	Size B	Aircraft Three-View with Dimensions
Scale 1:10	All Dimensions in Inches	Sheet 1 of 4

Parts List			
ITEM NO.	QTY.	ITEM NAME	MATERIAL
1	1	Nose Landing Gear	Aluminum
2	1	Nose Wheel	Rubber
3	1	Banner Deployment System	3D Printed PLA
4	1	Main Landing Gear	Carbon Fiber
5	2	Main Wheel	Rubber
6	14	Wing Ribs	Plywood and Balsa
7	2	Aileron	Balsa
8	3	Passenger Restraint	Foam
9	1	Cargo/Passenger Separation Wall	Balsa
10	1	Cargo Restraint Box	Plywood
11	1	Horizontal Stabilizer	Plywood and Balsa
12	2	Elevator	Balsa
13	1	Rudder	Balsa
14	1	Vertical Stabilizer	Plywood and Balsa
15	1	Fuselage	Plywood and Balsa
16	1	Passenger Bay Door	Plywood
17	1	Wing Spar	Carbon Fiber
18	1	Front Hatch	Balsa
19	1	Motor Mount	Plywood
20	1	Nose Fairing	3D Printed PLA

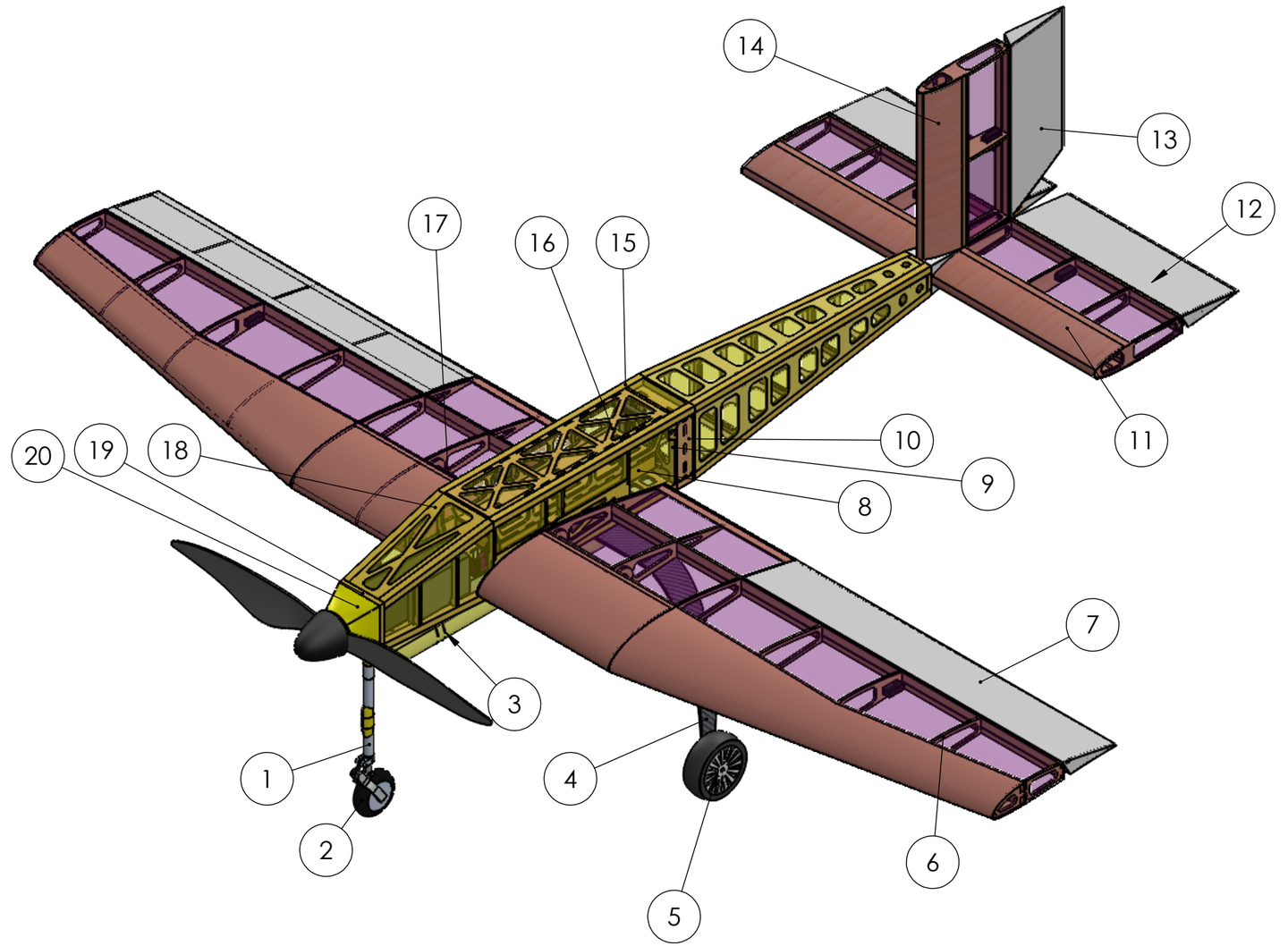

2/15/2026	**Georgia Institute of Technology**	
Drawn by: Neel Koney	Buzzerang	
Checked by: George P. Burdell	Size B	Aircraft Structural Arrangement
Scale 1:6	All Dimensions in Inches	Sheet 2 of 4

4	3	2	1

B

Systems List

ITEM NO.	QTY.	ITEM NAME	DESCRIPTION
1	1	Receiver Battery	1450mAh LiFe
2	1	Receiver	Futaba R7014SB
3	1	Fuse	100 Amps
4	2	Aileron Servo	MKS HV-6120
5	2	Banner Deployment Servo	MKS HV-69
6	2	Elevator Servo	MKS HV-6120
7	1	Rudder Servo	MKS HV-6120
8	1	Battery	6S 3300mAh LiPo OR 6S 4500mAh LiPo
9	1	Electronic Speed Controller	Castle Phoenix Edge Lite 130A
10	1	Propeller	APC 20 X 12E
11	1	Motor	Hacker A60-7XS

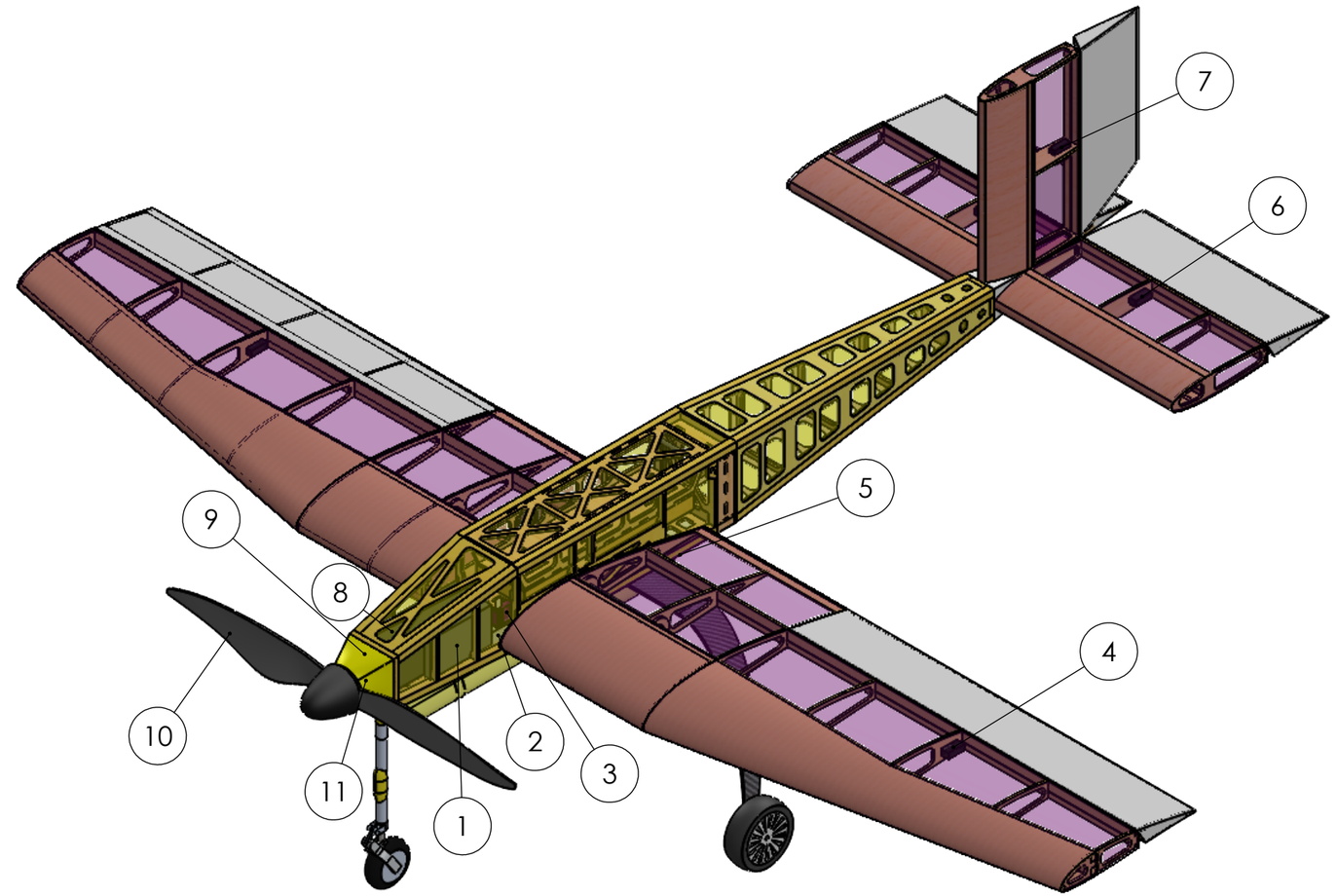

A

2/15/2026	**Georgia Institute of Technology**	
Drawn by: Neel Koney	Buzzerang	
Checked by: George P. Burdell	Size B	Aircraft Systems Layout
Scale 1:6	All Dimensions in Inches	Sheet 3 of 4

4 3 2 1

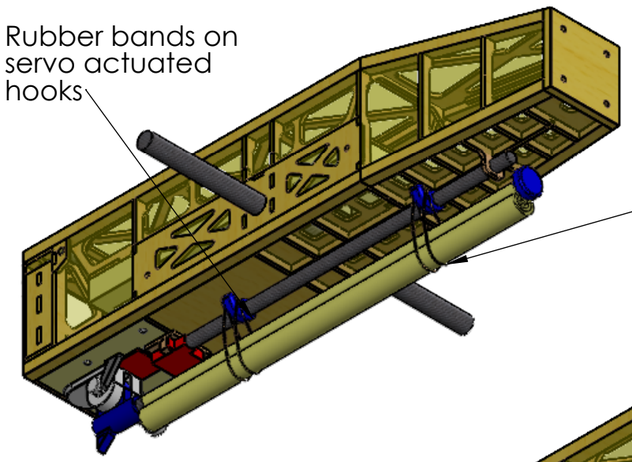

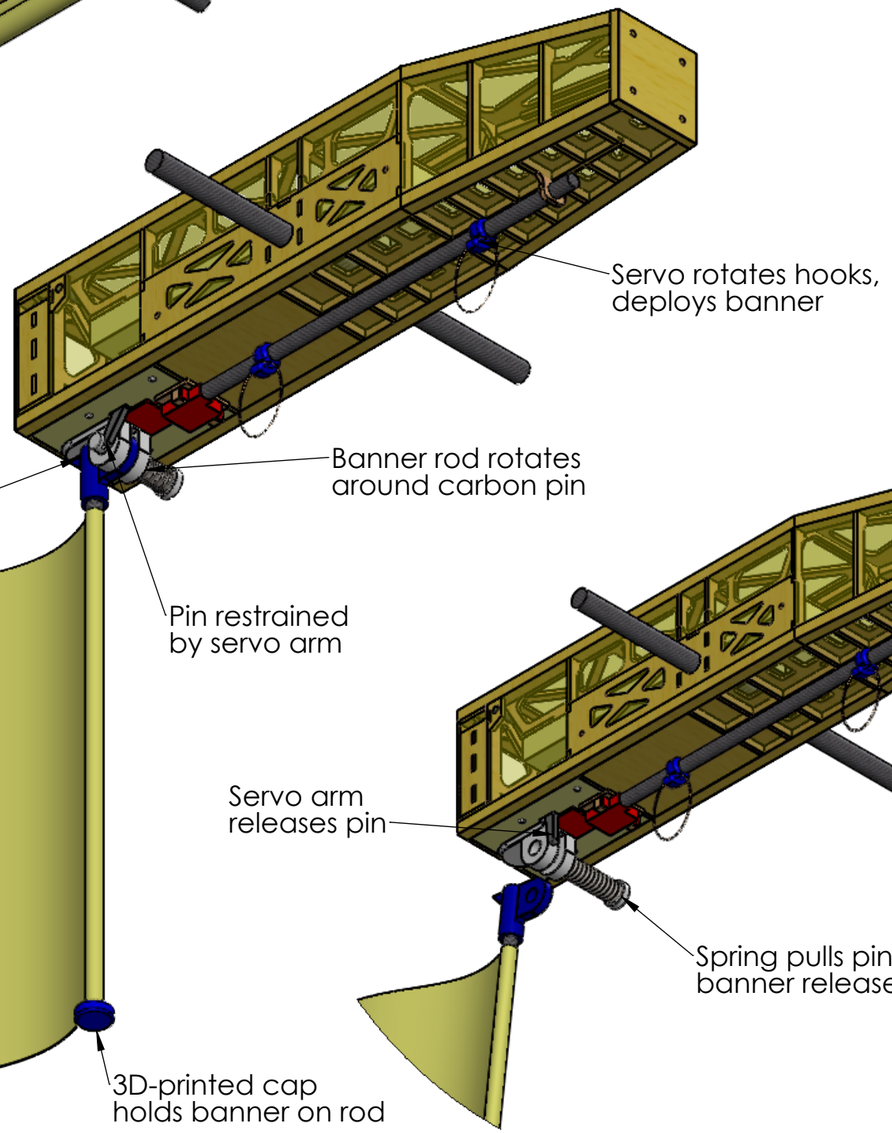

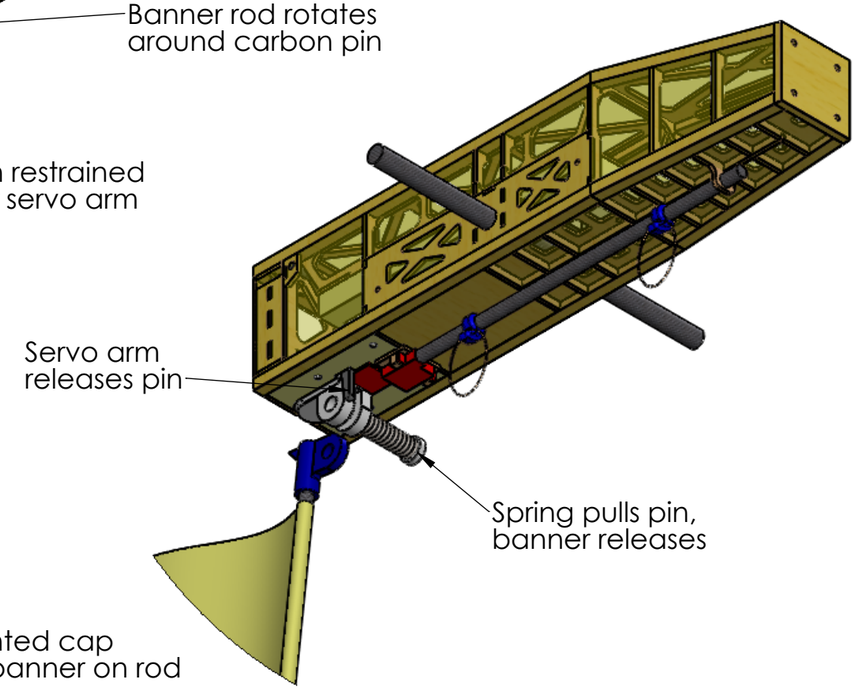

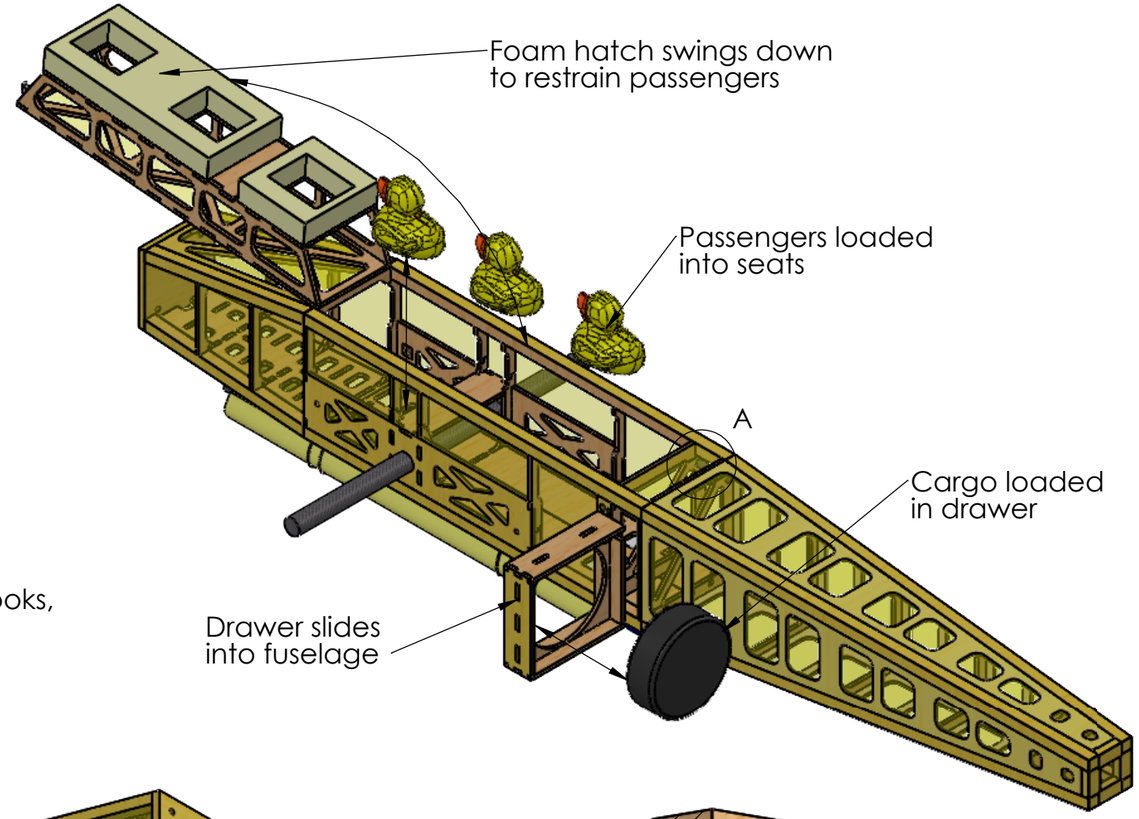

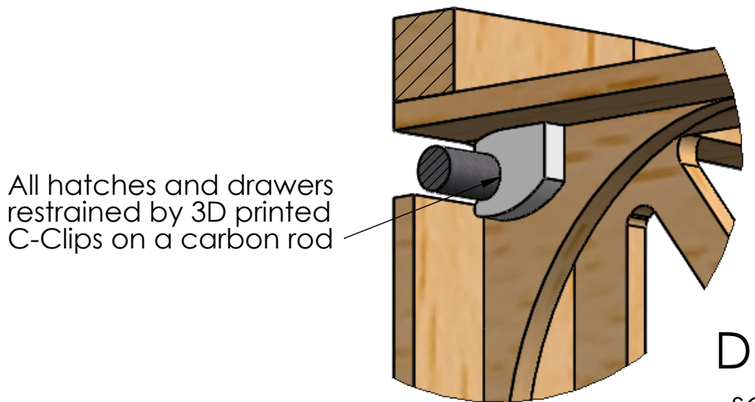

DETAIL A

SCALE 1.5 : 1

2/20/2026	**Georgia Institute of Technology**	
Drawn by: Adam Rupsis	Buzzerang	
Checked by: George P. Burdell	Size B	Payload Accommodations
Scale 1:8	All Dimensions in Inches	Sheet 4 of 4

6. MANUFACTURING

6.1 Processes Selected

The team selected manufacturing processes for the aircraft based on the analysis in Section 6.2 with the goal to ensure that the aircraft has minimum weight while maintaining structural integrity throughout all of the expected flight and landing load conditions. The construction methods used for different key components are detailed below:

- *Fuselage:* A balsa and plywood skeleton is assembled, fastened with CA, and covered in Monokote to form the fuselage shape. All bulkheads are laser-cut, connected with balsa stringers, and epoxied to a carbon fiber spine. Panels are cut into the fuselage to allow access to the internal structure and articulate via tape hinges. Additionally, plywood bulkheads and ribs form a box structure that strengthens the area near the payload bay, the wing spar, and main landing gear.
- *Wing:* Laser-cut balsa and plywood ribs form the lifting surfaces, which are scaffolded into position using a jigging matrix for support. Given the large bending loads in flight, carbon fiber tubes are used in the first two sections of the wing, with a strip of carbon fiber running along the top of the remaining wing. To ensure correct alignment, the wood pieces are fitted together on a flat surface using set squares, glued, and then left to set. To handle the high dynamic pressure around the leading edge during flight, the team bends a sheet of 1/32-inch balsa over this portion of the wing. All the servos and wiring are installed before coating the entire structure in Monokote.
- *Empennage:* Like the wing, the empennage employs the same manufacturing techniques of laser cutting, jigging and alignment, 1/32-inch balsa sheeting, and Monokote covering. The horizontal and vertical stabilizers are then slotted together into a plywood tail box, which is subsequently slotted into the back of the fuselage. The tail couples to the fuselage via plywood bulkheads, providing greater stiffness than balsa.
- *Landing Gear*: The main landing gear consists of two 3-inch wheels mounted on a carbon fiber bow. The main gear mounts via six bolts to a quarter-inch plywood plate. This mounting structure provides a load path for landing forces while dissipating some energy by elastically deforming the carbon bow. The nose gear is attached directly to the motor mount, allowing landing loads to follow a path along the already reinforced structure that carries motor loads.

Since the entire skeleton of the aircraft utilized built-up balsa and plywood construction, the following manufacturing methods were consistently used.

- *Task-Oriented Material Selection:* Balsa and plywood sheets are sorted by weight. Subsystem prototypes were built with the heaviest sheets, whereas aircraft prototypes and test articles were built with medium-weight sheets. The lightest wood is used to make the final aircraft for competition.
- *Lightening Holes:* To reduce aircraft weight without compromising structural integrity, the team removed sections of the structure that are subjected to lower loads.

- *Local Reinforcements*: The team reinforced key structural sections with additional balsa or plywood to ensure they could handle heavier loads. Restricting this reinforcement to the heavily loaded areas resulted in a stronger vehicle with minimal added weight.
- *Covering:* The airframe is covered with Monokote, a lightweight, heat-shrinking plastic, to reduce overall skin friction. This material was chosen since it successfully maintains the aircraft's general skin shape once applied and is easy to apply.

6.2 Processes Investigated

Numerous manufacturing techniques were considered to determine the simplest, most cost-effective, and most accessible materials for assembling the aircraft. The aircraft construction processes are described below, with a combination of techniques applied to each component of the airplane as required.

- *Built-Up Balsa:* The fuselage frame and wing rib components are designed using CAD and laser cut out of lightweight modeling-grade balsa, with select fuselage and critical wing rib components 47 cut out of thin plywood sheets. Components are glued together with cyanoacrylate (CA) and covered in Monokote.
- *Composite Layup:* By creating a mold of individual aircraft components, the manufacturing process involves fiberglass-epoxy or carbon fiber-epoxy layup to create different parts, which are then put together using bolts and nuts.
- *Foam Core Composite:* Components are cut out from a hard foam block using a CNC router or hot-wire cutter and are subsequently coated in a fiberglass monocoque. The components are put together using bolts and nuts, with additional structural elements supporting critical sections.
- *3D Printing:* CAD models are printed on a professional-grade 3D printer, with possible filament materials including PLA, PETG, SLA, and Carbon Fiber-Infused Nylon. Bolts and nuts are used to join these printed components.

The evaluation metrics used to decide manufacturing processes are listed below with their relative importance shown in Table 6-1:

- *Rate of Manufacture:* To manufacture flight-test prototype aircraft quickly and extensively, it is essential that the team can rapidly build, repair, and adjust the prototypes. This metric is critical to the project's timely progress, as a high rate of manufacture allows the team to produce numerous prototypes to test design iterations and repair damage incurred during flight tests.
- *Cost:* Due to limited finances, cost is a factor when deciding on manufacturing processes and materials. While the team's existing resources mitigate this concern to an extent, the team must still consider how to raise additional funding to obtain expensive new tools and components.
- *Experience:* While there are merits to new manufacturing processes, the existing expertise within the team with balsa and plywood construction must also be considered. Confidence and familiarity

with this manufacturing process also allow senior members to effectively train new members and to achieve consistent improvement of existing manufacturing processes.

- *Weight:* Throughout the manufacturing process, the weight of the aircraft is an integral part of all mission requirements, as it has the capacity to impact flight performance and payload capacity. It is also crucial for the aircraft's center of gravity to remain invariant from mission to mission.

Table 6-1: Score Factor Reasoning

Criteria	Factor	Rationale
Weight	5	Takeoff and flight performance.
Strength	5	Reliability under stress of travel and flight.
Durability	3	Longevity throughout competition.
Ease of Manufacturing	3	Manufacturing feasability and production speed.
Cost	2	Budget constraints.
Experience	4	Qualitty of components.

The manufacturing methods were evaluated on these metrics using a Pugh matrix shown in Table 6-2. The team chose to use balsa wood as the primary material for most of the aircraft's parts, while using composite materials for critical load paths and 3D printing for local parts. Carbon fiber spars served as the base of the aircraft and a balsa skeleton was used for the aerodynamic shell.

Table 6-2: Manufacturing Materials Pugh Matrix

Criteria	Score Factor	Balsa Wood	Plywood	Composites	Foam	3D Print	Monokote
Weight	5	4	3	3	5	2	5
Strength	5	4	5	5	3	3	4
Durability	3	4	4	5	3	4	4
Ease of Manufacturing	3	5	4	1	3	3	2
Cost	2	2	3	2	3	5	4
Experience	4	4	4	2	3	4	5
Totals		87	86	70	76	72	91

6.3 Manufacturing Timeline

The Gantt chart for Prototype 1, illustrated in Figure 6.1, demonstrates a manufacturing timeline in which delays in construction caused by equipment issues and weather conditions were effectively managed. Despite the delays in wing and tail construction, Prototype 1 was finished in five weeks, allowing

for sufficient testing to gather data to improve the next prototype. Prototype 2 was essentially Prototype 1 with different banners and banner release mechanisms.

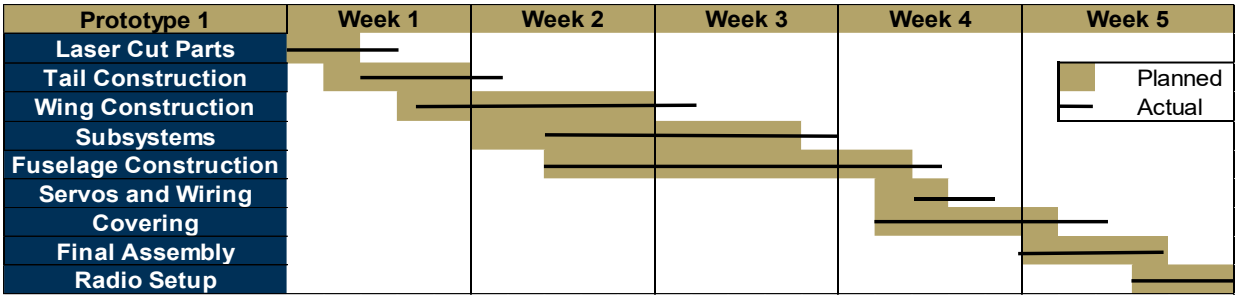

Figure 6.1: Manufacturing Timeline for Prototype 1

7. TESTING PLAN

7.1 Major Ground and Flight Tests Planned

The team's plans for subsystems, ground, and flight tests are contained in Table 7-1 and Table 7-2, respectively. The test methods and success criteria are derived from previous years' experience and mission requirements.

Table 7-1: Major Flight Testing Plan

Category	Test Type	Method	Objective	Success Criteria
Flight Testing	First Flight	Take off, fly lap, land	Evaluate stability and control at low speed	Aircraft is capable of safe flight and landing
	Envelope expansion	Incremental banner size increase	Evaluate high-speed vibration/buffet and controllability	Minimal high-speed vibrations Good maneuverability
	Banner Drag Test	Deploy banner after one lap	Characterize aircraft performance under banner drag	Banner performs as expected Aircraft performance remains predictable after deployment
	Banner Mechanism Test	Deploy banner after one lap	Evaluate release mechanism reliability and structural integrity	Release mechanism works as expected, little to no damage to mechanism
	Mission 2 Optimization	Evaluate turning/ flying techniques	Minimize battery capacity while maximizing laps completed	Identify flying techniques for best score
	Mission 3 optimization	Vary power settings and turn radii	Maximize number of laps completed	Identify power settings and turn rate for best score

Table 7-2: Major Subsystem Test Plan

Category	Test Type	Method	Objective	Success Criteria
Subsystem Testing	Static Thrust	Test stand	Evaluate varying propeller performance	Produce required thrust Battery discharge validation
	Payload Bay Test	Load cargo into payload bay	Simulate ground mission loading conditions	Payload Bay withstands applied load No observed fatigue or failure
	Passenger Compartment Test	Load passengers into compartment	Simulate ground mission loading conditions	Compartment withstands applied load, no observed fatigue or failure
Ground Testing	Landing Gear Test	Drop aircraft from a height of 6”	Evaluate robustness to hard landing	Little to no damage to aircraft or landing gear
	Wing Tip Load Test	Suspend fully loaded aircraft from wingtips	Evaluate aircraft structural integrity	No damage to aircraft Minimal wind bending
	Ground mission loading	Complete mock ground missions	Optimize GM loading times	Subsystems withstand loading conditions, minimize GM time
	Pre-Flight Inspection	Complete CG, controls, fail-safe, taxi, and ground test	Validate aircraft safety and operability	All controls operational Acceptable static margin Aircraft is controllable

7.2 Test Objectives

7.2.1 Propulsion Tests

While prototypes of *Buzzerang* are designed and manufactured, preliminary tests of the propulsion system are conducted to ensure it meets all technical requirements and matches predicted performance. Propulsion testing is divided into static thrust testing and wind tunnel testing.

7.2.2 Structural Tests

Buzzerang will undergo multiple structural tests to ensure its safety and mission capability. The team will perform a wingtip test to both comply with competition rules and ensure that the wings, while subjected to flight loads, are sufficiently stiff. A drop test will be conducted from a height of six inches to evaluate the aircraft’s structural integrity in the event of a hard landing.

7.2.3 Subsystem Tests

The primary subsystem tested on *Buzzerang* is the banner deployment and release mechanism and the banner material itself. The team will test various banner materials to find the material that minimizes drag and the negative effect on the handling of the aircraft. Once the best material is determined, the length

of the banner will be iteratively increased while keeping the aspect ratio constant to characterize how banner drag and handling are affected with longer banners. Concurrently, the banner deployment and release mechanism will undergo multiple tests and iterations to ensure safety and reliability. As the banner length, and therefore its drag contribution, increases the load on the banner system will also increase. The team will visually inspect the banner system for any damage after each flight and improve the strength of components as necessary. Additionally, the passenger and cargo restraints will be tested in mock ground missions to ensure their structural integrity under the loads sustained under such conditions while optimizing GM times. The passenger and cargo restraints will also be tested before flight with rigorous shake tests to ensure they will not shift in flight.

7.2.4 Flight Tests

Buzzerang will complete several milestone flight stages throughout its testing campaign. The objective of the first flight is to evaluate the aircraft's stability and flight worthiness. The aircraft is kept well within the expected limits of its flight envelope and all maneuvers are performed up and away in following with proper flight test principles. The aircraft is monitored for significant trim issues, excessive wing/fuselage bending, and the presence of Dutch roll. After the successful completion of the first flight, envelope expansion begins, with speed, load factor, and static margin. The objective of this phase is to validate predicted aircraft performance and assess high speed stability. The subsystems are then integrated to build up to final competition configuration. During the weeks leading up to competition, simulated M2 and M3 flights will be completed to increase the pilot's familiarity with the plane and ensure expected lap times are able to be met consistently.

7.3 Data to be Collected and Applications

7.3.1 Propulsion Tests

Propulsion tests use a test stand pictured in Figure 7.1 to validate static thrust production while monitoring battery discharge rates. This data is used for both propulsion system selection and scoring analysis.

Figure 7.1 Static Thrust Test Stand

7.3.2 Structural Tests

The primary objective for structural testing is to evaluate the structural integrity of subsystems and *Buzzerang* to determine load limits for flight testing and competition. The team's primary test is a wing tip, shake, and drop test. Any damage, deflections, or structural failures relating to both *Buzzerang*, payload, and the passenger compartment will be observed and noted for future iterations. The banner subsystems are evaluated in a wind tunnel to assess system controls, reliability, and load capacity.

7.3.3 Subsystem Tests

The passenger compartment and banner subsystems are integrated in *Buzzerang* P0, P1, P2, and P3. The subsystems will be loaded under conditions that simulate the GM, testing their structural integrity while optimizing GM loading times. The passenger and cargo restraint mechanisms will be tested to ensure that loading and unloading can be performed in an orderly and timely manner without damaging the aircraft. Additionally, the aircraft will undergo a shake test before each flight with the passengers and cargo installed to ensure their proper restraint, and after each flight, the passengers and cargo will be inspected for any in-flight shifting. Banner mechanism ground testing will explore quick and effective methods for rolling and loading the banner system onto the aircraft. Banner material and stitching will also be checked before and after every flight to ensure no rips or tears have developed. Flight testing with fully loaded subsystems evaluates their robustness and the strength of the fuselage's internal structure.

7.3.4 Flight Tests

Flight tests are conducted conservatively to avoid unnecessary damage. Each new prototype or modified aircraft undergoes a first flight without a payload to evaluate the aircraft's trim, airworthiness, and overall functionality. For each iteration, banner size and payload are gradually increased until the full mission configuration is reached. Each flight is equipped with an *Eagletree Airspeed Micro Sensor V3* and a GPS telemetry package to quantify performance. The sensor collects ground speed, all-axis acceleration, and position data. Ground-based camera recordings are also used to document all flights and evaluate pilot techniques.

7.4 Test Schedule

Several tests simulating various mission conditions were conducted to validate the results of banner sensitivity analysis, along with the structural and aerodynamic performance of *Buzzerang*. The scheduling of these tests is outlined in Table 7-3, and their results are noted in Section 8.

Table 7-3 Test Schedule

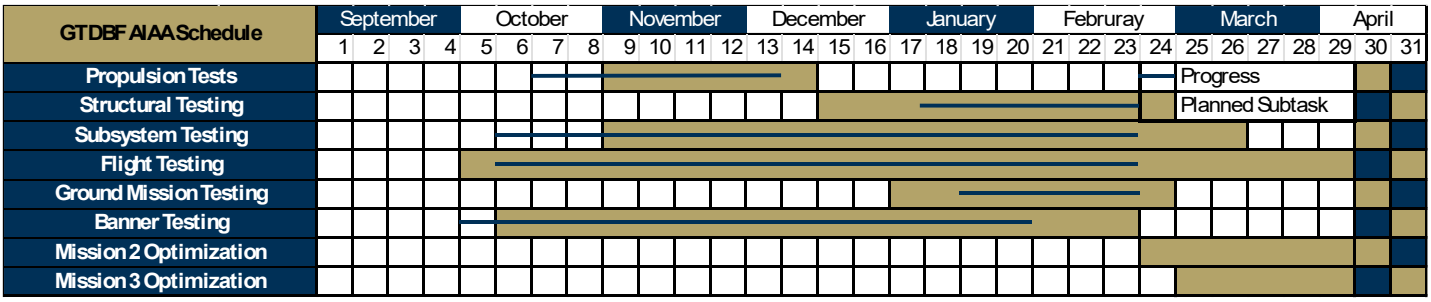

7.4.1 Checklists

Multiple test procedures were developed to minimize risks and ensure flight readiness. The propulsion checklist shown below in Table 7-4 was created to ensure the safety of the team while working with propulsion equipment. The checklist monitors the propeller, motor, and battery in several operating states.

Table 7-4: Propulsion Testing Checklist

Propulsion Test Checklist		
Before Test	**During Test**	**After Test**
✓ Propeller, Motor Mount, Wires Secure ✓ Batteries Checked ✓ Throttle Idle ✓ Test Rig Cleared	✓ Throttle Full ✓ Throttle Reversed ✓ Check Current and Voltage ✓ Propeller Rotation Check	✓ Throttle Idle ✓ Battery Disconnected ✓ Battery Check ✓ Data Extracted

Table 7-5 outlines the structural testing checklist for *Buzzerang*. The team utilizes this checklist to confirm that the aircraft is properly configured for testing and that the data is properly collected.

Table 7-5: Structural Testing Checklist

Structural Test Checklist		
Before Test	**During Test**	**After Test**
✓ Propeller, Connections, Fasteners Secure ✓ Passengers and Cargo Secure ✓ Banner Mechanism Attached	✓ Vehicle Hatches/Doors Closed and Secure ✓ Aircraft Remains Stable During Tests ✓ Passengers and Cargo Remain Restrained ✓ Banner Remains Secure	✓ Inspection for Damage ✓ Data Extracted

The subsystem testing checklist provided in Table 7-6 was created to ensure that all subsystems, including the passenger accommodation, cargo accommodation, and banner mechanism are safely handled. This checklist outlines the methods through which all the aircraft's subsystems are validated for testing and confirmed safe and secure.

Table 7-6: Subsystem Testing Checklist

Subsystem Test Checklist		
Before Test	**During Test**	**After Test**
✓ Fasteners, Connections Secure/Charged ✓ Passengers and Cargo Secure ✓ Banner Damage Inspection ✓ Banner Mechanisms Check	✓ Banner Drop Mechanism Functional ✓ Banner Release Mechanism Operational	✓ Inspection for Damage ✓ Banner Wear and Tear Check ✓ Data Extracted

The flight test checklist, as outlined in Table 7-7 was developed to reduce the failure risk of critical flight systems, thus ensuring the aircraft maintains its ability to achieve test objectives. The flight test checklist monitors a wide variety of *Buzzerang*'s systems, making thorough adherence to the checklist paramount to a successful flight.

Table 7-7: Flight Testing Checklist

Flight Test Checklist		
Before Test	**During Test**	**After Test**
✓ Propeller, Fasteners, Connections Secure ✓ Primary Battery Secure/Charged ✓ Control Surfaces Free/Operational ✓ Receiver Plugged In ✓ Receiver Battery Secure ✓ Banner/Passengers/Cargo Secure ✓ Banner Mechanism Check ✓ CG Validation ✓ Runway Clear	✓ Vehicle Hatches/Doors Closed and Secure ✓ Banner Deployment Functional ✓ Banner Release Operational	✓ Throttle Idle ✓ Battery Disconnected ✓ Flight Data Extracted

8. PERFORMANCE RESULTS

8.1 Component and Subsystem Performance

8.1.1 Propulsion

The results from static thrust testing were used to validate predictions made using the Whitmore tool. The team used the insights gained from propulsion test data to determine the ideal propeller size that optimizes both static thrust and power draw. Specifically, the team tested the APC 17x10E and APC 17x8E propellers, both powered by a T-motor AT4130 KV450 motor. Figure 8.1 and Figure 8.2 display the difference in predictions made using the Whitmore tool and results from testing for static thrust and current draw, respectively. Test data confirmed the decision to use the APC 17x10E propeller as it generated more thrust while drawing less power than the APC 17x8E propeller. Overestimates by the Whitmore tool [1] are

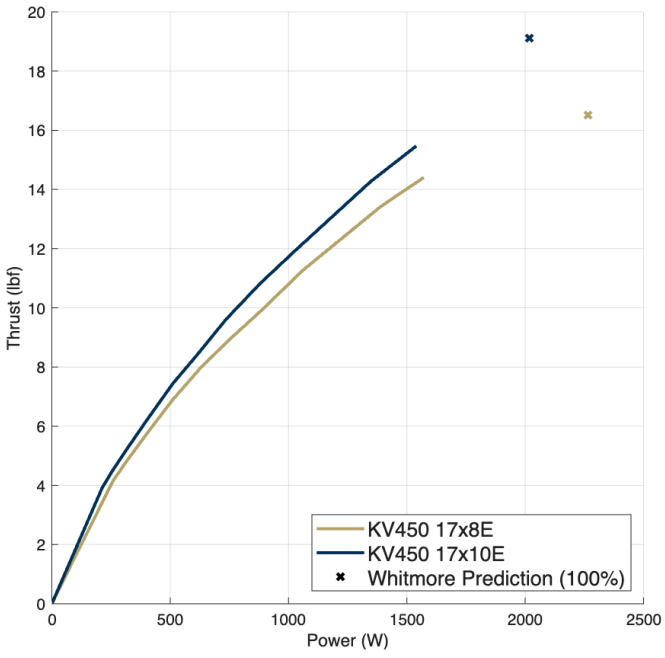

Figure 8.1 Predicted vs Actual Current Draw

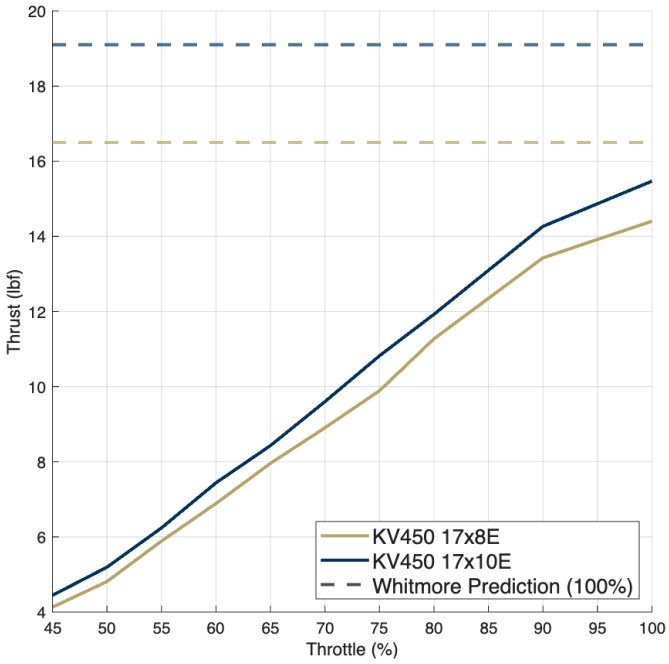

Figure 8.2 Predicted vs Actual Static Thrust

attributable to testing conditions that do not account for any manufacturing sources of error and use an ideal battery.

8.1.2 Structural Testing

The completed aircraft underwent various structural tests comprising of wing tip tests, drop tests, and shake tests. Wing tip load tests were performed at the aircraft's maximum weight, including the full payload of the passengers and passenger compartment, cargo and cargo bay, and banner subsystem as shown in Figure 8.3Figure 8.3. Drop testing on the aircraft was then conducted at MTOW from a height of six inches, assessing the durability of the landing gear and the structure. Finally, the aircraft was subject to a shake test to evaluate the sturdiness of the aircraft, particularly the banner mechanism connection to the fuselage. All subsystems were tested independently using testbeds prior to integration into the main aircraft, ensuring their durability and structural integrity. Structural testing confirmed the strength of the aircraft's structure and its subsystems.

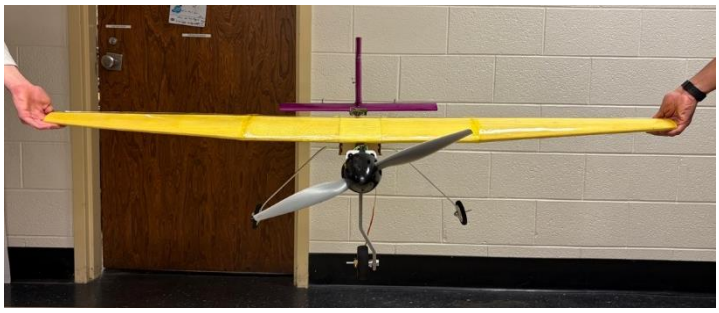

Figure 8.3 Wingtip Load Testing of Buzzerang 0

8.1.3 Banner Testing

Optimizing *Buzzerang's* performance with the banner deployed is crucial for maximizing the M3 score. Thus, the team tested several materials for the banner, including 30-denier and 420-denier ripstop nylon, chiffon, and nylon mesh. As seen in Figure 8.4, these materials were tested using Georgia Tech's wind tunnel to ensure that the banner mechanism would be strong enough to handle the loads. Additions and modifications to the banner, such as streamers made of 420 denier ripstop nylon, were considered and tested. While scoring analysis was the main factor in choosing the banner size, data from the *Eagletree Airspeed Micro Sensor V3* was the primary factor in determining the material, based on flight testing performed with the first simple prototype and banner system. Data was collected with multiple banner materials and modifications with an approximate power model estimated as a function of airspeed. As shown Figure 8.5, a 30-denier ripstop nylon banner resulted in the smallest decrease in performance compared to a clean configuration aircraft with a power penalty of roughly 70 percent, and it was therefore selected as the final banner material.

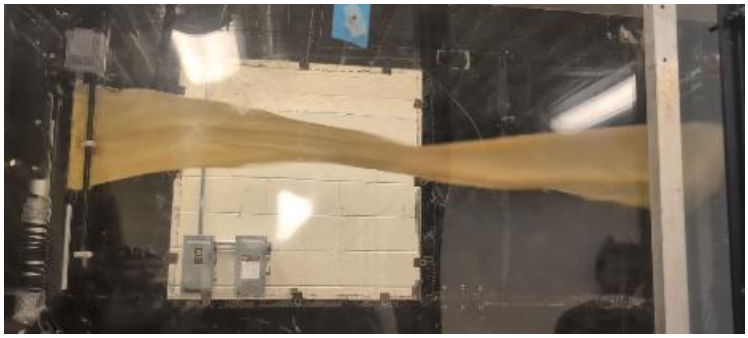

Figure 8.4 Banner Wind Tunnel Testing

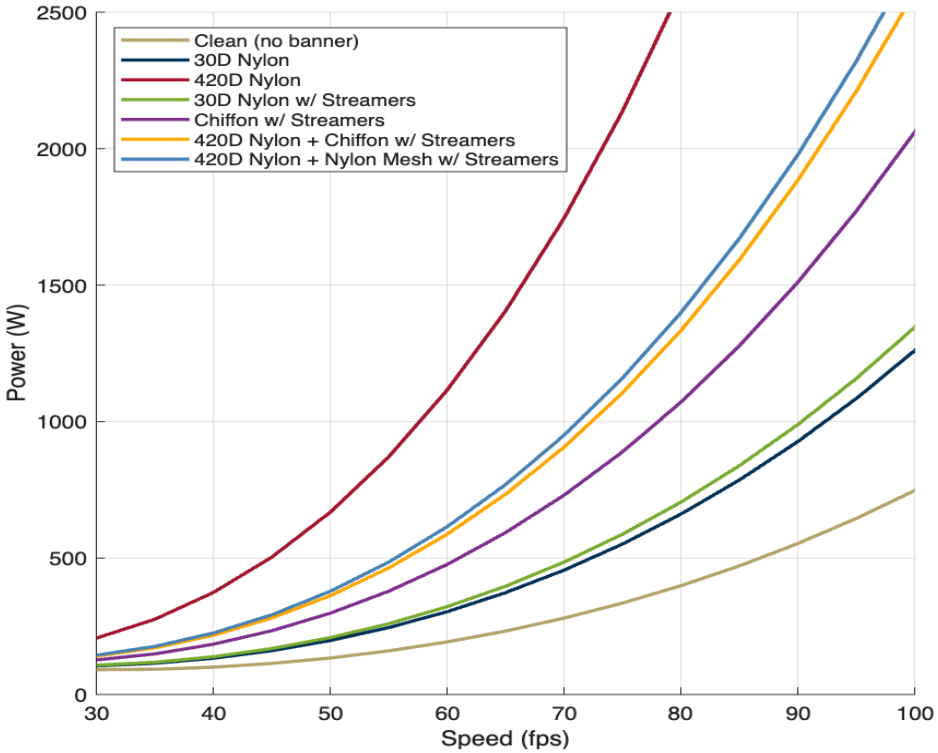

Figure 8.5 Comparison of Power Required as a Function of Airspeed for Different Banner Materials

8.2 System Performance

8.2.1 Ground Mission

The GM was rehearsed once the aircraft subsystems were finalized to allow the ground crew member to gain experience. The first section is to load the passengers and cargo, which requires approximately seven seconds for the passengers and approximately three seconds for the cargo. The next timed segment requires the member to remove the passengers and cargo, which takes about nine seconds, and then install and load the banner subsystem, which requires around ten seconds. The complete GM time is approximately 30 seconds, but the team expects the time to improve as the subsystems are refined to improve performance in GM, and the ground crew member continues to improve the loading process.

8.2.2 Flight Testing

Flight tests were conducted to confirm airworthiness, establish trim settings, and evaluate performance capabilities. The first flight test was conducted with no payloads to validate initial performance and handling benchmarks. The succeeding flights expanded the flight envelope to evaluate the aircraft's high-speed characteristics and capabilities. Passengers and cargo were then added for M2, with the banner mechanism later being added for M3.

Each flight was recorded using an Eagle Tree GPS inside the fuselage, which tracks the aircraft's position, altitude, acceleration, and speed. Ground Spotters signaled turns to the pilot during full competition laps. The recorded GPS data was used to validate the flight path against a competition-style lap, as illustrated in Figure 8.6.

Figure 8.6 Recorded Flight Path of Single Competition Lap

Table 8-1 presents the aircraft's system performance based on multiple flight tests and compares it to the predicted performance outlined in Section 4.

Table 8-1 Predicted vs Flight Test Performance Results

	1st Lap Times (s)		Time for 360 (s)		Laps Flown		Max Speed (fps)	
	Predicted	Actual	Predicted	Actual	Predicted	Actual	Predicted	Actual
M1	25.56	33.46	3.1	4.2	3	3	85.2	75
M2	20.30	28.25	2.7	4.0	10	9	85.1	89.0
M3	30.43	36.25	3.8	4.6	7	6	48.3	58.1

For M1, M2, and M3, the predicted lap times were consistently shorter than the actual lap times due to several factors that are not considered by the prediction model such as wind gusts and variation in flight path. These same factors also likely caused the minor discrepancies between the predicted and actual 360-degree turn times and maximum speeds. The M1 predictions have faster lap times due to the failure to account for a throttle limiter on the ESC. The seemingly large difference between predicted and actual maximum speed for M3 can likely be attributed to a brief tailwind gust during data collection.

Figure 8.7 compares the predicted speed and GPS-measured speed through one lap for M2. The speed predictions yielded a M2 lap time of 20.3 seconds, while experimental data had a lap time of 28.8 seconds. This difference can be attributed to an inconsistent heading through straightaways and an inconsistent altitude throughout the lap, causing greater decreases in air speed during flight testing as well as the prediction model's failure to account for wind gusts and the time it takes to rotate.

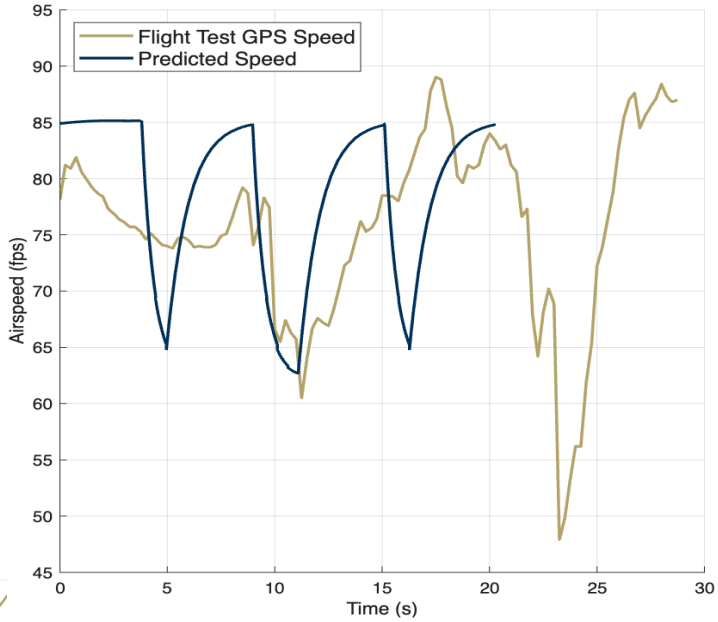

Figure 8.7 Measured and Predicted M2 Speed

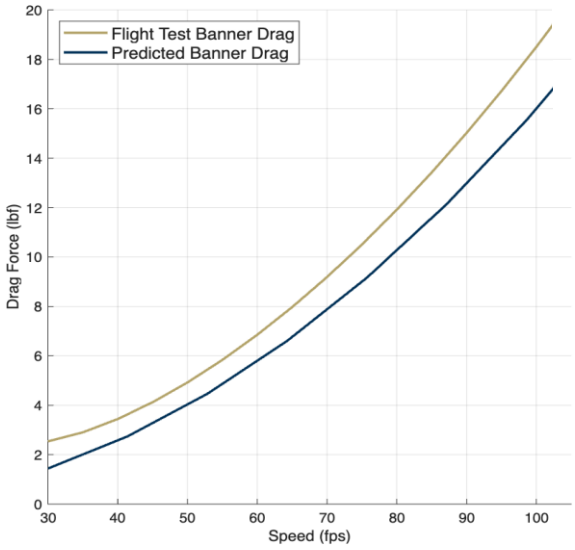

Figure 8.8 Measured and Predicted Banner Drag

Figure 8.8 compares the predicted and experimental drag force generated by the banner. The experimental drag force was 7.39% greater than predicted on average across various speeds. This discrepancy can be attributed to the prediction model's failure to account for various banner properties such as texture, stiffness, and denier.

9. CONCLUSION

This report has demonstrated the process undertaken to translate the ruleset into clear, measurable, and achievable design and test objectives, whilst also managing a team of varied experiences and skill levels. *Buzzerang* is a 4.32 lb aircraft built to carry three passengers and one cargo in M2 for 9 laps, tow a 75" x 15" banner in M3 for 6 laps, and achieve a GM score under 30 seconds. The team believes that *Buzzerang* will prove to be a strong competitor for the 2025-26 Design, Build, Fly Competition.

10. BIBLIOGRAPHY

[1] Whitmore, W. V., "*Development of a Multidisciplinary Design Analysis Framework for Unmanned Electric Flying Wings*," Master's Thesis, Georgia Institute of Technology, Atlanta, GA, 2019, SMARTech.

[2] Carruthers, A. C., Filippone, A., "Aerodynamic Drag of Streamers and Flags", *Journal of Aircraft* Vol. 42, No. 4, July-August 2005

[3] Drela, M., and Youngren, H., "*AVL Overview*", Massachusetts Institute of Technology [online], 2008, http://web.mit.edu/drela/Public/web/avl [retrieved 21 February 2018],

[4] Mattingly, J. D., Heiser, W. H., and Daley, D. H., *Aircraft Engine Design*, Third Edition | AIAA Education Series Available: https://arc.aiaa.org/doi/book/10.2514/4.105173.

[5] Drela, M., and Youngren, H., "XFOIL", Massachusetts Institute of Technology [online], 2013, https://web.mit.edu/drela/Public/web/xfoil [retrieved 21 February 2018]

[6] Lyon, C.A., Broeren, A.P., Giguere, P., Gopalarathnam, A., Selig, M.S., *Summary of Low-Speed Airfoil Data*, vol. 3, SoarTech Publications, 1997.

[7] *Parasite Drag Tool*. Available: http://openvsp.org/wiki/doku.php?id=parasitedrag. [retrieved 15 October 2019].

[8] Hoerner, S. F., *Fluid Dynamic Drag*, 2nd ed., Published by author, 1992.

[9] Wilk, A and Skuta, M., "Laboratory Tests of the Aerodynamic Drag Coefficient of the Flag as a Body with Low Stiffness". *Task Quarterly,* Vol. 13, Nos. 1-2, 2009, pp. 5-14

[10] Phillips, W. F., *Mechanics of Flight*, 1st ed., Wiley, Hoboken, NJ, 2004.

[11] *Average Wind Speed in Wichita*. Available: https://weatherspark.com/y/8281/Average-Weather-in-Wichita-Kansas-United-States-Year-Round#Figures-WindSpeed [retrieved 15 February 2024]

[12] Anderson, J.D., *Aircraft Performance and Design*, 1st ed., Boston, MA: McGraw-Hill, 1999.

[13] Bauchau, O. A. Craig, J. I, *Structural Analysis: with applications to aerospace structures*, SPRINGER,2009.